Universidad de Granada
Departamento de Física Teórica y del Cosmos

THE CHEMICAL HISTORY OF STAR-FORMING GALAXIES IN NEARBY CLUSTERS

Memoria presentada por
VASILIKI PETROPOULOU
realizada en el Instituto de Astrofísica de Andalucía, Consejo Superior de Investigaciones Científicas, bajo la dirección de
JOSÉ MANUEL VÍLCHEZ MEDINA & JORGE IGLESIAS-PÁRAMO,
para optar al grado de DOCTORA INTERNACIONAL

INSTITUTO de ASTROFISICA de ANDALUCIA
CSIC
I·A·A

CSIC
CONSEJO SUPERIOR DE INVESTIGACIONES CIENTÍFICAS

Editor: Editorial de la Universidad de Granada
Autor: Vasiliki Petropoulou
D.L.: GR 83-2013
ISBN: 978-84-9028-276-2

“Some are influenced by the love of wealth while others are blindly led on by the mad fever for power and domination, but the finest type of man gives himself up to discovering the meaning and purpose of life itself. He seeks to uncover the secrets of nature. This is the man I call a *philosopher*: for although no man is completely wise in all respects, he can love wisdom as the key to nature’s secrets”.

Pythagoras is believed to have coined the word philosopher (φιλό-σοφος): the man who loves wisdom.

Στους γονείς μου Ελευθερία και Χρήστο
που μου έμαθαν την υπομονή και την επιμονή

Resumen

El objetivo de esta tesis doctoral es el estudio de la influencia del entorno sobre la historia química de las galaxias con formacion estelar en una muestra de cúmulos cercanos del Universo local. Este fin se ha alcanzado mediante el estudio de las relaciones fundamentales entre la metalicidad de las galaxias y sus propiedades físicas más relevantes como la masa estelar, luminosidad, contenido de gas, actividad de formación estelar y su estructura.

Para llevar a cabo este estudio, se han realizado nuevas observaciones espectroscópicas del cúmulo A2151 en el rango óptico y con rendija larga utilizando los telescopios del Observatorio del Roque de los Muchachos WHT4.2m e INT2.5m. También se ha construido una base de datos espectroscópicos que se ha extraído del SDSS DR8, para una gran muestra de 781 galaxias de baja masa con formación estelar en los cúmulos A1656 (Coma), A1367, A779, A634, y A2147, A2151 y A2152 del supercúmulo de Hércules.

Se han calculado las abundancias químicas del medio interestelar ionizado de las galaxias de la muestra de esta tesis para las que se ha estudiado el comportamiento de las relaciones Masa-Metalicidad (MZR) y Luminosidad-Metalicidad (LZR) como función del entorno de las galaxias. El entorno de cada galaxia se ha parametrizado cuantitativamente en función de su distancia al centro del cúmulo y de su densidad local.

Entre las conclusiones más importantes de este trabajo destacamos que hemos encontrado que la relación MZR para el grueso de nuestra muestra de galaxias con formación estelar en cúmulos sigue el mismo comportamiento encontrado por otros autores para muestras de galaxies de campo en el Universo local (también para el cociente N/O en función de la masa estelar). De manera notable, fuera de las partes centrales de los cúmulos más masivos, la pendiente que se deriva para la MZR está de acuerdo con las predicciones de los modelos hidrodinámicos más recientes.

Aparte de este comportamiento general, hemos encontrado que las galaxias de baja masa que pueblan las regiones interiores de los cúmulos A2151, A1367 y (especialmente) Coma, presentan valores de O/H y N/O superiores al valor promedio de las galaxies de campo para masas similares, lo que produce el aplanamiento de la relación MZR en las zonas centrales de los cúmulos, más intenso para los cúmulos más ricos.

Este resultado nos revela que la huella del entorno del cúmulo en la evolución química de las galaxias depende fuertemente tanto de la masa de la galaxia como de la del cúmulo, y pone de manifiesto el papel que pueden jugar las propiedades

del medio intergaláctico en la evolución química de galaxias en cúmulos.

En este marco, proponemos un escenario físico que podría explicar el aumento observado de la metalicidad de las galaxias de baja masa con formación estelar en los cúmulos, que emerge de forma natural de las prediciones de recientes modelos hidrodinámicos de evolución de galaxias en cúmulos. Desde este trabajo de tesis pretendemos motivar la realización de nuevos esfuerzos teóricos para la modelización de la evolución química de galaxias en entornos densos.

Otras conclusiones de esta tesis son las siguentes:

Encontramos que las galaxias espirales con formación estelar de A2151 presentan abundancias de oxígeno cercanas al valor solar y gradientes suaves de la abundancia de O/H, un resultado que nos sugiere la existencia de caída de gas en las partes centrales de estas galaxias. Para la relacion N/O, se han obtenido valores incluso superiores al valor solar en las partes centrales de algunas de estas galaxias, encontrándose variaciones radiales significativas de dicho cociente de abundancias.

Para las galaxias de A2151 hemos obtenido una tendencia muy clara para la metalicidad del gas, que se va aproximando a la metalicidad estelar cuando esta última aumenta desde $Z_{\odot}/2$ a $Z_{\odot}$. Los objetos fuera de esta tendencia, es decir aquellos menos evolucionados químicamente y con metalicidades similares en el gas y las estrellas, han sido identificados con las galaxias que están entrando al cumulo por primera vez ("newcomers").

Se ha obtenido una correlación general entre las abundancias O/H y N/O del gas y la edad estelar promedio pesada con la masa estelar ($\tau_{\star,M}$), siendo esta correlación más prominente frente al cociente N/O.

Los mapas bidimensionales del color $g-i$ y de la anchura equivalente de Hα EW(Hα) del cúmulo A2151 revelan la presencia de un filamento de galaxias con formación estelar, principalmente galaxias de baja masa, que entra por la parte Norte del cúmulo y se prolonga hasta el centro del cúmulo. Los mapas bidimensionales del color $g-i$ y de la anchura equivalente de Hα de los cúmulos A2152 y A2147 indican estructuras más virializadas. Sin embargo, se observa un filamento de galaxias de baja masa con formación estelar que se adentra en A2147 por la parte Sur-Este.

Las relaciones LZR y N/O frente a la luminosidad, para las galaxias de baja masa con formación estelar en el supercúmulo de Hércules demuestran una dispersión intrínseca que aparece correlacionada con el color $g-i$ de las galaxias.

Las galaxias enanas para las que se ha podido estimar la masa de gas neutro, HI, bien están localizadas en las partes externas de los cúmulos, o bien han sido incorporadas recientemente a los cúmulos y siguen las predicciones del modelo de "caja cerrada" de evolución química. En las partes centrales de los cúmulos, la fracción de galaxias enanas detectadas en HI es mínima lo que implica que estas galaxias han sufrido el efecto de despojamiento del gas debido a la presión de arrastre (RPS) ejercida por el medio intergaláctico.

Se ha encontrado que el aumento de la metalicidad para las galaxias enanas con formación estelar en las partes centrales de los cúmulos es muy significativo en las partes centrales del cúmulo más masivo de nuestra muestra (Coma, $M_\star \sim 10^{15} M_\odot$). A pesar de la buena relación general observada entre la densidad local de galaxias y la distancia al centro del cúmulo, el aumento de metalicidad como función de la distancia al centro del cúmulo es más importante que como función de la densidad local de galaxias, lo cual sugiere que el parámetro fundamental que afectaría a la evolución química de estas galaxias podría estar asociado a la presencia del máximo central en el medio intracumular ICM.

Finalmente, en este trabajo de tesis se ha llevado a cabo un estudio de las propiedades morfológicas y estructurales de las galaxias en el cumulo A2151. Basado en el mismo se ha podido realizar el seguimiento espectroscópico de estas galaxias utilizando espectroscopía de rendija larga. Para esta muestra de galaxias se han derivado masas estelares utilizando ajustes de sus distribuciones espectrales de energía, a partir de la fotometría de SDSS. Los parámetros fundamentales de la componente estelar subyacente de estas galaxias, tales como la metalicidad promedio y la edad, se han derivado a partir del ajuste espectral mediante la utilización del código de síntesis de poblaciones STARLIGHT.

Abstract

The aim of this thesis is to investigate the influence of environment on the chemical history of star-forming galaxies in a sample of local Universe clusters. We have achieved this goal through the study of the fundamental relations between the metallicity of galaxies and their main physical properties, such as stellar mass, luminosity, gas content, star formation activity and structure.

In order to carry out this study, we have obtained new optical long-slit spectroscopy of the A2151 cluster with the telescopes INT2.5m and WHT4.2m at the ORM. Additionally an extensive spectroscopic database has been extracted from the SDSS DR8, for a large sample of 781 low-mass star-forming galaxies in the clusters: A1656 (Coma), A1367, A779 A634 as well as in A2147, A2151, A2152 of the Hercules supercluster.

We have derived the chemical abundances of the ionized interstellar medium of our sample galaxies, for which we have studied the behavior of the MZR and LZR as a function of their environment. The environment has been quantified as a function of cluster-centric distance and also as a function of the local density of galaxies.

Overall, our sample of star-forming galaxies exhibits well defined sequences of stellar mass and metallicity (as parametrized by O/H, and the N/O ratio), following the well known general behavior for star-forming galaxies. Notably outside the cores of more massive clusters, the derived slope of the MZR is in agreement with the predictions of state-of-the-art hydrodynamic models.

Besides this global behavior, we have found that dwarf/irregular galaxies populating the densest regions in the A2151 cluster show higher metallicity for their mass and crowd the upper part of the MZR and N/O versus stellar mass relations.

Furthermore, low-mass star-forming galaxies located at cluster-centric distances $R \leq R_{200}$ in Coma (especially) and A1367, appear preferentially located at the upper side of the derived MZR global relations of O/H and N/O versus mass. This observed enhancement in metallicity appears to be dependent of galaxy stellar mass, being higher for the lower mass bins, thus flattening the MZR slope in the core of these massive clusters.

This observed behavior reveals that the imprint of the cluster environment shows up in a mass-dependent way, being both, galaxy mass and cluster mass, relevant parameters. This result suggests the important role that intra-cluster medium properties could play in the chemical evolution of cluster galaxies. A physical scenario has been proposed to explain the metal enhancement of low-mass star-forming galaxies in clusters, in the light of the predictions of recent hydrodynamic simulations for

galaxy evolution in clusters. Within this framework, this thesis aims at motivating further efforts in theoretical modelling of chemical evolution in dense environments.

Additionally to these main conclusions, in the present thesis we have reached other relevant results. We found that star-forming spiral galaxies in A2151 present oxygen abundances close to solar and shallow oxygen abundance gradients, a result suggesting possible gas infall at their centers. For the N/O ratio, even oversolar values have been obtained for the central parts of some galaxies and a significant spatial variation has been observed.

A clear trend was found for the gas-phase metallicity of A2151 galaxies, gradually approaching the stellar metallicity as the latter increases from $Z_{\odot}/2$ to $Z_{\odot}$. The outliers of this trend (less chemically evolved systems with approximately equal gas-phase and stellar metallicity) are identifiable with "newcomers" in the cluster environment.

An overall positive trend has been found in the gas-phase oxygen abundance versus the mass-weighted stellar age $\tau_{\star,M}$, which becomes more prominent in the case of the N/O ratio.

The 2D color $g - i$ and $EW(\mathrm{H}\alpha)$ maps of A2151 cluster have revealed the presence of a filament, mainly of low-mass galaxies, to the North of A2151, that reaches down to the cluster core. The $g - i$ and $EW(\mathrm{H}\alpha)$ maps of A2152 ans A2147 indicate more virialized structures; nonetheless, a filamentary structure dominated by blue low-mass star-forming galaxies has been identified entering in A2147 R_{200} region from South-East.

The LZR and N/O ratio vs. stellar mass relation of the HSC low-mass star-forming galaxies have been found to show an intrinsic dispersion that correlates with galaxy color.

In the clusters with available HI measurements we have found that most of the dwarf galaxies with available HI mass are either located outside the cluster core or have been recently accreted to the cluster environment and appear consistent with the predictions of the "closed box" model. In the cores of these clusters HI detections are scarce, thus star-forming dwarf galaxies there should have suffered an important ram-pressure stripping.

The metal enhancement of star-forming dwarfs in the cluster core has been found to be more important when considering the R_{200} region of the most massive cluster Coma ($M_{\star} \simeq 10^{15} M_{\odot}$). Despite the general good relation of local galaxy density with cluster-centric distance, this effect appears diluted in terms of local galaxy density, suggesting that the relevant parameter able to affect the chemical evolution of star-forming dwarf galaxies should be the presence of an intra-cluster medium.

Finally, for the aims of this thesis we performed a study of the morphological and structural properties of the star-forming galaxies in A2151 cluster. This work allowed a careful spectroscopic follow-up of these galaxies with long-slit spectroscopy. For this specific sample of cluster galaxies we derived galaxy stellar masses using SED fitting on SDSS broadband photometry. The fundamental parameters of the underlying stellar component, such as mean metallicity and age were derived via spectral fitting using the population synthesis code STARLIGHT.

Acknowledgments

My more profound acknowledgments go to my thesis supervisors, Pepe Vílchez Medina and Jorge Iglesias Páramo, for trusting me for this PhD project, giving me the marvelous opportunity to accomplish two of my major dreams: doing a PhD in Astronomy and living in my beloved Spain.

Pepe is an inexhaustible source of knowledge and ideas, and sharing these generously with me, during all these years, has made my research experience deeply rewarding. Not only the everyday work has been fun and exciting, but he also gave me the opportunity to travel a lot and do real observing, these being among my great wishes since childhood. Pepe has also given me inestimable support, guidance, and encouragement, that relieved so many overwhelming for me situations.

Jorge is the other mainstay of this work: from the deepest astronomical discussions to the most technical issues, he has always been my resource for help and learning. His positive attitude and prompt support have made my life easier during the course of this thesis.

I owe a debt of gratitude to Mary and Vangelis Kontizas, who stand like parents by me since the beginning of this journey: their unfailing help led me to Strasbourg and then directed me towards Granada, paving the way for the fulfillment of my wish.

I would like to thank Polis Papaderos, for our collaboration, for our enlightening discussions, and for the Starlight fitting.

Particular thanks also goes to Laura Magrini, for helping with multifiber data reduction and other spectroscopy problems, and above all for inviting me to Arcetri, permitting me an unforgettable experience in Florence.

I also thank Daniel Reverte Payá for his help in the beginning of this thesis, with the preparation of observing proposals, and the hospitality in the CALP.

I am in debt with Alba Fernández Martín, for helping with the IFU data reduction.

Thanks also goes to Enrique Pérez Montero, Ricardo Amorín, Ana Monreal Ibero, and Ovidiu Vaduvescu for discussions and collaboration.

This thesis would not have been possible without the care and understanding of my closest people. Words would never be enough to thank them. To them is dedicated this work.

Contents

Chapter 1

Introduction

Contents

1.1 The cosmic history of heavy-element production

1.1.1 How and where are metals produced?

It seems well established where and how are the chemical elements produced in the Universe. Hydrogen and most helium were created during the Big Bang, together with few isotopes and light elements, while heavier elements (that are generally called "metals") are formed by nucleosynthesis in stellar interiors or during stellar explosions (Burbidge et al. 1957). Heavier elements are basically produced by two main fusion processes: the proton-proton chain reaction, which dominates in stars with mass less than 1.5 solar masses ($M \lesssim 1.5 M_{\odot}$), and the CNO cycle dominating in massive stars ($M \gtrsim 1.3 M_{\odot}$). However, the energy input in the stellar interior is not sufficient for the production of elements heavier than Fe; these are produced in the explosive phenomena in the Universe, such as supernovae (SN).

Thus, by means of recurring cycles of star formation, galaxies are getting gradually enriched in heavy elements through time. Galaxy chemical enrichment depends crucially on three intercorrelated parameters: 1) the history of star formation, 2) the time and environmental dependence of the initial mass function (IMF) and 3) the star formation feedback effects.

Regarding star formation, it is well established (Lilly et al. 1996; Madau et al. 1996; Hopkins 2004) that the global average galaxy star formation rate (SFR) evolves with time, showing an increase by an order of magnitude from $z = 0$ to $z \sim 1 - 2$ (Figure 1.1). In addition, the star formation history (SFH) of galaxies has also been proved to be affected by the environment in which a galaxy resides (see §1.2.2).

Moreover, given that the process of nucleosynthesis depends on stellar mass, the fraction of massive stars -and specially the rate of SN explosions- is a key parameter for the chemical enrichment of a galaxy. Thus, the dependence of the IMF on time, location, and galaxy mass among other parameters would be important for galaxy enrichment. Most of the present evidences seem consistent with a nearly universal IMF; however Weidner & Kroupa (2005, 2006) suggest that the upper IMF (the fraction of stars more massive than 10 $M_{\odot}$, that are responsible for the important feedback effects) depends on SFR.

Finally, the circulation of matter in the cosmic phase space (i.e. overdensity vs. temperature) is a key parameter to understand galaxy chemical enrichment. For example, the formation of massive stars leads to a number of negative feedback effects (e.g. ionization, stellar winds, SN explosions) that may reduce the efficiency of star formation. The "life cycle" of metals after having been delivered into the interstellar medium (ISM) is literally an odyssey: they are blown to lower densities through outflows, compressed to higher densities by gravitational collapse, heated by gravitational shocks, cooled via radiative processes and Hubble expansion. The heavy-elements abundance, thus, is intimately linked to the physical processes governing star formation and it is a key astrophysical property for the understanding of galaxy evolution.

1.1.2 Chemical enrichment and cosmic structure

A conventional misconception has been that metallicity, being the integral of stellar nucleosynthesis over all epochs, should be just a vector of time, showing a gradual increase as we move from high to lower redshifts. Early hierarchical, three-dimensional chemodynamical simulations (Cen & Ostriker 1999), though, predict a quite more complicated picture, illustrated intelligibly in Figure 1.2. Although the overall cosmic (gas) metallicity, averaged globally, does show a quasi-uniform increase with time (dot-dashed curve), there is a stronger dependence of metallicity on cosmic overdensity. At all redshifts, higher density regions, e.g. $\delta = 10^3$ typical of galaxy clusters (thick solid curve), have much higher metallicity than lower density regions, and a shallower evolution of metallicity with redshift.

In this general context, the present thesis aims at investigating whether the observations of the ISM metal content of star-forming (SF) galaxies in local Universe clusters confirm the above described picture. This investigation shall deepen our understanding on the mechanisms that mostly affect the chemical evolution of cluster galaxies and shall provide fundamental constraints to models of galaxy formation and evolution, as well as of the cosmic chemical evolution. In what follows, we begin with a general description of the environmental effects on cluster galaxies and a brief introduction on how we quantify the gas-phase metallicity of SF galaxies.

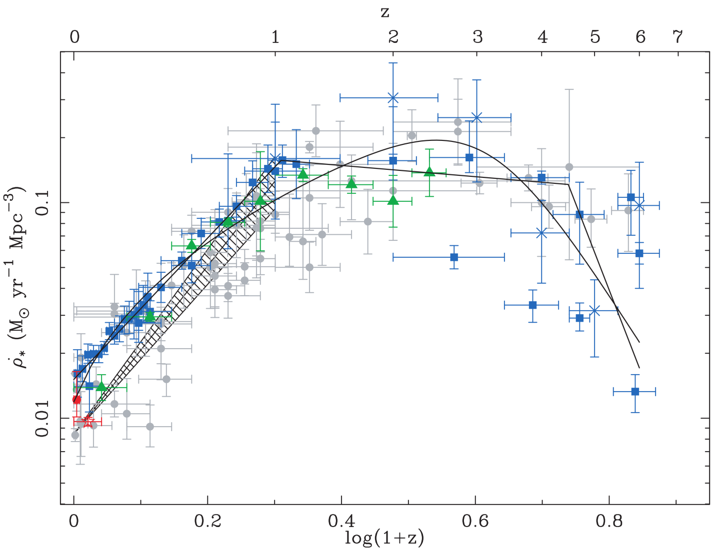

Figure 1.1: Evolution of SFR density with redshift. The colored points represent observational estimates of the SFR density in different redshifts, from X-ray, radio, FIR, optical emission lines, UV, and the *Hubble Ultra Deep Field* datasets taken from the literature. The solid lines indicate best-fitting parametric forms. (Figure 1, Hopkins & Beacom 2006)

1.2 Star-forming galaxies in clusters

1.2.1 Environmental effects on galaxy evolution

Located at the nodes of the cosmic web, clusters of galaxies are the largest collapsed structures in the Universe with total masses up to $10^{15} M_\odot$. The high local galaxy density and the presence of a hot ($\sim 10^8$ K) intracluster medium (ICM) render clusters the best places to investigate the influence of the environment on galaxy evolution.

Several cluster-related environmental processes can affect the SFH or the gas exchange between the galaxy and its environment. For simplicity we can classify the various processes under three broad headings, 1) galaxy-ICM interactions, 2) galaxy-cluster gravitational potential interactions and 3) small scale galaxy-galaxy interactions (a classification introduced by Treu et al. (2003), see also Hernández-Fernández et al. (2012)).

The ram-pressure stripping (RPS, Gunn & Gott 1972) removes the ISM of a galaxy as it moves through the hot intracluster gas, and can produce observable gas tails. Simulations (e.g., Abadi et al. 1999; Mori & Burkert 2000; Tonnesen et al. 2007) suggest that RPS is efficient even up to the cluster virial radius and can remove completely the gas content in timescales of $\sim 10^9$ yr, comparable to the cluster crossing time. Additionally, RPS has been found to depend on galaxy orbits (Balkowski et al. 2001; Vollmer et al. 2001) and to be a multi-stage process

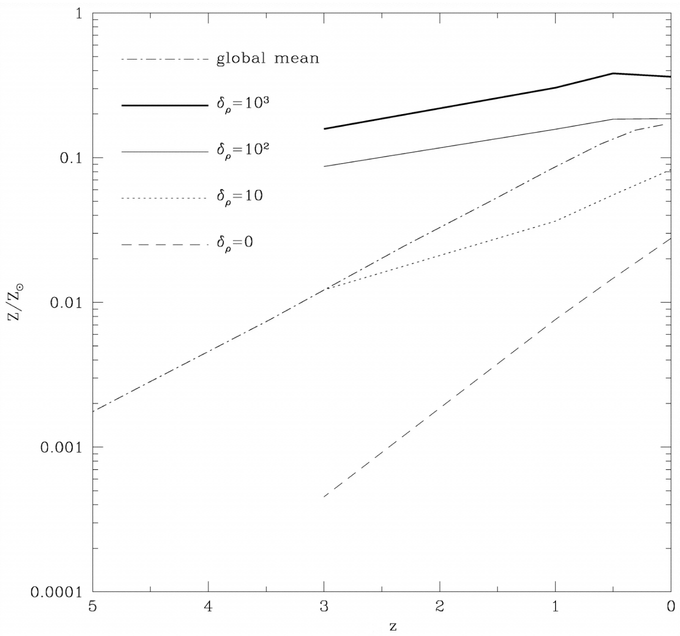

Figure 1.2: Pioneering large-scale hydrodynamic simulations of galaxy formation have shown that metallicity is a strong function of redshift *and* cosmic overdensity. The average metallicities, averaged over the whole Universe (dotdashed curve), and in overdensities 10^3 (thick solid curve), 10^2 (thin solid curve), 10 (dotted curve), and 0 (dashed curve), respectively, are plotted as a function of redshift (Figure 1, Cen & Ostriker 1999).

(Roediger & Hensler 2005). Recent simulations indicate that both varying ICM density (Brüggen & De Lucia 2008; Tecce et al. 2010) and inhomogeneities in the ISM (Tonnesen & Bryan 2009) are expected to play an important role in the gas stripping effect.

Ram-pressure has long been confirmed by the HI deficiency and disturbed HI morphologies observed in galaxies in nearby clusters e.g., in Virgo (Cayatte et al. 1990; Kenney et al. 2004; Vollmer et al. 2004; Balkowski & Chemin 2005; Abramson et al. 2011), Coma (Bravo-Alfaro et al. 2000, 2001), Abell 3627 (Vollmer et al. 2001), even in Pegasus I cluster (Levy et al. 2007), a cluster with low level of X-ray emission. More recently, Chung et al. (2009) found many HI deficient galaxies in the Virgo cluster core, and at intermediate distances, at ∼1 Mpc from the center (approximately the virial radius), a remarkable number of galaxies were found with long, one-sided HI tails pointing away from the M87 (see Figure 1.3). Additionally, Koopmann & Kenney (2004) found that the majority of Virgo spirals have their Hα disks truncated, while most of these truncated galaxies have relatively undisturbed stellar disks, suggesting that the ICM-ISM stripping is the main mechanism causing the reduced SFRs of Virgo spirals.

A spectacular example of a galaxy suffering RPS has been found by Sun et al. (2007) in the "Norma" cluster (Abell 3627), one of the closest (∼68 Mpc) rich clusters

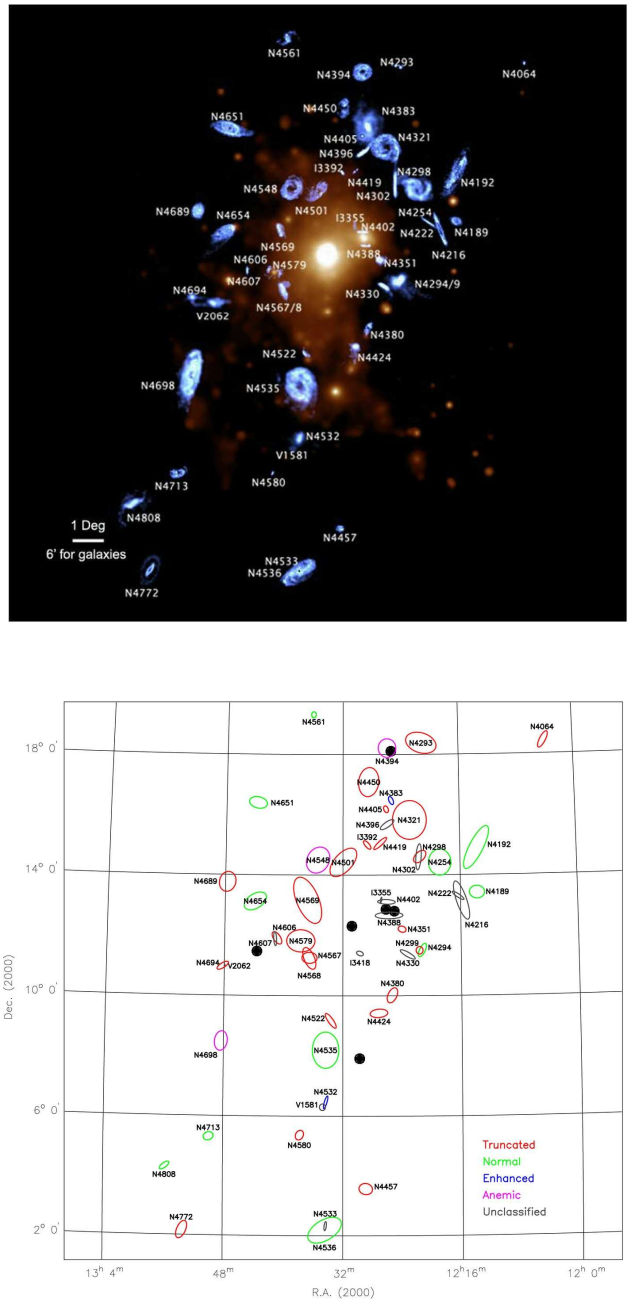

Figure 1.3: Upper panel: Composite image of the total HI images of the individual galaxies of the VIVA (VLA Imaging of Virgo in Atomic gas) sample (in blue) overlaid on the ROSAT X-ray image (orange). The galaxies are located at the proper position in the cluster but each HI image is magnified by a factor 10 to show the details of the HI distribution (Figure 7, Chung et al. 2009). Lower panel: VIVA galaxies are shown at their proper positions. Galaxies are color coded based on the star formation properties classified in the Hα study by Koopmann & Kenney (2004) (Figure 1, Chung et al. 2009).

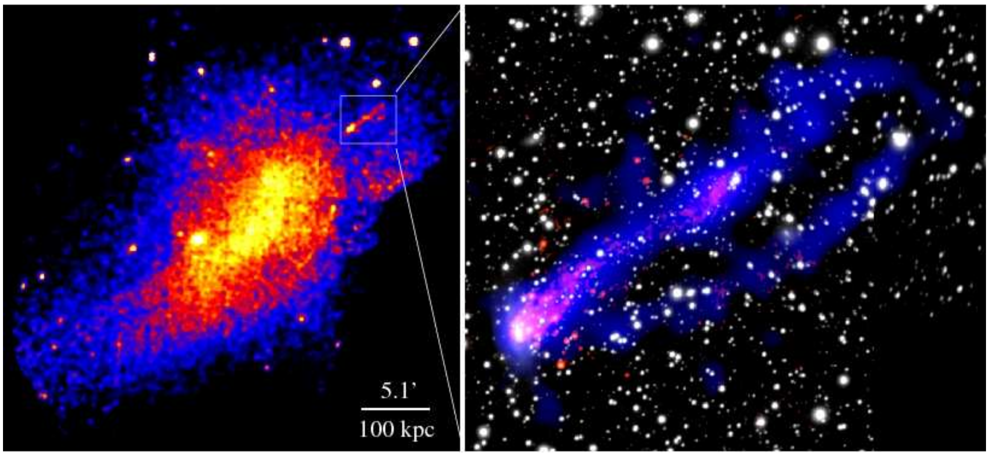

Figure 1.4: A spectacular example of a galaxy approaching the cluster Abell 3627. Left: the X-ray emission of the ICM. Right: the galaxy ESO0137-001 at a distance of ∼280 kpc from the cluster center shows two spectacular gas tails, reaching ∼80 kpc and emitting in X-rays (in blue) and in Hα (in red). (Figure 2, Sun et al. 2010)

(today thought to be in the center of the "Great Attractor"). The left plot of Figure 1.4 is a mosaic of the emission in X-rays of the hot intracluster gas of Abell 3627 cluster, detected by the Chandra X-ray Observatory. In this X-ray image, at a distance of ∼280 kpc from the cluster center, the galaxy ESO0137-001 has been found showing two tails reaching up to ∼80 kpc. The right plot of Figure 1.4 is a composite image of the galaxy from Chandra in blue, optical emission in yellow and Hα in red. These gas tails, emitting in X-ray and Hα, are the evidence of the evaporation of the cool (∼10 K) ISM as the galaxy travels towards the cluster center.

Simulations suggest that ram-pressure can also compress the gas to cause the collapse of giant molecular clouds within a galaxy (Bekki & Couch 2003; Kronberger et al. 2008; Kapferer et al. 2009), leading to an initial burst of star formation, mechanism known as pressure-triggered star formation. Kronberger et al. (2008), in particular, found that SFR can be enhanced up to a factor of 3 in the disk of a ram-pressure stripped galaxy, which moves face-on through an ICM with temperature and density typical of that found in the outskirts of a massive cluster. Most of the new stars form in the disk, mainly in the compressed central region; however star formation occurs also in the stripped material in the wake of the galaxy, to distances up to hundred kpc behind the plane of the disk (Figure 1.5).

This kind of "jellyfish" morphologies and starburst knots within trails have recently been observed frequently in nearby clusters (Gavazzi et al. 2003; Sun et al. 2007; Yoshida et al. 2008, 2012; Yagi et al. 2010; Smith et al. 2010; Fumagalli et al. 2011; Abramson et al. 2011), and even in higher redshift clusters (Owen et al. 2006; Cortese et al. 2007; Owers et al. 2012), supporting the presence of pressure-triggered star formation. For example, Figure 1.6 shows two galaxies identified in Abell 1367 (Gavazzi et al. 2001), showing large-scale tails of ionized gas and ongoing massive

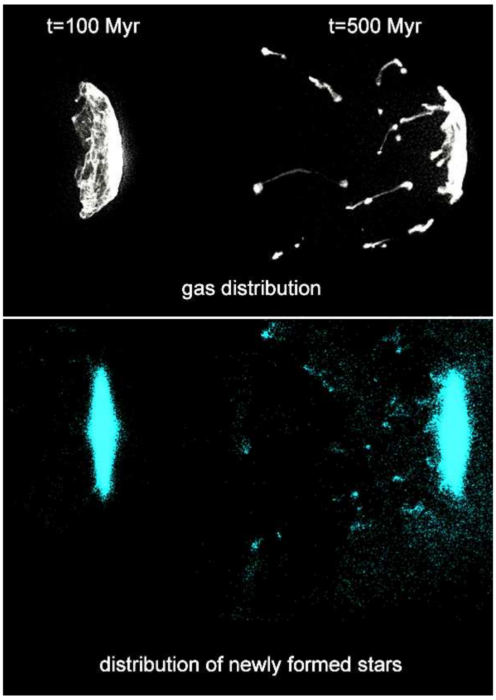

Figure 1.5: The evolution of a ram-pressure stripped model galaxy, which moves face-on through an ICM with typical temperature (3 keV $\approx 3.6 \times 10^7$ K) and density ($\rho = 10^{-28}$ g/cm^3) of that found in the outskirts of a massive cluster. The distribution of the gas (white, top) and the newly formed stars (turquoise, bottom) is presented, after 100 Myr (first column) and after 500 Myr (second column). The gas of the galaxy and the ICM have been treated via smooth particle hydrodynamics (SPH) and the dark matter and stellar component are modeled via N-body simulations. (Figure 7, Kronberger et al. 2008).

starbursts in the opposite side, indicating that these galaxies are in the course of their first infall toward the dense cluster region. Therefore, although the high pressure ICM can be responsible for the stripping of the HI gas within disks and the diffuse halo gas in cluster galaxies, leading to the eventual truncation of star formation, it is linked to an initial phase of starburst triggering. This process would lead naturally to the formation of post-starburst galaxies that are actually been observed more frequently in clumpy clusters (e.g., Caldwell & Rose 1997; Poggianti et al. 2004, 2009a).

Other processes that could affect the gaseous content of a galaxy are the re-accretion of the stripped gas (Vollmer et al. 2001), the turbulence and viscosity (e.g. Quilis et al. 2000) and the removal of the outer gas envelope, called starvation or strangulation (Larson et al. 1980). Bekki (2009) simulations suggest that even moderately strong ram-pressure, e.g., in clusters of $M \sim 10^{14} M_{\odot}$ or even in groups, could strip the hot gas halos of galaxies. In these simulations, the stripping of galactic halo gas seems to be more efficient than that of disk gas, and the efficiency

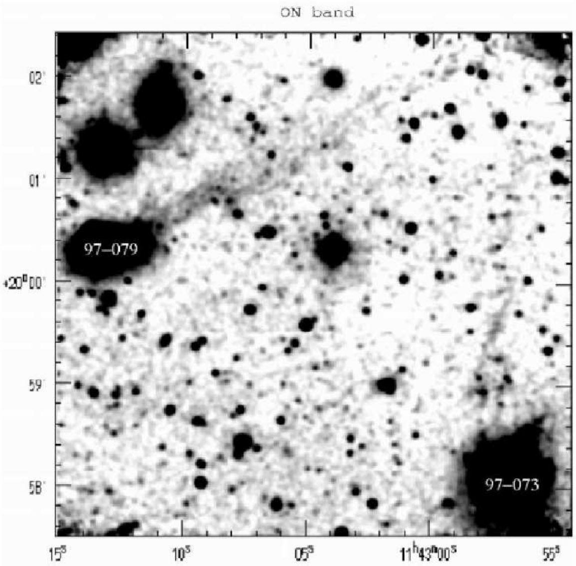

Figure 1.6: 75 kpc trails of ionized gas behind two irregular galaxies (CGCG97-073 and CGCG97-079) in Abell 1367 (Figure 2, Gavazzi et al. 2001).

increases with decreasing galaxy mass.

A galaxy can also interact with the cluster potential, which can strip both gas and stars, or compress the gas to cause an increased SFR. Finally, the galaxy-galaxy interactions can be either mergers between galaxies with low relative velocities (e.g. Mihos & Hernquist 1996; Barnes & Hernquist 1996; Mamon 1996; Conselice 2006), or galaxy harassment, that is high speed interactions among cluster galaxies (Moore et al. 1998, 1999; Struck 1999). These interactions can cause an increased SFR and will also affect both the stellar and gas components. Mihos et al. (2005) present deep optical imaging of the inner parts of Virgo, where several long (>100 kpc) tidal streamers have been found, small-scale tidal tails, bridges between galaxies and several galaxies that are embedded in common envelopes: in short a web of diffuse intracluster light confirming the action of tidal interactions (Figure 1.7).

There still remains significant debate on the relative importance of these processes, although it is likely that all occur in clusters. However a complete picture of the overall transformation of galaxies as they enter the cluster environment is still missing, as well as the degree to which this transformation could affect the SFH and the chemical evolution of these galaxies.

1.2.2 Star formation history versus environment

Dressler (1980) seminal work pointed out that galaxies in dense environments tend to show early-type morphologies (the well known morphology-density relation). Several authors have investigated the galaxy star formation activity as a function of the environment, from nearby to distant clusters (e.g. Kennicutt 1983; Balogh et al. 1999; Poggianti et al. 1999; Treu et al. 2003; Balogh et al. 2004; Rines et al. 2005;

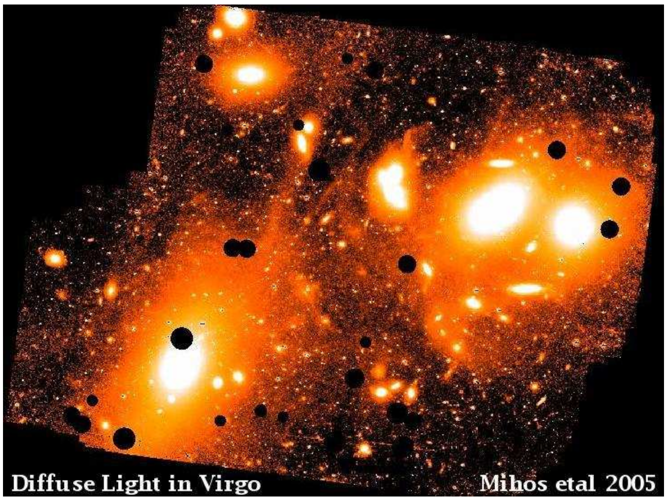

Figure 1.7: The diffuse halo of M87 is traced out to ∼200 kpc, while significant diffuse light is also detected around the M84/M86 pair in the core of Virgo cluster. Several galaxies there are embedded in common envelopes, suggesting they are true physical subgroups, product of an hierarchical cluster assembly. (Image credit: Mihos et al. 2005).

Finn et al. 2005; Haines et al. 2007; Poggianti et al. 2008; Reverte 2008, among others) and have found a similar trend. For example Rines et al. (2005) showed that, in a sample of local Universe clusters, the fraction of galaxies with current star formation, as traced by their Hα emission, increases with the distance from the cluster center and converges to the "field" value at 2-3 virial radii (Figure 1.8). Furthermore, Reverte (2008) studied the differences in SFH between cluster and field SF galaxies and found that their Hα luminosity and $EW(\mathrm{H}\alpha)$ distributions are clearly different (see Figure 2.12).

Though, intense discussions on the underlying cause of these observational results are still ongoing. One interpretation has been that this trend could be the mere result of the fact that high density regions have favored the formation mostly of massive galaxies, which in turn convert their gas in stars faster than dwarf galaxies (Kennicutt 1998) and they have already finished forming stars earlier in the past (Merlin & Chiosi 2006). Recent observational evidences support the idea that the stellar mass function can be associated with the environment (Vulcani et al. 2012; Bolzonella et al. 2010).

Another interpretation is that the cluster environment suppresses galaxy SFH, as galaxies move from low-density regions into the cluster core. In the previous section we presented different environmental mechanisms acting on cluster galaxies. Each one of these mechanisms is expected to be effective in different regions of clusters and their outskirts, and to affect star formation in different ways and timescales (see, e.g. the review by Boselli & Gavazzi 2006).

For low-mass galaxies, however, the picture appears somewhat clearer. Due to

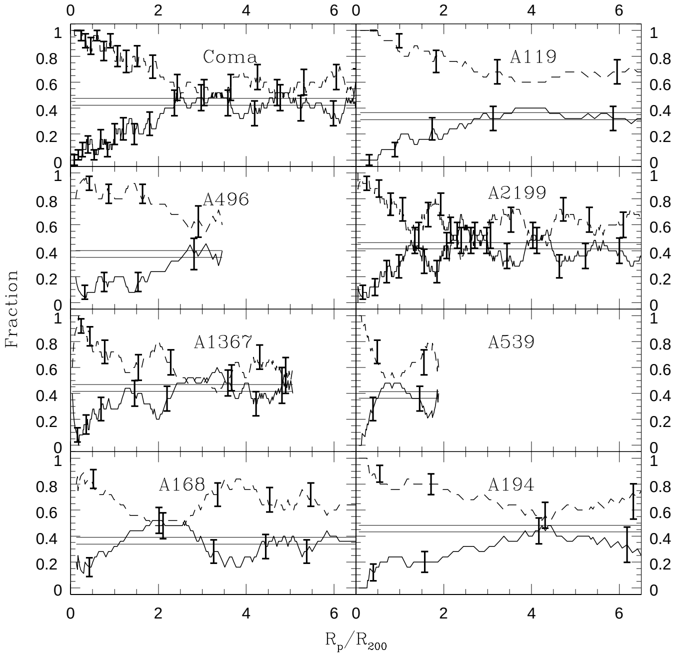

Figure 1.8: The fraction of galaxies with current star formation, as traced by Hα emission, increases with the distance from the cluster center and converges to the "field" value (the horizontal line) at 2-3 virial radii (Figure 1, Rines et al. 2005).

their low mass surface density and rotation velocity, dwarf galaxies are the most vulnerable systems to environment-related processes that quench star formation, such as the stripping of their halo and/or disk gas. Haines et al. (2007), based on a large sample of dwarf galaxies, have found that passive dwarfs are found only in very dense environments, typical of a cluster virial region, or as satellites of a more massive companion. Studies of three of the richest clusters in the local Universe, Abell 2199 (Haines et al. 2006), Coma and Abell 1367 (Mahajan et al. 2010), suggest that star formation in dwarf galaxies is quenched only in the center of the clusters, in contrast with massive galaxies that can become passive in all environments. All these evidences seem to imply that there exist fundamental differences in the evolution of giant and dwarf galaxies in clusters: while various physical mechanisms could be co-responsible for the evolution of massive galaxies, the evolution of dwarf galaxies seems to be primarily driven by the environment in which they are found.

1.3 Galaxy chemical evolution

1.3.1 Metallicity of star-forming galaxies

Most metals are formed and ejected into the ISM by massive stars through stellar winds and SN explosions. Additionally, intermediate mass stars produce important contributions of elements, like carbon and nitrogen. Metals play a fundamental role in the process of star formation. Metallicity, therefore, provides an important record of the SFH of a galaxy.

SF galaxies are those which have had a recent star formation episode and still contain O and B stars, hot enough ($> 35\,000$ K) to ionize the ISM gas and create HII regions. The HII regions have the nice property, from the observational point of view, to exhibit characteristic emission line spectra; an HII region could be thought as a machine that converts the Lyman continuum photons ($\lambda < 912$Å, $E > 13.6$ eV) emitted by a hot, massive star into a collection of narrow emission lines mainly in the UV/optical/IR bands. Figure 1.9 shows a typical emission-line spectrum in the optical wavelength range of a nearby HII galaxy, where there can be measured the emission lines Hα, Hβ, Hγ, Hδ, [OII]λ3727, [OIII]$\lambda\lambda$4959,5007, [NII]$\lambda\lambda$6548,6584, [SII]$\lambda\lambda$6717,6731, among others.

The radiation emitted by an ionized nebula depends basically on the abundances of the chemical elements and the physical state of the gas, specially its average electron temperature and electron density. So, physical and chemical properties of nebulae can be derived by measuring ratios between intensities of recombination or collisionally excited emission lines. After hydrogen and helium, the most abundant element in the Universe is oxygen. It is convenient to measure the oxygen abundance because it exhibits emission lines (of different ionization states) which are very bright and easy to measure in the optical. In practice the metallicity of SF galaxies is quantified via the oxygen abundance, i.e. number of atoms of oxygen relative to hydrogen, defined as 12 + log (O/H) (the astronomical scale to measure chemical abundances).

Accurate oxygen abundance derivations require the determination of the electron temperature, which is usually obtained from the ratios of auroral to nebular line intensities such as [OIII]λ4363 over [OIII]$\lambda\lambda$4959,5007, or [NII]λ5755 over [NII]$\lambda\lambda$6548,6584 among others. This method of abundance derivation is often referred to as the “direct” (electron temperature) method. A well-known difficulty however arises from the fact that as the metallicity increases, the electron temperature decreases, as the cooling of the gas is made via metal lines, and the optical auroral lines become too faint to be measured. For example, [OIII]λ4363 line becomes extremely weak at metallicities above $\sim$0.5 solar and is virtually undetectable given its low signal-to-noise (S/N) in the spectra of metal-rich extragalactic HII regions. In this case, strong-line methods, based on different ratios of collisionally excited forbidden lines to hydrogen recombination lines have been developed.

The most widely used abundance indicator is the R_{23} index, defined by Pagel et al. (1979) as R_{23}=([OII]λ3727+[OIII]$\lambda\lambda$4959,5007)/Hβ. This work was the first to point out that the measured electron temperature T_e , the O/H abundance and the parameter R_{23} all correlate, as shown in Figure 1.10. This method, however, carries significant hazards.

First, the relation between O/H and R_{23} is double-valued. A particular value of R_{23} corresponds to two different values of metallicity, one in the higher metallicity branch and one in the lower metallicity branch of the relation. This degeneracy is due to the fact that on the lower metallicity branch, R_{23} scales with metallicity

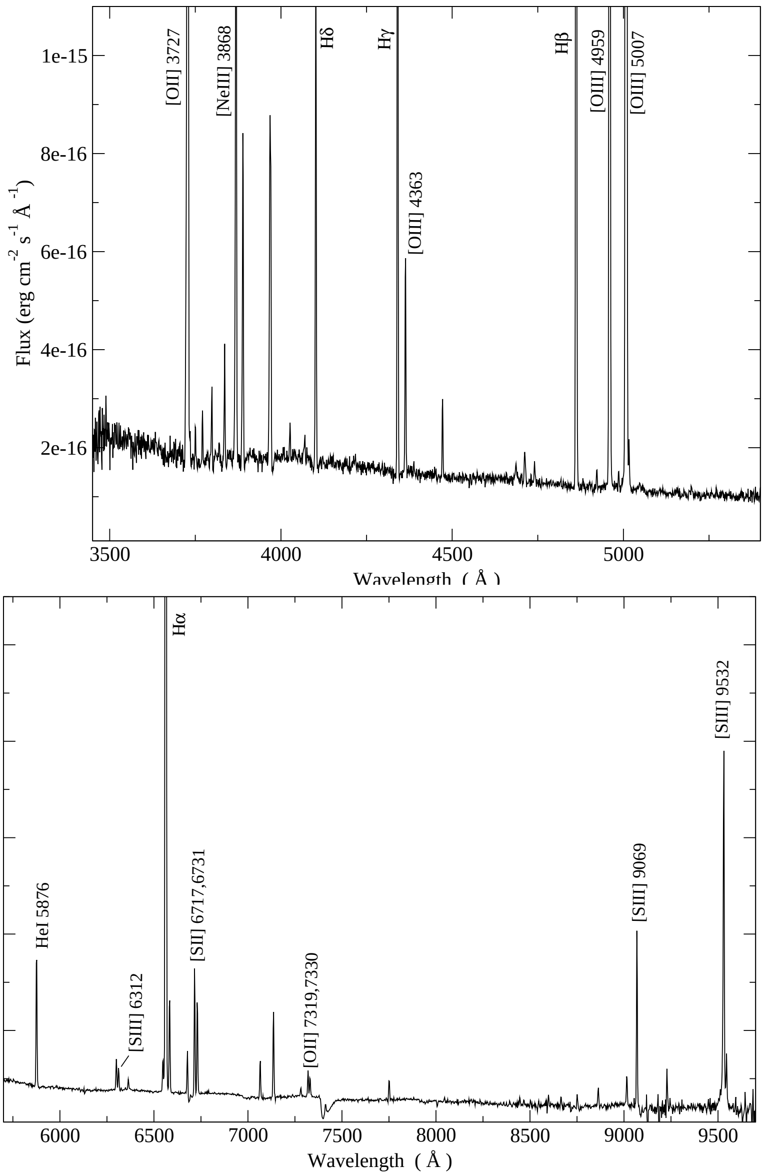

Figure 1.9: Typical emission-line spectrum in the optical wavelength of a nearby Hii galaxy obtained at Calar Alto Observatory (CAHA) with the 3.5m telescope (Figure 1, Hägele et al. 2008).

because the intensity of the [Oii]λ3727 and [Oiii]λλ4959,5007 lines scales with the abundance. On the upper branch, nebular cooling effectively decreases the electron temperature of the gas and as a consequence decreases the rate of collisional excitation of the [Oii]λ3727 and [Oiii]λλ4959,5007 lines. It should be mentioned however that an important fraction of Hii galaxies lie on this "problematic" turn-over region, i.e. 12+log(O/H) ~8.1 dex, where the abundance determination can be very uncertain.

Another problem is the existence of scatter larger than what can be accounted

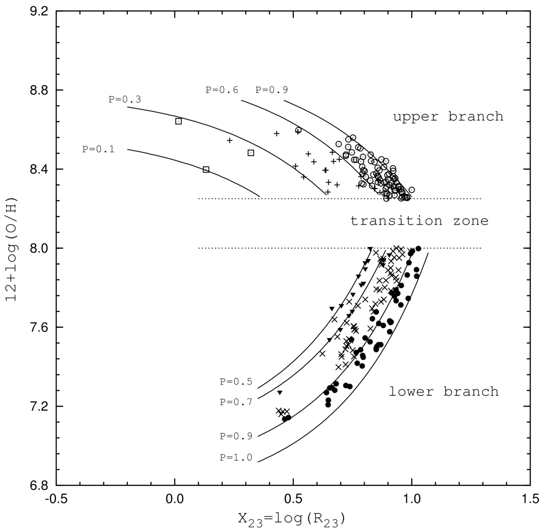

Figure 1.10: The measured electron temperature T_e (P is a proxy of temperature), O/H and the parameter R_{23} all correlate. The oxygen abundance is derived with the direct method for extragalactic H ii regions and SF galaxies (Pilyugin & Thuan 2005, Figure 12,).

for by observational errors. Pérez-Montero & Díaz (2005) argue that this scatter is due to the fact that the parameter R_{23} can be affected by different geometries of the emitting gas, quantified by what is called the ionization parameter U, and different ionizing temperatures, as illustrated in Figure 1.11, left.

Another extensively used parameter is N2, defined as N2=log([N ii]λ6584/Hα) (Storchi-Bergmann et al. 1994). The use of this parameter has two important advantages: first the relation between N2 and the oxygen abundance is single-valued and second the emission lines involved are very close in wavelength, so the N2 parameter is almost free of uncertainties introduced by reddening correction or flux calibration. Again, the main source of dispersion is mainly related to different ionization parameters and the stellar effective temperatures (Figure 1.11, right). But there exists an additional source of scatter, related to the possible different N/O relative abundance of each object.

It is well known that for low metallicities (12+log(O/H)$\leq$8.0), the N/O ratio remains constant vs. the oxygen abundance, when the primary creation of nitrogen dominates, while for higher metallicities, it shows a strong slope (Figure 1.12), a behavior well explained by the secondary production of nitrogen (Vila Costas & Edmunds 1993). But, there does not exist a precise separation line between primary and secondary behavior: Mollá et al. (2006) have argued that the production of nitrogen depends sensibly on the stellar lifetimes and on the star formation efficiencies, as derived by their chemical evolution models. For this reason, Pérez-Montero & Contini (2009) have found a strong correlation between the metallicity derived from the N2 parameter and the N/O ratio, in such a way that the metallicity predicted

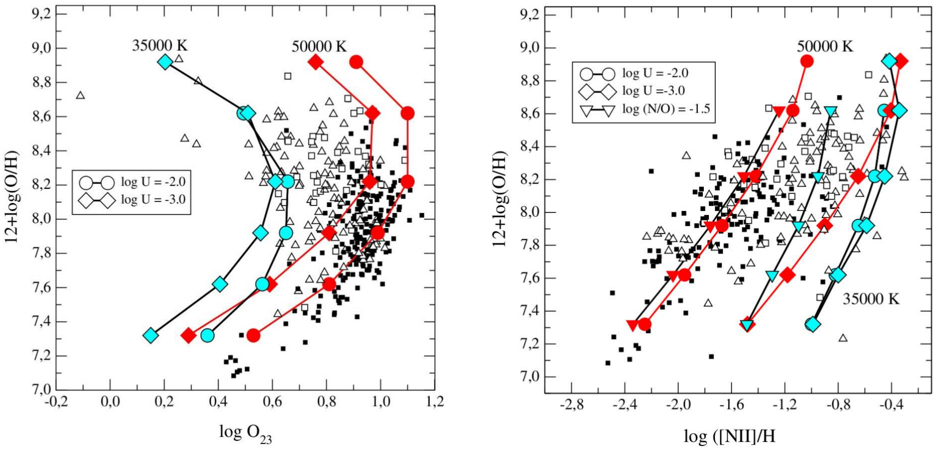

Figure 1.11: Left: The relation between R_{23} (here named O_{23}) and oxygen abundance for a large sample of galactic and extragalactic HII regions and HII galaxies. Overposed are the predictions of CLOUDY photoionization models for different ionization temperatures (green: 35 000 K and red: 50 000 K) and ionization parameters (circles: log U=-2.0 and diamonds: log U=-3.0). Right: The same plot for the relation between the N2 parameter and 12+log(O/H). (Figures 3 and 7, Pérez-Montero & Díaz 2005).

by N2 is overestimated for objects with a high N/O ratio and vice-verse.

As a result of this complex situation, there exists an extensive literature on the calibration of the correlation between the oxygen abundance and R_{23} or N2 parameters, as well as using other strong-line ratios (for example S_{23} Vilchez & Esteban 1996; Pérez-Montero & Díaz 2005), eventually more useful to explore the chemical enrichment of galaxies. The calibration of these parameters can be empirical (e.g. Pettini & Pagel 2004; Pilyugin & Thuan 2005; Pilyugin et al. 2010), that is using direct measurements of the oxygen abundance in the local Universe, or theoretical (e.g. McGaugh 1991; Kewley & Dopita 2002; Tremonti et al. 2004), that is using photoionization models covering different physical parameters, as well as semi-empirical using both direct measures and photoionization models (e.g. Denicoló et al. 2002). Though, it has long been reported by several authors (Kewley & Ellison 2008; Bresolin 2008) that there exists a difference up to ~0.4 dex between O/H predictions by model and empirical calibrations.

Apart from the complicated part of evaluating the calibrations offered and their accuracy, there is also another issue: how should we define the metallicity of a whole galaxy? It is well known that spiral galaxies in the local Universe show abundance gradients, which can reach up to 1 dex difference from the metal-rich nuclear regions to the metal-poor outskirts, as observed for example in M33 (Vílchez et al. 1988; Magrini et al. 2007), M101 (Kennicutt et al. 2003), and NGC300 (Bresolin et al. 2009). Moustakas & Kennicutt (2006) have found that the metallicity given by an integrated spectrum of an entire galaxy correlates well with the so-called "charac-

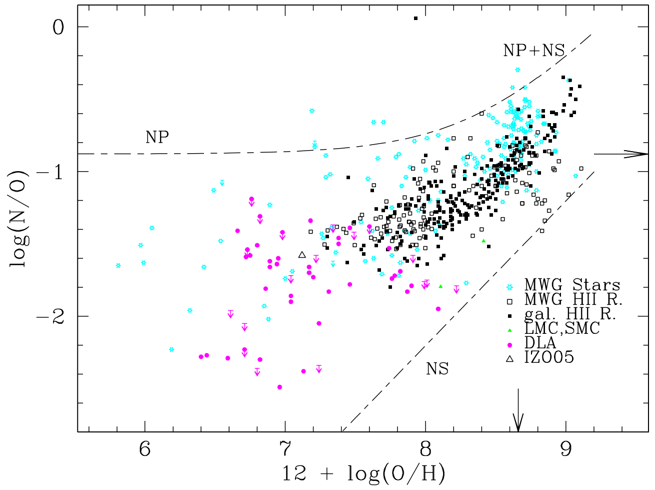

Figure 1.12: The N/O ratio as a function of 12+log(O/H), when the nitrogen is secondary (line NS), primary (line NP) and a combination of both primary and secondary (line NP+NS). The points correspond to Milky Way stars, galactic and extragalactic HII regions, the LMC and SMC. The arrows mark the solar values. (Figure 1, Mollá et al. 2006)

teristic" metallicity at $0.4r_{25}$, r_{25} being the radius where the surface brightness is 25 mag arcsec^{-2} in B band.

1.3.2 The mass-metallicity relation

One standard approach to investigate the chemical evolution of galaxies is to derive the stellar mass vs. gas metallicity relation (MZR). From the observational point of view, Lequeux et al. (1979) was the first to point out that metallicity is strongly correlated with galaxy luminosity, defining the luminosity-metallicity relation (LZR), with the more luminous galaxies being metal richer. Since then a lot of work has been done, extending this correlation and the more fundamental one between metallicity and stellar mass, to large samples of galaxies (Skillman et al. 1989; Zaritsky et al. 1994; Lamareille et al. 2004; Tremonti et al. 2004; Zahid et al. 2012, among others), and to as lower galaxy masses as possible (e.g., Lee et al. 2006; Vaduvescu et al. 2007). For example, Figure 1.13 shows the MZR derived by Lee et al. (2006), spanning nearly 4 orders of magnitude in the low-mass range.

The MZR has been found to hold for many samples of galaxies at different redshift ranges: e.g., $0.5 < z < 0.9$ (Savaglio et al. 2005; Lamareille et al. 2009; Zahid et al. 2011), $1.0 < z < 1.6$ (Shapley et al. 2005), $2.0 < z < 2.5$ (Erb et al. 2006), $3.0 < z < 4.0$ (Maiolino et al. 2008; Mannucci et al. 2009). An evolution of both the zero point and the slope of the MZR as a function of redshift has been observed, though there is still an open debate on this issue.

A variety of underlying physical mechanisms have been proposed to explain this relation. Galactic outflows could be more efficient at expelling metal-enriched gas in low-mass galaxies due to their shallower gravitational potentials (e.g., Larson 1974; De Lucia et al. 2004). Higher-mass galaxies could be more efficient at converting their gas into stars and vice versa (Brooks et al. 2007; Calura et al. 2009) (this is often named "downsizing"). For dwarf galaxies, where supernova winds are expected to be more important, a combination of downsizing and winds could affect the shape and slope of the MZR (Spitoni et al. 2010). The inflows scenario, whether smooth or in the form of gas-rich satellites, has been explored by Davé et al. (2010), (see also Dalcanton 2007). Köppen et al. (2007) have claimed that the MZR is linked to the initial mass function, which presents a higher upper mass cutoff in more massive galaxies. Finally, Davé et al. (2011) presented state-of-the-art hydrodynamic simulations that incorporate momentum-driven wind scaling (Finlator & Davé 2008) to explain the MZR finding among the most successful overall fits to a wide range of observed galaxy properties.

Although the MZR is well defined, it shows a significant scatter, that observational errors do not account for (Cooper et al. 2008). Other explanations have been offered, e.g., that outliers are observed in special states of their evolution (Contini et al. 2002; Berg et al. 2011), or are being affected by mergers (Kewley et al. 2006; Michel-Dansac et al. 2008; Rupke et al. 2010). The effects of SFR (e.g., Ellison et al. 2008) and local galaxy density (e.g., Cooper et al. 2008) have been also discussed, and the MZR scatter has been found to increase with decreasing stellar mass (Zahid et al. 2012). A recent idea gaining significant ground is that the MZR is a projection of a more fundamental 3D relation between mass, metallicity, and SFR (Mannucci et al. 2010), which would reflect the equilibrium established between gas infall, star formation, and metal content. This fundamental metallicity relation (FMR) seems to reduce the scatter observed in the MZR and it has been claimed to cancel its redshift evolution up to $z \sim 2.5$ (Mannucci et al. 2010).

1.4 The scope of this thesis

Galaxy chemical evolution is connected with the SFH and the process of interchange of gas between a galaxy and its environment. Both these factors can be affected by the cluster environment as we have seen in Sections 1.2.1 and 1.2.2. The question that we propose to answer in the present thesis is how these effects could leave their imprint on the metal content of galaxies and on the chemical evolution of cluster galaxies. Important questions still remain open regarding the influence of the environment on the chemical evolution of galaxies, particularly its effect on the scatter of the MZR, and the relative importance of cluster membership vs. local galaxy density. Figuring out the responsible mechanism(s) of the intrinsic scatter of the MZR would help constrain the physical processes driving this relation and subsequently elucidate galaxy evolution scenarios.

To this goal we derive ISM chemical abundances for cluster SF galaxies, and study their relation with the environment (e.g. galaxy cluster-centric distance and local galaxy density) and with fundamental galaxy properties (e.g. galaxy stellar

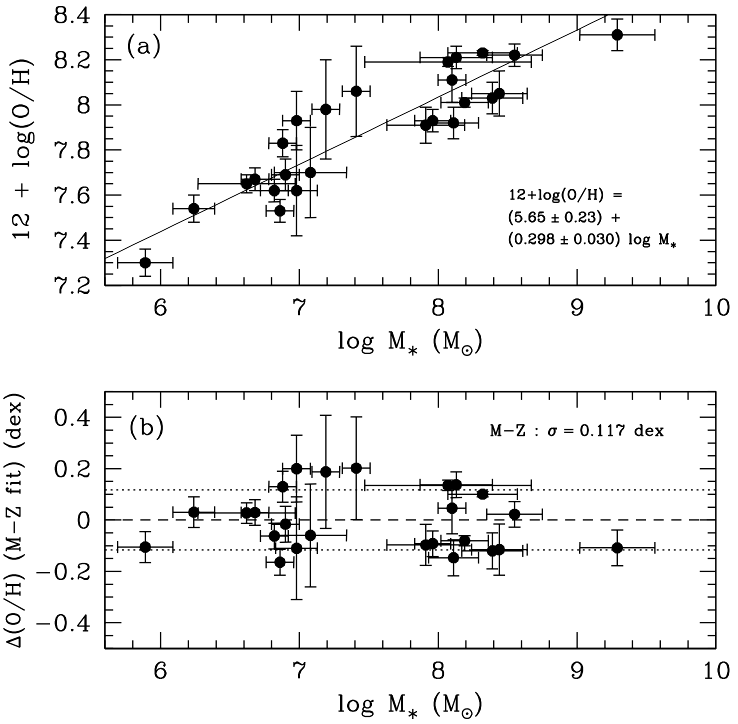

Figure 1.13: The MZR (up) for 25 nearby dIrr and the residuals in oxygen abundance from the fit to the MZR (down). Accurate stellar masses have been derived using IR *Spitzer* photometry and most of the oxygen abundances estimates are calculated using the "direct" method (Figure 8, Lee et al. 2006).

mass, luminosity, gas content). We study a sample of northern-hemisphere Abell clusters (Abell 1656, Abell 1367, Abell 779, Abell 634) at a distance of ~100 Mpc, and the Hercules Supercluster (that includes: Abell 2151, Abell 2152, and Abell 2147) at ~160 Mpc. This sample of clusters spans a variety of physical properties (such as mass, X-ray luminosity, and evolutionary state), permitting to study the impact on the SFH and the chemical evolution of SF galaxies in a wide range of different environments and at large-scale structures.

In the central part of Abell 2151 (the Hercules cluster) we have performed new observations of long-slit spectroscopy, considered in Chapter 3. This new spatially resolved spectroscopy has been used to test the metallicity gradients for Abell 2151 SF galaxies. In Chapter 4 we study a region of 22.5 deg^2 around the Hercules Supercluster, and we investigate the distribution of star formation activity and the metal content of galaxies in large scales. Finally, focusing our attention in the low-mass SF population, in Chapter 5 we study the relatively closer-by clusters Abell 1656 (Coma), Abell 1367, Abell 779, and Abell 634.

Overall, the physical mechanisms/processes giving rise to the observed behaviors are discussed on the light of the predictions of recent hydrodynamic models of galaxy evolution in dense environments. The results of such an investigation are expected to constrain both the environmental mechanisms that affect cluster galaxies and the the physical processes that govern galaxy evolution, as well as provide new tests for chemical evolution models.

Chapter 2

The sample of clusters

Contents

2.1 Definition of the sample

The starting point of this thesis has been the previous deep Hα imaging surveys performed by our group, in a sample of nearby ($z \sim 0.02-0.04$) clusters visible from the northern hemisphere ($\delta \gtrsim -25$ deg). Thus, this work is part of a bigger project which intends creating a census of a well defined sample of emission-line cluster galaxies, for which spectroscopic information as well as integrated Hα luminosities and EW(Hα) will be available. This information permits deriving total galaxy SFRs from the Hα flux, avoiding slit and fiber aperture effects. The environmental effects on the chemical evolution of this new sample of cluster galaxies can therefore be considered in relation with the effects on their SFH.

Iglesias-Páramo et al. (2002) presented a deep Hα imaging survey of the central regions of the two nearby clusters Coma (Abell 1656) and Abell 1367, taken with the Wide Field Camera (WFC) at the Isaac Newton Telescope INT2.5m. Reverte (2008) complemented this survey with WFC, observing 5 more Abell clusters: Abell 779, Abell 634, Abell 400, Abell 539, and Abell 2666. In total, these seven clusters fulfill the criteria: (1) to be visible from the northern hemisphere and (2) to be located at the same distance at $\sim$ 100 Mpc ($0.02 < z < 0.03$), belonging thus to a semi-spherical shell of the local Universe.

Additionally, moving to a distance of $\sim$ 160 Mpc, there is the Hercules Supercluster formed by Abell 2151 (the Hercules cluster), Abell 2147, and Abell 2152. Cedrés et al. (2009) presented a deep Hα survey of the central region of Abell 2151, using the William Herschel Telescope WHT4.2m and the Nordic Optical Telescope NOT2.5m. In the Hercules Supercluster region, a field of 2 deg^2 has been recently observed in Hα by our group, using WFC at INT2.5m and the results will be presented in a forthcoming publication. Figure 2.1 is an illustration of the large-scale structures in the local Universe, where are included all the clusters of our sample.

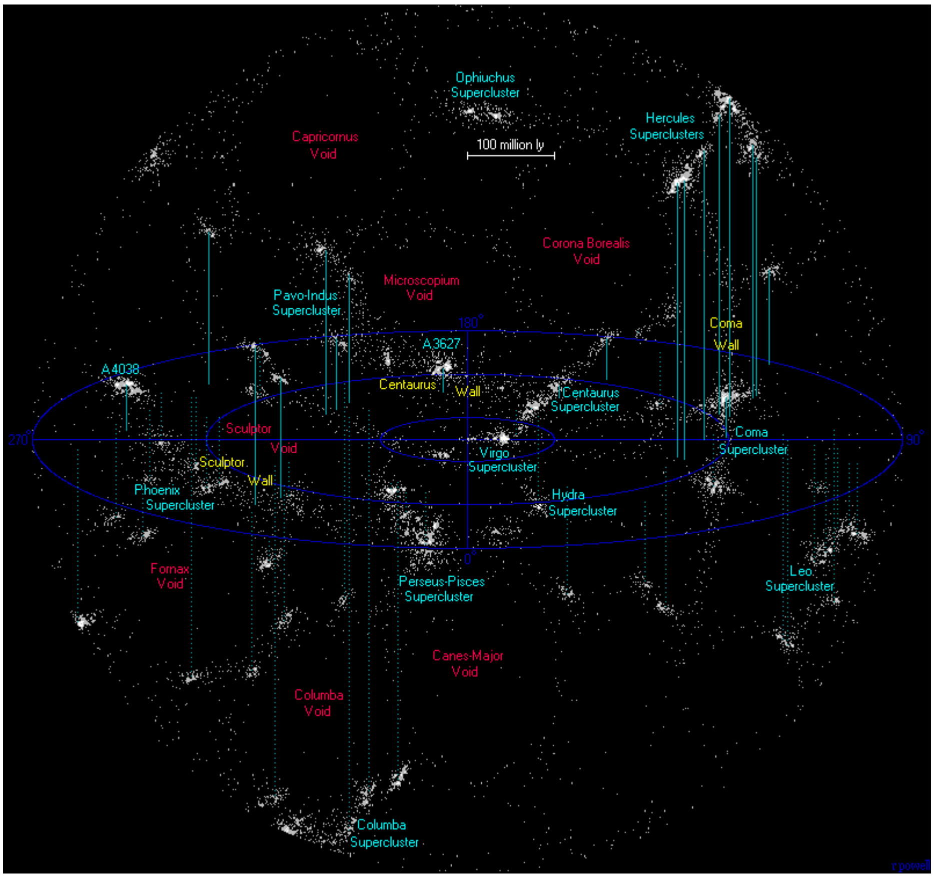

Figure 2.1: Illustration of the large-scale structures in the local Universe, including the clusters considered in the present work.

The sample of clusters of this thesis consists of the Abell clusters observed by our group in Hα, that additionally have SDSS spectroscopy: Abell 1656 (Coma cluster), Abell 1367, Abell 779, Abell 634, and the Hercules Supercluster that includes: Abell 2151 (Hercules cluster), Abell 2152, and Abell 2147. Table 2.1 summarizes the properties of our cluster sample. In Column 1 we give the name of the Abell catalog (Abell et al. 1989, from now on we use the abbreviated version for the cluster names, e.g. A1656 stands for Abell 1656), in column 2 and 3 we give the coordinates R.A. and declination in J2000.0 as given in NED, in column 4 the mean cluster redshift as given in NED. The area considered for each cluster is given in degrees projected in the sky (column 5), and in Mpc considering the distance of each cluster (column 6). We have searched for galaxies with SDSS spectroscopy in the indicated regions, and in column 7 we give the total number of galaxies found in the surveyed areas and within the redshift range considered for each cluster (this is our basic spectroscopic galaxy sample for each cluster; concerning the galaxy sample selection we give further details in Chapters 4 and 5).

Table 2.1 columns 8, 9, and 10 we give the cluster R_{200}, cluster mass and X-ray total luminosity respectively. R_{200} is defined (Carlberg et al. 1997) as the radius from the cluster center which defines a sphere with interior mean density 200 times the critical density and is used as an approximation of virial radius. It is derived by the formula given by Finn et al. (2005):

$$R_{200} = 1.73 \frac{\sigma}{1000\text{km s}^{-1}} \frac{1}{\sqrt{\Omega_\Lambda + \Omega_o (1+z)^3}} h_{100}^{-1} \text{ Mpc} \tag{2.1}$$

considering the velocity dispersion that we find from our basic spectroscopic sample for each cluster.

We derive the cluster mass as:

$$M_{cl} = 1.2 \times 10^{15} \left(\frac{\sigma}{1000\text{km s}^{-1}} \right)^3 \frac{1}{\sqrt{\Omega_\Lambda + \Omega_o (1+z)^3}} h_{100}^{-1} \ M_\odot \tag{2.2}$$

(again following Finn et al. 2005) and the total X-ray luminosities are taken from Ledlow et al. (2003). We note here that throughout this Thesis the cosmological parameters adopted are: $\Omega_\Lambda = 0.73$, $\Omega_o = 0.27$ and $H_0 = 73$ km s^{-1} Mpc^{-1}.

Figures 2.2, 2.3, 2.4 and 2.5 show the SDSS images of the central regions of the seven clusters (except for Coma where a composite optical and IR image has been dispayed). Figures 2.6, 2.7, 2.8, and 2.9 show the X-ray emission of the hot ICM of the central part of each cluster of our sample; these are composite images of the three channels of the ROSAT PSPC survey and cover 1.°6 × 1.°6. We see that our sample of seven clusters spans two orders of magnitude in mass $\sim 10^{13} - 10^{15} M_\odot$, a wide range of X-ray total emission, and significant variations in the X-ray and optical morphology, indicating a wealthy of evolutionary states.

2.2 Cluster properties

Coma (A1656) is a very massive cluster, with very high velocity dispersion and X-ray luminosity (Ledlow et al. 2003). In visible images, over a thousand of galaxies are seen to lie within a volume of 6 Mpc across. However, infrared images of *Spitzer Space Telescope* have now revealed the presence of thousands previously undiscovered dwarf galaxies (Figure 2.2). In the central part of the cluster there are two central cD galaxies NGC4874 and NGC4889, and a subcluster, projected to ~ 1.5 Mpc to the southwest of the core, and centered on NGC4839, appears to be merging with the main cluster (Briel et al. 1992; Neumann et al. 2003). Figure 2.6 shows the X-ray emission where the merging of the larger, brighter central cluster and the fainter group of galaxies to the lower right is nicely illustrated.

A1367 reveals a complex dynamical state (Cortese et al. 2004), with an elongated X-ray emission (Figure 2.6), showing multiple clumps, supporting a multiple merger scenario (Donnelly et al. 1998; Sun & Murray 2002). Additionally, substructures falling into the cluster core (Cortese et al. 2006; Gavazzi et al. 2003) suggest an early stage of formation of the cluster. Cortese et al. (2008a), based on UV photometry, have found that star formation in Coma is substantially suppressed compared to

Table 2.1: **CLUSTER SAMPLE**

Cluster (1)	R.A. J2000.0 (2)	DEC. J2000.0 (3)	z (4)	Area deg^2 (5)	Area Mpc^2 (6)	Galaxies (7)	R_{200} Mpc (8)	Mass ($M_\odot$) (9)	Lx (10^{43} erg s^{-1}) (10)
A1656	12 59 48.7	27 58 50	0.0231	5.7×5.7	10.2×10.2	1017	1.73	1.2×10^{15}	9.30 ± 0.14
A1367	11 44 29.5	19 50 21	0.022	5.2×5.2	8.9×8.9	564	1.51	8.1×10^{14}	2.30 ± 0.08
A779	09 19 50.8	33 46 17	0.0225	2×2	3.4×3.4	106	0.58	4.6×10^{13}	0.29 ± 0.04
A634	08 14 33.7	58 02 52	0.0265	2×2	3.9×3.9	97	0.67	7.1×10^{13}	< 0.08
A2151†	16 05 15.0	17 44 55	0.0366	1.6×1.6	4.4×4.4	300	1.37	6.1×10^{14}	1.60 ± 0.10
A2152	16 05 22.4	16 26 55	0.041	1.6×1.6	4.9×4.9	135	0.61	5.5×10^{13}	0.28 ± 0.07
A2147	16 02 17.2	15 53 43	0.035	1.6×1.6	4.2×4.2	348	1.07	2.9×10^{14}	3.00 ± 0.12
HSC†				4.6×5.0	$\sim 13 \times 14$	1379			

Note. Column 1: cluster name; column 2: right ascension of the cluster center as given in NED (Abell et al. 1989) in hours, minutes, seconds; column 3: declination of the cluster center as given in NED (Abell et al. 1989) in degrees, minutes, seconds; column 4: redshift as given in NED; column 5: area considered in deg^2; column 6: area considered converted in Mpc for each cluster distance; column 7: total number of galaxies with SDSS spectroscopy in the area considered and the redshift range of each cluster; column 8: R_{200} derived using the velocity dispersion we derive; column 9: cluster mass derived using the velocity dispersion we derive; column 10: *ROSAT* total X-ray luminosity (Ledlow et al. 2003).

† Additionally a follow-up with long-slit optical spectroscopy of 27 SF galaxies has been performed in the central 1.4 Mpc ($= R_{200}$) region of A2151.

‡HSC stands for Hercules Supercluster. The region considered is defined by Barmby & Huchra (1998): 239.0<R.A.<243.6 , 14.35<DEC.<19.34, in a redshift range $0.0283 < z < 0.0483$.

Figure 2.2: Upper panel: Composite image of infrared *Spitzer Space Telescope* (red and green) with visible SDSS data (blue) for the central part of the Coma cluster, over 1 deg wide ($\sim$ 1.7 Mpc). The two giant elliptical galaxies NGC4874 and NGC4889 are easily distinguished in blue, and many dwarf galaxies, comparable to the Small Magellanic Cloud, appear as green points in the field (Image credit: NASA/JPL-Caltech/GSFC/SDSS). Lower panel: SDSS image of the center of A1367.

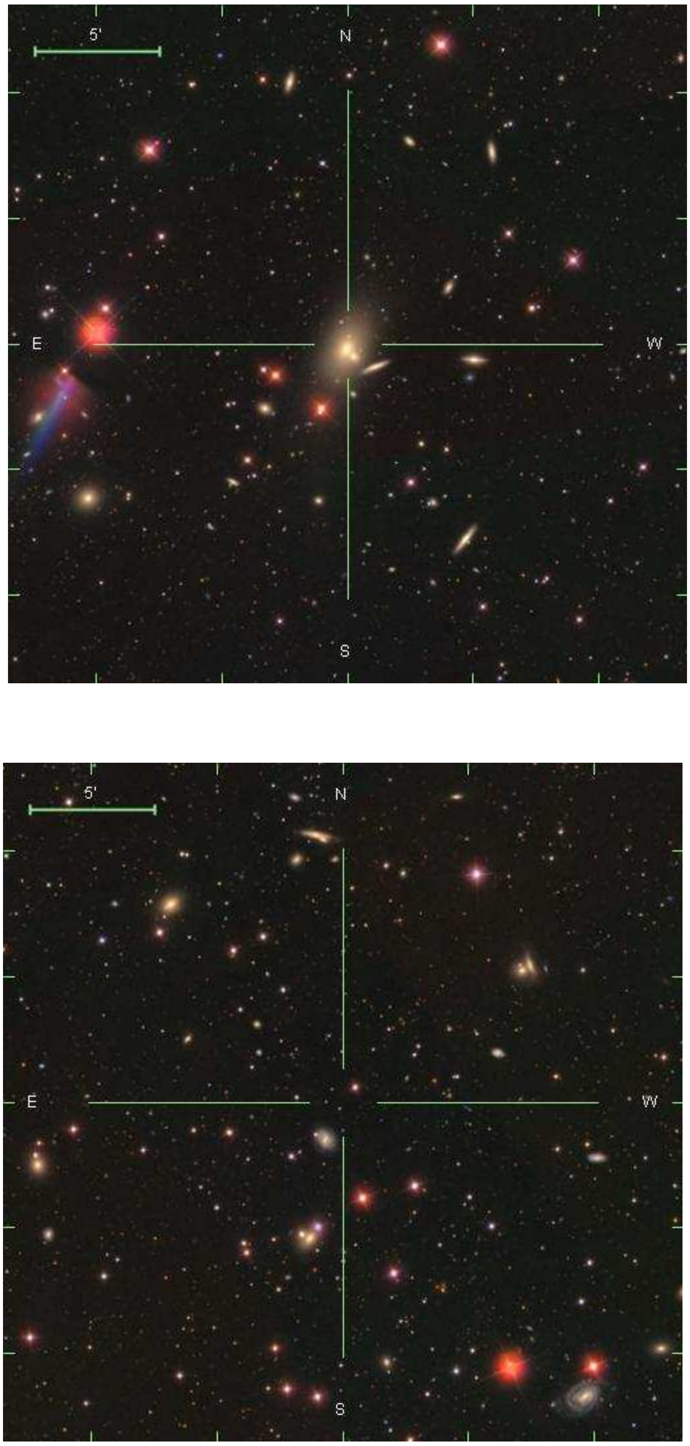

Figure 2.3: SDSS image of the center of A779 (upper panel) and A634 (lower panel).

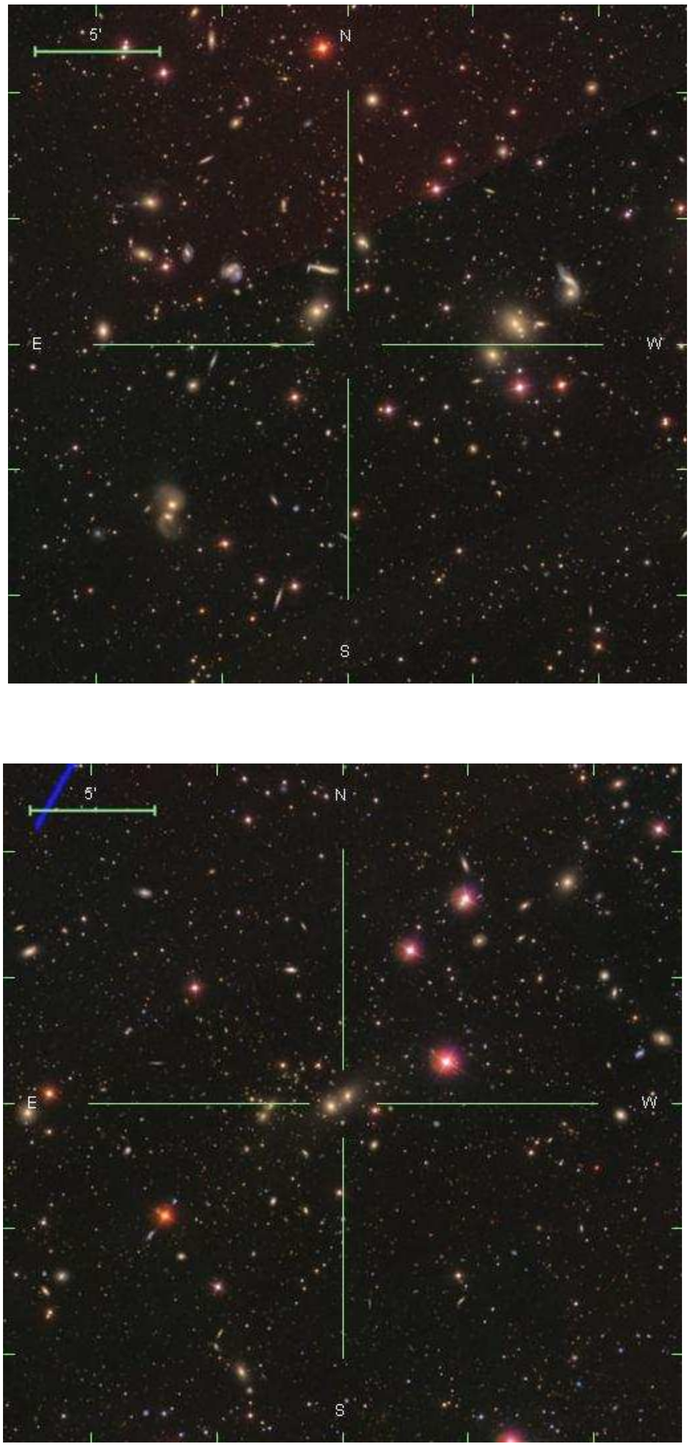

Figure 2.4: SDSS image of the center of A2151 (upper panel). There is a rich variety of phenomena evident in this image, such as many SF spirals and dwarfs (clearly distinguished by their blue colors), and interactions among spirals and among ellipticals. SDSS image of the center of A2152 (lower panel).

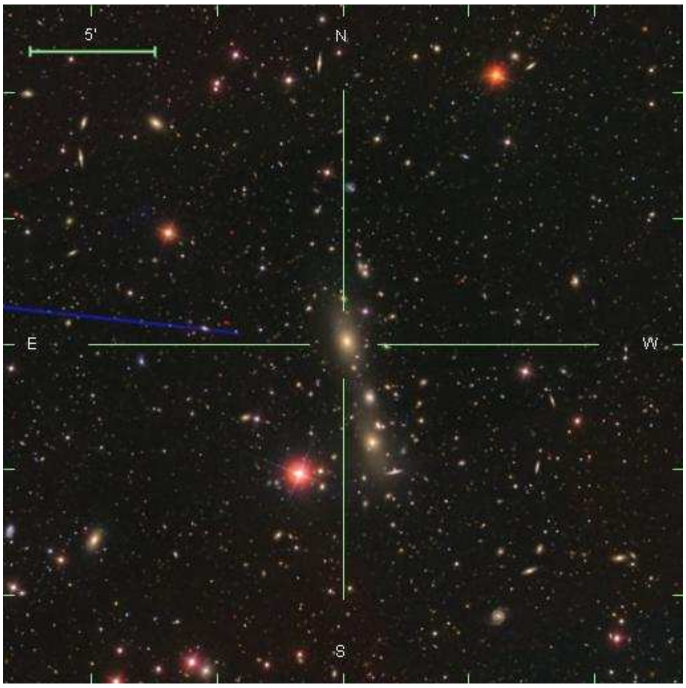

Figure 2.5: SDSS image of the center of A2147.

that in the field, while A1367 has an abundance of bright SF galaxies. The optical luminosity function of galaxies has a much steeper faint-end slope in Coma than in A1367 (Iglesias-Páramo et al. 2003a). On the other hand, A779 and A634 are two clusters of very low velocity dispersion. A779 presents a nearly circular X-ray emission around the cD galaxy NGC2832 while A634 X-ray luminosity is at the ROSAT detection limits.

The Hercules cluster (A2151) is the richest and densest among the three members of the Hercules supercluster and appears to be a collection of groups, gravitationally bound but far from dynamical relaxation; the galaxy surface density as well as the velocity space reveals the presence of subclusters in the galaxy distribution (Bird et al. 1995; Maccagni et al. 1995). Sánchez-Janssen et al. (2005) report the presence of at least three distinct regions with a varying dwarf to giant galaxy ratio within the A2151 cluster. Giovanelli et al. (1981) studied the supercluster neutral hydrogen content and found that A2147 is clearly deficient in contrast with A2151 which shows normal to mildly gas deficient galaxy population, concluding that A2151 may still be in the process of formation. Dickey (1997) reported the presence of strong environmental effects on the mass of HI in the A2151 cluster.

The extended X-ray emission coming from the hot intracluster gas (Figure 2.10) shows an irregular pattern which divides the cluster into two components (Huang & Sarazin 1996; Bird et al. 1995). There is a primary X-ray maximum concentric with the the brighter cluster galaxy NGC6041A. However, the maximum of the cluster galaxy distribution is not coincident with that primary X-ray maximum, but with a

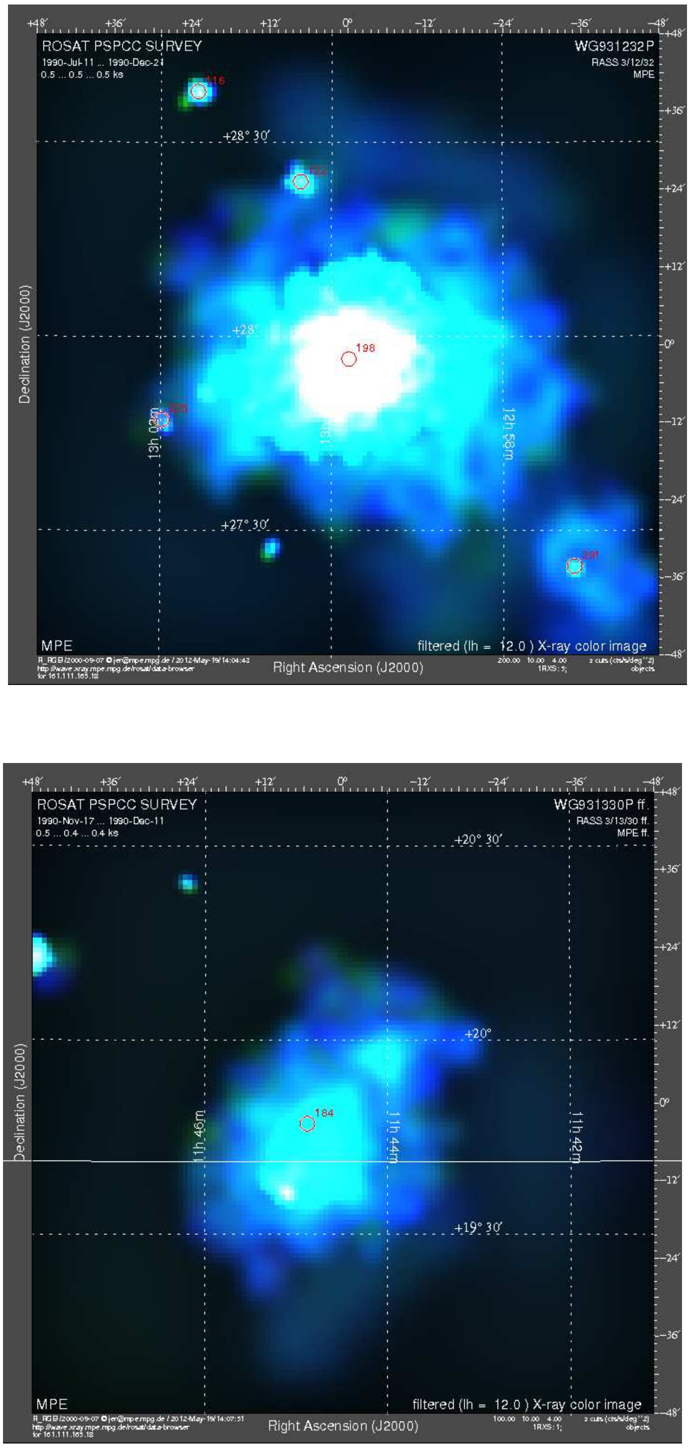

Figure 2.6: ROSAT PSPC survey images of the central 1.°6 × 1.°6 of A1656 (upper panel) and A1367 (lower panel). Red circles indicate objects from Rosat All-Sky Survey Bright Source Catalogue (1RXS-B).

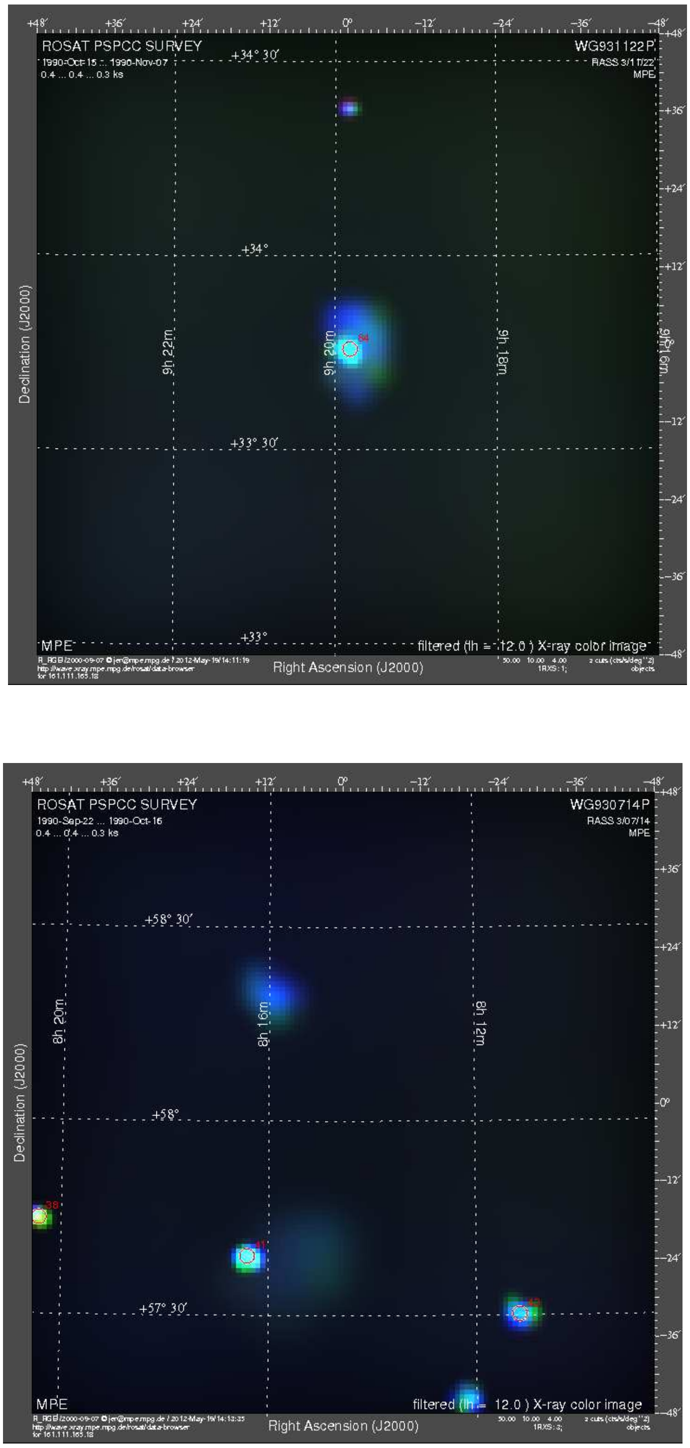

Figure 2.7: The same as in Figure 2.6 for A779 (upper panel) and A634 (lower panel).

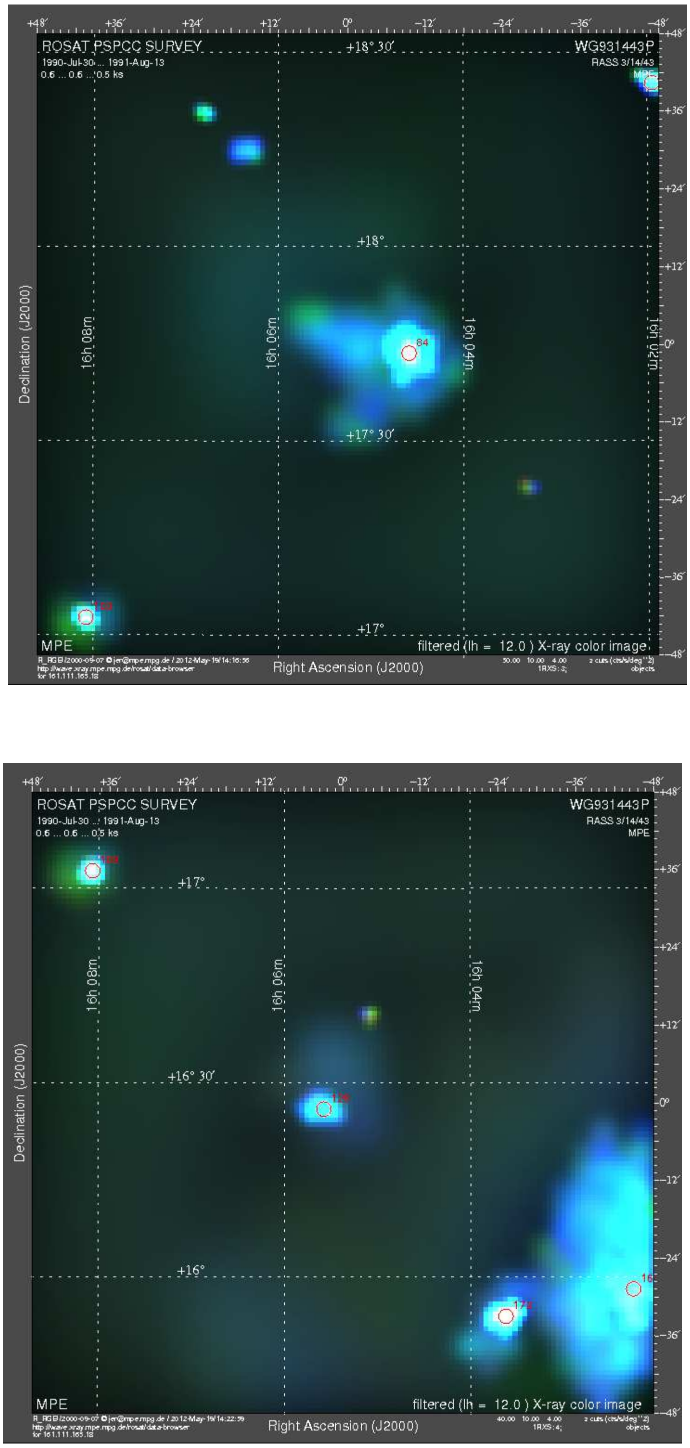

Figure 2.8: The same as in Figure 2.6 for A2151 (upper panel) and A2152 (lower panel).

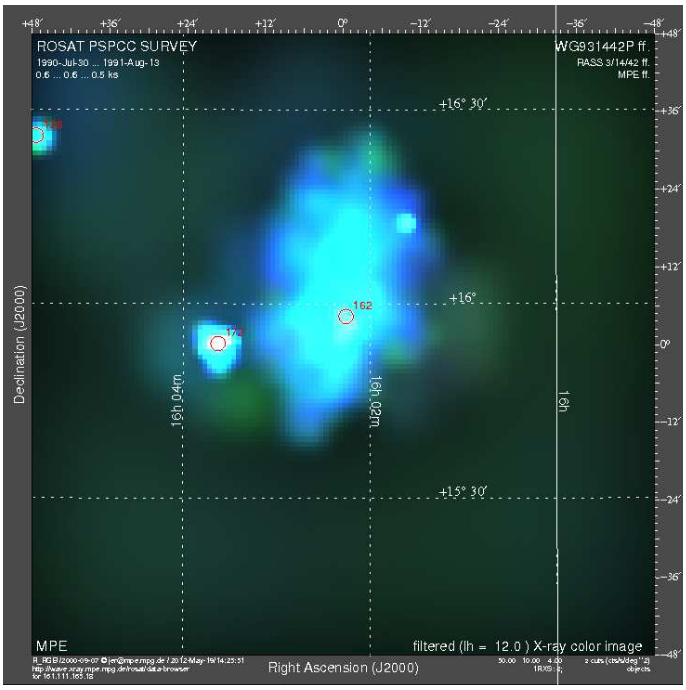

Figure 2.9: The same as in Figure 2.6 for A2147.

secondary one located 10-15 arcmin to the East of the primary. Given the abundant substructures seen in X-ray and in optical emission, Bird et al. (1995) claimed that central and eastern sub-clusters of A2151 have recently undergone a merger event, which implies that many A2151 galaxies are not expected to be embedded in a hot X-ray ICM. Thus, Hercules cluster provides an ideal case in which the different effects of the cluster environment on the evolution of the galaxies can be studied "caught in the act" (Figure 2.4).

A2147 appears to be the most regular among the three, with the highest X-ray luminosity, and contains "an unusual diffuse radio source" reported by Burns et al. (1994). Recent high-quality X-ray data from *Chandra* reveal (Hudson et al. 2010) that the X-ray peak of A2147 matches with the position of the BCG, the northernmost of the three bright galaxies forming a line in the core of the cluster. A2152 is the more distant among the three and it shows very low X-ray emission.

2.3 Hα imaging surveys of our sample clusters

The Hα imaging studies performed by our group have offered valuable information on the properties of the SF galaxy population in our sample clusters. These previous results reveal the effect of the environment on the SFH of cluster galaxies. Summarizing, an important number of low-mass SF galaxies have been observed in all these clusters, differences in the Hα luminosity and *EW* distributions between clusters have been found, and also scale relations between properties of the host

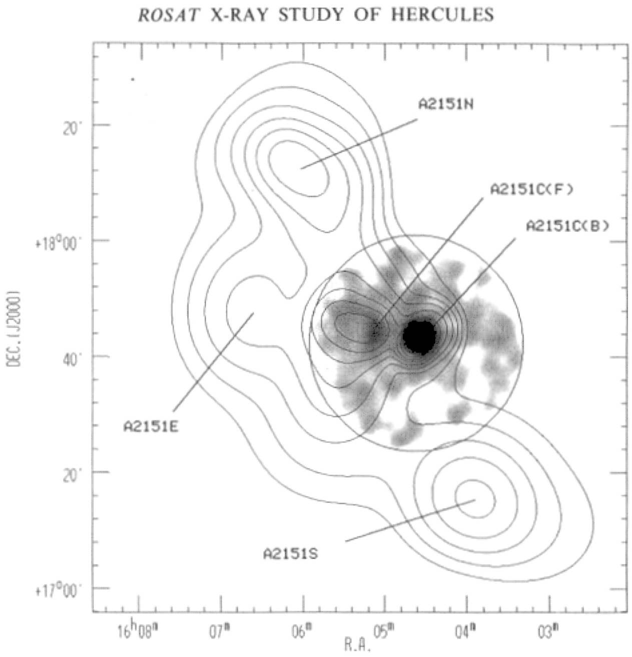

Figure 2.10: High-Resolution ROSAT data reveal the irregular X-ray emission pattern of the Hercules cluster (gray-scale). The contours correspond to the luminosity weighted surface galaxy density distribution of the cluster. The primary X-ray maximum is concentric with the the brighter cluster galaxy NGC6041A (Figure 2, Huang & Sarazin 1996).

clusters and the SF galaxy population.

For example, the upper panel of Figure 2.11 shows the Hα fluxes for the volume limited samples of A2151 (Cedrés et al. 2009), Coma, and A1367 (Iglesias-Páramo et al. 2002) and the Hα survey of the local 11 Mpc volume from Kennicutt et al. (2008). We note that the lower limit of the Hα luminosities for the sample of cluster galaxies is approximately L(Hα)≈ 10^{39} erg s^{-1} and the B absolute magnitudes reach $M_{\rm B} \approx -14$, meaning that this sample of cluster galaxies includes a non-negligible fraction of dwarf SF galaxies. We see that all four galaxy samples follow the same relation on this plot, which is almost linear in the case of the field sample and shows a larger scatter in the case of the clusters, with a maximum scatter for Coma cluster.

The bottom panel shows the histograms of the Hα luminosity distributions of the four samples. The total histogram for the three clusters is represented with the dashed black line, weighting each cluster by the inverse of the surveyed volume. This is done in order to compare the shape of the distribution of the field sample to the one of the clusters. To this reason the two distributions were normalized in the range between log(L(Hα))/erg s^{-1}=41 and 42. In the range from log(L(Hα))/erg s^{-1}=39 to 41, the two distributions show different shapes reflecting a relative deficit of cluster SF galaxies with respect to the field galaxies.

In Figure 2.12 is presented the EW(Hα) distribution for the sample of clusters

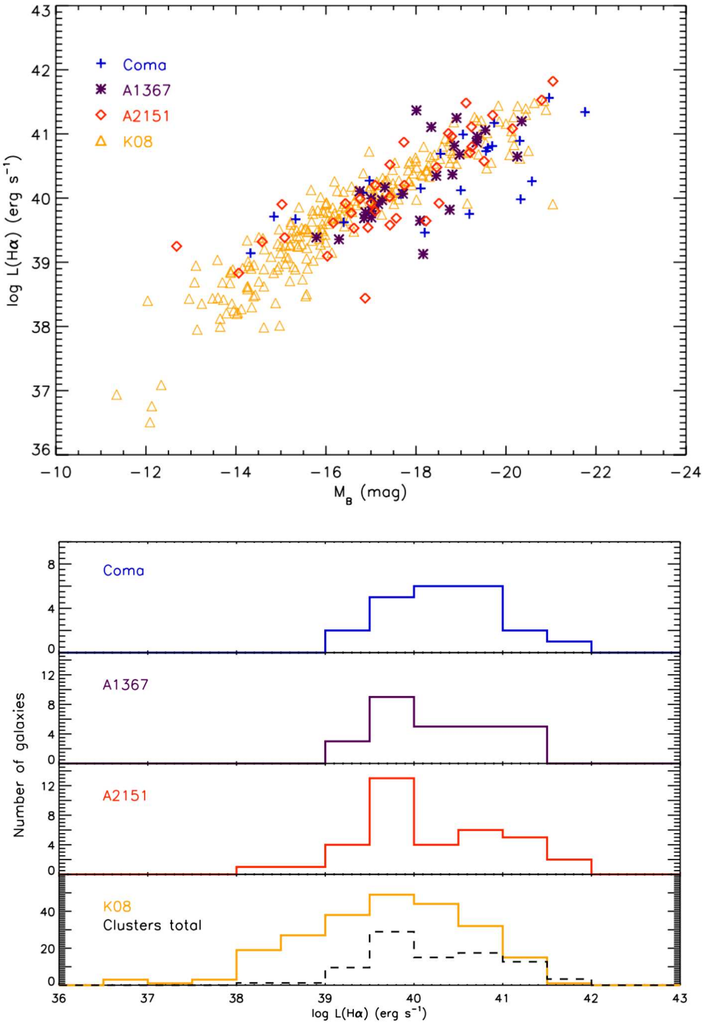

Figure 2.11: Upper panel: Log(L(Hα)) versus $M_{\rm B}$ for Coma (blue crosses), A1367 (violet asterisks), A2151 (red diamonds), and K08 (orange triangles) SF galaxies (Figure 8, Cedrés et al. 2009). Lower panel: Histogram of the Hα luminosity for the same four samples. The black dashed line in the bottom panel corresponds to the combined distribution of the three clusters weighted each one to the corresponding surveyed volume (Figure 10, Cedrés et al. 2009).

of Reverte (2008), which appears to be different from the corresponding distribution for the sample of field galaxies from James et al. (2004) (plotted with the dotted line). The EW(Hα) distribution for field galaxies presents a peak EW greater than the peak found for the clusters, that means that in these clusters we find galaxies with low values of the EW(Hα), which appear rare in the field sample. These results clearly reveal that the cluster environment affects the star formation activity in galaxies. Additionally, Reverte (2008) found tight correlations between the fraction of bright galaxies ($M_{\rm R} < -20$) with ongoing SF (f_{sf}) and both the

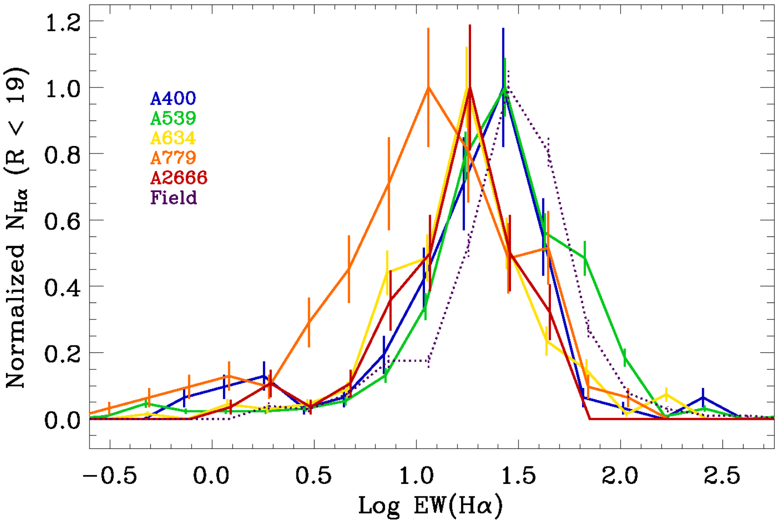

Figure 2.12: Normalized frequency distribution of the logarithm of EW(Hα) for cluster galaxies and a field sample (Figure 7.3, Reverte 2008).

velocity dispersion and the bolometric X-ray luminosity for his sample of clusters plus the two clusters (Coma and A1367) observed by Iglesias-Páramo et al. (2002) (Figure 2.13). These results suggest that the population of SF galaxies in a cluster must be sensitive to the *global properties* of the host cluster.

Therefore, for the goal of the present study, that is to search for the imprint of the environment on the chemical evolution of cluster galaxies, it has been a natural choice to start with this sample of well-known nearby clusters. Moreover, this previous knowledge has been the background in order to design the spectroscopic follow-up we performed for a subsample of these clusters (see Chapters 3 and 6). For example, a detailed morphological study of the Hα emission of A2151 SF galaxies permitted to define the best placement of the long-slit to cover the major SF regions (see Figure 3.3 in the following).

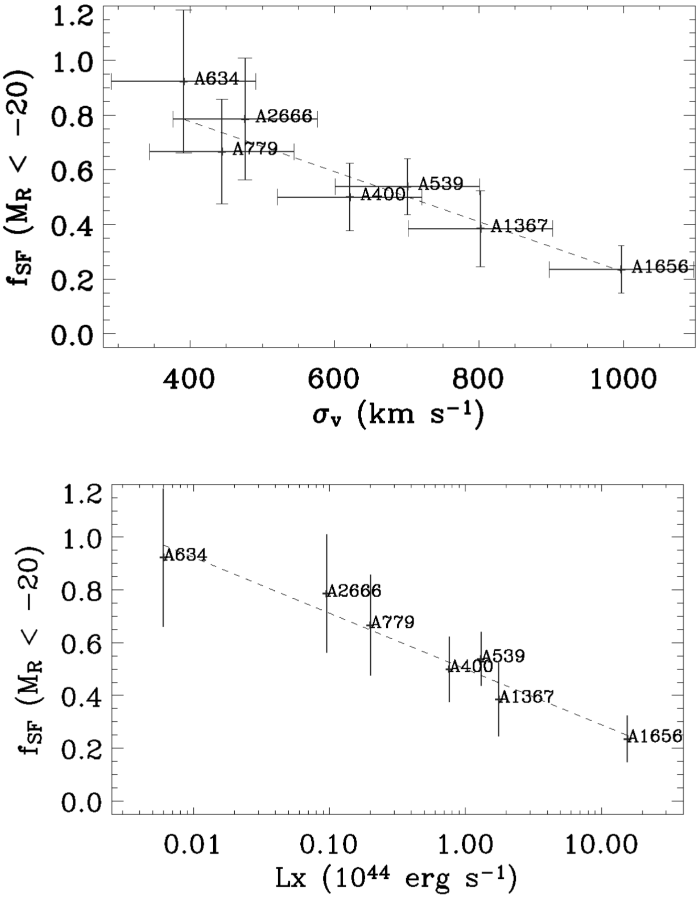

Figure 2.13: Fraction of bright ($M_{\rm R} < -20$) SF galaxies as a function of the cluster velocity dispersion (upper panel) and the X-ray luminosity (lower panel): Figures 7.17 and 7.19 from Reverte (2008).

CHAPTER 3

Spatially resolved spectroscopy of star-forming galaxies in the Hercules cluster

Contents

3.1 Introduction

SFH, gas-content and the mass exchange with the environment (infall of metal-poor gas and/or outflow of enriched material) are fundamental variables that regulate the chemical evolution of a galaxy. Clusters of galaxies host large numbers of galaxies of various sizes, luminosities and morphologies as well as a large mass of gas confined within a given volume of space. Thus galaxy clusters can provide an excellent place to study the impact of the environment on the aforementioned fundamental variables regulating the metal content of a galaxy.

A number of works have been devoted to searching for the possible effects of cluster environment on the chemical properties of spiral galaxies in the Virgo cluster (Shields et al. 1991; Henry et al. 1992, 1994, 1996; Skillman et al. 1996; Pilyugin et al. 2002). The spirals at the periphery of the cluster are indistinguishable from the field galaxies, whereas for the HI deficient Virgo spirals near the core it has been claimed that their abundances are higher than for the spirals located at the periphery of the cluster or in the field with comparable luminosity or Hubble type. On the other hand, several works devoted to the study of the star formation and the metal content of dwarfs in nearby clusters such as Virgo, Coma, and Hydra have revealed that some of them show a different behavior with respect to field galaxies, and this fact has been attributed to the effect of the cluster environment (Vilchez 1995; Duc et al. 2001; Iglesias-Páramo et al. 2003b; Vílchez & Iglesias-Páramo 2003; Lee et al. 2003; Vaduvescu et al. 2007; Smith et al. 2009; Mahajan et al. 2010).

In the era of the large surveys, observational clues which constrain galaxy evolution scenarios in dense environments have lately started to be investigated on the basis of large samples of galaxies. Mouhcine et al. (2007) suggested that the evolution of SF galaxies is driven primarily by their intrinsic properties and is largely independent of their environment over a large range of local galaxy density. On the contrary, Cooper et al. (2008) find a strong relationship between metallicity and environment, such that more metal-rich galaxies favor regions of higher overdensity. Ellison et al. (2009) also support the environmental influence, and specially of the local density, on the MZR. It is clear that a full understanding of the role played by the environment on galaxy evolution still remains a major issue. All these works based on SDSS spectroscopic data present a deficit of important observational information on dwarf cluster galaxies. In addition, SDSS provides aperture spectroscopy, thus missing spatially resolved information that can be much needed, e.g. to analyze the spatial properties of galaxies in clusters.

In this chapter we focus our attention on the nearby Hercules (A2151) cluster of galaxies and we investigate the impact of the cluster environment on the chemical history of galaxies. The Hercules cluster shows an amazing variety of sub-structures seen in X-ray emission and broad-band imaging (see Section 2.2), which makes it one of the more interesting nearby (at a distance of 158.3 Mpc) dense environments, never studied before from the chemical evolution point of view.

3.2 The galaxy sample

In this work we have benefited from our deep search for Hα emitting galaxies in the Hercules cluster (Cedrés et al. 2009, C09 from now on) to define our sample of SF galaxies. Tracing Hα emission in order to study the population of galaxies with recent star formation has two important advantages: 1) it is not aperture biased as many of the spectroscopic studies using fibers and 2) it reveals star forming dwarfs which would not have been classified as SF galaxies with an optical flux criterion. We investigate gas-phase metallicities and stellar properties of galaxies which span a large range of magnitudes ($-21 \leq M_{\rm B} \leq -16.5$ mag) and morphologies (from grand design spirals to blue compacts and tidal dwarfs).

Spatially resolved spectroscopy has been obtained for 27 Hercules SF galaxies of the C09 sample[1]. We complement our sample with two more galaxies of the C09 sample which have SDSS spectroscopy. In addition, two more galaxies are considered from Iglesias-Páramo et al. (2003b) (IP03 from now on) A2151 sample of dwarf galaxies (see section 3.6.2 for more details). Thus our spectroscopic sample comprises a total of 31 galaxies and our spectroscopic follow-up of the C09 sample is completed up to an absolute magnitude $M_{\rm B} = -17$ mag. To illustrate this, in Figure 3.1 we show the histogram of the C09 sample of SF galaxies as a function of their $M_{\rm B}$ absolute magnitude and the fraction of the galaxies with no spectroscopic data.

Our sample is composed of 15 luminous SF galaxies ($M_{\rm B} \leq -19$) and 16 dwarf and Magellanic type irregular galaxies ($M_{\rm B} > -19$). Among the spiral/irregular galaxies, 9 show discernible spatial structure and therefore their different parts have been analyzed independently (see also Section 3.4.2 and Figure 3.9). For three luminous galaxies and three dwarfs/irregulars we have gathered together evidences that they are affected/perturbed from galaxy-galaxy interactions, either being members of mergers, tidal dwarf candidates, or their HI morphology showing evidences of interaction. In Section 3.3 and in Appendix A.1 we give details on these interacting objects and in Appendix A.2 some additional peculiar cases are presented.

Figure 3.2 illustrates the positions of our spectroscopic sample galaxies (pluses and squares) with respect to the density of the ICM (as seen in X-ray surface brightness map from the ROSAT All-Sky Survey; in blue) and the galaxy surface density of the cluster (derived counting Hercules members[2] with SDSS spectroscopy; red color). Most Hα emitters are located around the secondary X-ray maximum, in the regions of higher density of A2151 galaxies (indicated by the NED position of the mass center; blue cross in Figure 3.2) within the central region $< R_{200} \simeq 1.4$ Mpc of the Hercules cluster. In Figure 3.2 the open squares mark the dwarf/irregular galaxies with radial velocity different from the radial velocity of NGC6041A ΔV larger than σ_v, the radial velocity dispersion[3] of Hercules cluster, i.e. abs$(\Delta V) > \sigma_v$, a possible indication of an infalling population as we will discuss in Sections 3.7 and 3.9.

---

[1] From our spectroscopic data it is shown that the radial velocity of one (SDSSJ160547.17+173501.6) of the C09 galaxies is out of the velocity range of the Hercules cluster, rendering its membership to the cluster unlikely. The various SDSS photo-z estimates were consistent with the criteria adopted by C09 for cluster membership. More details are given in Appendix A.2.

[2] within the velocity range of the subclusters of A2151 defined in Bird et al. (1995)

[3] The radial velocity dispersion of the Hercules cluster $\sigma_v = 752$ km s^{-1} (Bird et al. 1995).

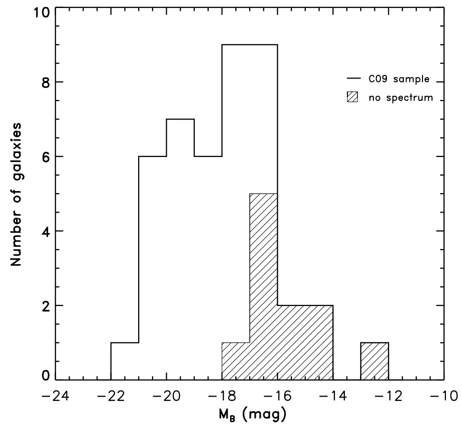

Figure 3.1: The histogram of the C09 sample of SF galaxies as a function of their M_B absolute magnitude where we show the fraction of galaxies with no spectroscopic data (filled region). Our spectroscopic follow-up of the C09 Hercules SF galaxies is complete up to absolute magnitude $M_\mathrm{B} = -17$ mag.

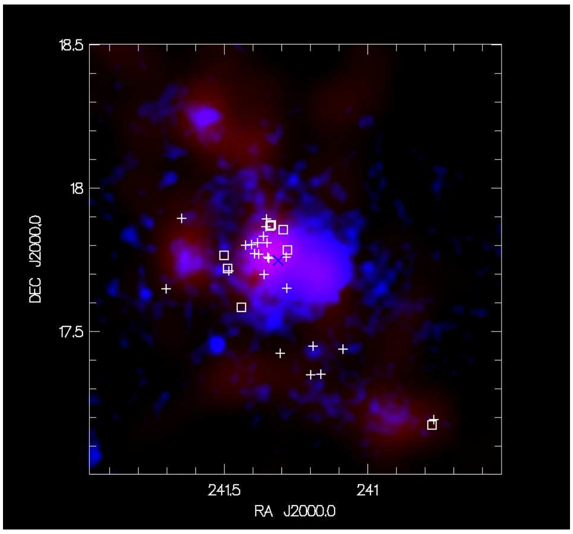

Figure 3.2: Superposision of the density map of the Hercules cluster (red) and the ROSAT All-Sky Survey X-ray map (blue). For the density map we have counted the Hercules cluster galaxies with SDSS spectroscopy. Locations of SF galaxies of the present sample are superposed (crosses and squares). Open squares indicate dwarf galaxies with abs(ΔV) $> \sigma_v$. North is at the top and East is to the left. The galaxy surface density reveals the presence of subclusters. The extended X-ray emission coming from the hot intra-cluster gas shows an irregular pattern which divides the cluster into two components. Most Hα emitters are located around the secondary X-ray maximum, in the regions of higher density of the A2151 galaxies. The blue × indicates the cluster center position given in NED.

3.3 2D morphological study of Hercules star-forming galaxies

In order to study the structural properties of the A2151 emission line galaxies, we have produced their color maps, using the g and i-band images from the SDSS (Figure 3.3, left). Additionally we have produced EW(Hα) maps, using the continuum subtracted Hα images and the images of the adjacent broad-band continuum, using the data from the deep Hα survey of the central part of A2151 cluster, presented by Cedrés et al. (2009).

The Hα images were obtained during two observational runs. The first one was from 6 to 7 of May 2003 at the NOT2.5m located at the Roque de los Muchachos Observatory (ORM). The instrumentation used was the ALFOSC spectrograph in direct imaging mode with a redshifted Hα filter centered at $\lambda_c = 6803$Å and with FWHM of $\Delta\lambda = 50$Å for the emission line, and a Gunn-r centered at $\lambda_c = 6800$Å and with FWHM of $\Delta\lambda = 1020$Å broad-band filter for the continuum. The second run was during 4 and 5 of June 2003 at the WHT4.2m, at the ORM. The instrumentation used was the Prime Focus Camera with two redshifted Hα filters centered at $\lambda_c =$ 6785Å and 6834Å, and with FWHM of $\Delta\lambda = 51$Å and 58Å respectively for the emission line, and a Harris-R centered at $\lambda_c = 6408$Å with a FWHM of $\Delta\lambda = 1562$Å broad-band filter for the continuum.

This detailed morphological study permitted to prepare carefully our long-slit spectroscopic observations, placing (whenever possible) the slit over the major SF regions (Figure 3.3 and Appendix A.1 where all the galaxies with rich spatial structure are included). Moreover, we identified some interesting cases of intense starburst galaxies. For example the galaxy PGC057077 (Figure 3.4), which is classified in LEDA as an elliptical galaxy. The C09 Hα survey showed that PGC057077 is a very intense and compact Hα emitter with $f_{H_\alpha} = 87 \times 10^{-15}$ erg cm^{-2} s^{-1} and EW(Hα)=148Å. Although the galaxy is very compact and does not show any structural properties, we noted on its $g - i$ map a conspicuous color gradient. In our long-slit spectrum (see next section) we were able to identify two regions with important difference of the continuum emission. In order to check for velocity gradient and differences in the chemical content between these two regions, we separated the 2D spectrum in two corresponding 1D spectra. The important continuum emission difference of the 1D spectra can be contemplated in Figure 3.10. From our emission-line analysis we do not find any significant velocity variation between the two different galaxy parts, neither any difference in the chemical abundances. The difference in the continuum emission is attributed then to the high extinction suffered by both the stellar population and the gas in the NW part of the galaxy which correspond to our (a) spectrum part. This peculiar galaxy is situated close to the edge of the principal X-ray emitting region, at 650 kpc from the X-ray center. In the NE of the galaxy there is discernible a low surface blue plume, that could point toward the existence of a faint companion. The existing data are not conclusive whether it could have been the ICM-ISM interaction or a galaxy merger

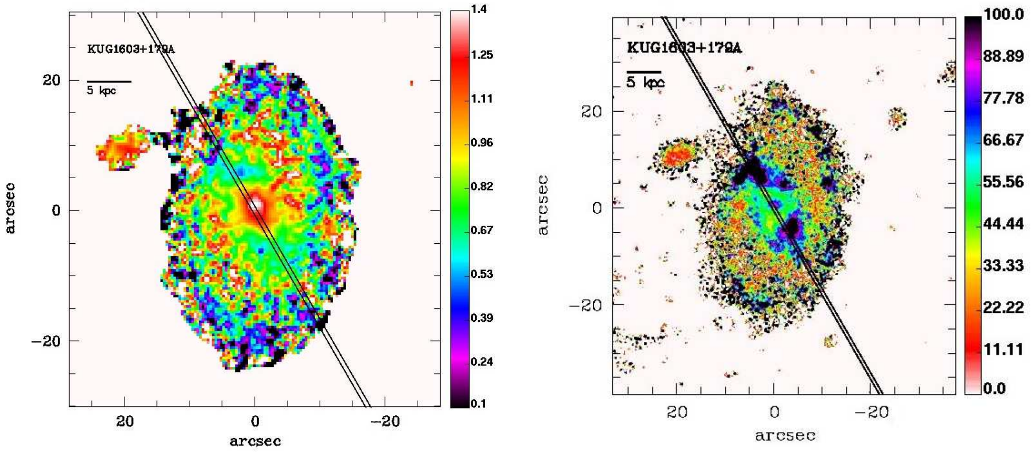

Figure 3.3: An example of emission-line galaxy in A2151. We produced the color $(g-i)$ map (left) and the $EW(\mathrm{H}\alpha)$ map (right), and adequately defined the position of the long-slit for our spectroscopic follow-up, to cover the major SF regions. In Appendix A.1 we give the color $(g-i)$ map and $EW(\mathrm{H}\alpha)$ map for all the galaxies with rich spatial structure.

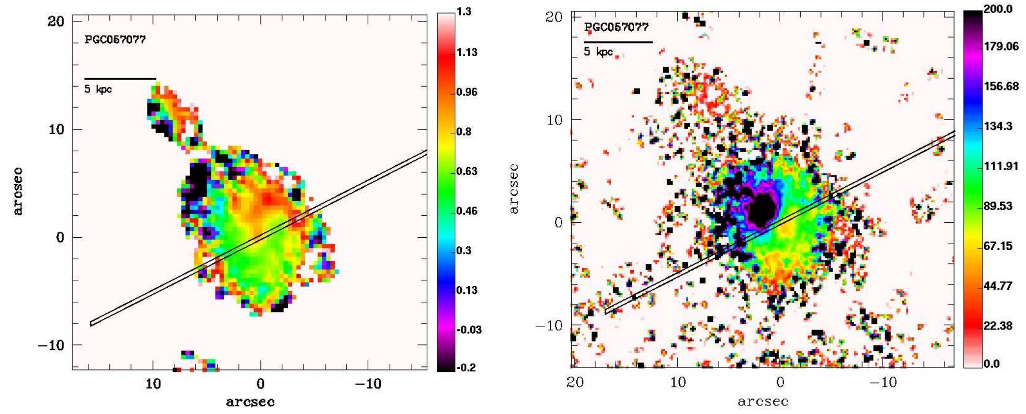

Figure 3.4: The $g-i$ color map (upper left), $EW(\mathrm{H}\alpha)$ map (upper right), and SDSS composite image (lower panel) of the peculiar galaxy PGC057077 in A2151.

that could have triggered the unusual starburst of this galaxy. Further mid-infrared observations would be of interest there.

Another particularly interesting example is the case of IC1182. IC1182 is a late-merger that undergoes vigorous nuclear starburst activity with a SFR, estimated from its infrared and extinction-corrected Hα luminosity, to be between 11 and 90 $M_\odot$ yr^{-1} (Radovich et al. 2005; Moles et al. 2004). IC1182 shows an extended ($\sim$60 kpc) stellar tail to the east, where a tidal dwarf candidate (TDC) IC1182:[S72]d is discernible (identified by IP03; named ce-061 after Dickey (1997)). To the north of the system and to a comparable distance there are also distinguished faint tidal features and plumes.

In addition, to the west of the merging system, at a projected distance of ∼60 kpc, there is the dwarf galaxy SDSSJ160531.84+174826.1 which has been claimed (Dong et al. 2007) to be a Seyfert 1 AGN (but see Section 3.6). Dickey (1997) reports a long HI structure extending northwest of IC1182, creating a bridge of HI clumps towards SDSSJ150531.84+174826.1 (see Figure 3.a of IP03), although the galaxy SDSSJ150531.84+174826.1 itself was not detected as a consequence of the velocity cuttoff (9820 km s^{-1}) of the spectrometer used by Dickey (1997). These lines of evidence point towards a physical connection among the three galaxies.

The upper panel of Figure 3.5 is the $g - i$ color map, and illustrates the blue colors of the TDC on this extended stellar tail as well as a prominent dust lane ∼ 2 arcsec West of the optical center. The lower panel is the $EW(\mathrm{H}\alpha)$ map, showing an extended ionized gas emission, most notably a bipolar structure, indicating a pair of off-center maxima in the close vicinity of the unresolved nuclear starburst source. As seen in Figure 3.6, the $EW(\mathrm{H}\alpha)$ maxima do not coincide with the optical maximum and their intensity is reversed to that we see in the Hα map. In general, this detailed photometric work helped us define the exact positions of the tidal features and outflows and we observed them spectroscopically with ISIS at WHT4.2m, during a Director Discretionary Time (DDT) night devoted to this object, on 9 July 2009.

3.4 Spatially resolved spectroscopy

3.4.1 Observations

Long-slit spectroscopy was carried out at the WHT4.2m and the INT2.5m at the ORM, in Spain (Figure 3.7). Table 3.1 shows the journal of the spectroscopic observations. We present for each galaxy the object name as quoted by C09, RA, DEC, observation date, telescope, effective wavelength range, slit position angle and total exposure time. Most of the galaxies were observed as closer to the zenith as possible, always with air-mass less than 1.3, in order to minimize any differential atmospheric refraction effects; except in four cases, as indicated in Table 3.1, for which the paralactic angle was used.

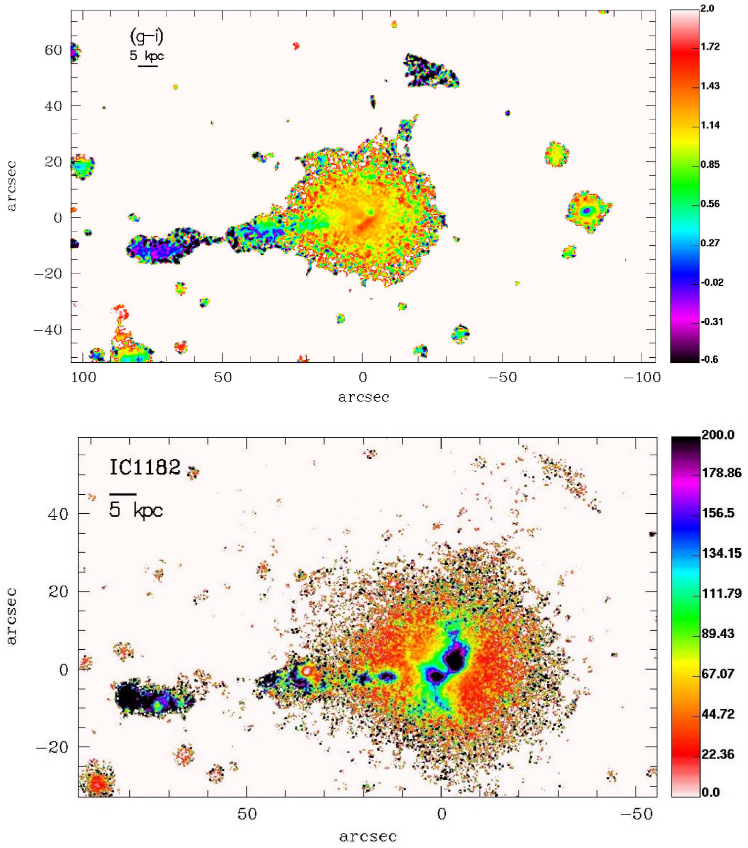

Figure 3.5: The $g-i$ color map (upper panel) and $EW(\mathrm{H}\alpha)$ map (lower panel) of the interesting late merger IC1182.

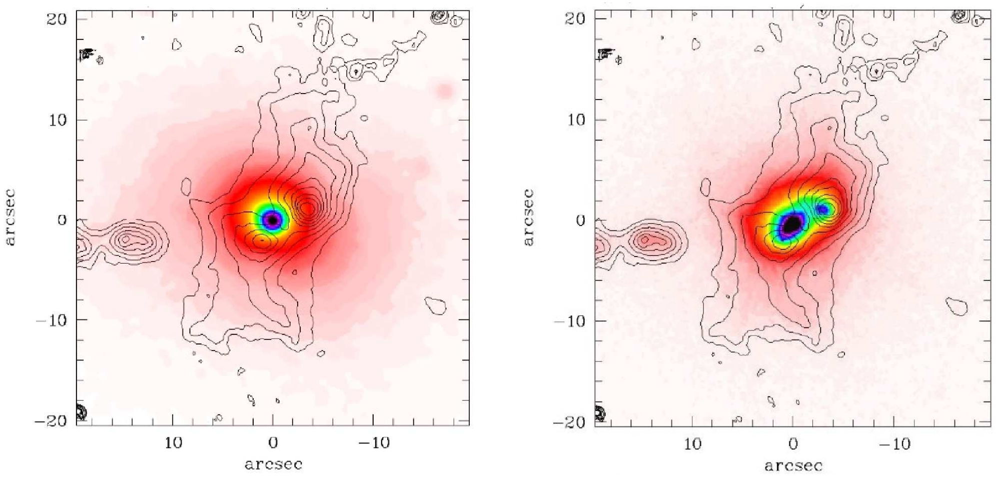

Figure 3.6: Left: Superposition of $EW(\mathrm{H}\alpha)$ contours with the R band image of IC1182. Right: $EW(\mathrm{H}\alpha)$ contours overlaid with the continuum-subtracted Hα image of IC1182. Note the bipolar emission in Hα, indicating a pair of off-center maxima that do not coincide with the optical maximum and their intensity in $EW(\mathrm{H}\alpha)$ is reversed to that we see in the Hα.

Table 3.1: **Log of Observations**

Galaxy (1)	R.A. J2000.0 (2)	DEC J2000.0 (3)	Date (4)	Tel. (5)	Range (6)	P.A. (7)	Exp. (8)
PGC057185	16 06 48.2	17 38 51.6	2008 Jun 06	INT	3500-7730	13	3600
IC1173	16 05 12.6	17 25 22.3	2008 Jun 06	INT	3500-7730	45	3600
KUG1603+179A	16 05 30.6	17 46 07.2	2008 Jun 06	INT	3500-7730	30	4500
NGC6050A,B‡	16 05 23.4	17 45 25.8	2008 Jun 06	INT	3500-7730	67†	3600
LEDA1543586	16 05 10.5	17 51 16.1	2008 Jun 07	INT	3500-7730	297	5300
NGC6045	16 05 07.9	17 45 27.6	2008 Jun 07	INT	3500-7730	75	4500
KUG1602+174A	16 04 39.0	17 20 59.9	2008 Jun 07	INT	3500-7730	59†	5400
LEDA084719	16 05 07.1	17 38 57.8	2008 Jun 07	INT	3500-7730	67†	4200
PGC057077	16 05 34.2	17 46 11.8	2008 Jun 08	INT	3500-7730	297	4500
UGC10190	16 05 26.3	17 41 48.6	2008 Jun 08	INT	3500-7730	150	4500
LEDA140568	16 06 00.1	17 45 52.0	2008 Jun 08	INT	3500-7730	10	5400
[*D*97]ce-200	16 05 06.8	17 47 02.0	2008 Jun 08	INT	3500-7730	66†	5400
PGC057064	16 05 27.2	17 49 51.6	2008 Jun 09	INT	3500-7730	115	5400
LEDA084703	16 03 05.7	17 10 20.4	2008 Jun 09	INT	3500-7730	82	5400
KUG1602+175	16 04 45.4	17 26 54.3	2009 May 26	INT	3400-7630	315	3600
LEDA084710	16 04 20.4	17 26 11.2	2009 May 26	INT	3400-7630	105	3600
CGCG108-149	16 06 35.3	17 53 33.2	2009 May 26	INT	3400-7630	172	3600
KUG1602+174B	16 04 47.6	17 20 52.0	2009 May 26	INT	3400-7630	67	2400
LEDA084724	16 05 45.5	17 34 56.7	2009 Jun 26	WHT	3600-9230	0	3000
SDSS J160556.98+174304.1	16 05 57.0	17 43 04.1	2009 Jun 26	WHT	3600-9230	90	3600
[DKP87]160310.21+175956.7	16 05 25.0	17 51 50.6	2009 Jun 26	WHT	3600-9230	114	3600
SDSS J160524.27+175329.3	16 05 24.3	17 53 29.4	2009 Jun 27	WHT	3600-9230	102	3600
SDSS J160547.17+173501.6	16 05 47.2	17 35 01.7	2009 Jun 27	WHT	3600-9230	170	3600

Table 3.1: **Log of Observations**

Galaxy	R.A.	DEC	Date	Tel.	Range	P.A.	Exp.
	J2000.0	J2000.0					
(1)	(2)	(3)	(4)	(5)	(6)	(7)	(8)
SDSS J160523.66+174832.3	16 05 23.7	17 48 32.3	2009 Jun 27	WHT	3600-9230	140	3600
IC1182	16 05 36.8	17 48 07.5	2009 Jul 19	WHT	3160-8263	127	3000
IC1182:[S72]d	16 05 41.9	17 47 58.4	2009 Jul 19	WHT	3160-8263	96	3600
SDSS J150531.84+174826.1	16 05 31.8	17 48 26.2	2009 Jul 19	WHT	3160-8263	66	3600

Note: Column 1: Galaxy name following Cedrés et al. (2009); Column 2: right ascension in hours, minutes, and seconds; Column 3: declination, in degrees, arcminutes, and arcseconds; Column 4: observation date; Column 5: telescope used; Column 6: wavelength range coverage in Å; Column 7: position angle in degrees from North to East; Column 8: exposure time in seconds.
† Observed at paralactic angle through air-mass ≥ 1.3. ‡ This pair is also known as Arp 272.

Observations at the WHT were performed during two observing runs on June and July 2009, using the double arm spectrograph ISIS with slightly different instrumental set-ups. On June 2009 the dichroic splitting the beam was set at 5300 Å and the gratings used were R300B and R158R giving nominal dispersions of 0.86 Å pix^{-1} and 1.82 Å pix^{-1} respectively and a spectral coverage of ∼3600-9230 Å. On July 2009 the dichroic was set at 5700 Å and the gratings used were R300B and R316R giving respective dispersions 0.83 and 0.89 Å pix^{-1} and a spectral coverage ∼3160-8263 Å. During both runs the CCD set-up was the same: on the blue arm the EEV12 detector, providing a spatial scale 0.19 arcsec pix^{-1}, and on the red arm the RED+ detector sampling 0.22 arcsec pix^{-1}. Observations at the INT were also performed during two observational runs, on June 2008 and May 2009, using the Intermediate Dispersion Spectrograph (IDS) with the EEV10 detector and R300V grating, giving a nominal dispersion of 1.86 Å pix^{-1} and a spatial scale of 0.4 arcsec pix^{-1}. The total wavelength coverage free of vignetting with this set-up was ∼3400-7700 Å. In both ISIS and IDS spectra the slit width was set to 1.5 arcsec. The orientation of the slit, as listed in Table 3.1, was selected to cover the maximum surface of the Hα emission detected by Cedrés et al. (2009), with few exceptions that were observed on paralactic angle.

3.4.2 Data reduction

The spectra were reduced in the standard manner using IRAF routines. First, the two-dimensional spectra were bias subtracted and flat-field corrected. For this, dome flat exposures were used to remove pixel-to-pixel variations in response. Wavelength calibration was achieved using spectra of CuNe and CuAr comparison lamps, reaching an accuracy of ∼0.3 Å for IDS and less than 0.1 Å for ISIS spectra. Several exposures were taken for each object in order to remove cosmic ray hits. The spectra were corrected for atmospheric extinction using an extinction curve for ORM and all observing nights were photometric, according to Carlsberg Meridian Telescope records. Enough slit length free of any object permitted an adequate sky-subtraction. For the flux calibration, during the observational runs each night at least 3 spectrophotometric standard stars were observed, varying in color, except during the June 2009 run, when we observed two and one stars during each night respectively. The expected spectrophotometric error is estimated 10% (June 2008) 8% (May 2009) 3% (June 2009) and 2% (July 2009). ISIS matching between red and blue arm spectra was successful as can be seen in the spectra shown in Figure 3.10 below.

Figure 3.8 shows the SDSS images and 2D spectra at the wavelengh range of Hα and [NII]λ6584 for six galaxies of our sample. There are clearly evident the rich spatial structure of these galaxies and their velocity curves. From the 2D frames an integrated 1D spectrum was produced for those galaxies showing no significant spatial structure. Conversely for galaxies showing rich spatial structure, their 2D spectrum is divided into different 1D spectra corresponding to their different sub-regions.

Figure 3.7: The INT2.5m (left) and the WHT4.2m (right) at the ORM, in Spain. At the INT2.5m, the Intermediate Dispersion Spectrograph (IDS) was used, and at the WHT4.2m the double arm spectrograph ISIS.

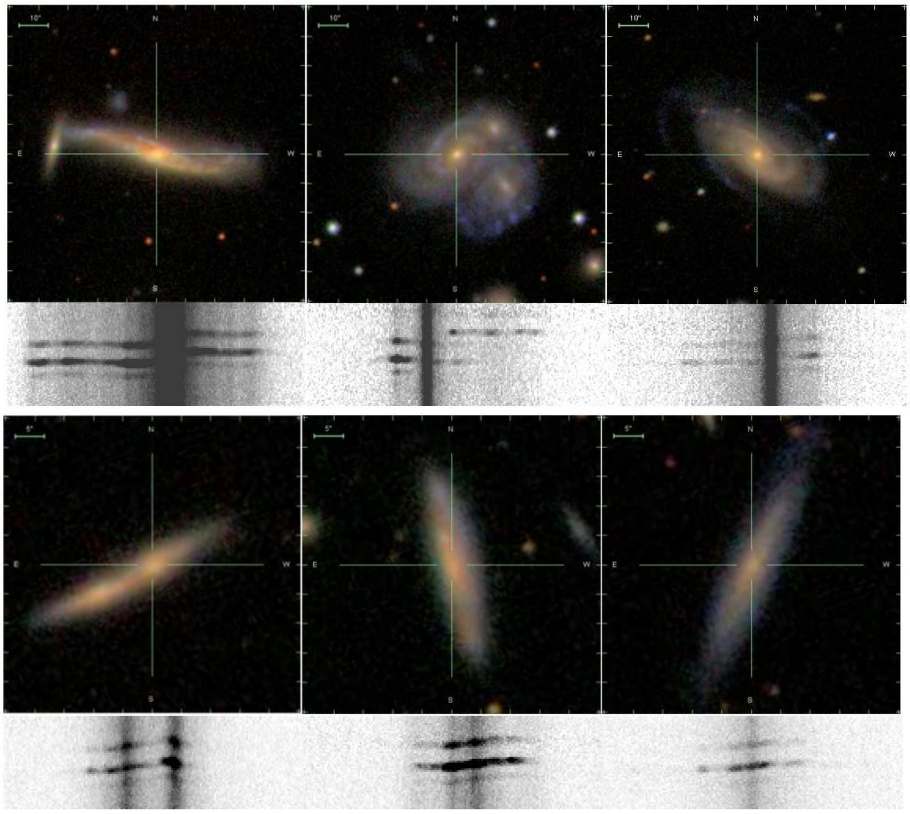

Figure 3.8: The SDSS image and the 2D spectrum at the wavelengh range of Hα and [NII]λ6584 for six galaxies of our sample (from left to right and from top to bottom: NGC6045, NGC6050, IC1173, PGC057064, PGC057185, UGC10190). There are clearly evident the rich spatial structure of these galaxies and their velocity curves.

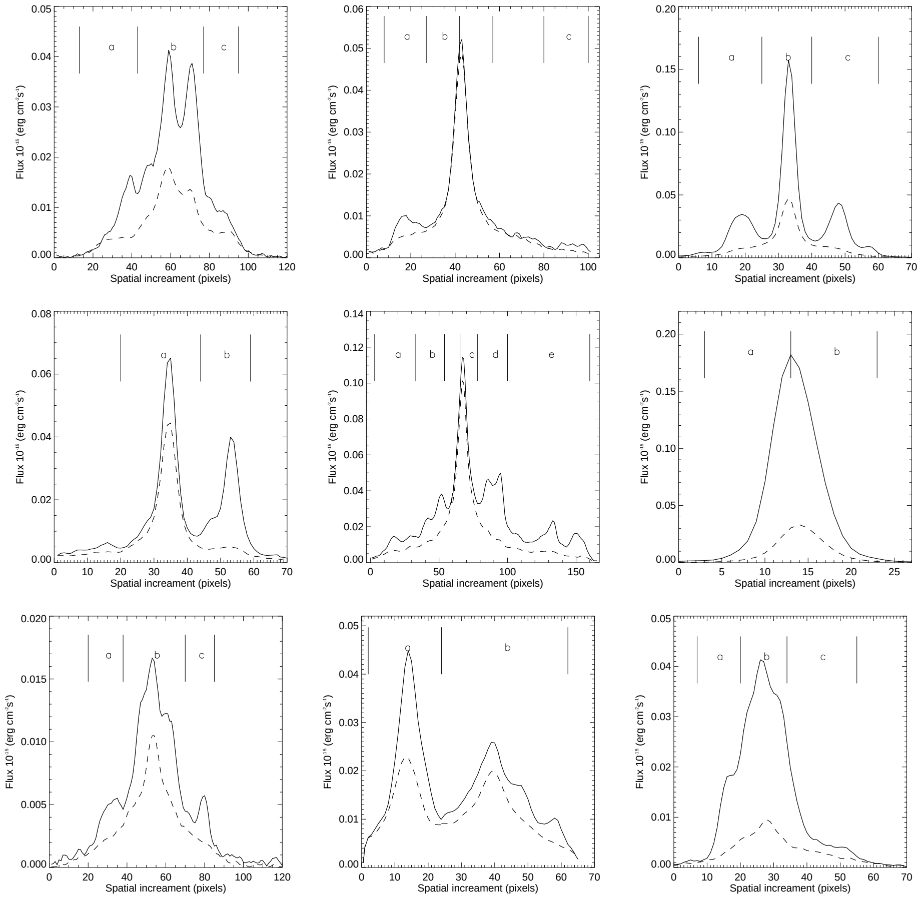

Figure 3.9: The spatial profiles of the Hα line (solid line) and nearby continuum (dashed line) along the slit extracted from the 2D spectra, for the galaxies showing rich spatial structure. There are indicated the different galaxy parts considered to extract the 1D spectra.

In Figure 3.9 we give the spatial profiles of the Hα line and the nearby continuum emission along the slit position extracted from the 2D-spectra. The different galaxy parts considered in this analysis are highlighted on these profiles. All the 1D spectra extracted in this study are presented in Figure 3.10.

3.5 Spectral synthesis model fitting

We use the population synthesis code STARLIGHT to fit spectral synthesis models to all our spectra and we compute some characteristic properties of the underlying stellar component as the luminosity-weighted and mass-weighted stellar age and metallicity (see, e.g. Asari et al. 2007). We also use the model fits to correct our spectra for underlying stellar absorption.

Our galaxy sample spans a considerable range in its emission-line properties,

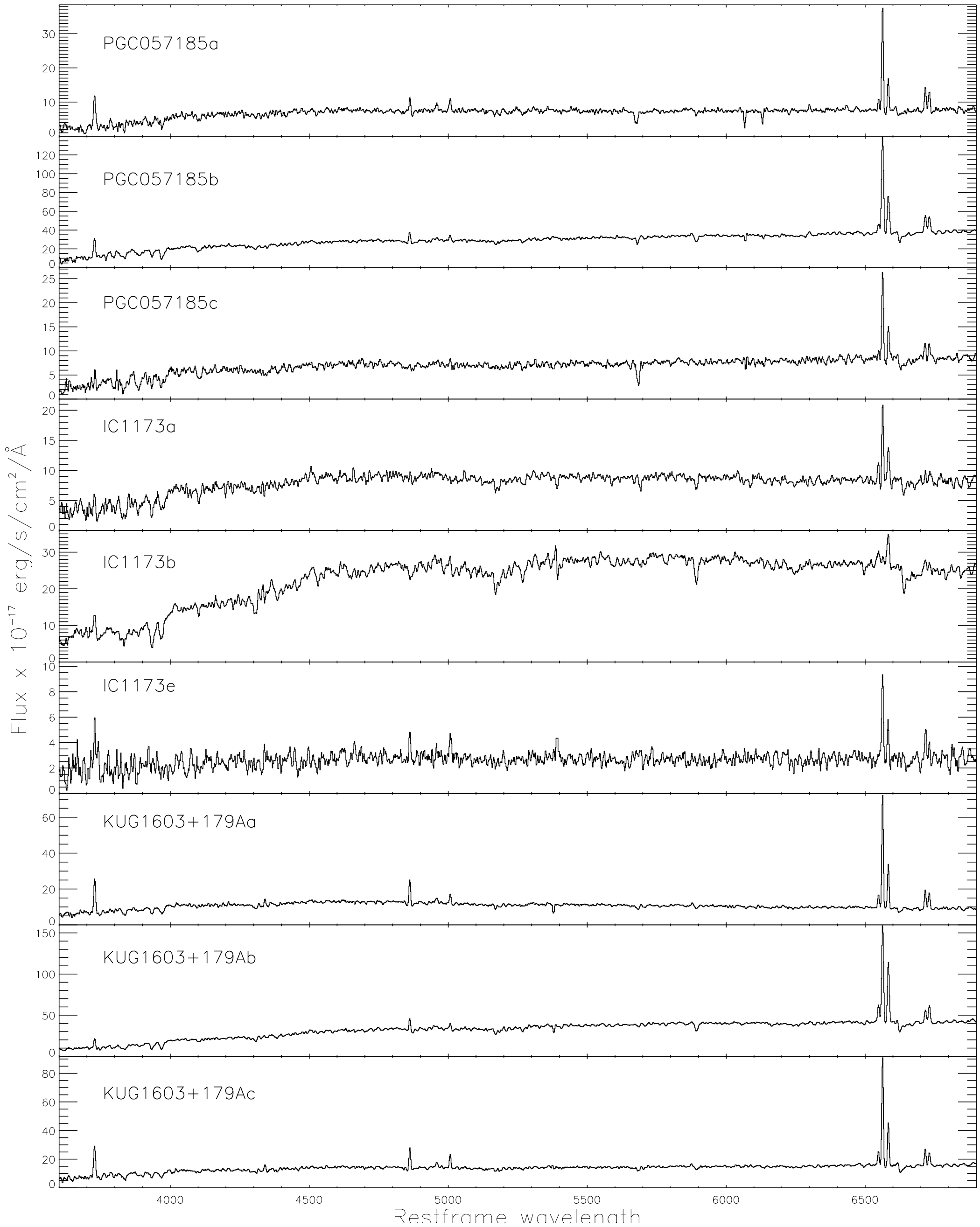

Figure 3.10: Integrated 1D observed spectra for each galaxy or part of a galaxy obtained at INT2.5m and WHT4.2m.

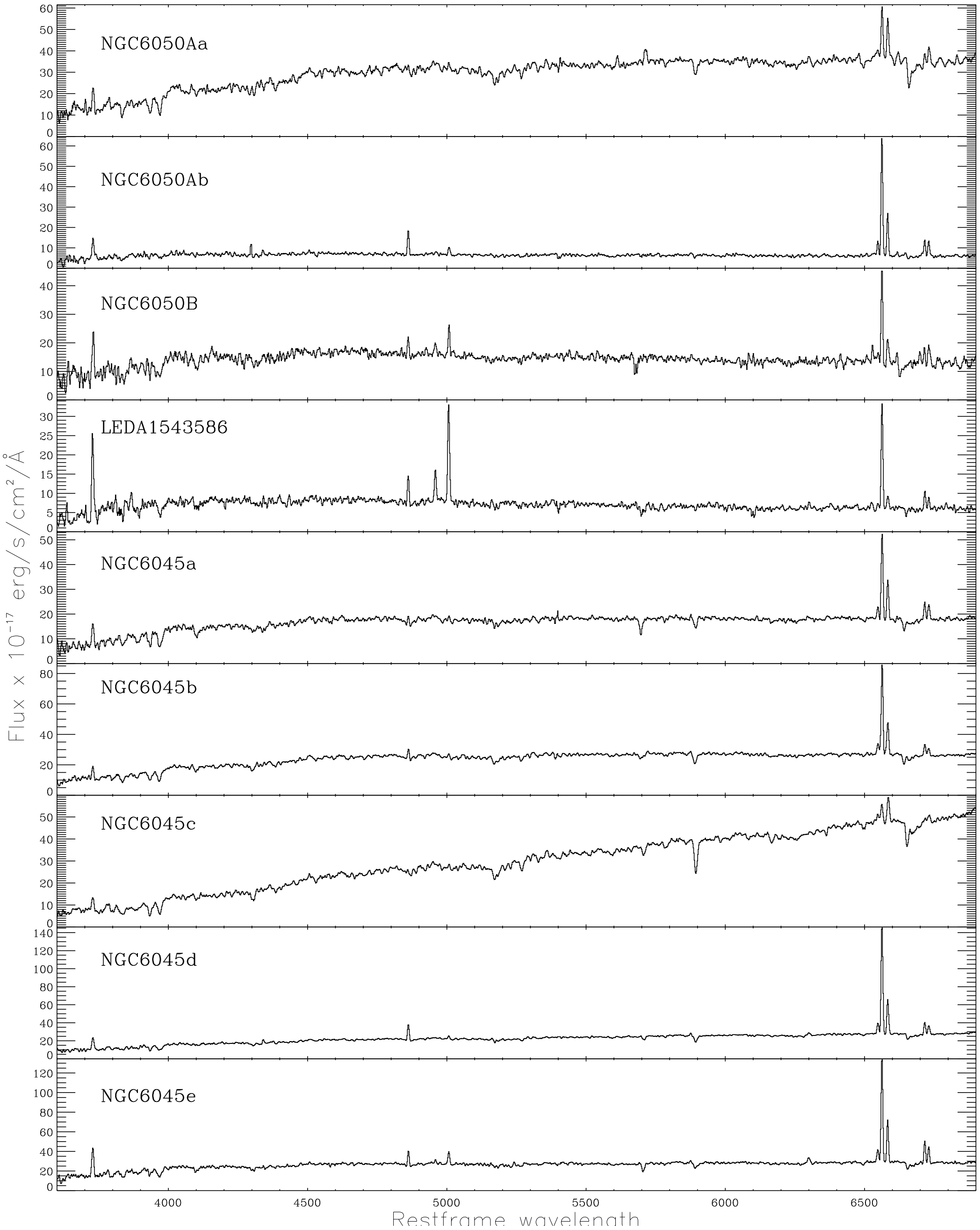

Figure 3.10: Continued.

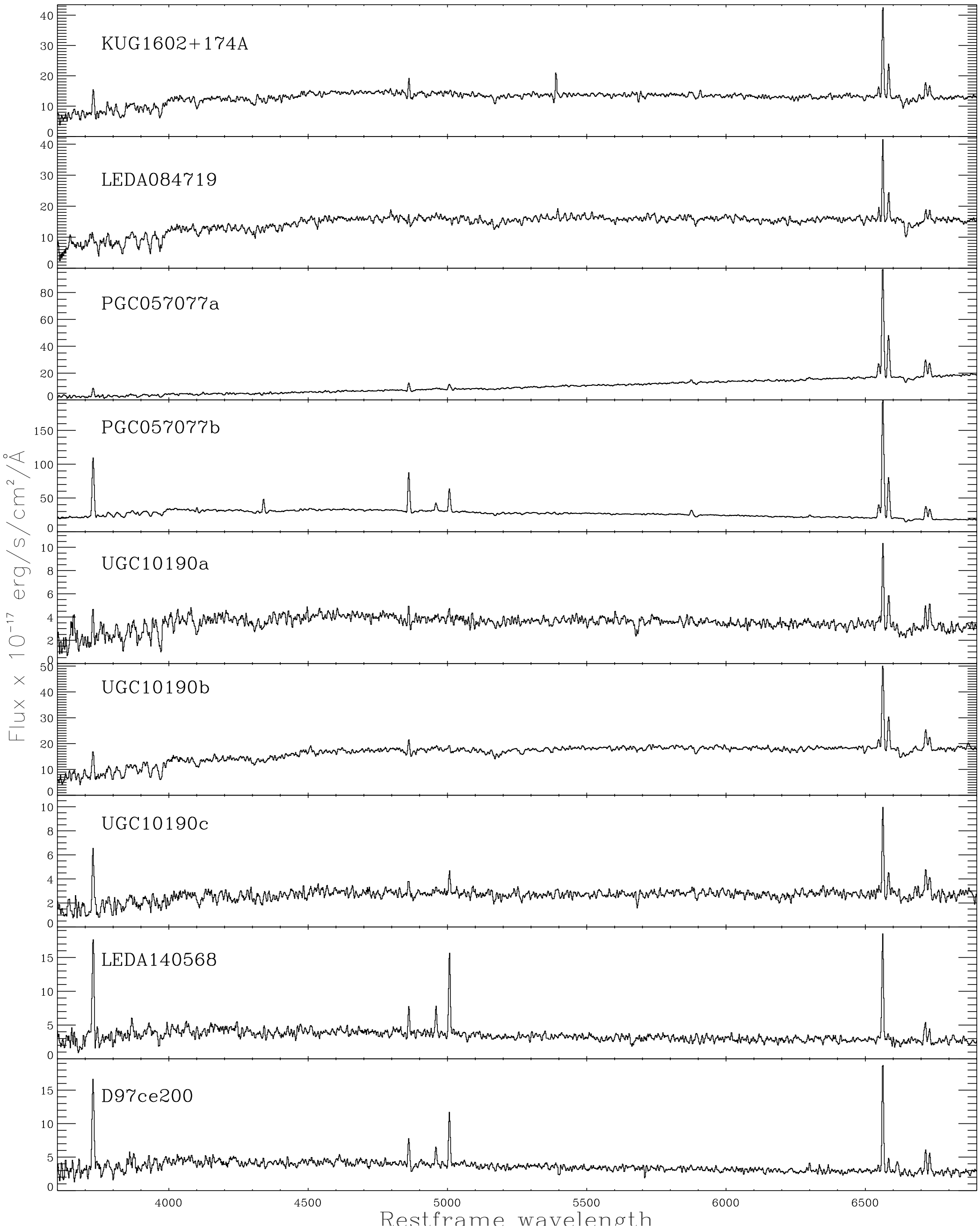

Figure 3.10: Continued.

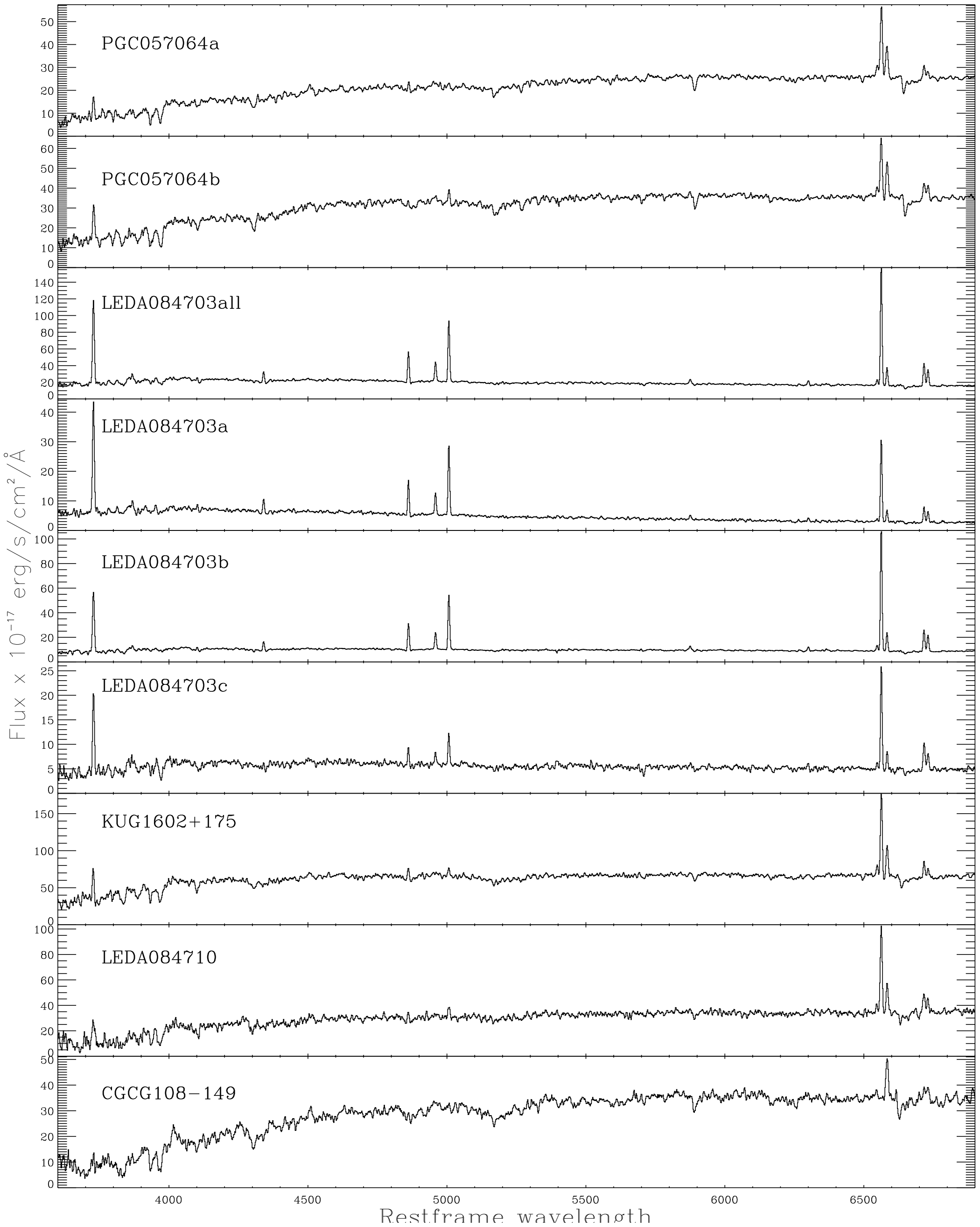

Figure 3.10: Continued.

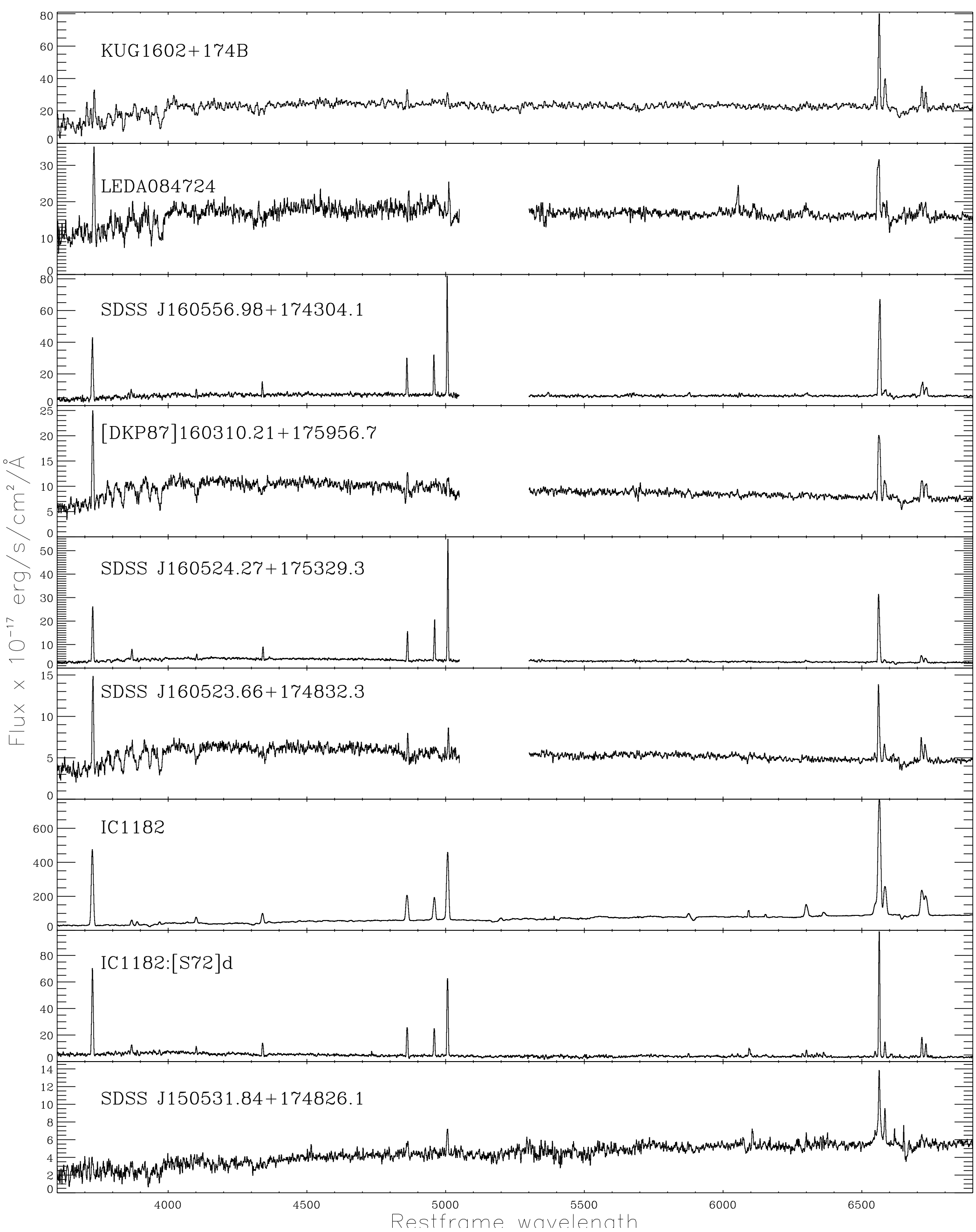

Figure 3.10: Continued.

from systems with very strong Balmer emission lines to systems where the Hβ is just detectable above a high level of stellar continuum. Especially in the latter cases, an accurate correction for underlying stellar absorption is crucial. The usual practice of adopting an $EW_{\rm abs} \sim 2$Å for stellar Balmer lines, though generally justifiable, bears the risk of introducing significant systematic errors in the analysis of systems with faint emission lines. This is because the exact value for $EW_{\rm abs}$ depends on the stellar population mixture i.e. the SFH in a galaxy.

For example, González Delgado et al. (1999) infered for a single stellar population (SSP) a monotonous increase of the $EW_{\rm abs}$'s for the Balmer Hβ through Hδ lines from $\leq$3 Å at an age $\leq$3 Myr to >10 Å at ages $\sim$0.5 Gyr, followed by a decrease for older ages. Star-forming galaxies, consisting of different SSPs of young to intermediate age, in addition to a (significantly) older underlying host galaxy, likely follow a considerably more complex time evolution in their luminosity-weighted $EW_{\rm abs}$. This issue has been explored in much detail by e.g. Guseva et al. (2001) who have considered a variety of SFHs and mass proportions between the young and older stellar components in SF dwarf galaxies. Obviously, for systems with low emission-line EWs, improper correction for underlying stellar absorption may propagate into significant errors in e.g., the intrinsic extinction or spectroscopic classification using BPT (Baldwin et al. 1981) diagrams. For example, for an intermediate luminosity-weighted age of $0.2 - 0.6$ Gyr, where Balmer $EW_{\rm abs}$ are the largest, the underestimation of Balmer line fluxes due to incomplete correction for underlying stellar absorption may shift a star forming galaxy on the log([O III]λ5007/Hβ) vs. log([N II]λ6583/Hα) BPT diagram into the zone of active galactic nuclei (AGNs).

The determination of the $EW_{\rm abs}$ may be carried out by simultaneous fitting of two Gaussians to each emission and absorption Balmer line profile. Another adequate, and arguably more efficient, technique for correcting for underlying stellar absorption is the fitting and subsequent subtraction of the observed spectrum of a synthetic stellar spectrum in order to isolate the net nebular line emission fluxes. To this end, we used the population synthesis code STARLIGHT (Cid Fernandes et al. 2004, 2005a,b; Garcia-Rissmann et al. 2005). This code synthesizes the observed stellar continuum as due to the superposition of SSPs of different age and metallicity. The SSP library used is based on stellar models by Bruzual & Charlot (2003) for a Salpeter IMF for three metallicities ($Z = 0.004, 0.008, 0.02$)[4] and 59 ages (between 0.25 Myr and 13 Gyr). Output of the model is the list of those SSPs with a mass contribution $M_i > 0$ (%) and their luminosity contribution L_i (%) to the wavelength interval to which the input spectra have been normalized (5100–5300 Å in this work).

Prior to modeling the observed spectra were de-redshifted and resampled to 1 Å pixel^{-1}. Additionally, emission lines and residuals from the night sky subtraction were identified and interactively flagged using a code developed by us. Throughout, we preferred not to correct the input spectra for intrinsic extinction or to strongly constrain its allowed range in the STARLIGHT models for a twofold reason: first,

---

[4] The solar metallicity is assumed $Z_\odot = 0.0134$, which is translated to an oxygen abundance 12+log(O/H)$_\odot$=8.69 (Asplund et al. 2009).

the extinction coefficient $c(\mathrm{H}\beta)$ computed prior to correction of Balmer emission line fluxes for underlying stellar absorption is, especially for galaxies with faint nebular emission, uncertain. An a priori de-reddening of the input spectra using this approximate $c(\mathrm{H}\beta)$ value would therefore yield no advantage towards reliability and computational expense. For the same reason, and in order to minimize biases in the STARLIGHT solutions, we have allowed the intrinsic extinction to vary between $+4.5$ and -0.7 V mag. The allowance for a negative A_{V} is justified by possible uncertainties in flux calibration, the (partial) coverage of the physical spatial area of the galaxy, as well as the incompleteness of the SSP library. As evident from Table 3.2, solutions with $A_{\mathrm{V}} \leq 0$ are the exception in our analysis. Secondly, fixing the intrinsic extinction in the STARLIGHT models to the observed $c(\mathrm{H}\beta)$ would imply that ionized gas and stars are subject to equal extinction. No compelling evidence exists for this as yet. On the other hand, for the sake of simplicity and to keep computational time low, we have throughout assumed a single foreground extinction model, although provision is given in STARLIGHT to solve for a different extinction in the young (≤10 Myr) and older stellar population.

A typical example of the spectral synthesis for a galaxy with relatively faint nebular emission in our sample is shown in Figure 3.11. The left panel shows the observed, normalized spectrum (orange color) with the best-fitting synthetic spectrum overlaid (blue color). Flagged intervals in each spectrum are marked with shaded vertical bars. The smaller panels to the upper-right and lower-right show the age distribution of the SSPs evaluated by STARLIGHT as a function of, respectively, their luminosity and mass fraction in %. Thin vertical lines in the upper right panel indicate the ages of the library SSPs. The shaded area in the lower diagram shows the smoothed M_i distribution and is meant as schematic illustration of the SFH. It may be seen from the left panel that synthetic spectra fit well broad stellar absorption features, thus permitting an adequate determination and correction for underlying absorption. The corrected emission line fluxes, as measured from the observed spectra after subtraction of the synthetic stellar spectra are listed in Table 3.3 (see Section 3.6 for a detailed discussion).

Although an elaborated study of the SFH of the sample galaxies is beyond the scope of this work, we took advantage of the STARLIGHT models to compute some characteristic properties of our sample galaxies. These include the luminosity-weighted and mass-weighted metallicity $Z_{\star,L}$ and $Z_{\star,M}$ and stellar age $\tau_{\star,L}$ and $\tau_{\star,M}$ along with their standard deviations (see, e.g., Asari et al. 2007). These quantities and the intrinsic extinction A_{V} of the stellar component, are listed in Table 3.2 and will be further discussed in Section 3.10.

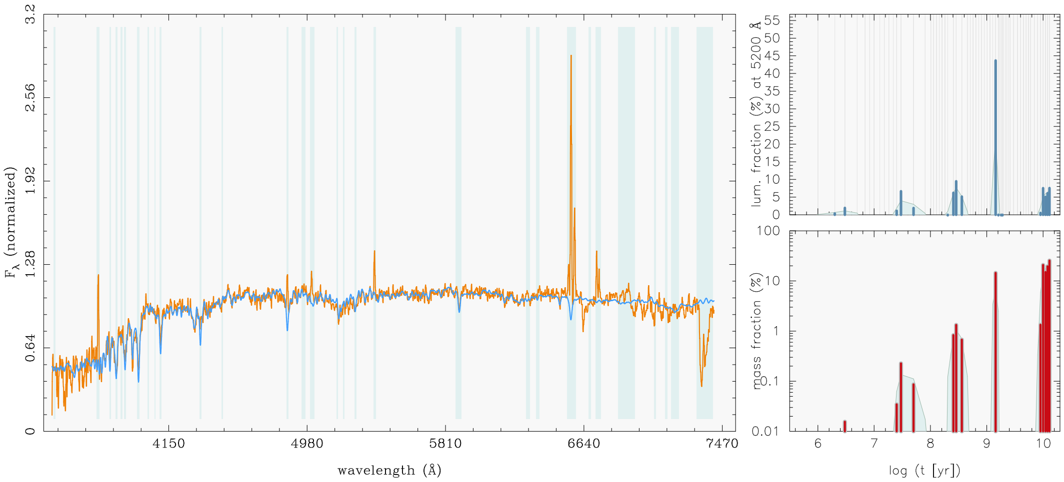

Figure 3.11: A typical example of spectral synthesis with STARLIGHT for the galaxy KUG1602+175. The left panel shows the observed, normalized spectrum (orange color) with the best-fitting synthetic spectrum overlaid (blue color). Flagged intervals in each spectrum are marked with shaded vertical bars. The smaller panels to the upper-right and lower-right show the age distribution of the SSPs evaluated by STARLIGHT as a function of, respectively, their luminosity and mass fraction in %. Thin vertical lines in the upper right panel indicate the ages of the library SSPs. The shaded area in the lower diagram shows the smoothed M_i distribution and is meant as schematic illustration of the SFH.

Table 3.2: **STARLIGHT Output**

Galaxy	$Z_{\star,L}$	$Z_{\star,M}$	$\tau_{\star,L}$ Gyr	$\tau_{\star,M}$ Gyr	A_V mag
PGC05185a	0.014 ± 0.008	0.012 ± 0.008	0.94 ± 0.30	1.08 ± 0.28	0.98
PGC05185b	0.009 ± 0.005	0.007 ± 0.004	2.02 ± 1.02	7.28 ± 3.07	1.68
PGC05185c	0.014 ± 0.007	0.009 ± 0.004	2.64 ± 1.24	8.54 ± 2.07	1.32
IC1173a	0.016 ± 0.006	0.019 ± 0.009	7.73 ± 1.92	11.10 ± 0.80	−0.21
IC1173e	0.018 ± 0.009	0.016 ± 0.007	2.09 ± 0.72	5.66 ± 1.86	0.63
KUG1603+179Aa	0.014 ± 0.007	0.012 ± 0.005	3.69 ± 1.35	6.60 ± 1.81	−0.56
KUG1603+179Ab	0.015 ± 0.006	0.018 ± 0.011	7.27 ± 2.25	11.62 ± 0.76	0.91
KUG1603+179Ac	0.012 ± 0.004	0.008 ± 0.005	4.80 ± 1.98	11.07 ± 0.77	1.09
NGC6050Aa	0.011 ± 0.004	0.014 ± 0.005	8.10 ± 1.93	11.36 ± 0.58	0.47
NGC6050Ab	0.013 ± 0.003	0.012 ± 0.005	5.67 ± 1.87	11.58 ± 0.54	0.41
NGC6050B	0.007 ± 0.002	0.004 ± 0.002	5.82 ± 1.35	8.54 ± 0.97	−0.12
LEDA1543586	0.006 ± 0.002	0.008 ± 0.003	1.98 ± 0.91	6.66 ± 1.71	0.42
NGC6045a	0.015 ± 0.005	0.018 ± 0.010	4.87 ± 1.94	10.82 ± 1.20	0.57
NGC6045b	0.013 ± 0.004	0.017 ± 0.008	5.42 ± 1.74	10.10 ± 1.31	0.27
NGC6045c	0.016 ± 0.008	0.017 ± 0.013	8.30 ± 2.45	12.68 ± 0.28	2.13
NGC6045d	0.013 ± 0.005	0.015 ± 0.008	4.25 ± 1.78	11.14 ± 1.38	1.33
NGC6045e	0.011 ± 0.007	0.010 ± 0.008	1.06 ± 0.30	2.71 ± 1.60	0.93
KUG1602+174A	0.007 ± 0.002	0.008 ± 0.003	4.66 ± 1.34	8.34 ± 0.87	0.19
LEDA084719	0.008 ± 0.004	0.012 ± 0.004	4.45 ± 1.41	8.34 ± 1.53	0.15
PGC057077a	0.013 ± 0.006	0.018 ± 0.017	4.24 ± 2.86	12.03 ± 1.19	3.23
PGC057077b	0.014 ± 0.009	0.013 ± 0.008	1.75 ± 0.41	2.10 ± 0.60	−0.70
UGC10190a	0.007 ± 0.003	0.005 ± 0.002	3.43 ± 1.46	8.14 ± 1.91	0.22
UGC10190b	0.007 ± 0.002	0.006 ± 0.002	5.85 ± 1.22	10.04 ± 0.71	0.79
UGC10190c	0.014 ± 0.005	0.009 ± 0.005	5.45 ± 2.16	11.63 ± 0.64	0.82
LEDA140568	0.008 ± 0.004	0.006 ± 0.003	0.86 ± 0.45	4.84 ± 2.17	0.56
D97ce200	0.007 ± 0.003	0.008 ± 0.005	0.73 ± 0.25	1.09 ± 0.11	0.33
PGC057064a	0.014 ± 0.005	0.017 ± 0.008	5.06 ± 1.36	8.13 ± 0.85	0.74

Table 3.2: **STARLIGHT Output**

Galaxy	$Z_{\star,L}$	$Z_{\star,M}$	$\tau_{\star,L}$ Gyr	$\tau_{\star,M}$ Gyr	$A_{\rm V}$ mag
PGC057064b	0.011 ± 0.004	0.017 ± 0.007	6.56 ± 1.75	10.52 ± 0.80	0.36
LEDA084703int	0.009 ± 0.002	0.009 ± 0.002	1.22 ± 0.26	2.42 ± 0.50	0.31
LEDA084703a	0.007 ± 0.005	0.008 ± 0.007	0.71 ± 0.26	1.00 ± 0.02	-0.34
LEDA084703b	0.009 ± 0.003	0.012 ± 0.004	1.97 ± 0.52	5.93 ± 1.60	0.50
LEDA084703c	0.009 ± 0.005	0.008 ± 0.005	0.94 ± 0.29	1.75 ± 0.63	0.43
KUG1602+175	0.013 ± 0.006	0.017 ± 0.007	3.76 ± 1.54	9.74 ± 1.55	0.55
LEDA084710	0.015 ± 0.007	0.017 ± 0.008	2.86 ± 1.24	9.05 ± 2.05	1.02
CGCG108-149	0.018 ± 0.008	0.019 ± 0.010	7.68 ± 2.46	11.11 ± 1.08	0.40
KUG1602+174B	0.016 ± 0.007	0.018 ± 0.008	2.91 ± 1.11	7.76 ± 1.31	0.48
LEDA084724	0.007 ± 0.003	0.008 ± 0.003	3.15 ± 1.24	7.57 ± 0.92	0.37
SDSSJ160556.98+174304.1	0.008 ± 0.006	0.008 ± 0.007	0.82 ± 0.49	1.26 ± 0.21	0.61
[DKP87]160310.21+175956.7	0.006 ± 0.001	0.006 ± 0.002	3.11 ± 1.48	7.72 ± 0.69	0.31
SDSSJ160524.27+175329.3	0.004 ± 0.004	0.004 ± 0.004	1.06 ± 0.21	1.06 ± 0.10	-0.01
SDSSJ160523.66+174832.3	0.007 ± 0.004	0.004 ± 0.002	2.25 ± 0.99	6.16 ± 2.52	0.38
IC1182	0.012 ± 0.004	0.014 ± 0.008	6.37 ± 1.97	11.56 ± 0.88	1.47
IC1182:[S72]d	0.019 ± 0.011	0.018 ± 0.011	1.92 ± 1.49	11.51 ± 0.76	0.42
SDSSJ160531.84+174826.1	0.007 ± 0.003	0.008 ± 0.004	6.11 ± 2.46	11.10 ± 1.13	1.11
SDSSJ160304.20+171126.7	0.007 ± 0.002	0.006 ± 0.002	3.88 ± 0.71	5.78 ± 0.63	0.48
SDSSJ160520.58+175210.6	0.008 ± 0.003	0.008 ± 0.003	5.76 ± 0.65	7.11 ± 0.46	0.50

Note: The luminosity-weighted and mass-weighted stellar metallicity (e.g. the mass fraction of metals over H, where the solar value is assumed to be $Z_{\odot} = 0.019$) $Z_{\star,L}$ and $Z_{\star,M}$ and stellar age $\tau_{\star,L}$ and $\tau_{\star,M}$ along with their the standard deviations and the intrinsic extinction $A_{\rm V}$ of the stellar component as given by fitting STARLIGHT models.

3.6 Results

3.6.1 Line fluxes

After subtracting the best-fitting spectral energy distribution (SED) of the underlying stellar population (Section 3.5), we used the corrected emission-line spectra to measure line fluxes. We used the SPLOT task of IRAF to integrate the flux under the line profile over a linearly fitted continuum. In order to account for the main source of error in our data, driven by the continuum placement, five independent measurements of the emission line flux were carried out for each line and we assume the mean and the standard deviation as the flux measurement and the corresponding statistical error.

The reddening coefficients c(Hβ) were calculated adopting the galactic extinction law of Miller & Mathews (1972) with $R_V = 3.2$, as presented in Hägele et al. (2008), using the expression:

$$log\left[\frac{I(\lambda)}{I(\mathrm{H}\beta)}\right] = log\left[\frac{F(\lambda)}{F(\mathrm{H}\beta)}\right] + c(\mathrm{H}\beta)f(\lambda) \tag{3.1}$$

where $I(\lambda)/I(\mathrm{H}\beta)$ is the theoretical and $F(\lambda)/F(\mathrm{H}\beta)$ the observed Balmer decrements. The theoretical Balmer decrement depends on electron temperature and density and we used the data for Case B and assuming low-density limit and 10 000K (Storey & Hummer 1995). In those cases where we measured at least three Balmer lines with S/N>5 we have performed a least-squares fit to derive $c(\mathrm{H}\beta)$ and the corresponding error was taken to be the uncertainty of the fit. When only Hα and Hβ were available, $c(\mathrm{H}\beta)$ was derived applying expression (3.1) and its error was calculated as the rms of a gaussian error distribution produced by a random sampling simulation, taking into account the errors in the line fluxes of Hα and Hβ.

Reddening-corrected line fluxes and reddening coefficients $c(\mathrm{H}\beta)$ are presented in Table 3.3. The errors quoted account for the uncertainties in the line flux measurement and in the extinction coefficient. Table 3.3 also presents the Hβ flux not corrected for extinction and equivalent width, as well as the galaxy recessional velocity, as derived by our spectroscopic data. The Hβ equivalent width quoted was determined from the net emission spectrum, i.e. the observed spectrum after subtraction of the best-fitting stellar SED, and the level of the adjacent continuum in the original spectrum.

Figure 3.12 shows the extinction of the gas-phase component $A_{\mathrm{V,gas}} = 2.18 \times c(\mathrm{H}\beta)$ as a function of the intrinsic extinction of the stellar component derived by STARLIGHT in the previous section. A linear fit, considering (the reliable range, see Section 3.5) $A_{\mathrm{V,star}} > -0.1$ and weighted by the errors of the $c(\mathrm{H}\beta)$ estimation, yield the relation $A_{\mathrm{V,gas}} = 0.81{+}0.89A_{\mathrm{V,star}}$. We find that stars suffer less extinction than gas, that can be explained if the dust has a larger covering factor for the ionized gas than for the stars (Calzetti et al. 1994). In the same line are recent results presented by Monreal-Ibero et al. (2010) and Alonso-Herrero et al. (2010), who explore the relation between the extinction suffered by the gas and by the stellar populations

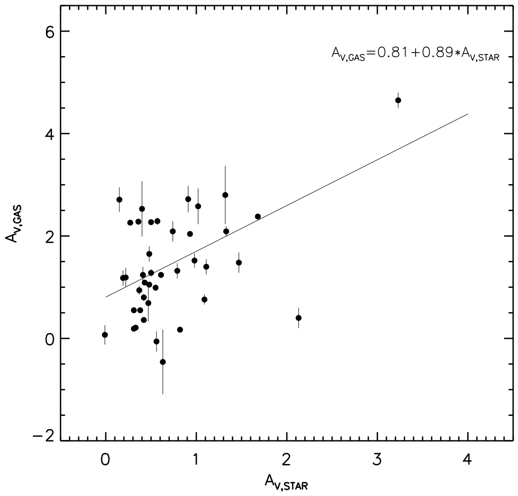

Figure 3.12: The gas-phase extinction estimated using the Balmer emission lines vs. the extinction of the stellar component derived by STARLIGHT model fits on the continuum emission. A weighted linear fit to the data (solid line) yields the relation $A_{\mathrm{V,gas}} = 0.81 + 0.89 A_{\mathrm{V,star}}$.

in the central regions of SF galaxies using IFU data.

3.6.2 Comparison with previous data

SDSS spectroscopic data exist for 22 out of the 43 SF galaxies of the C09 sample. In most of the cases the 3-arcsec SDSS fiber covers only the central part of the galaxy; for 3 galaxies, NGC6050, NGC6045 and PGC057064, SDSS provides 2 different apertures on each of them. We have applied the same procedure to these spectra as to our spatially resolved spectra, removing the continuum emission by fitting STARLIGHT and measuring line fluxes on the subtracted emission-line spectrum as described in Sections 3.5 and 3.6.1. We then have compared these line fluxes with our line fluxes for 19 galaxies for which we have ORM long-slit spectrum. We have checked first whether the SDSS aperture position matches the long-slit locus, and then we have extracted the spectrum from the corresponding area of the long-slit. The comparison is shown in Figure 3.13 where the principal emission lines are shown when measured, without applying any reddening correction to them (cyan: [OII]λ3727, red: Hα, blue: [OIII]λ5007, pink: [NII]λ6584, green: [SII]λ6717 and yellow: [SII]λ6731). Despite the fact that the covered regions are not identical (this could be a problem because of the inhomogeneous nature of SF regions), we can see that line ratios show a good agreement. While most of the points lie within the 0.2 dex scatter region from the 1:1 line, there are some emission features that display larger discrepancy. This mostly happens in the cases of galaxies that SDSS aperture is not completely coincident with our long-slit spectrum.

In addition, IP03 have spectroscopic data for 7 galaxies belonging to C09 sample

Table 3.3: Reddening-corrected line fluxes

Line	$f(\lambda)$	PGC057185			IC1173		
		a	b	c	a	b	e
3727 [O II]	0.271	305 ± 20	231 ± 5	239 ± 53	206 ± 37	991 ± 131	118 ± 9
3869 [Ne III] . . .	0.238	. . .	. . .	. . .	. . .	. . .	. . .
3889 He I+H8 . .	0.233	. . .	. . .	. . .	. . .	. . .	. . .
3968 [Ne III]+H7. . .	0.216	. . .	. . .	. . .	. . .	. . .	. . .
4069 [S II]	0.195	. . .	. . .	. . .	. . .	. . .	. . .
4102 Hδ.	0.188	. . .	26 ± 5	. . .	. . .	. . .	. . .
4340 Hγ.	0.142	50 ± 16	47 ± 8	. . .	. . .	. . .	48 ± 2
4861 Hβ.	0.00	100 ± 8	100 ± 9	100 ± 18	100 ± 13	100 ± 12	100 ± 7
4959 [O III]	-0.024	. . .	12 ± 2	. . .	. . .	. . .	. . .
5007 [O III]	-0.035	57 ± 4	36 ± 2	54 ± 10	25 ± 15	236 ± 18	88 ± 6
5876 He I	-0.209	. . .	11 ± 1	. . .	. . .	. . .	. . .
6300 [O I]	-0.276	21 ± 5	16 ± 1	. . .	. . .	71 ± 15	. . .
6548 [N II]	-0.311	31 ± 3	39 ± 6	30 ± 7	62 ± 11	180 ± 26	. . .
6563 Hα.	-0.313	302 ± 14	294 ± 8	282 ± 54	285 ± 40	285 ± 41	287 ± 15
6584 [N II]	-0.316	85 ± 5	113 ± 7	94 ± 18	140 ± 21	492 ± 68	103 ± 10
6717 [S II]	-0.334	64 ± 4	46 ± 4	50 ± 11	38 ± 7	157 ± 24	84 ± 3
6731 [S II]	-0.336	55 ± 4	41 ± 4	44 ± 11	54 ± 19	152 ± 24	63 ± 8
$F(\mathrm{H}\beta)$		4.8 ± 0.4	15.7 ± 1.5	2.1 ± 0.4	1.7 ± 0.2	2.3 ± 0.3	2.2 ± 0.2
$EW(\mathrm{H}\beta)$		6.5 ± 0.8	5.5 ± 0.6	3.0 ± 0.6	1.9 ± 0.3	1.6 ± 0.4	8.1 ± 1.6
$c(\mathrm{H}\beta)$		0.70 ± 0.06	1.09 ± 0.02	1.29 ± 0.26	1.02 ± 0.19	0.96 ± 0.19	−0.21 ± 0.29
velocity		11403 ± 27	11204 ± 19	11122 ± 30	10617 ± 15	11204 ± 19	10248 ± 44

$F(\mathrm{H}\beta)$ in 10^{-16} erg s^{-1} cm^{-2}; $EW(\mathrm{H}\beta)$ in Å; velocity in km s^{-1}.

Table 3.3: (Continued)

Line	$f(\lambda)$	KUG1603+179A			NGC6050A		NGC6050B
		a	b	c	a	b	
3727 [O ii]	0.271	205 ± 5	133 ± 11	172 ± 7	151 ± 16	128 ± 15	176 ± 45
3869 [Ne iii] . . .	0.238	…	…	…	…	…	…
3889 He i+H8 . .	0.233	…	…	24 ± 1	…	35 ± 2	…
3968 [Ne iii]+H7. . .	0.216	17 ± 3	…	…	…	18 ± 2	…
4069 [S ii]	0.195	14 ± 2	…	…	…	…	…
4102 Hδ	0.188	25 ± 4	…	28 ± 5	…	27 ± 8	…
4340 Hγ	0.142	46 ± 2	41 ± 5	49 ± 2	…	43 ± 8	48 ± 11
4861 Hβ	0.00	100 ± 3	100 ± 3	100 ± 3	100 ± 10	100 ± 3	100 ± 5
4959 [O iii]	-0.024	…	13 ± 3	17 ± 3	…	…	38 ± 6
5007 [O iii]	-0.035	43 ± 2	37 ± 4	48 ± 2	61 ± 5	33 ± 3	107 ± 6
5876 He i	-0.209	12 ± 2	…	9 ± 1	…	…	…
6300 [O i]	-0.276	8 ± 1	16 ± 2	…	41 ± 6	5 ± 1	…
6548 [N ii]	-0.311	36 ± 2	44 ± 5	40 ± 1	53 ± 8	34 ± 3	…
6563 Hα	-0.313	279 ± 4	261 ± 23	306 ± 10	286 ± 38	285 ± 15	293 ± 9
6584 [N ii]	-0.316	105 ± 2	148 ± 13	116 ± 4	184 ± 23	100 ± 6	82 ± 7
6717 [S ii]	-0.334	46 ± 1	36 ± 4	47 ± 2	36 ± 7	37 ± 3	45 ± 4
6731 [S ii]	-0.336	39 ± 1	47 ± 5	38 ± 2	69 ± 11	36 ± 3	65 ± 10
F(Hβ)		11.2 ± 0.4	16.0 ± 0.5	14.4 ± 0.5	8.0 ± 0.8	10.2 ± 0.4	7.7 ± 0.4
EW(Hβ)		9.3 ± 0.7	4.9 ± 0.3	10.4 ± 0.7	2.6 ± 0.3	15.1 ± 1.5	4.9 ± 0.5
c(Hβ)		0.49 ± 0.02	1.25 ± 0.12	0.35 ± 0.05	0.32 ± 0.17	0.57 ± 0.07	0.16 ± 0.03
velocity		11280 ± 30	11162 ± 20	11121 ± 17	9524 ± 38	9686 ± 37	11134 ± 39

Table 3.3: (Continued)

Line	$f(\lambda)$	LEDA1543586	NGC6045				
			a	b	c	d	e
3727 [O II]	0.271	281 ± 4	334 ± 21	214 ± 8	141 ± 12	152 ± 9	310 ± 5
3869 [Ne III] . . .	0.238	. . .	. . .	. . .	. . .	. . .	. . .
3889 He I+H8 . .	0.233	. . .	. . .	. . .	. . .	. . .	. . .
3968 [Ne III]+H7. . .	0.216	. . .	. . .	. . .	. . .	19 ± 4	. . .
4069 [S II]	0.195	. . .	. . .	. . .	. . .	. . .	. . .
4102 Hδ	0.188	. . .	. . .	. . .	. . .	25 ± 6	. . .
4340 Hγ	0.142	46 ± 8	45 ± 6	47 ± 5	. . .	49 ± 3	48 ± 9
4861 Hβ	0.00	100 ± 2	100 ± 8	100 ± 1	100 ± 6	100 ± 4	100 ± 5
4959 [O III]	-0.024	103 ± 4	. . .	. . .	. . .	. . .	20 ± 4
5007 [O III]	-0.035	310 ± 4	40 ± 8	35 ± 3	44 ± 2	19 ± 1	65 ± 3
5876 He I	-0.209	. . .	. . .	. . .	. . .	8 ± 1	8 ± 1
6300 [O I]	-0.276	22 ± 2	. . .	. . .	. . .	14 ± 2	23 ± 1
6548 [N II]	-0.311	17 ± 4	44 ± 5	42 ± 1	. . .	31 ± 1	37 ± 2
6563 Hα	-0.313	286 ± 4	280 ± 7	288 ± 2	287 ± 20	288 ± 10	292 ± 6
6584 [N II]	-0.316	44 ± 5	118 ± 6	109 ± 3	203 ± 16	92 ± 3	110 ± 3
6717 [S II]	-0.334	46 ± 2	46 ± 3	37 ± 2	38 ± 4	28 ± 1	51 ± 1
6731 [S II]	-0.336	29 ± 2	44 ± 4	27 ± 3	44 ± 3	22 ± 1	38 ± 1
F(Hβ)		6.9 ± 0.1	5.2 ± 0.4	8.5 ± 0.1	5.4 ± 0.3	17.2 ± 0.7	15.4 ± 0.7
EW(Hβ)		8.9 ± 1.0	3.0 ± 0.3	3.3 ± 0.1	2.1 ± 0.2	7.9 ± 0.4	5.7 ± 0.4
c(Hβ)		0.17 ± 0.01	1.05 ± 0.03	1.04 ± 0.01	0.18 ± 0.09	0.96 ± 0.05	0.94 ± 0.02
velocity		9849 ± 13	10284 ± 11	10335 ± 12	9830 ± 71	9703 ± 15	9789 ± 23

Table 3.3: (Continued)

Line	$f(\lambda)$	KUG1602+174A	LEDA084719	PGC057077		UGC10190		
				a	b	a	b	c
3727 [O II]	0.271	175 ± 10	318 ± 97	328 ± 17	165 ± 3	241 ± 36	182 ± 18	230 ± 52
3869 [Ne III] . . .	0.238	. . .	. . .	. . .	. . .	. . .	. . .	. . .
3889 He I+H8 . .	0.233	55 ± 8	. . .	. . .	13 ± 1	. . .	. . .	. . .
3968 [Ne III]+H7. . .	0.216	. . .	. . .	. . .	23 ± 2	. . .	. . .	. . .
4069 [S II]	0.195	. . .	. . .	. . .	. . .	. . .	. . .	. . .
4102 Hδ.	0.188	. . .	. . .	26 ± 4	25 ± 2	. . .	. . .	. . .
4340 Hγ.	0.142	43 ± 5	. . .	42 ± 2	45 ± 1	. . .	43 ± 8	46 ± 18
4861 Hβ.	0.00	100 ± 5	100 ± 8	100 ± 5	100 ± 1	100 ± 6	100 ± 7	100 ± 10
4959 [O III]	-0.024	. . .	48 ± 11	. . .	20 ± 1	. . .	. . .	24 ± 3
5007 [O III]	-0.035	25 ± 7	. . .	63 ± 3	55 ± 1	36 ± 2	24 ± 3	79 ± 3
5876 He I	-0.209	. . .	. . .	12 ± 2	13 ± 1	. . .	. . .	. . .
6300 [O I]	-0.276	14 ± 2	. . .	14 ± 3	6 ± 1	. . .	. . .	. . .
6548 [N II]	-0.311	31 ± 3	46 ± 7	36 ± 2	33 ± 1	35 ± 11	32 ± 4	. . .
6563 Hα.	-0.313	272 ± 14	286 ± 23	277 ± 13	277 ± 5	286 ± 18	272 ± 14	282 ± 7
6584 [N II]	-0.316	99 ± 6	112 ± 12	103 ± 5	93 ± 2	111 ± 8	98 ± 7	73 ± 6
6717 [S II]	-0.334	49 ± 4	42 ± 5	38 ± 2	34 ± 1	64 ± 5	60 ± 5	90 ± 8
6731 [S II]	-0.336	41 ± 5	40 ± 7	31 ± 2	27 ± 1	83 ± 7	38 ± 3	64 ± 5
F(Hβ)		5.9 ± 0.3	2.7 ± 0.2	5.9 ± 0.3	52.0 ± 0.5	1.4 ± 0.1	7.2 ± 0.5	1.9 ± 0.2
EW(Hβ)		4.1 ± 0.3	1.7 ± 0.2	7.8 ± 0.6	17.3 ± 0.7	3.5 ± 0.4	4.1 ± 0.3	6.8 ± 1.2
c(Hβ)		0.54 ± 0.07	1.24 ± 0.11	2.14 ± 0.07	0.13 ± 0.02	0.55 ± 0.09	0.61 ± 0.07	0.08 ± 0.02
velocity		10614 ± 18	10155 ± 14	10209 ± 15	10200 ± 14	11171 ± 30	11046 ± 13	10915 ± 25

Table 3.3: (Continued)

Line	$f(\lambda)$	LEDA140568	$[D97]ce-200$	PGC057064		LEDA084703	
				a	b	int	a
3727 [O II]	0.271	314 ± 20	326 ± 23	256 ± 23	636 ± 21	331 ± 5	339 ± 10
3869 [Ne III] . . .	0.238	44 ± 9	. . .	. . .	. . .	22 ± 1	22 ± 2
3889 He I+H8 . .	0.233	. . .	. . .	. . .	. . .	22 ± 1	15 ± 2
3968 [Ne III]+H7. . .	0.216	. . .	. . .	. . .	. . .	18 ± 1	20 ± 3
4069 [S II]	0.195	. . .	. . .	. . .	44 ± 8	. . .	. . .
4102 Hδ.	0.188	. . .	. . .	. . .	. . .	26 ± 2	27 ± 2
4340 Hγ.	0.142	47 ± 10	46 ± 3	. . .	46 ± 8	49 ± 1	49 ± 1
4861 Hβ.	0.00	100 ± 6	100 ± 8	100 ± 7	100 ± 5	100 ± 1	100 ± 1
4959 [O III]	-0.024	70 ± 4	53 ± 6	. . .	41 ± 10	57 ± 3	61 ± 2
5007 [O III]	-0.035	214 ± 5	163 ± 4	45 ± 4	134 ± 8	177 ± 1	187 ± 2
5876 He I	-0.209	. . .	. . .	. . .	. . .	14 ± 1	14 ± 2
6300 [O I]	-0.276	. . .	20 ± 1	13 ± 4	16 ± 2	14 ± 1	12 ± 1
6548 [N II]	-0.311	. . .	12 ± 3	44 ± 4	56 ± 3	16 ± 2	11 ± 2
6563 Hα.	-0.313	286 ± 20	286 ± 2	286 ± 19	282 ± 6	292 ± 6	$219^{\dagger}$
6584 [N II]	-0.316	16 ± 5	35 ± 2	126 ± 10	155 ± 5	43 ± 2	31 ± 1
6717 [S II]	-0.334	39 ± 3	60 ± 1	48 ± 4	77 ± 5	55 ± 2	39 ± 2
6731 [S II]	-0.336	23 ± 3	51 ± 1	27 ± 2	64 ± 6	40 ± 2	29 ± 1
$F(\mathrm{H}\beta)$		4.1 ± 0.3	3.8 ± 0.3	6.0 ± 0.4	5.5 ± 0.3	30.2 ± 0.2	9.2 ± 0.1
$EW(\mathrm{H}\beta)$		10.4 ± 10.1	9.7 ± 1.4	2.9 ± 0.2	1.7 ± 0.1	14.4 ± 0.8	17.1 ± 1.5
$c(\mathrm{H}\beta)$		−0.03 ± 0.09	0.10 ± 0.01	0.96 ± 0.09	1.04 ± 0.02	0.25 ± 0.03	0.00 ± 0.05
velocity		11992 ± 25	9915 ± 8	10308 ± 24	10048 ± 21	10033 ± 6	10008 ± 4

†Uncertain value.

Table 3.3: (Continued)

Line	$f(\lambda)$	LEDA084703		KUG1602+175	LEDA084710	CGCG108−149	KUG1602+174B
		b	c				
3727 [O II]	0.271	360 ± 8	514 ± 10	159 ± 12	361 ± 110	159 ± 53	164 ± 18
3869 [Ne III] . . .	0.238	21 ± 2	. . .	. . .	. . .	. . .	. . .
3889 He I+H8 . .	0.233	12 ± 7	. . .	. . .	. . .	. . .	. . .
3968 [Ne III]+H7. . .	0.216	. . .	. . .	22 ± 4	. . .	. . .	. . .
4069 [S II]	0.195	. . .	. . .	. . .	. . .	. . .	. . .
4102 Hδ.	0.188	24 ± 1	. . .	25 ± 3	. . .	. . .	. . .
4340 Hγ.	0.142	47 ± 1	47 ± 8	47 ± 5	. . .	. . .	46 ± 7
4861 Hβ.	0.00	100 ± 1	100 ± 2	100 ± 8	100 ± 11	100 ± 17	100 ± 6
4959 [O III]	-0.024	57 ± 1	44 ± 2	. . .	. . .	. . .	. . .
5007 [O III]	-0.035	186 ± 2	131 ± 3	56 ± 7	82 ± 9	53 ± 4	50 ± 5
5876 He I	-0.209	13 ± 2	11 ± 1	. . .	7 ± 4	. . .	. . .
6300 [O I]	-0.276	13 ± 1	20 ± 5	. . .	15 ± 4	. . .	. . .
6548 [N II]	-0.311	14 ± 1	20 ± 1	37 ± 2	30 ± 5	. . .	34 ± 6
6563 Hα.	-0.313	280 ± 7	290 ± 3	282 ± 7	285 ± 34	283 ± 52	283 ± 6
6584 [N II]	-0.316	42 ± 1	49 ± 2	103 ± 6	89 ± 12	165 ± 32	97 ± 5
6717 [S II]	-0.334	48 ± 1	84 ± 2	45 ± 3	63 ± 9	50 ± 14	55 ± 4
6731 [S II]	-0.336	38 ± 1	48 ± 2	23 ± 4	36 ± 6	54 ± 15	44 ± 4
F(Hβ)		17.0 ± 0.0	3.7 ± 0.1	27.2 ± 2.1	10.0 ± 1.1	4.1 ± 0.7	11.6 ± 0.7
EW(Hβ)		16.5 ± 0.8	6.2 ± 0.6	4.2 ± 0.4	3.3 ± 0.5	1.4 ± 0.2	4.8 ± 0.5
c(Hβ)		0.59 ± 0.03	0.50 ± 0.01	0.45 ± 0.03	1.18 ± 0.16	1.16 ± 0.25	0.48 ± 0.02
velocity		10032 ± 11	10087 ± 16	10574 ± 20	10781 ± 32	11121 ± 15	10622 ± 15

Table 3.3: (Continued)

Line	$f(\lambda)$	LEDA084724	SDSS J160556.98	[DKP87]160310.21	SDSS J160524.27	SDSS J160523.66
3727 [O II]	0.271	493 ± 14	317 ± 19	281 ± 13	214 ± 13	405 ± 5
3869 [Ne III] . . .	0.238	. . .	21 ± 6	. . .	30 ± 3	. . .
3889 He I+H8 . .	0.233	. . .	19 ± 6	. . .	16 ± 2	. . .
3968 [Ne III]+H7. . .	0.216	. . .	36 ± 5	. . .	28 ± 2	. . .
4069 [S II]	0.195	. . .	. . .	. . .	. . .	. . .
4102 Hδ.	0.188	. . .	25 ± 3	. . .	30 ± 3	. . .
4340 Hγ.	0.142	49 ± 6	47 ± 4	46 ± 5	49 ± 5	47 ± 3
4861 Hβ.	0.00	100 ± 8	100 ± 6	100 ± 8	100 ± 3	100 ± 4
4959 [O III]	-0.024	. . .	95 ± 4	. . .	114 ± 3	. . .
5007 [O III]	-0.035	91 ± 5	282 ± 4	47 ± 3	337 ± 4	69 ± 8
5876 He I	-0.209	. . .	10 ± 1	. . .	13 ± 2	. . .
6300 [O I]	-0.276	. . .	16 ± 4	. . .	10 ± 1	. . .
6548 [N II]	-0.311	. . .	. . .	27 ± 2	. . .	29 ± 8
6563 Hα.	-0.313	296 ± 13	280 ± 7	284 ± 4	320 ± 21	289 ± 2
6584 [N II]	-0.316	62 ± 8	27 ± 6	75 ± 3	13 ± 2	61 ± 2
6717 [S II]	-0.334	74 ± 8	40 ± 2	72 ± 2	35 ± 3	72 ± 3
6731 [S II]	-0.336	50 ± 6	27 ± 2	66 ± 4	22 ± 2	64 ± 3
$F(\mathrm{H}\beta)$		3.8 ± 0.3	9.6 ± 0.5	3.6 ± 0.3	6.6 ± 0.2	2.0 ± 0.1
$EW(\mathrm{H}\beta)$		2.7 ± 0.4	18.1 ± 2.3	4.4 ± 0.5	19.3 ± 1.9	3.6 ± 0.4
$c(\mathrm{H}\beta)$		0.43 ± 0.04	0.57 ± 0.03	0.09 ± 0.01	0.03 ± 0.09	0.25 ± 0.01
velocity		11714 ± 60	11621 ± 24	10308 ± 56	11101 ± 38	10337 ± 35

Table 3.3: (Continued)

Line	$f(\lambda)$	IC1182	IC1182:[S72]d	SDSS J150531.84	SDSS J160304.20	SDSS J160520.58
3727 [O II]	0.271	379 ± 22	399 ± 9	74 ± 4	455 ± 26	108 ± 30
3869 [Ne III]	0.238	23 ± 2	35 ± 1	...	...	...
3889 He I+H8	0.233	21 ± 2	20 ± 2	...	...	...
3968 [Ne III]+H7	0.216	24 ± 3	24 ± 3	...	...	...
4069 [S II]	0.195	...	...	...	...	...
4102 Hδ	0.188	30 ± 2	27 ± 1	...	...	...
4340 Hγ	0.142	48 ± 2	47 ± 3	...	44 ± 3	46 ± 4
4861 Hβ	0.00	100 ± 2	100 ± 2	100 ± 5	100 ± 2	100 ± 10
4959 [O III]	-0.024	73 ± 2	87 ± 1	...	...	...
5007 [O III]	-0.035	218 ± 4	253 ± 2	96 ± 3	66 ± 4	11 ± 3
5876 He I	-0.209	11 ± 1	...	...	...	...
6300 [O I]	-0.276	36 ± 3	14 ± 1	18 ± 2	11 ± 1	...
6548 [N II]	-0.311	...	13 ± 1	...	24 ± 2	35 ± 2
6563 Hα	-0.313	317 ± 21	298 ± 7	287 ± 15	272 ± 13	286 ± 2
6584 [N II]	-0.316	83 ± 8	36 ± 1	87 ± 5	73 ± 4	99 ± 2
6717 [S II]	-0.334	78 ± 7	48 ± 1	27 ± 8	65 ± 4	33 ± 2
6731 [S II]	-0.336	73 ± 10	31 ± 1	14 ± 2	48 ± 3	33 ± 2
F(Hβ)		167.5 ± 3.5	13.1 ± 0.2	1.9 ± 0.1	6.3 ± 0.1	3.0 ± 0.3
EW(Hβ)		28.5 ± 0.9	29.7 ± 4.6	4.3 ± 0.5	0.0 ± 0.0	0.0 ± 0.0
c(Hβ)		0.68 ± 0.09	0.37 ± 0.03	0.64 ± 0.07	0.76 ± 0.07	1.04 ± 0.01
velocity		10191 ± 43	10186 ± 4	9485 ± 2	10830 ± 24	10320 ± 36

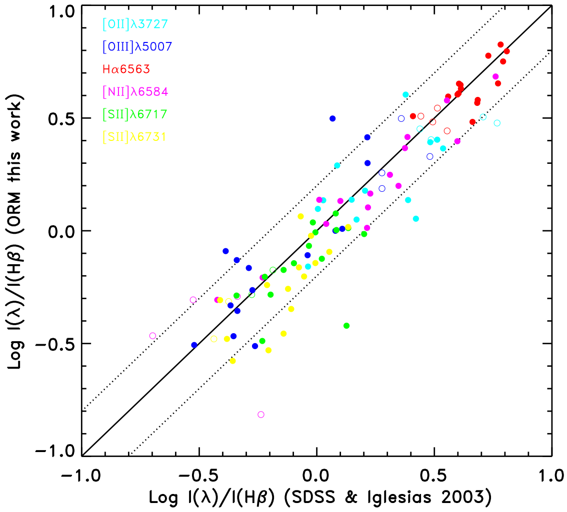

Figure 3.13: Emission line ratios $I(\lambda)/I(\mathrm{H}\beta)$ for the principal emission lines (without applying reddening correction) as derived by the ORM long-slit spectra observed for this work vs. corresponding ratios from SDSS (filled points) or IP03 spectra (open cycles) for the same galaxy regions. Cyan: [OII]λ3727, red: Hα, blue: [OIII]λ5007, pink: [NII]λ6584, green: [SII]λ6717 and yellow: [SII]λ6731. The continuous line is the line of equality and the dotted lines indicate a variation by ±0.2 dex.

of SF galaxies in the Hercules cluster. We have compared the line fluxes, before the reddening correction, for 5 galaxies for which we have spectra in common (Figure 3.13 open circles). We also see a very good agreement, with a small variation expected given the different position angles and different data analyzes.

The galaxies SDSSJ160304.20+171126.7, SDSSJ160520.58+175210.6 and SDSS-J160305.24+171136.1, quoted in the C09 sample, only have SDSS spectroscopy. The same procedure described in Sections 3.5 and 3.6.1 has been applied to these galaxies. For the latter, even after applying STARLIGHT on the SDSS spectrum, we do not appreciate any emission line, because the SDSS fiber is placed in the center of the galaxy where no Hα emission is present. The other two are included in our sample and their STARLIGHT outputs and line flux measurements are also quoted in Table 3.2 and 3.3 respectively. Finally, in this work are also incorporated 2 galaxies, (LEDA3085054 and [D97]ce-143), which belong to the C09 sample and for which spectroscopic data are available by IP03; all these spectra giving a final coverage of the C09 sample of 72%.

3.6.3 Abundance derivation

The radiation emitted by a nebula depends on the abundances of the chemical elements and the physical state of the gas, specially its average temperature and density. So, physical and chemical properties of nebulae can be derived by measuring the intensities of collisionally excited emission lines.

Prior to the determination of the gas-phase chemical abundances, the excitation conditions of the gas have to be explored. In order to do that we use the BPT diagrams (Baldwin et al. 1981). The derivation of gas-phase metal abundances is constrained to nebular emission-line spectra generated by photoionization from massive stars. Non-stellar ionizing sources, such as AGN, produce generally distinctive emission-line ratios compared to ordinary HII regions. In Figure 3.14 we present the BPT diagram with Kauffmann et al. (2003) empirical demarcation curve with dotted blue line, and Kewley et al. (2001) theoretical upper limit for starburst galaxies with dashed black line, in order to identify non-stellar ionizing sources.

We use four distinctive colors/symbols for our sample of galaxies. With blue filled circles we plot the 16 integrated dwarf/irregular galaxies ($M_{\rm B} > -19$) of our sample[5]. With red stars we plot the nuclei of 6 spirals and with green triangles their corresponding disk regions. Magenta squares are used for luminous ($M_{\rm B} \leq -19$) galaxies for which we integrate the 2D long-slit spectrum into one 1D spectrum (PGC057077 is ploted with magenta squares and PGC057064 with blue filled circles, although the spectra of these peculiar galaxies have been divided into two parts each, for different reasons, see Section 3.3 Appendix A.2 for details). Although we have divided the spectrum of the irregular galaxy LEDA084703 into three parts, from now on we consider the integrated values, because it shows homogeneous chemical composition (see Appendix A.1 for details on this galaxy).

In Figure 3.14 we see that the nuclei of NGC6045, NGC6050A, KUG1602+175A, galaxy CGCG108+149 and the South-East part of the peculiar object PGC057064 (see Appendix A.1 for special notes on this object) belong to the transition zone between the two separation curves. IC1182 (see Section 3.3 for details on this object) lies on the separation curve of Kauffmann et al. (2003) and there is a controversy in the literature whether there is an AGN hosted in the nucleus of this merger (see Radovich et al. (2005) and references therein), but our long-slit spectrum is slightly off-set from the optical center. The nucleus of IC1173 is clearly lying in the AGN region and we do not include it in our abundance analysis. We mark with a square the galaxy SDSSJ160531.84+174826.1. It has been claimed (Dong et al. 2007) that this galaxy hosts a Seyfert 1 AGN; the position of this galaxy in the BPT diagram, set by the ratios of the lines in our emission line spectrum, is consistent with the area of the plot populated by SF objects.

In Figure 3.15 we show the histograms of the distribution of the N2S2 (where N2S2=log([NII]λ6584/[SII]$\lambda\lambda$6717,6731) see Pérez-Montero & Contini (2009)) and R_{23} (see Section 1.3.1)[6] parameters for our sample of galaxies, using the same colors to separate out our sample in four categories as in Figure 3.14. The histograms in both left and right panel starting from the top correspond to: dwarf/irregulars, disks of spirals, integrated spirals, nuclei of spirals. The most populated N2S2 bin for the dwarf/irregular galaxies of our sample (left panel, first histogram from the

---

[5] In figures where the ploted quantities involve measurement of [NII]λ6584 and [SII]$\lambda\lambda$6717,6731 lines, the galaxy LEDA3085054 is not included

[6] When [OIII]λ4959 is not measured, we assume the theoretical ratio: [OIII]λ4959/[OIII]λ5007=0.33

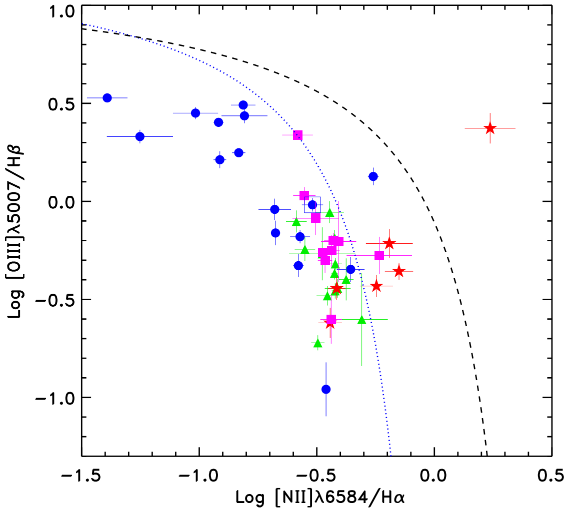

Figure 3.14: BPT diagram and Kauffmann et al. (2003) (dotted blue) and Kewley et al. (2001) (dashed black) separation curves between objects with ionized gas produced by photoionization from massive stars and from non-stellar ionizing sources. We use four distinctive colors/symbols for our galaxies: blue filled circles for dwarf/irregular galaxies ($M_{\rm B} > -19$), magenta squares for luminous ($M_{\rm B} \leq -19$) but integrated galaxies, red stars for the nuclei of 6 spirals that we divide into different parts and green triangles for their corresponding disk components. The two parts of PGC057077 are plotted in magenta filled squares; similarly, the two parts of PGC057064 are plotted in blue filled circles. We mark with a square the galaxy SDSSJ160531.84+174826.1 for which which it has been claimed (Dong et al. 2007) to host a Seyfert 1 AGN.

top, with blue line) lies around N2S2=-0.4, although there are few objects sorting out to higher values. These high values, as we will see later in the discusion, seem consistent with the properties of these galaxies. Spiral galaxies are separated into 3 categories. The galaxies for which we only have integrated spectrum (magenta line, third from the top) show N2S2 values extending up to 0.4 and the most populated range is around 0.1-0.2. The other two categories correspond to massive galaxies divided into nuclei (red line, forth from the top) and disks (green, second from the top). Although both distributions show a common range of N2S2 values from 0.0 to 0.3, there is a tendency for the spectra of the central parts to present higher N2S2 than the disks which can reach values as low as -0.3. In the same line for the R_{23} distribution, the dwarfs (right panel, first histogram from the top, with blue line) present the larger values of R_{23} up to 8 with few objects presenting values as low as R_{23}=1-3 (as we will show later this is a hint on the nature of these objects). However, as a possible consequence of the bi-valuated nature of the O/H vs. R_{23} function, the separation among the bright galaxies is not as clear as in the left panel. Nonetheless it can be seen that, for integrated bright galaxies (magenta, third from the top), R_{23}

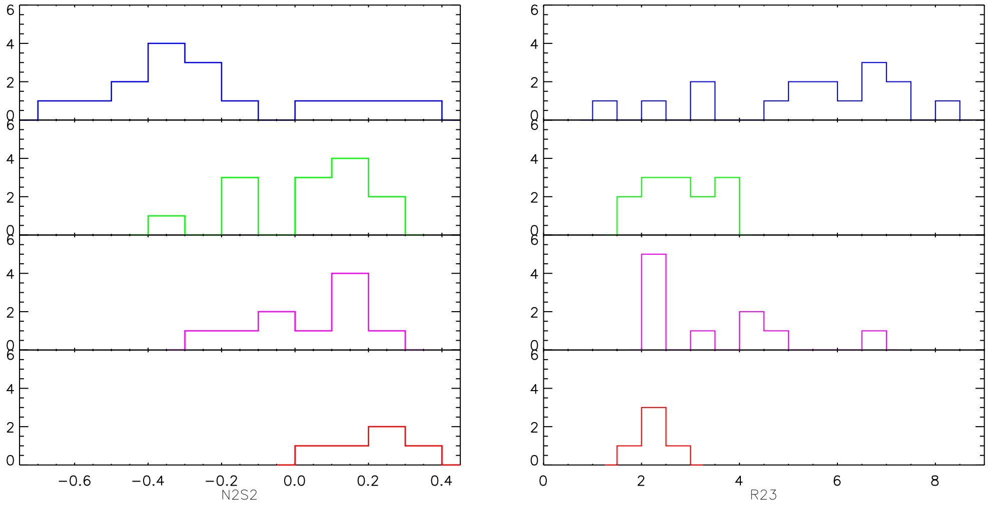

Figure 3.15: The histograms of the distribution of the N2S2 (left) and R_{23} (right) parameters for our sample of galaxies, using the same colors to separate out our sample in four categories as in Figure 3.14. The histograms in both left and right panel correspond to top to bottom: dwarf/irregulars, disks of spirals, integrated spirals, nuclei of spirals.

distribution shows a large range with values from 2 to 7 with the most populated values close to 2; for the spatially resolved galaxies, the range of disks reaches higher values (up to 4) compared to nuclei (up to 3). This analysis highlights the fact that using SDSS spectroscopy, which most probably means sampling only galaxy centers (bottom histogram, with red line), could introduce a bias in the abundance results.

There are two commonly used methods to determine oxygen abundances in HII regions. The direct method is founded on a direct measurement of the electron temperature, applicable when the collisionally excited lines such as [OIII]λ4363, [NII]λ5755, [SIII]λ6312 are measured. We do not detect any of the temperature diagnostic lines in our spectra. In addition, considering Hercules distance and the resolution of our observations, we are constrained to integrate galaxy spectra over large spatial scales, in some cases containing several HII regions, with potentially different ionization conditions. In these cases, the use of the direct method to derive abundances could result misleading (e.g Kobulnicky et al. 1999).

The other way to determine oxygen abundances in HII regions is to use semi-empirical calibrations. There are two different types of calibrations: the empirical ones, based on fits to objects for which an accurate direct derivation of O/H is available (e.g. Pettini & Pagel 2004; Pérez-Montero & Contini 2009; Pilyugin & Thuan 2005; Pilyugin et al. 2010) and the ones based on predictions of theoretical photoionization models (e.g. McGaugh 1991; Kewley & Dopita 2002; Tremonti et al. 2004). For an extensive review see and Kewley & Ellison (2008).

A strong hint that the direct measures and the empirical calibrations should yield metallicities closer to reality was given by Bresolin et al. (2009). These authors derived the metallicities of 28 H II regions in the galaxy NGC300 using the direct method, and found that these metallicities agree with the abundances derived from young massive stars, with stellar and nebular abundances giving virtually coincident slopes and intercepts of radial gradients. An important quantity that should be taken into account when comparing stellar and nebular oxygen abundances is the amount of oxygen depleted onto dust grains in ionized nebulae. According to Peimbert & Peimbert (2010) this fraction amounts to about 0.10 dex for low-mass galaxies. Bresolin et al. (2009) discussed this effect and found that, even considering a gas depletion factor of −0.1 dex, the intercepts of the nebular and stellar abundance gradients would be consistent. Then they compared their direct estimates of the metallicity of the ionized gas with the most widely used model calibrations, and they report that model calibrations yield higher metallicities of about a factor of two in the O/H range derived. On the contrary, the abundances derived using empirical calibrations use to be in good agreement with their direct measurements. Another strong hint was given recently by Dors et al. (2011). These authors produced models that reproduce O/H estimates consistently with the values derived using the direct method, for the upper range of O/H values, where all previous models showed systematic discrepancies. For our sample we also find a 0.3 dex positive shift between the abundances predicted using McGaugh (1991) model calibration (formulated by Kobulnicky et al. 1999) and the empirical calibration calculated by Pilyugin et al. (2010). Taking this into account, in this analysis we have chosen using empirical calibrations.

Our sample spans from very low metallicity dwarfs to evolved disks and galaxy centers, with an important fraction lying in the turn-over region of the R_{23} vs. oxygen abundance relation (see Figure 3.15). Among the empirical calibrations we use the N2-calibration given by Pérez-Montero & Contini (2009) (from now on PMC09) and the recent calibration by Pilyugin et al. (2010) (from now on P10), because they have the advantage of being valid along the whole metallicity range of our sample.

The N2 parameter defined by PMC09 as N2=log([N II]λ6584/Hα), shows a monotonic relation with oxygen abundance, thus avoiding the degeneracy problem of R_{23}; though this calibration involves a large rms error of up to $\sim$ 0.3 dex. In order to circumvent this problem P10 has provided with a new improved calibration which uses a multiparametric function of P, R_2, R_3, S_2, N_2[7] parameters and produces a very small rms error $\sim$ 0.07 dex.

In Table 3.4 we give the oxygen abundance derived using both abundance calibrations. We are aware that using the nitrogen as an abundance indicator to derive oxygen abundances can be potentially dangerous in case of objects with particular evolution, for example for nitrogen enriched galaxies (see PMC09). Comparing both abundance calibrations, we interpret PMC09 abundances as an upper estimate while

---

[7] Defined in P10 as N_2=[N II]$\lambda\lambda$6548,6584/Hβ, S_2=[S II]$\lambda\lambda$6717,6731/Hβ, and $P = R_3/R_{23}$. The theoretical ratio [N II]λ6548/[N II]λ6584=0.3 is assumed when necessary.

P10 as a lower estimate and, being conservative, we have adopted the mean of the two oxygen abundances. For each galaxy of our sample the adopted O/H value is consistent with the prediction of both calibrations within the statistical errors.

For each O/H determination we have estimated the corresponding error as the rms of a gaussian error distribution produced by a random sampling simulation taking into account the errors of the P, R_2, R_3, S_2, N_2 and R_{23} parameters. This error estimation has been adopted in all cases except in those cases for which it is less than the statistical error provided by the P10 calibration (~ 0.07 dex), which was finally adopted. As can be noted in Table 3.4, the error adopted is very close to the half of the difference in O/H provided by both calibrations.

Nitrogen is also an important element to investigate galaxy evolution. Nitrogen abundance deserves a more thorough determination; in particular the importance of possible self-enrichment (López-Sánchez & Esteban 2010; Monreal-Ibero et al. 2010) and the differential chemical evolution of N vs. O could add some degree of uncertainty. These effects have been extensively considered by PMC09, thus in this work we have adopted their calibration for nitrogen given by the N2S2 parameter which has a typical rms error of ~ 0.3 dex. In Table 3.4 the N/O values are also presented.

For the spatially resolved spirals of our sample we have explored the abundance gradients. Figures 3.16, 3.17 show the O/H and N/O abundance profiles, respectively, for the 6 spiral galaxies of our sample for which individual spectra, corresponding to different spatial regions, have been extracted. We plot the chemical abundances derived for each region in bins of galactocentric distance in arcsec, normalized to the r_{25} radius[8] extracted from SDSS r band images (see Table 3.5). The plots show mild or flat O/H abundance gradients across a limited radial extension of the disk.

---

[8] Radius r_{25} is the radius of the galaxies at a surface brightness of 25 mag arcsec^{-2}.

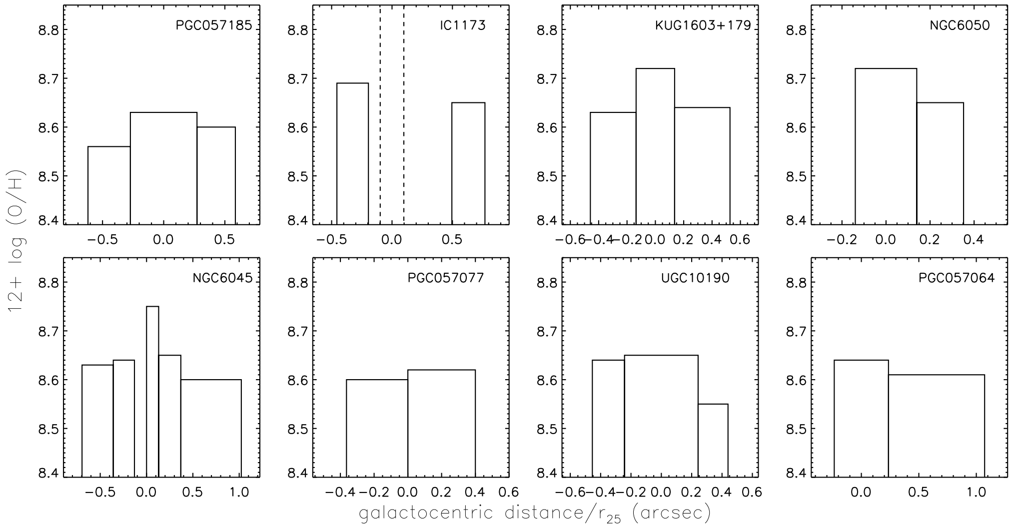

Figure 3.16: Oxygen abundances of the galaxies with spatially resolved spectroscopy in radial bins of galactocentric distance in arcsec normalized to r_{25}. For IC1173, dashed lines indicate the radial bin of the AGN extracted spectrum.

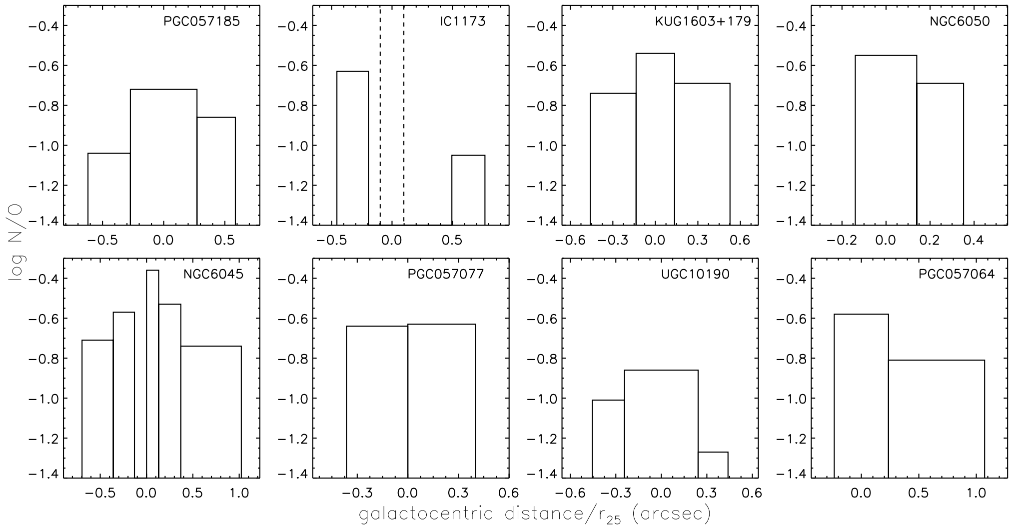

Figure 3.17: The same as in Figure 3.16 for N/O.

Table 3.4: **Chemical Abundances**

GALAXY	12+log(O/H) PMC09	12+log(O/H) P10	12+log(O/H) adopted	error adopted	log(N/O) PMC09
PGC057185a	8.64	8.48	8.56	0.07	-1.04
PGC057185b	8.74	8.53	8.63	0.07	-0.72
PGC057185c	8.69	8.50	8.60	0.12	-0.86
IC1173a	8.83	8.56	8.69	0.26	-0.63
IC1173e	8.72	8.57	8.65	0.07	-1.05
KUG1603+179Aa	8.73	8.53	8.63	0.07	-0.74
KUG1603+179Ab	8.88	8.57	8.72	0.07	-0.54
KUG1603+179Ac	8.74	8.53	8.64	0.07	-0.69
NGC6050Aa	8.92	8.53	8.72	0.07	-0.55
NGC6050Ab	8.71	8.59	8.65	0.07	-0.69
NGC6050B	8.63	8.52	8.58	0.07	-1.02
LEDA1543586	8.43	8.34	8.38	0.07	-1.15
NGC60545a	8.77	8.49	8.63	0.09	-0.71
NGC6045b	8.74	8.54	8.64	0.07	-0.57
NGC6045c	8.95	8.54	8.75	0.07	-0.36
NGC6045d	8.68	8.61	8.65	0.07	-0.53
NGC6045e	8.74	8.46	8.60	0.07	-0.74
KUG1602+174A	8.72	8.58	8.65	0.12	-0.81
LEDA084719	8.75	8.46	8.61	0.26	-0.69
PGC057077a	8.73	8.46	8.60	0.07	-0.64
PGC057077b	8.70	8.54	8.62	0.07	-0.63
UGC10190a	8.75	8.53	8.64	0.07	-1.01
UGC10190b	8.72	8.58	8.65	0.07	-0.86
UGC10190c	8.61	8.50	8.55	0.07	-1.27

Table 3.4: **Chemical Abundances**

GALAXY	12+log(O/H) PMC09	12+log(O/H) P10	12+log(O/H) adopted	error adopted	log(N/O) PMC09
LEDA140568	8.08	8.05	8.07	0.11	-1.60
[D97]ce-200	8.35	8.19	8.27	0.07	-1.49
PGC57064a	8.79	8.50	8.64	0.07	-0.58
PGC057064b	8.86	8.35	8.61	0.07	-0.81
LEDA084703int	8.41	8.28	8.35	0.07	-1.29
LEDA084703a	8.40	8.24	8.32	0.07	-1.29
LEDA084703b	8.42	8.29	8.35	0.07	-1.25
LEDA084703c	8.46	8.26	8.36	0.07	-1.40
KUG1602+175	8.72	8.54	8.63	0.07	-0.63
LEDA084710	8.67	8.44	8.56	0.27	-0.92
CGCG108-149	8.88	8.53	8.71	0.12	-0.61
KUG1602+174B	8.70	8.54	8.62	0.07	-0.87
LEDA084724	8.53	8.42	8.48	0.07	-1.24
SDSSJ160556.98+174304.1	8.27	8.21	8.24	0.11	-1.36
[DKP87]160310.21+175956.7	8.61	8.50	8.56	0.07	-1.19
SDSSJ160524.27+175329.3	7.97	8.01	7.99	0.07	-1.67
SDSSJ160523.66+174832.3	8.54	8.28	8.41	0.07	-1.30
IC1182	8.61	8.41	8.51	0.07	-1.19
IC1182:[S72]d	8.34	8.27	8.31	0.07	-1.29
SDSSJ160531.84+174826.1	8.66	8.64	8.65	0.07	-0.45
SDSSJ160304.20+171126.7	8.62	8.44	8.53	0.07	-1.10
SDSSJ160520.58+175210.6	8.71	8.68	8.69	0.15	-0.64
[D97]ce-143	8.43	8.26	8.35	0.07	-1.40

Table 3.4: **Chemical Abundances**

GALAXY	12+log(O/H) PMC09	12+log(O/H) P10	12+log(O/H) adopted	error adopted	log(N/O) PMC09
LEDA3085054		7.43^a	7.58	0.07	-0.86^a

Note: The oxygen abundance derived using Pérez-Montero & Contini (2009) and Pilyugin et al. (2010) calibrations. N/O is derived using N2S2 calibration by Pérez-Montero & Contini (2009). ^{a}These values are given by the used calibration assuming upper limits for the [NII]λ6584and [SII]$\lambda\lambda$6717,6731lines. The adopted O/H value is the one provided by Iglesias-Páramo et al. (2003b) calculated using the P-method; we see that is in very good agreement with the O/H value that we calculate with the P10 method.

3.6.4 Physical properties

We derive stellar mass for each galaxy using the kcorrect_v4 algorithm (version 4_2) of Blanton & Roweis (2007). This IDL code corrects implicitly for dust and assumes a universal IMF of Chabrier (2003) form. The SEDs used to best fit the observed SDSS u g r i z photometry are based on Bruzual & Charlot (2003) stellar evolution synthesis codes. The best-fitting SED provides an estimate of the stellar mass-to-light ratio[9]. Drory et al. (2004) argue that broad-band color mass estimators, can yield fairly reliable stellar masses for galaxies within ~ 0.2 dex over almost 4 decades in mass. Li & White (2009) demonstrate that, once all estimates are adapted to assume the same IMF, the Blanton & Roweis (2007) masses agree quite well with those obtained from the single-colour estimator of Bell et al. (2003) and also with those derived by Kauffmann et al. (2003) from a combination of SDSS photometry and spectroscopy. More recently, Zahid et al. (2011) also state that optical bands are sufficient to constrain the SED fit for determining masses of SF galaxies. The galaxy stellar masses given from the algorithm were converted to H_0=73 km s^{-1} Mpc^{-1} adopted in this work and are presented in Table 3.5.

We also calculate the two-dimensional local galaxy density Σ, using two methods. We use the density estimator based on an average of the projected distances (d, in Mpc) to the fourth and fifth nearest neighbor as given by Mouhcine et al. (2007) and used by Ellison et al. (2009)

$$\log \Sigma_{4,5} = \frac{1}{2} \log \left(\frac{4}{\pi d_4^2} \right) + \frac{1}{2} \log \left(\frac{5}{\pi d_5^2} \right) \tag{3.2}$$

considering all galaxies with SDSS spectra in the Hercules region at the corresponding redshift range, and presenting a difference in radial velocity smaller than 750 km s^{-1}, a value approximately equal to σ_v of the cluster. $\Sigma_{4,5}$ units are Mpc^{-2}.

To account for possible fiber collisions which may lead to an under-estimate of the local density in regions rich in projected galaxies as cluster centers, we calculate the local galaxy number density to the 10^{th} nearest neighbor Σ_{10}, using a magnitude limited sample of galaxies taken out from SDSS database without velocity constrain. Counts of galaxies as a proxy of local environment has the main weakness that is missing the luminosity information of the counted galaxies. To account for this problem, we limit to luminous galaxies $M_r = -19, m_r = 17$ mag when corrected for Galactic extinction. To correct for background and foreground galaxies, we use the field galaxy counts as given by Yasuda et al. (2001). The local galaxy number density is calculated to the 10^{th} neighbor in order to improve statistics. Σ_{10} units are Mpc^{-2}. As expected, the corresponding densities were higher, but they do not affect the conclusions of the MZR analysis as will be discused in Section 3.8. The density estimates $\log \Sigma_{4,5}$ and $\log \Sigma_{10}$ are quoted in Table 3.5.

We then estimate the projected distance of our galaxies to the cluster center. As already mentioned in Section 3.1, Hercules is a peculiar cluster of galaxies, where

---

[9] The χ^2 of the fit is less than 5 (1) for 73% (27%) of our sample

the maximum of the cluster galaxy distribution ($16^{\rm h}05^{\rm m}15.0^{\rm s}$ $+17^{\rm d}44^{\rm m}55^{\rm s}$, extracted from NED) is not coincident with the primary X-ray maximum found by Huang & Sarazin (1996). The center of the brightest X-ray component coincides with the brightest cluster galaxy NGC6041A ($16^{\rm h}04^{\rm m}35.8^{\rm s}$$+17^{\rm d}43^{\rm m}18^{\rm s}$). In Table 3.5 we give the projected distance of our sample galaxies to both centers in Mpc, referred to the cosmological corrected distance of Hercules cluster 158.3 Mpc.

We calculate the SFR of our galaxies, from their Hα emission given by C09 using the Kennicutt (1998) calibration. We use c(Hβ) derived by our optical spectroscopy to correct Hα emission from extinction, assuming the Miller & Mathews (1972) extinction law with $R_{\rm V}$ = 3.2. When spectra of different parts of a galaxy are considered, the c(Hβ) used to calculate the global SFR of the galaxy is the mean value of all these c(Hβ) derived spectroscopically. We also correct the Hα flux from [NII]λ6584 contamination using the empirical correction given by Reverte (2008):

$$\begin{aligned}\log EW(\mathrm{H}\alpha) &= (-0.34 \pm 0.03) + \\ &(1.13 \ \pm \ 0.02) \log EW(\mathrm{H}\alpha + [\mathrm{N\,II}])\end{aligned} \tag{3.3}$$

This empirical correction was derived using line fluxes integrated for entire galaxies, extracted from the extended spectrophotometric galaxy sample of Jansen et al. (2000), suitable for this kind of analysis. The errors on SFR quoted take into account only the Hα flux error.

Finally we note that the HI survey of Dickey (1997) covers the whole central region of A2151 where all our SF galaxies lie. We have adopted the HI masses provided in that work (converting them to H_0=73 km s^{-1} Mpc^{-1}).

Table 3.5 summarizes for each galaxy the physical properties calculated in this work and others extracted from the literature: the $M_{\rm B}$ absolute magnitude, the galaxy radius at 25 mag arcsec^{-2} in arcsec (extracted from the SDSS iso_A parameter for the r band), the local density estimates log$\Sigma_{4,5}$ and logΣ_{10}, the projected distance to the cluster center and the projected distance to the X-rays center in Mpc, the stellar mass calculated with kcorrect algorithm, the HI mass from Dickey (1997), and the SFR in $M_\odot$ yr^{-1}.

Table 3.5: **Physical Properties**

Galaxy	M_{B} mag	iso_A arcsec	$\log \Sigma_{4,5}$ Mpc^{-2}	$\log \Sigma_{10}$ Mpc^{-2}	R Mpc	R_{X} Mpc	$M_\star$ $10^8 M_\odot$	M_{HI} $10^8 M_\odot$	SFR $M_\odot$ yr^{-1}
PGC057185	-19.51	24.24	1.4	1.5	1.06	1.47	169.8	...	0.8 ± 0.1
IC1173	-20.79	30.68	1.1	1.5	0.9	0.92	444.7	37.3	7.3 ± 0.7
KUG1603+179A	-20.05	23.54	2.0	2.4	0.18	0.62	275.9	128.5	3.9 ± 0.2
NGC6050A	-20.87	30.10	1.7	2.4	0.1	0.53	27.6	53.1	...
NGC6050B	-19.30	...	2.3	2.4	0.1	0.53	262.7	...	...
LEDA1543586	-18.46	13.43	1.8	1.9	0.3	0.53	6.3	27.6	0.19 ± 0.01
NGC6045	-21.04	36.76	2.0	2.4	0.08	0.37	806.9	46.8	15.2 ± 1.0
KUG1602+174A	-19.24	13.47	1.2	2.3	1.17	1.03	72.6	...	0.6 ± 0.1
LEDA084719	-19.20	10.60	1.6	1.9	0.29	0.4	83.7	...	1.5 ± 0.3
PGC057077	-19.11	11.00	2.0	2.2	0.22	0.65	53.3	...	8.8
UGC10190	-19.21	26.40	1.9	2.1	0.19	0.56	60.8	100.8	0.4 ± 0.1
LEDA140568	-17.42	13.65	1.2	1.5	0.49	0.93	2.1	36.4	0.017 ± 0.002
[*D*97]ce-200	-17.74	8.54	2.3	2.3	0.13	0.38	3.0	9.0	0.091 ± 0.006
PGC057064	-18.65	18.65	2.1	1.9	0.26	0.64	104.0	...	3.9 ± 0.9
LEDA084703	-18.79	15.94	1.6	1.7	2.13	1.81	37.9	26.5	0.73 ± 0.03
KUG1602+175	-20.57	21.92	1.3	1.6	0.89	0.76	191.4	99.6	4.7 ± 0.3
LEDA084710	-19.23	18.85	1.2	1.7	1.05	0.8	122.9	...	3.9 ± 0.2
CGCG108-149	-20.14	18.87	1.3	1.6	0.97	1.39	311.5	15.5	3.2 ± 0.3
KUG1602+174B	-19.70	18.65	1.2	1.8	1.15	1.04	96.1	49.9	1.9 ± 0.2
LEDA084724	-18.72	14.82	1.0	1.4	0.57	0.86	42.6	...	1.002 ± 0.03
SDSS J160556.98+174304.1	-17.09	5.54	1.2	1.5	0.47	0.89	3.3	...	0.210 ± 0.009
[DKP87]160310.21+175956.7	-17.41	7.59	2.0	1.8	0.34	0.67	5.7	...	0.06 ± 0.02
SDSS J160524.27+175329.3	-16.16	3.53	1.3	1.8	0.41	0.71	1.1	...	0.022 ± 0.002

Table 3.5: **Physical Properties**

Galaxy	$M_{\rm B}$ mag	iso_A arcsec	$\log\Sigma_{4,5}$ Mpc^{-2}	$\log\Sigma_{10}$ Mpc^{-2}	R Mpc	$R_{\rm X}$ Mpc	$M_\star$ $10^8 M_\odot$	M_{HI} $10^8 M_\odot$	SFR $M_\odot$ yr^{-1}
SDSS J160523.66+174832.3	-16.76	5.88	1.9	2.1	0.19	0.58	3.4	...	0.07 ± 0.02
IC1182	-20.98	27.24	2.1	2.0	0.28	0.7	654.9	...	22.1 ± 0.6
IC1182:[S72]d	-17.73	9.62	1.9	1.9	0.33	0.76	1.3	186.0	0.83 ± 0.02
SDSS J150531.84+174826.1	-17.23	5.21	2.2	2.0	0.25	0.66	15.5	...	0.146 ± 0.009
SDSS J160304.20+171126.7	-17.42	9.05	1.6	1.7	2.1	1.78	24.8	...	0.55 ± 0.03
SDSS J160520.58+175210.6	-18.51	13.85	1.9	1.9	0.34	0.64	10.6	...	0.20 ± 0.02
[*D*97]ce-143	-17.56	8.29	1.4	1.9	0.33	0.64	14.9	16.7	0.025 ± 0.004
LEDA3085054	-16.23	4.65	1.4	1.5	0.46	0.88	0.7	19.7	0.045 ± 0.002

Note: Column 1: galaxy name from C09; Column 2: $M_{\rm B}$ absolute magnitude, calculated from SDSS g magnitudes, assuming a distance to A2151 of 158.3 Mpc and an average correction of g-B=-0.3 mag (Fukugita et al. 1995). All the quantities of this table are refered to the cosmological corrected distance of Hercules cluster assuming H_0=73 km s^{-1} Mpc^{-1}; Column 3: SDSS iso_A parameter for the r band in arcsec; Column 4: local density estimator $\log\Sigma_{4,5}$; Column 5: local density estimator $\log\Sigma_{10}$; Column 6: projected distance to the cluster center in Mpc; Column 7: projected distance to the X-Rays center in Mpc; Column 8: stellar mass calculated with kcorrect; Column 9: HI mass from Dickey (1997); Column 10: SFR in $M_\odot$ yr^{-1}.

3.7 Metallicity versus local density

In the following we study the relation between metallicity and environment for our sample of SF galaxies in the Hercules cluster. We examine the potential impact of the environment on the MZR and LZR and investigate different evolutionary scenarios of these cluster galaxies. The Hercules cluster three dimensional galaxy distribution is extremely clumpy (Bird et al. 1995), rendering it a very interesting vivid environment difficult to be disentangled only in the projected space without taking into account galaxy velocity. The local density of galaxies has been widely used as an indicator of their environment; in this work we have studied the behavior of metallicity vs. local density. The local density $\Sigma_{4,5}$, derived to the 4^{th} and 5^{th} nearest neighbor would describe the local environment at the group-scale.

In Figure 3.18 we plot the galaxy gas-phase oxygen abundances vs. the local density estimators $\Sigma_{4,5}$ (upper panel) and Σ_{10} (lower panel) calculated in Section 3.6.4. We keep the same color/symbol distinction as in Figure 3.14. Additionally, the points corresponding to the same galaxy (nuclei and disks), are connected with straight lines. We see that for luminous galaxies, the oxygen abundance does not show any significant dependence on the local galaxy number density. Luminous galaxies of this sample span the whole range of densities and all are found to have nearly solar oxygen abundance. Dwarf galaxies show a noticeable variation: the $\sim$ 80% of the less metallic dwarfs (12+log(O/H)$<$ 8.4) are located at $\Sigma_{4,5} < 1.85$, whereas the $\sim$ 70% of the higher metallicity (12+log(O/H)$>$ 8.4) dwarf galaxies are located at very high local densities $\Sigma_{4,5} > 1.85$. A substantial fraction of these more metallic dwarfs have been identified to be affected by interactions and they are described in detail in Appendices A.1 and A.2. This dual behavior is not so evident when Σ_{10} density estimator is used.

The dependency observed in Figure 3.18 of the metallicity of dwarf/irregular galaxies with local density could be interpreted as follows: at the highest local densities, i.e. approaching the cluster center, only the more “robust” –i.e. more massive and more metallic– dwarf galaxies can survive. Conversely, the less metallic dwarf galaxies should have been incorporated recently to the cluster. This “newcomers” scenario for dwarfs is additionally supported by the fact that the majority of the low metallicity dwarf galaxies present radial velocities which differ from the radial velocity of the brighter cluster galaxy NGC6041A –located at the X-ray maximum of the cluster– by more than σ_v, possible evidence of infall.

One point worth of mentioning here is that, in this work, we study the effect of local galaxy density sampling much denser environments (from $\log\Sigma_{4,5} = 1.0$ to 2.5) than in previous works (Mateus et al. 2007; Mouhcine et al. 2007; Cooper et al. 2008; Ellison et al. 2009) typically reaching $\log\Sigma \sim 1.5$. Additionally, the works mentioned above use the SDSS database and include few dwarf galaxies, mainly due to the magnitude limit of SDSS in combination with galaxy-size limits or redshift constraints applied in order to minimize possible aperture effects. This study, therefore, is complementary and goes beyond these previous works, dealing also with the dwarf galaxy population. In this sense, the Hercules cluster, being an ideal laboratory to study the environmental effects on SF galaxies, was not included in the SDSS-DR4 used in all these previous studies.

3.8 Mass and luminosity versus metallicity

Figure 3.19 (upper panel) shows the gas-phase oxygen abundance vs. galaxy stellar mass for our sample of galaxies (colors and point features as in Figure 3.18). We see that Hercules SF galaxies follow a well defined sequence on this plot, which reaches a saturation value $\sim Z_{\odot}$ for galaxies with $\sim 10^{10} M_{\odot}$. We observe that the set of dwarfs/irregulars populating the higher local densities (i.e. $\log \Sigma_{4,5} > 1.85$, see Section 3.7), marked here with circles, appear shifted towards higher metallicities for their mass. This fact suggests a different evolution for these galaxies in the environment of the cluster, thus providing a physical reason for the dispersion in the MZR. These findings are in the line of the results of Cooper et al. (2008) who attribute $\sim 15\%$ of the measured scatter of the MZR to the environment.

For the sake of clarity, in Figure 3.19 (lower panel) we added the 15 Virgo dIs and BCDs (light blue open circles) from Vaduvescu et al. (2007) and references therein (excluding VCC641 because of its uncertain oxygen abundance). For consistency with our data, when a direct abundance estimation is not available, we recalculate their abundances using the P10 method. We have recalculated the stellar mass for the Virgo dwarf galaxy sample using the kcorrect code (as for the Hercules sample) and we found a good agreement with the mass estimate given by Vaduvescu et al. (2007) calculated via K-band photometry (we use the latter values in our Figure 3.19). We see that Virgo dwarf galaxies couple nicely with our Hercules data on the mass vs. metallicity plot.

We also compare with the extensive sample of SF galaxies used by Amorín et al. (2010), comprised by all the emission-line galaxies listed in the Max Planck Institute for Astrophysics/Johns Hopkings University (MPA/JHU) Data catalog of the SDSS DR 7[10] which covers a redshift range $0.03 \leq z \leq 0.37$. Oxygen abundances were calculated using the N2 calibration of PMC09 and mass estimates were driven from the MPA/JHU catalog. On this plot Hercules SF galaxies lie within the same range as the emission-line galaxies of SDSS DR7, except in the higher mass range, where our data show a shift towards lower metallicities by ~ 0.15 dex as compared to the Amorín et al. (2010) sample. We tentatively attribute this observed shift to the different oxygen abundance calibration used in each case; in addition, another important effect is the different spatial coverage of SDSS spectra vs. the spatially resolved spectra used in this work.

In Figure 3.20 (upper panel) we plot the gas-phase oxygen abundance vs. galaxy M_{B} absolute magnitude. Our galaxy sample follows a LZR, where the same differential behavior identified in the MZR is clear for the dwarf/irregular galaxies at high local densities (i.e. $\log \Sigma_{4,5} > 1.85$). On the lower panel we show again the Virgo dI and BCDs (light blue open circles) from the samples of (Vílchez & Iglesias-Páramo

---

[10] Available at http://www.mpa-garching.mpg.de/SDSS/

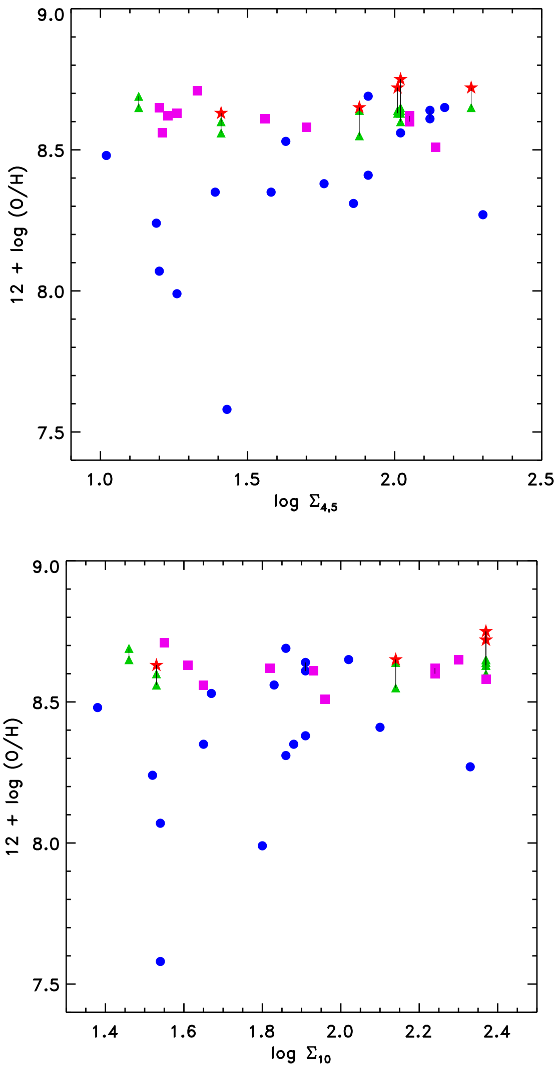

Figure 3.18: Oxygen abundance of galaxies vs. their local density. Upper panel: O/H vs. $\Sigma_{4,5}$, the local galaxy number density to the average of the projected distances to the fourth and fifth nearest neighbor, where the galaxies considered are secure members of the Hercules cluster, as follows by their SDSS spectroscopic redshift. Lower panel: O/H vs. Σ_{10}, the local galaxy number density to the 10^{th} nearest neighbor, where a magnitude limited sample ($M_r \leq -19$ mag) of galaxies is used and we remedy for background and foreground galaxies using the field galaxy counts of Yasuda et al. (2001). Colors and point features as in Figure 3.19: blue filled circles for dwarf/irregular galaxies ($M_{\rm B} > -19$), magenta squares for spirals ($M_{\rm B} \leq -19$) integrated galaxies, red stars for the nuclei of 6 spirals that we divide into different parts and green triangles for their corresponding disk components (nuclei and disks are connected with lines). Both parts of PGC057077 are plotted in magenta filled squares; similarly, both parts of PGC057064 are plotted in blue filled circles.

2003; Vaduvescu et al. 2007), and the (centers of) Virgo spirals (red open triangles) from Pilyugin et al. (2002) and references therein. We also add the Hydra dwarfs (green open diamonds) from Duc et al. (2001, 1999). All the abundances were recalculated using P10 method and $M_{\rm B}$ of the Virgo spirals was derived by the $L_{\rm B}$ given by Skillman et al. (1996). We see that SF galaxies of Hydra, Virgo, and Hercules clusters appear to follow the overall LZR, though is apparent that the scatter has increased.

Moreover, Hercules SF galaxies also follow a well defined sequence on the plots of the N/O ratio vs. galaxy stellar mass and galaxy $M_{\rm B}$ absolute magnitude shown in Figure 3.21. In this plot we can see how some of the dwarf galaxies shifted towards higher O values in the MZR appear overabundant in N/O (see also Section 3.10). Additionally, the N/O ratio makes evident a significant abundance difference between nuclei and disks (points connected with straight lines), that will be discussed in more detail in Section 3.11.

Recent works (Mannucci et al. 2010; Lara-López et al. 2010) discuss the existence of a more general relation between stellar mass, gas-phase metallicity and star formation rate in the local Universe. We have checked that, for the galaxy mass range we have in common, Hercules SF galaxies lie in the same range as Lara-López et al. (2010) sample in the 3D plot which combines stellar mass, gas-phase metallicity and star formation rate. In Chapter 5 we will discuss the fundamental plane for SF galaxies in clusters, using a larger sample of cluster SF galaxies for which metallicities, stellar masses, and SFR are computed.

3.9 Comparison with the "closed-box" model

In order to study possible environmental effects on the (gas-phase) chemical enrichment in galaxies, it is useful to compare with the predictions of the so-called "closed-box" model (Edmunds 1990). According to this model, a galaxy consists initially of gas with no stars and no metals. The stellar IMF is assumed to be constant on time and the products of stellar nucleosynthesis are assumed to enrich the ISM instantaneously. Throughout its life, the metal content of a galaxy is neither diluted by infalling pristine gas nor lost via outflow of enriched gas. Hence, the metallicity at any given time is only determined by the fraction of baryons which remains in gaseous form. The model equation can be written as

$$Z_o = y_o \ln(1/\mu) \tag{3.4}$$

where Z_o is the oxygen mass fraction, y_o is the yield by mass and μ is the ratio of the gas mass to the baryonic mass, $\mu = M_{gas}/M_{bar}$. The gas mass corresponds to the hydrogen atomic gas with a correction for neutral helium ($M_{gas} = 1.32 M_{HI}$; molecular gas mass was not taken into account here) and $M_{bar} = M_{gas} + M_\star$ where $M_\star$ is the mass in stars.

Figure 3.22 compares the observed oxygen abundances for our sample galaxies to the prediction of the "closed-box model", plotted with lines with different y_o. The

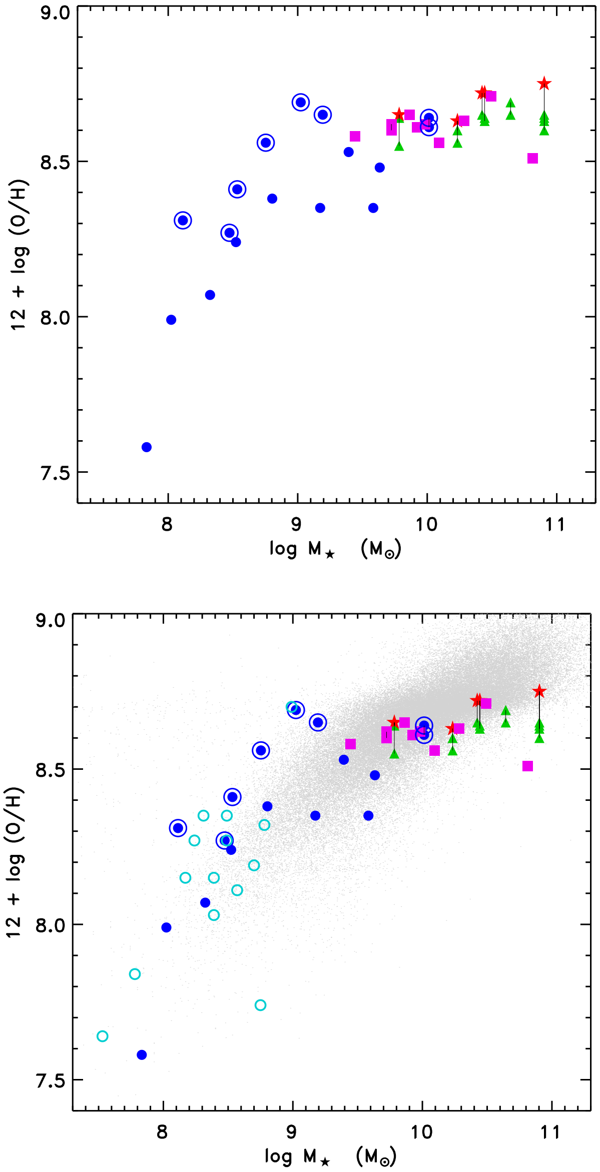

Figure 3.19: Upper panel: Gas-phase oxygen abundance vs. galaxy stellar mass for the Hercules galaxies. We keep the same color distinction as in Figure 3.18. We mark with circles the galaxies located at densities $\log \Sigma_{4,5} > 1.85$ which appear preferentially located above the general relation. Lower panel: On the same plot we add the Virgo dIs and BCDs from Vaduvescu et al. (2007) (light blue open circles) and the MPA/JHU SF galaxies (gray points) used as a reference sample by Amorín et al. (2010).

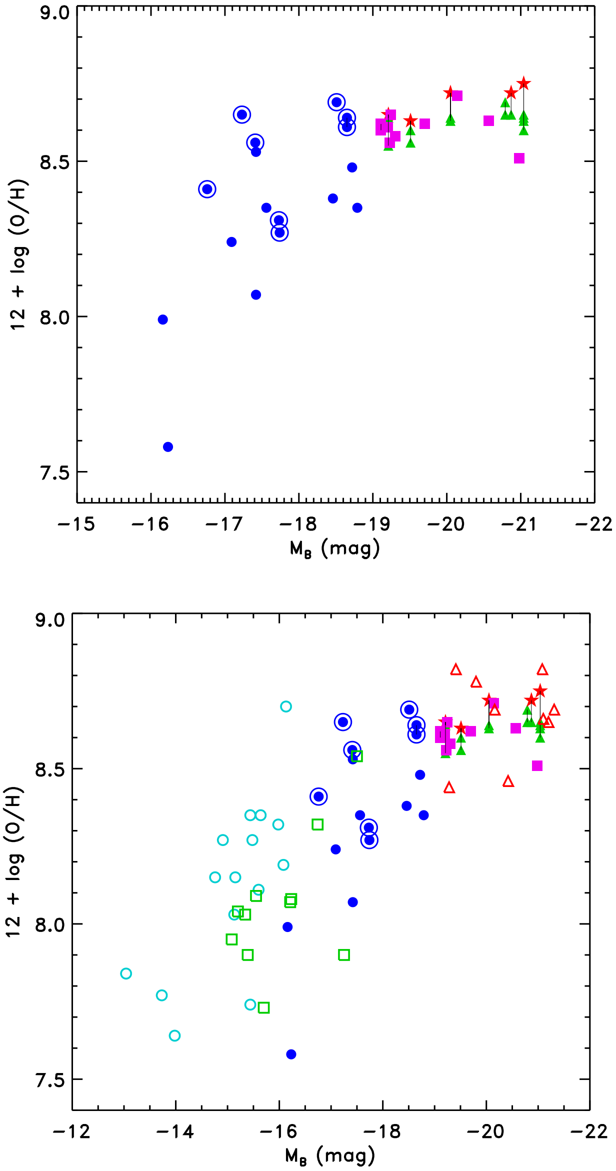

Figure 3.20: Upper panel: Gas-phase oxygen abundance vs. galaxy M_B absolute magnitude for the Hercules sample (colors and symbols as in Figure 3.19). As in the MZR, galaxies (marked with circles) at high density ($\log\Sigma_{4,5} > 1.85$) appear shifted towards higher O/H. Lower panel: We add the Virgo dI and BCDs (light blue circles) as given by Vílchez & Iglesias-Páramo (2003) and Vaduvescu et al. (2007), the Virgo spirals (central abundance; red open triangles) from Pilyugin et al. (2002) and references therein, as well as the Hydra dwarfs (green open squares) by Duc et al. (2001, 1999).

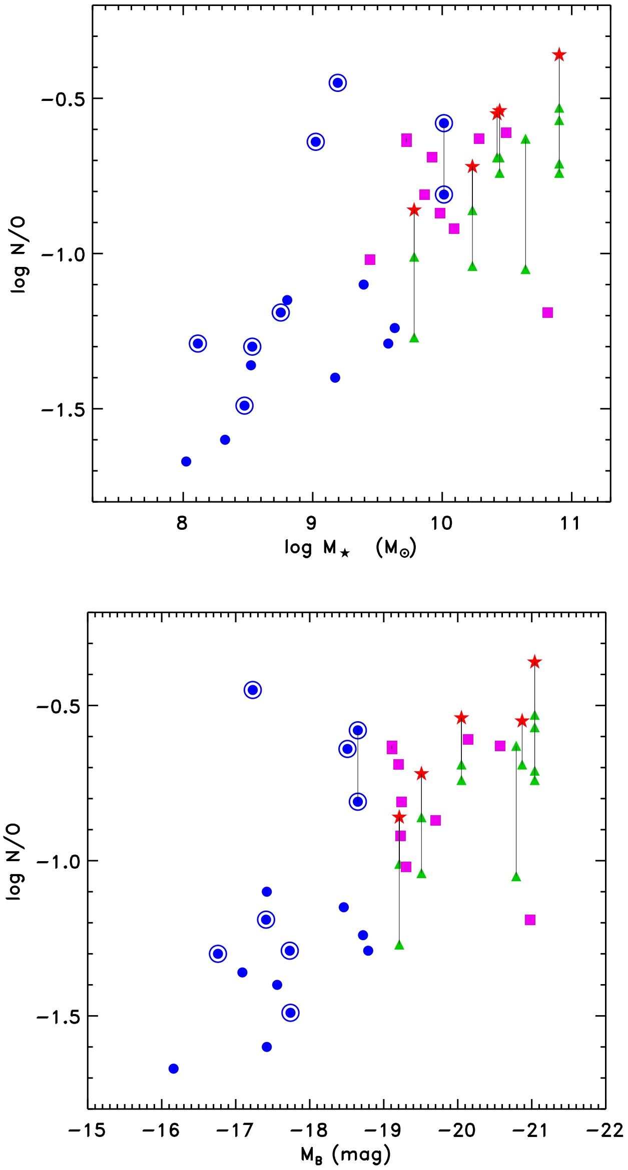

Figure 3.21: N/O vs. galaxy stellar mass (upper panel) and M_{B} absolute magnitude (lower panel) for the Hercules galaxies (colors and symbols as in Figure 3.19). A significant N/O abundance difference can be seen between galaxy nuclei and disks (points connected with straight lines).

green continuous line indicates the model with $y_o = 0.0074$, that is the theoretical yield of oxygen expected for a Salpeter IMF and constant star formation rate, for stars with rotation following Meynet & Maeder (2002) models (van Zee & Haynes 2006). Both, infall and outflow of well-mixed material will result in effective yields that are less than the true yields, as the enriched material is either diluted (infall) or lost from the system (outflow). A fraction of the sample of isolated dwarf irregular (dI) galaxies of van Zee & Haynes (2006) was found to follow the theoretical yield, and the rest appears consistent with a lower yield $y_o = 0.002$, almost 1/4 of the model prediction (blue dashed line in Figure 3.22). The gray strip indicates the relationship given by Lee et al. (2003) between oxygen abundance and the baryonic gas fraction for a sample of local Universe dIs. The cyan open circles correspond to the Virgo dI and BCDs from Vaduvescu et al. (2007). Most of Virgo dwarfs appear consistent with the Lee et al. (2003) locus for local dwarf galaxies, though some of them still present lower gas fractions.

We can see in Figure 3.22 that four of our low mass galaxies for which we have HI measurements (LEDA1543586, LEDA140568, [D97]ce-200, and LEDA3085054), are in agreement with the "closed-box" model predictions with $y_o = 0.0074$ (green line). This fact suggests that these galaxies are falling into the central region of the cluster and encountering now the dense ICM gas for the first time; as a consequence, gas removal by RPS might not yet be observable. These four galaxies can be considered as prototypes of the "newcomers" to the cluster introduced in Section 3.7. This result is additionally supported by their disturbed Hα characteristic morphologies (as seen in the Hα maps in C09) as described below.

The Hα emission map of LEDA1543586 reveals a strong episode of star formation concentrated into an asymmetric arc located on the side of the galaxy facing the cluster center and almost no emission in the opposite side. This typical "bow-shock" morphology has been observed in other cluster galaxies (e.g. Gavazzi et al. 2001) and is very suggestive of a ram-pressure event. After closer inspection of the C09 Hα maps we identify that the galaxy LEDA140568 also show a "bow-shock" morphology on the side of the galaxy facing the cluster center. Additionally, the other 2 galaxies, [D97]ce-200, and LEDA3085054 present strongly asymmetric Hα emission, one-sided and offset from the galaxy optical center. These starbursts could be the signature of pressure-triggered star formation by the ICM within the cluster environment (Kronberger et al. 2008). Additionally these four galaxies have abs(ΔV) $> \sigma_v$ (see Section 3.2) and they have a median projected distance to the center of the X-ray distribution of $\sim$ 700 kpc; thus they are approaching to the edge of the main X-ray emitting region which extends up to R_X = 678 kpc (Huang & Sarazin 1996).

The blue points close to the blue dashed line in Figure 3.22 ($y_o = 0.002$) correspond to the dwarf/irregular galaxies [D97]ce-143 and LEDA084703 (see the Appendix A.1 and A.2 for details). [D97]ce-143 is located at high local density (Section 3.7) and Dickey (1997) reports that its correspondent HI cloud shows two elongations and is highly reminiscent of the Magellanic Stream. LEDA084703 shows a long HI plume (Dickey 1997) reaching about $1'$ from the optical center to the South-East (also at the East part of this galaxy is located the supernova quoted by Zwicky et al. 1969). These peculiar HI morphologies suggest that some gas mass-loss effect has taken place, explaining thus their location on Figure 3.22.

A very interesting case is the galaxy IC1182:[S72]d labeled in Figure 3.22. This TDC (IP03) shows an HI distribution which extends well beyond the galaxy disk (Dickey 1997). This morphology, combined with the information we got on its gas-phase chemical content (this galaxy lies above the MZR and mass-N/O relations), together with its old stellar population (see Section 3.10), indicate a particular formation scenario for this galaxy. This galaxy has probably been produced during the merger IC1182 and seems dominated by an old stellar population. This galaxy could have acquired a large mass of gas from the late type galaxy of the merger IC1182. This formation scenario can explain why IC1182:[S72]d shows a much higher gas fraction than the value expected according to the "closed-box" model. Thus, the active environment of the cluster can provide an explanation for the location of a galaxy in such forbidden region on Figure 3.22 (Edmunds 1990; van Zee & Haynes 2006). There exist examples of dwarf galaxies formed from the gas lost in a merger, e.g. the old TDC VCC2062 in the Virgo cluster studied by Duc et al. (2007); according to these authors this galaxy has probably been formed out of the gas clouds lost by a gas-rich galaxy involved in a merger.

For the galaxies of our sample that were not detected in Dickey (1997) we assume an HI mass upper limit corresponding to the detection threshold of this survey ($\leq 2.6 \times 10^8 M_\odot$). In Figure 3.22 we add those galaxies with right pointing arrows (representative of the central oxygen abundance) to indicate the upper limit for their HI mass. Excluding the galaxies already discussed, the rest of the galaxies in Figure 3.22 (including upper limits) on average suggest effective yields below the closed box model and are consistent with the field sample of Lee et al. (2003). Finally, some points (few Virgo dwarfs and one Hercules upper limit for the IC1182 merger) still appear in Figure 3.22 displaced towards even lower values of gas fractions, as it would be expected if these cluster galaxies suffered important environmentally induced gas removal (e.g. from RPS).

3.10 Gas-phase metallicity versus properties of the underlying stellar component

In order to search for possible environmental footprints on the chemical history of our sample galaxies, we compare the stellar population properties, such as the mass-weighted stellar metallicity $Z_{\star,M}$ and mass-weighted stellar age $\tau_{\star,M}$, brought forth by the STARLIGHT model fitting (§3.5), with the gas-phase abundances derived in this work. The fact that these properties (for stars and gas) have been obtained following a completely different methodology should render our analysis more robust.

Figure 3.23 shows the gas-phase oxygen abundance (upper panel) and the N/O ratio (lower panel) vs. the mass-weighted stellar age $\tau_{\star,M}$. We see an overall positive trend, more prominent for N/O, which should reflect the different time-scales

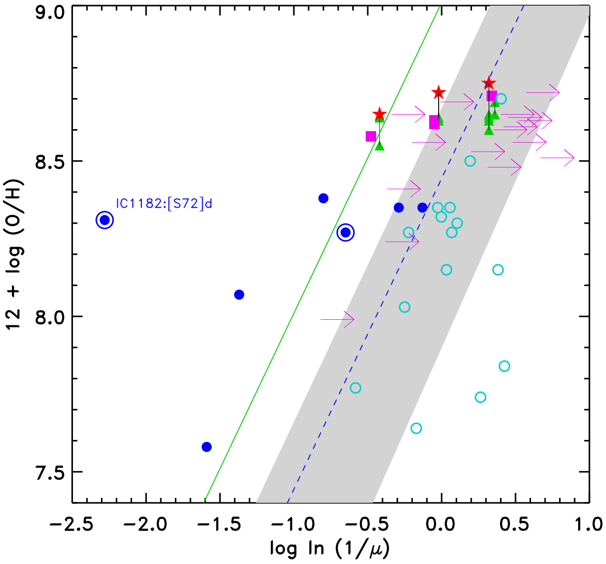

Figure 3.22: Oxygen abundances for our sample galaxies vs. the ratio of the gas mass to the baryonic mass, $\mu = M_{gas}/M_{bar}$ (colors and symbols as in Figure 3.19). The green continuous line indicates the "closed-box" model with $y_o = 0.0074$ and the blue dashed line corresponds to $y_o = 0.002$. The gray strip gives the best fit of Lee et al. (2003) to their field dIs. The cyan circles correspond to the Virgo dI and BCDs from Vaduvescu et al. (2007). Arrows mark objects with upper limit in HI.

for the delivery of these two elements to the ISM. Oxygen, produced in Type II supernovae, is released after $\sim$ 10 Myr, while nitrogen is produced and released over a substantially longer period, $\gtrsim$ 250 Myr. Overall, we can see how nitrogen abundance seems to correlate better with the mass-weighted stellar age. Additionally, the dispersion in N/O becomes smaller at larger age, possibly reflecting the averaging effects of many star formation episodes, while the larger dispersion seen at small ages could reflect the stochastic effects of few episodes of star formation or other possible environmental effects such as e.g. gas inflows.

In Figure 3.23 we can see that $\gtrsim$ 85% of the dwarf galaxies residing at high local density environments ($\log \Sigma_{4,5} > 1.85$) present old stellar populations of mass weighted age $\geqslant$ 6 Gyr. Conversely, $\sim$ 70% of the dwarfs located at density $\log \Sigma_{4,5} < 1.85$ present mass weighted ages below this value; a hint suggesting that only the more robust galaxies –e.g. more massive, evolved and more metallic– could have survived in the environment of highest galaxy density. The outliers to this general correlation also can give us important clues on possible environmental effects on their chemical histories. On the lowe panel of Figure 3.23 we can identify the galaxy merger IC1182 and the two dwarfs associated with it (SDSSJ150531.84+174826.1 and IC1182:[S72]d; see Section 3.3). Interestingly enough, all three objects present almost the same (very old) stellar age. Moreover, the galaxy SDSSJ150531.84+174826.1 appears to be more chemically enriched with respect to galaxies of similar mass (see also Figures 3.19 and 3.21). Taken altogether, these properties of SDSSJ150531.84+174826.1 remind those of the central part of a massive galaxy after having lost its outer parts (e.g. during a past interaction with the neighbor merger IC1182).

The TDC galaxy IC1182:[S72]d, despite hosting an old stellar population, does not seem to be that chemically evolved (especially in N/O) in accordance with the scenario already proposed for it: the accretion of a large mass of gas from the late type galaxy of the merger IC1182. For IC1182, our spectrum sampled the slightly off-center starburst giving a gaseous oxygen abundance slightly lower than the average observed trend in the MZR. This fact, together with its low N/O ratio, suggest that this gas should have an origin external to the host underlying galaxy. A similar scenario has been invoked before by Moles et al. (2004) (see also Radovich et al. 2005) who claimed that this gas was provided by the late type galaxy of the merger.

Two other objects can be seen above the correlation in Figure 3.23: the eastern part of the disk of NGC6045 (NGC6045e) and PGC057077b, both galaxies appear affected by interactions and show intense star formation (the highest SFR values measured for our sample after the merger IC1182). Though it has been shown that high star formation efficiency can be a key ingredient to enhance N/O (Mollá et al. 2006), what moves these two objects out of the general age-N/O relation seems to be related to their derived ages: the spectra of these objects are sampling just the starbursts, hence the derivation of $\tau_{\star,M}$ should then be dominated by the contribution of the young starburst; in contrast, the results derived for other parts of these two galaxies follow the general trend of N/O vs. $\tau_{\star,M}$.

In Figure 3.24 we compare the gas-phase and the stellar oxygen abundances derived for the sample of galaxies. We compute the latter abundance using the mass-weighted metallicity, $Z_{\star,M}$, given by STARLIGHT, assuming 12+log(O/H)$_\odot$ = 8.69 (Asplund et al. 2009). We plot the difference between gas-phase and stellar oxygen abundance $\Delta\log(\mathrm{O/H})_{gas-\star}$ vs. the stellar oxygen abundance 12+log(O/H)$_\star$. In this plot we can see two main behaviors. For luminous galaxies ($M_\mathrm{B} \leq -19$), we can see the following correlation:

$$y = (7.99 \pm 0.47) - (0.925 \pm 0.055)x \tag{3.5}$$

where $y = \Delta log(O/H)_{gas-\star}$ and $x = 12 + \log(O/H)_\star$ ($\chi^2 = 0.074$). Assuming our model fitting hypotheses, this "upper bound" correlation would mean that for a chemically evolved stellar population, of order $\sim Z_\odot$, gas and stars present the same metallicity. However, even when the stellar metal content of these galaxies goes down, we can see the observed gas abundance remains close to $\sim Z_\odot$ (see also Gallazzi et al. 2005; Asari et al. 2007). This behavior could reflect the fact that, for our more massive galaxies, gradients of stellar metallicity can be more conspicuous than for gas, consistent with model predictions (Ferrini et al. 1994) suggesting that abundance gradients should flatten with age.

For the lower luminosity galaxies we can see that the two groups of dwarfs (referred to in Sections 3.8 and 3.9) split up in Figure 3.24 too. The "newcomers" show similar oxygen abundances for gas and stars whereas the more chemically evolved dwarfs found at high local densities (marked with circles), hosting older stellar populations ($\geqslant$ 6 Gyr), show that the gas oxygen abundance is higher than the abundance of the stars by up to 0.3 dex. An outlier to this relation, given its peculiar formation already unraveled, is the galaxy IC1182:[S72]d, for which the derived stellar metallicity is higher than the gaseous one. Whether these two behaviors, shown in Figure 3.24, result from different chemical evolutionary paths or rather reflect the environmental impact of the cluster remains to be disentangled.

3.11 Environmental effects on the chemical enrichment of Hercules star-forming galaxies

In this chapter we have searched for possible observable imprints of the cluster environment on the metallicity and the chemical history of a sample of SF galaxies in the Hercules cluster. Most of our sample galaxies are located within the central region of the Hercules cluster ($< R_{200}$) where the cluster potential is expected to be steep, the ICM is measurable and most of the physical mechanisms proposed above are effectively at work. We have examined the metal content of our sample galaxies as a function of local density, stellar mass, luminosity and chemical evolution. On the basis of this analysis, three main subgroups of objects have emerged: 1) the more massive SF galaxies (including all spirals), 2) the set of dwarf/irregulars labeled "newcomers" in Section 3.9 and 3) a group of more chemically evolved dwarfs residing at the highest local densities observed in our sample. In addition, three dwarf/irregular galaxies SDSSJ160524.27+175329.3, SDSSJ160556.98+174304.1 and LEDA084724, could not be fully adscribed to any of these groups (see the Appendix A.2).

Massive galaxies ($M_{\rm B} \leq -19$) follow the global MZR/LZR, though they present evidences of being affected by the cluster environment, judging from their Hα structure/morphology and their abundance gradients. Most spirals in Hercules show Hα emission (see Hα maps in C09) less extended than their optical disks and sometimes offset from the center of the stellar continuum. This can be an evidence for truncation of ionized gas in the disks of these cluster spirals, since we observe star formation occurring mostly in the inner parts. Gas removal from the outer parts of cluster spirals is believed to be a consequence of the ISM-ICM interaction. This effect has been observed e.g. in the Virgo cluster spirals by Koopmann & Kenney (2004), where over half of their Virgo sample show truncation of the star formation in the disks. In fact, RPS could be effective on our Hercules spirals since all are located within R_{200}.

The oxygen abundances derived for massive galaxies are close to solar, and for the more Hα extended spirals, mild or flat O/H abundance gradients have been obtained, a result in the line of previous findings by Skillman et al. (1996) for Virgo spirals. In contrast, for the N/O ratio even oversolar values have been measured for the central part of some galaxies, showing prominent N/O spatial variations;

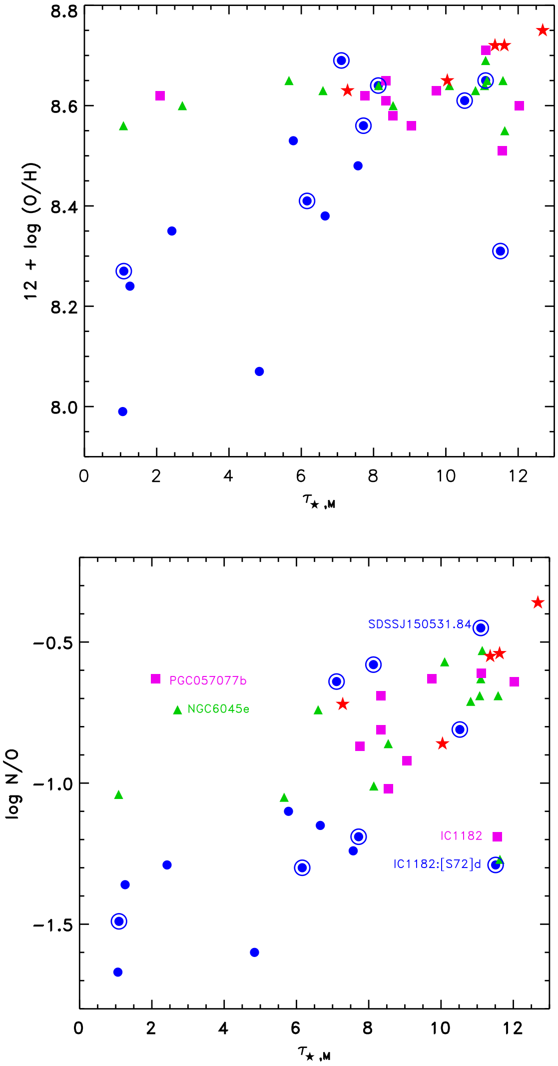

Figure 3.23: The gas-phase oxygen abundance (upper panel) and N/O ratio (lower panel) vs. the mass-weighted stellar age $\tau_{\star,M}$ as given by STARLIGHT model fitting (colors and symbols as in Figure 3.19). An overall positive trend can be seen (see the text for details).

this picture could result from the effect of gas infall in the center of these galaxies, suffering the action of the ICM (Vollmer et al. 2001). Such infall would dilute the abundance at the central parts of the galaxies flattening the O/H gradient, while the N/O ratio is not expected to be affected. Overall, the question which remains to be explored is whether these spirals are chemically evolved because they reside in such high density environments or we are just observing an effect of the morphology density relation (Dressler 1980). Further observations are needed to answer this question.

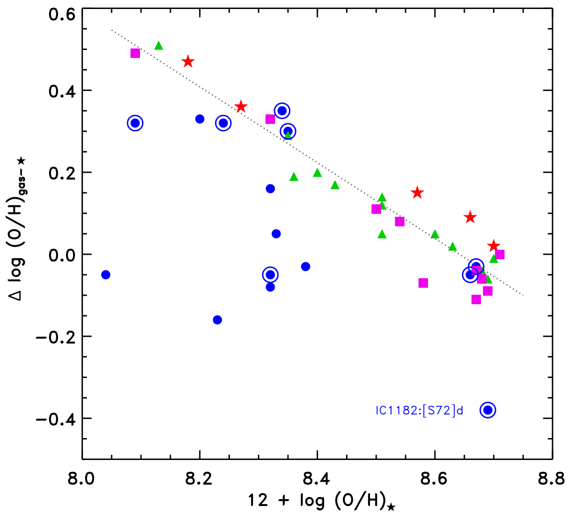

Figure 3.24: The difference between gas-phase and stellar oxygen abundances vs. stellar oxygen abundance 12+log(O/H)$_\star$ derived from the STARLIGHT mass-weighted stellar metallicity $Z_{\star,m}$ (colors and symbols as in Figure 3.19).

Regarding the dwarf/irregular galaxies, they appear to form two main groups with substantial differences as it has emerged in the previous sections. Overall, all the dwarfs present similar levels of SFR as derived from their Hα luminosities. The group of "newcomers" are metal poor dwarfs, they present a young stellar population (Figure 3.23), and their stellar and gas metallicities are similar (Figure 3.24). They avoid the highest local densities (Section 3.7), appear located close to the boundaries of the X-ray cluster core and show "bow-shock"/offset Hα morphologies. These structures host intense bursts of star formation, possibly tracing the contact discontinuity of the ISM of the galaxy with the X-ray emitting ICM, an observable signature of pressure-triggered star formation. Though, the "newcomers" follow the "closed-box" model predictions, suggesting that RPS has not yet substantially reduced their HI gas. Ram-pressure stripping is expected to act on a time-scale $\sim 5 \times 10^7$ yr (Abadi et al. 1999), while typical HII regions lifetimes are $\sim 5 - 10 \times 10^6$ yr. Based on this scheme we should conclude that the "newcomers" are those dwarfs observed right on time when they are set to fire by their first encounter with the ICM; before removal of the galactic gas is accomplished by the ICM and prior to subsequent quenching of star formation rendering them undetectable in Hα.

The majority of the dwarf/irregulars populating the highest local densities of our sample ($\log \Sigma_{4,5} > 1.85$) show higher metallicities for their mass and luminosity and they appear located above the overall MZR and LZR (see Figures 3.19,3.20). Their gaseous and stellar abundances differ by up to $\sim$ 0.3 dex, pointing towards a dominant old stellar population. Indeed, as seen in Figures 3.23 their stellar population presents ages exceeding $\sim$ 6 Gyr. These galaxies have been also found close to the X-ray cluster core, but their Hα morphologies do not suggest ISM-ICM interaction. However we can not discard they could have been possibly affected by RPS. Although HI masses are not available for the vast majority of these objects, if we assume an HI mass upper limit for them as in Section 3.9, many of these galaxies would be shifted in Figure 3.22 out of the canonical “closed-box” model, towards the zone of HI deficiency.

We have seen that high local density is a key parameter that separates this group of chemically evolved dwarfs from the rest of the dwarfs. At these high density environments pre-processing has been claimed to operate under the combined action of tidal forces among group members and the ram-pressure by the ICM (Cortese et al. 2006). We suggest that these dwarf galaxies –over-metallic for their mass– could originate from enriched material stripped by tidal forces among group members, as it has been suggested for the group of galaxies falling into Abell 1367 by Cortese et al. (2006). Indeed we have identified a good number of these more metallic dwarfs affected by tidal interactions.

Mahajan et al. (2011) have found two sets of blue dwarf galaxies with different Hα emission properties in the Coma supercluster, presenting strong environmental dependence. These authors suggest that the more evolved dwarf population could be the progenitors of passive dwarf galaxies seen in the centers of clusters. The two dwarf galaxy groups we have identified in Hercules could match this scheme.

3.12 Summary

The Hercules cluster is one of the most exciting nearby dense environments, showing abundant sub-structures unraveled in X-ray emission and broad-band imaging. This cluster constitutes an ideal laboratory to explore the effects of the environment on galaxy evolution. We have studied the environmental effects on the metallicity and the chemical evolution of 31 SF cluster galaxies.

Spatially resolved spectroscopy has been obtained for a sample of SF galaxies and spectral synthesis model fitting has been performed for all the spectra analyzed in order to provide an effective correction of the underlying stellar absorption on emission line spectra, as well as to derive the characteristic properties of the galaxy stellar populations. Line fluxes and chemical abundances of O/H and N/O have been obtained for all the galaxies, and whenever possible for different part of galaxies, of the sample.

The main conclusions of this work can be summarized as follows:

1. From the study of the metallicity vs. galaxy local density we have seen a dual behavior separating the dwarfs from the more luminous galaxies. The luminous galaxies have metallicities $\sim Z_{\odot}$ and reside at all densities studied in this work. The set of dwarfs found at higher local densities ($\log \Sigma_{4,5} > 1.8$) are found to be more metallic ($12 + \log(\mathrm{O/H}) > 8.4$) while the observed less metallic dwarfs ($12{+}\log(\mathrm{O/H}) < 8.4$ are found preferentially at lower densities and some of them seem to be “newcomers" to the cluster.

2. We have found that our sample of Hercules SF galaxies shows well defined sequences of blue luminosity vs. metallicity and stellar mass vs. metallicity (using both O/H and also the N/O ratio), following the general behavior found for SF galaxies. Besides this global behavior, we have found that dwarf/irregular galaxies populating the densest regions seem to crowd the upper part of the global sequences, thus providing a source of the dispersion observed in these relations. These more metallic dwarfs could be parts of more massive galaxies, fragmented by tidal interactions among group members.

3. Most of the luminous galaxies are chemically evolved spirals with oxygen abundance close to solar and truncated disks of ionized gas, possibly by the action of RPS. From our spatially resolved spectroscopy we have found that the Hα extended spiral galaxies present shallow oxygen abundance gradients, an expected result of possible gas infall at their centers. For the N/O ratio, even oversolar values have been obtained for the central parts of some galaxies and a significant spatial variation has been observed.

4. A detailed study of the chemical history of the sample galaxies has been performed, combining information on their gas-phase abundances, HI content and stellar mass. Most of the dwarf galaxies with available HI mass seem to be "newcomers" to the cluster and appear consistent with the predictions of the closed box model. This fact agree with the scenario that these galaxies experience a pressure-triggered starburst, right before the RPS privies them from their gas component. The rest of the galaxies with HI measurement on average show lower values of gas fractions, though most of them are still consistent with the loci defined by samples of field galaxies.

5. The properties of the underlying stellar population, such as stellar age and stellar metallicity, have been explored and compared with the gas-phase metallicity. The "newcomers" dwarfs present a young stellar population and their stellar and gas metallicities are similar. The more metallic dwarf galaxies host an old stellar population, resembling to the evolved blue dwarfs refered by Mahajan et al. (2011). An overall positive trend has been found in the gas-phase oxygen abundance vs. the mass-weighted stellar age $\tau_{\star,M}$, which becomes more prominent in the case of the N/O ratio.

CHAPTER 4

Star-formation and chemical history in the large-scale structure of the Hercules Supercluster

---

Contents

4.1 Introduction

In the previous chapter we have studied the central part of A2151 and in the variety of its ecosystem we have seen galaxy-galaxy interactions, galaxy ISM-ICM interactions and tidal dwarf galaxy candidates. We have found that the local environment of a galaxy is one of the key parameters that help to understand the chemical history, in agreement with previous results (e.g. Ellison et al. 2009; Cooper et al. 2008). The exciting environment of A2151 justifies a study of larger spatial coverage, sampling the outskirts and the infalling regions of the cluster. In this large scale-region we encounter other two clusters A2152 and A2147, projected very close and possibly overlapping in the plane of the sky. These three clusters are the main components of the Hercules supercluster (HSC), a large-scale structure at a distance of $\sim$ 160 Mpc, that covers an area of 22.5 deg^2 in the sky (Barmby & Huchra 1998).

The environmental impact on galaxy evolution is expected to be magnified in a supercluster environment, where groups and clusters are in the course of merging, and individual galaxies are also incorporated, at high infall velocities, possibly through large-scale filaments. Cluster mergers can drive abnormal rates of galaxy evolution, both during the pericentric passage and at the shock fronts produced by these major mergers (Roettiger et al. 1996; Bekki et al. 2010). Additionally, a statistical enhancement of the SFRs of galaxies in local Universe filaments has been observed (Mahajan et al. 2010; Porter et al. 2008) suggesting the effect of ram-pressure triggered star formation (see Section 1.2.1), as there should be a significant number of galaxies encountering the hot ICM for the first time. Thus, for the purpose of the present thesis, the study of the massive and dynamically active system of the HSC presents ultimate interest.

A2151 is the richest among the three clusters and shows a wealthy sub-structure. Bird et al. (1995) using optical and X-ray data suggested the presence of at least three distinct subclusters, the central A2151C, eastern A2151E and northern A2151N, see also Figure 3.2. These authors suggested that the A2151E and A2151C subclusters have recently undergone a merger event. Additionally, they suggested that there are two subgroups in A2151C, defined by their different velocity distributions, one possibly originating from A2151N via infall. The X-ray emission is associated with these two galaxy groups in the central subcluster (Figure 2.10).

High-quality X-ray data from Chandra reveal (Hudson et al. 2010) that the X-ray peak of A2147 matches with the position of the BCG, the northernmost of the three bright galaxies forming a line in the core of the cluster. The X-ray properties of this cluster indicate that this could also be a merging cluster (Hudson et al. 2010; Sanderson et al. 2006). A2152, in turn, shows very low X-ray emission. Nevertheless previous kinematic studies have claimed a strikingly high velocity dispersion for this cluster ($>$700 km s^{-1}, e.g., Barmby & Huchra 1998; Zabludoff & Franx 1993).

In the optical, several works have studied the galaxy distribution of A2151 (Maccagni et al. 1995; Bird et al. 1995; Sánchez-Janssen et al. 2005); however, the supercluster region has not gathered so much attention. As a matter of fact, the last study of the dynamical state of the supercluster, performed by Barmby & Huchra (1998), involved 414 galaxies with velocity information.

In this chapter we take advantage of the SDSS database to create a larger census of galaxies in the HSC region, and study the SFH and the metallicity of SF galaxies as a function of the large-scale structure. We note that at the HSC distance, the 3 arcsec of the SDSS fiber correspond to $\sim$2.5 kpc, sampling a significant part of the central galaxy region. Additionally the [O II]λ3727 emission line, redshifted to the redshift of HSC, enters the wavelength range covered by SDSS spectroscopy. This permits to obtain accurate metallicities of SF galaxies using most recent calibrations including those based on the indicator R_{23} (See Section 1.3.1).

Besides the unprecedented number of galaxies with spectroscopic data in SDSS for the HSC region, for the purpose of this study we take advantage of a further improvement. After we have completed the work discussed in the previous chapter, there has been a new data release (DR8) of SDSS, which provides new emission line measures (Tremonti et al. 2004; Brinchmann et al. 2004), derived after correcting the spectra for the underlying stellar continuum, using the high-resolution population synthesis models of Bruzual & Charlot (2003). This is basically the same we did for our long-slit sample in Section 3.5, and provides an important step for the kind of analysis we do here. We know that Balmer emission lines can be severely affected by the absorption of the underlying stellar component (e.g., Martín-Manjón et al. 2008, 2010) and this would affect the derived values of the reddening coefficient, the line fluxes and indices and, as a consequence, the SFH and gas-phase metallicity. This effect is expected to be negligible after the correction, allowing a reliable study of the galaxies' gas chemical abundances.

4.2 The large-scale structure of the Hercules Supercluster

In this work we consider the HSC region, comprising 22.5 deg^2 as defined by Barmby & Huchra (1998): 239.0<R.A.<243.6 deg, 14.35<DEC.<19.34 deg, in a redshift range $0.0283 < z < 0.0483$. In this region, we find 1379 galaxies with SDSS-DR8 spectroscopic data. In Figure 4.1 we give the 2D position map of all the galaxies in the field, color coded to their radial velocities. The overposed squares indicate regions of 1.6×1.6 deg^2 around the center of each cluster in this region: A2151, A2152, and A2147. Based on the cluster velocity dispersions derived by Barmby & Huchra (1998) (705, 715, 821 km s^{-1}, for A2151, A2152, and A2147 respectively), these square regions would correspond to a region $\sim 4R_{200}$ across (from Equation 2.1), around each cluster center.

In Figure 4.1 we see that, in projection, the $4R_{200}$ square regions of A2151 and A2147 are separated, while the region of A2152 overlaps with the other two. In the 3D space, however, A2152 is located in the background, as indicated by the higher value of its mean redshift, illustrated by the red/orange points that dominate in this region in Figure 4.1. Previous works (Barmby & Huchra 1998; Tarenghi et al. 1980) have pointed out the difficulty to unequivocally assign the galaxies to each of the three clusters. However, our large sample of galaxies with redshift (1379) put us in an optimal position to perform this classification.

For this purpose we perform a 3D consideration, taking into account the distribution of galaxies in the position and velocity space. Initially we consider galaxies within the square regions indicated in Figure 4.1, forming three groups. In Figure 4.2 we plot the velocity distributions of the galaxies of each group, corresponding to each one of the three regions. The velocity distribution of a separate dynamical entity is composed of a single Gaussian, and we see that a well behaved velocity distribution appears around the mean cluster velocity for each cluster region. Particularly, in the region of A2152, two separated distributions appear, indicating that two dynamically separated systems are projected on the sky.

We perform Gaussian fits to the velocity distributions of the three regions and we assign to each cluster the galaxies that have a radial velocity within $v_{clus} \pm 3\sigma_v$, where v_{clus} is the mean cluster velocity and σ_v is the dispersion for each cluster given by the fits. The radial velocity range considered for each cluster is indicated by crosses on the distributions of Figure 4.2. Under these constraints, no galaxy is

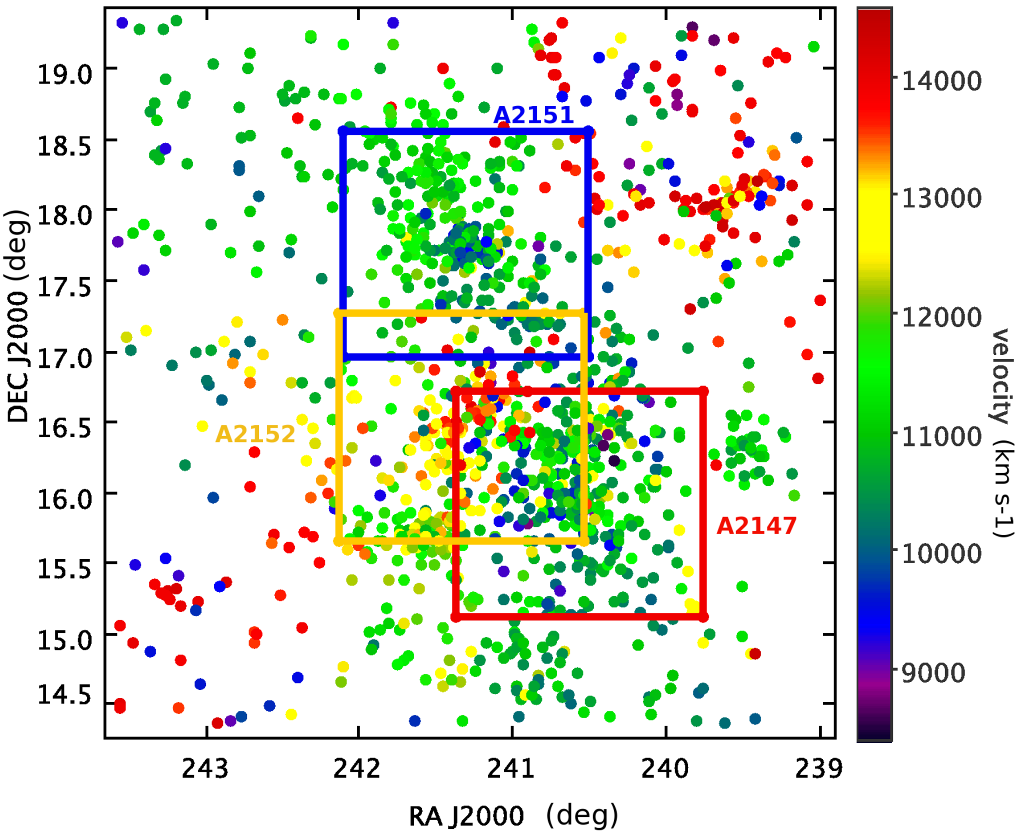

Figure 4.1: 2D position map of all the galaxies in the Hercules supercluster field, color coded to their radial velocities. Square zones indicate regions $\sim 4R_{200}$ across around the center of each cluster: A2151 (blue), A2152 (yellow), A2147 (red).

assigned to two clusters simultaneously. The majority of the galaxies that form the left peak of the velocity distribution in zone of A2152 (overploted in the histogram in red), have been assigned either to A2147 or to A2151. The galaxies of the HSC that are not assigned in neither of the three clusters are labelled "DISP" standing for "dispersed component".

In Table 4.1 we give the name of the cluster (column 1), the coordinates of the cluster center (columns 2, 3), the scale at the distance of each cluster (column 4), the mean radial velocity (column 5) and velocity dispersion (column 6) derived in this work, as given by the Gaussian fit. Column 7 and 8 give the R_{200} and cluster mass derived using Equations 2.1 and 2.2. In column 9 we give the total X-ray luminosities taken by Ledlow et al. (2003).

We note that the velocity dispersion we derive for A2152 is significantly different

Table 4.1: **Properties of the clusters in the HSC**

Cluster (1)	R.A. J2000.0 (2)	DEC. J2000.0 (3)	Scale Mpc deg^{-1} (4)	$v_{\rm clus}$ km s^{-1} (5)	σ_v km s^{-1} (6)	R_{200} Mpc (7)	M_{cl} ($M_\odot$) (8)	L_X (10^{43} erg s^{-1}) (9)
A2151	16 05 15.0	17 44 55	2.76	10972	801	1.37	6.1×10^{14}	1.60 ± 0.10
A2152	16 05 22.4	16 26 55	3.08	13255	359	0.61	5.5×10^{13}	0.28 ± 0.07
A2147	16 02 17.2	15 53 43	2.65	10741	628	1.07	2.9×10^{14}	3.00 ± 0.12

Note. Column 1: cluster name; column 2: right ascension of the cluster center as given in NED (Abell et al. 1989) in hours, minutes, seconds; column 3: declination of the cluster center as given in NED (Abell et al. 1989) in degrees, minutes, seconds; column 4: cluster scale as given in NED; column 5: mean cluster velocity $v_{\rm clus}$ derived by the Gaussian fit; column 6: σ_v derived by the Gaussian fit; column 7: R_{200}; column 8: cluster mass; column 8: *ROSAT* total X-ray luminosity in units 10^{43} erg s^{-1} (Ledlow et al. 2003).

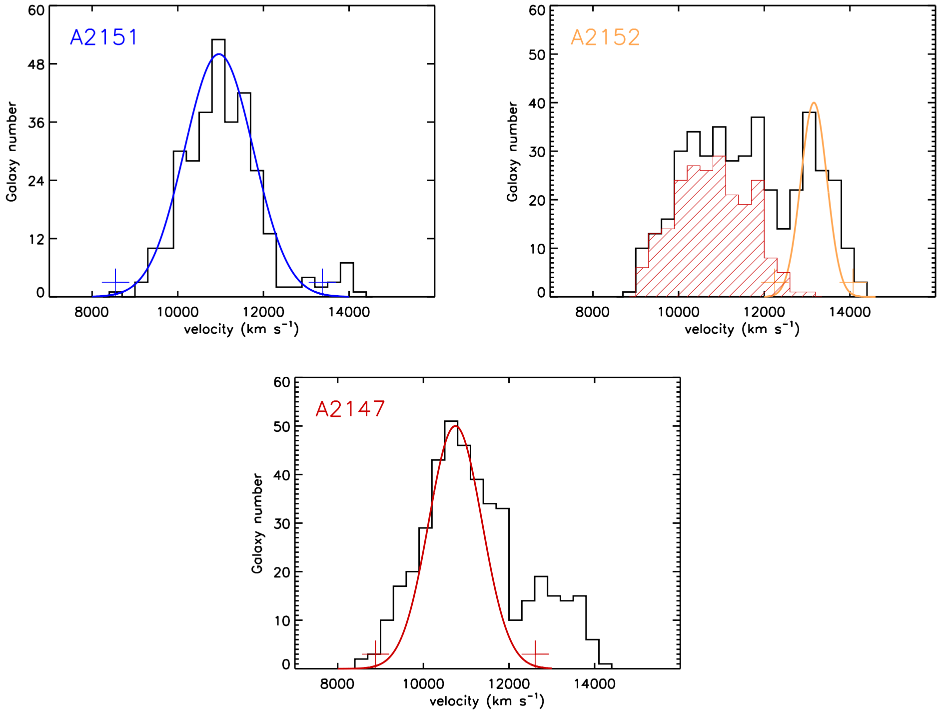

Figure 4.2: Velocity distributions for the galaxies located in the three regions indicated in Figure 4.1. In each region a well behaved Gaussian velocity distribution appears around the mean radial velocity for each cluster. We perform Gaussian fits to define the mean cluster velocity and velocity dispersion. In the region of A2152, the left part of the distribution is principally due to galaxies that are assigned to A2147 or A2151 (overploted in red). We assign to each cluster the galaxies with radial velocity within $v_{clus} \pm 3\sigma_v$, where v_{clus} is the mean cluster velocity and σ_v is the dispersion for each cluster given by the fits. The crosses indicate the range $v_{clus} \pm 3\sigma_v$.

from the values derived previously (see e.g. Barmby & Huchra 1998); however, the sample of galaxies used by these authors was very limited, and possibly, in their considerations, A2152 was biased by galaxies belonging to A2151 and A2147. The value derived here implies that A2152 is a cluster of much lower mass, in agreement with the low level of X-ray emission of this cluster.

4.3 Star formation activity in the Hercules Supercluster

Starting with the spectroscopic sample of all galaxies with SDSS spectroscopy in the HSC region, and based on our 3D analysis to assign galaxies to A2151, A2152, A2147, and DISP, we study now their galaxy populations. We use the emission line measures (Tremonti et al. 2004; Brinchmann et al. 2004), the BPT (Baldwin et al. 1981) diagram classification and the median estimate of the total stellar mass of

Table 4.2: **Galaxy populations in HSC field**

Cluster	Assigned	SF %	LM %	LM SF %	AGN %	AGN+C %
A2151	300	55	56	75	14	20
A2151 $R \leq R_{200}$	182	50	52	71	14	20
A2152	135	53	50	75	10	15
A2152 $R \leq R_{200}$	27	33	37	50	11	11
A2147	348	34	56	46	7	12
A2147 $R \leq R_{200}$	147	24	52	32	5	7
DISP	569	59	54	80	11	19

Note. Column 1: cluster name; column 2: number of galaxies assigned to each cluster and the dispersed component DISP; column 3: ratio of SF galaxies; column 4: ratio of low-mass galaxies with $\log(M_\star/M_\odot) < 10.$; column 5: ratio of SF over the total low-mass population; column 6: ratio of AGN galaxies; column 7: ratio of AGN and composite galaxies.

the galaxies (derived using spectral fitting, see Kauffmann et al. 2003). We have found that the SDSS DR8 galaxy mass estimate is consistent with the mass we derived using the k-correct algorithm (Blanton & Roweis 2007). Considering SDSS upper magnitude limit $r = 17.77$ mag and approximately $m - M = 36.0$ mag at the HSC distance, our sample is limited to galaxies brighter than $M_r = -18.23$ mag, which corresponds $\sim \log(M_\star/M_\odot) > 8.5$. A close inspection of the sample has been performed to exclude galaxies with problematic photometry.

In Table 4.2, we give the name of each component (column 1) and the number of galaxies assigned (column 2). In column 3 we give the fraction of SF galaxies. Here we select SF galaxies as those having flag 1 and 2 on the BPT SDSS classification. In column 4, we give the fraction of low-mass galaxies, adopting the criterion for stellar mass of a dwarf $\log(M_\star/M_\odot) < 10$. For HSC a mass limit is more appropriate than a cut in luminosity, as the different components span a wide range in radial velocity dispersion. In column 5 we give the fraction of low-mass galaxies that are SF in each cluster. Column 6 and 7 give the fractions of AGN, and AGN plus composite (flagged 4 and 3 respectively in BPT SDSS classification). Additionally in Table 4.2 we include the number of assigned galaxies, located within a distance $R < R_{200}$ from each cluster center, considering the new R_{200} that we derive here (Table 4.1, column 7) and the above mentioned fractions for these three cluster-core ($R < R_{200}$) galaxies.

We see that A2147, being the cluster with higher X-ray emission, hosts the lowest fraction of SF galaxies in agreement with previous results quoting increasing fractions of passive galaxies with increasing cluster mass (e.g. Poggianti et al. 2006). The quenching of star formation in A2147 is highlighted when considering the low-mass galaxy population. Although we find a high fraction of $> 75\%$ of low-mass SF galaxies in A2151, A2152 and DISP, in A2147 we find only a 46 % of low-mass SF galaxies.

In turn, we see that A2151 hosts a very active SF population, even within the cluster core: inside the R_{200} region 50% of the A2151 selected galaxies are SF, compared to 33% and 24% of A2152 and A2147 respectively. The same holds for the low-mass population which is SF in 71% (versus 50% and 32% in the other two clusters). A higher fraction of late-type galaxies in A2151 compared to the other two clusters of the HSC has been remarked already by Tarenghi et al. (1980). Due to their limited sample (124 galaxies in HSC), these authors considered A2152 and A2147 a merging, non-relaxed system, and reached the striking conclusion that the early type galaxies were dominant in such an environment, and lacking from the "relaxed" (for them) A2151 cluster.

Finally, we see that the AGN fraction drops in clusters A2147 and A2152 as compared to that of A2151 and DISP. This result is in agreement with the results of Hwang et al. (2012), who have found that the AGN fraction decreases in clusters, and there is an anti-correlation between the AGN fraction and the velocity dispersion of clusters. A2151 shows a higher fraction of AGNs, but as already discussed in Chapter 3, due to the peculiar evolutionary status of this cluster (Bird et al. 1995), we encounter there a large number of galaxy-galaxy interactions and mergers, these being possible drivers of AGN formation according to Hwang et al. (2012).

The differences in the galaxy populations, assigned into the different components of the HSC, are evident also in Figure 4.3. The left plots are the normalized $g-i$ color distributions, and the right plots are the same considering only the low-mass galaxies. In the left plots, A2151 and DISP show a two-peaked distribution, with a relevant secondary peak to $g-i \simeq 0.7$ mag, while A2147 hosts a somewhat more suppressed population of blue galaxies. In the right plots we see that for DISP the peaks of the distribution are reversed, and blue dwarfs are dominant. A2152 and A2147 appear to follow the general trend found in clusters, with a dominant early-type population even for the low-mass galaxies, while A2151 hosts approximately similar fractions of blue and red dwarfs. KS tests show that the A2151 and A2152 $g-i$ distributions show more than 50% probability to be similar (for both all galaxies and low-mass galaxies); for all the remaining combinations the probability is null.

In the upper left plot of Figure 4.4 we show the radial profile of the mean log $EW(\mathrm{H}\alpha)$[1] for all assigned galaxies in A2151 (blue), A2152 (yellow), A2147 (red) and in the upper right plot we show the same, but considering only actively SF galaxies adopting the criterion $EW(\mathrm{H}\alpha)>2$ Å (Haines et al. 2007; Rines et al. 2005). It is worth noting that our Hα measurements are already corrected for the underlying absorption, thus the criterion adopted is appropriate for the selection of galaxies with high SFRs. The cluster-centric distance is given in R_{200} units and the error bars represent the standard error of the mean.

The lower plots of Figure 4.4 depict the average $EW(\mathrm{H}\alpha)$ as a function of the

---

[1] We derive $EW(\mathrm{H}\alpha)$ from the stellar absorption corrected Hα flux and the adjacent continuum as provided in DR8.

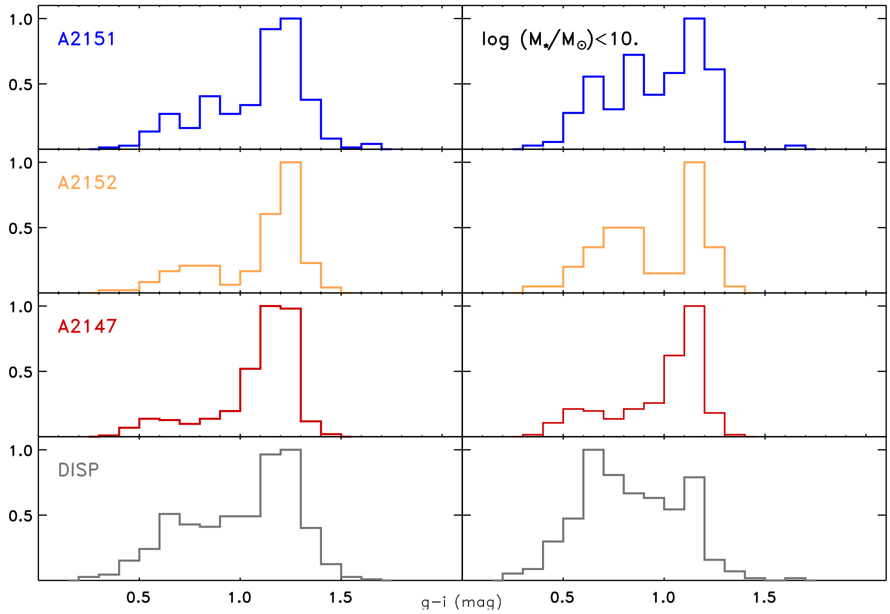

Figure 4.3: Left: Color $g-i$ normalized histogram of the galaxies in A2151 (blue), A2152 (yellow), A2147 (red), and the dispersed component (DISP, grey). Right: The same, considering only low-mass galaxies with $\log(M_{\star}/M_{\odot}) < 10$.

local galaxy density $\Sigma_{4,5}$, again for all assigned galaxies (left) and for actively SF with EW(Hα)>2 Å (right). $\Sigma_{4,5}$ is the density estimator we have defined in Chapter 3, given in Mpc^{-2}, derived from the average of the projected distances to the fourth and fifth nearest neighbor (Equation 3.2). We note that we have considered the different distance modulus of each cluster. Additionally, for A2151 and A2147, the neighbors considered are those presenting a difference in radial velocity smaller than 2000 km s^{-1}, and for A2152 the velocity window we allow is 1000 km s^{-1} ($\sim 3\sigma_v$). Here again the error bars represent the standard error of the mean.

In the left column plots of Figure 4.4 we see that the average EW(Hα) drops smoothly both as a function of cluster-centric distance and as a function of local galaxy density for all three clusters of our sample. Previous works (e.g. Rines et al. 2005; Balogh et al. 2004; Lewis et al. 2002) have explored the fraction of SF galaxies as a function of both cluster-centric distance and local galaxy density, in low-redshift clusters, obtaining clear trends of the same kind, representing a star-formation-density relation. Furthermore, Lewis et al. (2002) have argued that the star-formation-density relation is not a simple expression of the morphology-density relation (Dressler 1980), as galaxies in dense regions show lower SFRs than field galaxies of the same morphological type.

In the left column plots of Figure 4.4 we see that the average EW(Hα) drops smoothly both as a function of cluster-centric distance and as a function of local galaxy density for all three clusters of our sample. Previous works (e.g. Rines et al. 2005; Balogh et al. 2004; Lewis et al. 2002) have explored the fraction of SF galaxies

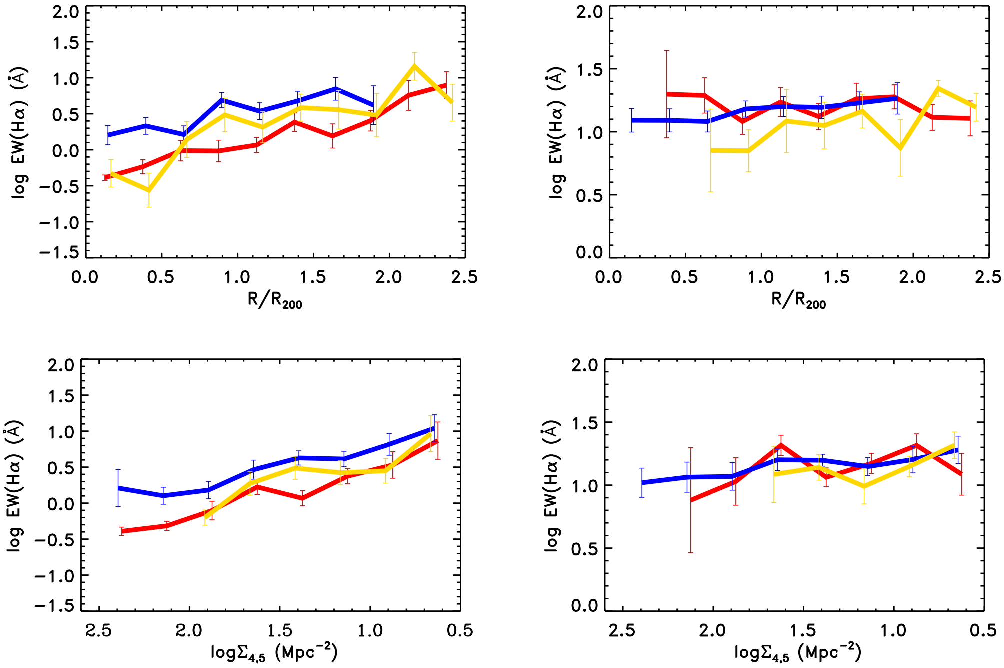

Figure 4.4: Upper panels: Radial profiles of the mean log EW(Hα) for all (left) assigned galaxies in A2151 (blue), A2152 (yellow), A2147 (red) and for SF galaxies with EW(Hα)>2 (right). Lower panels: The same as a function of local galaxy density $\Sigma_{4,5}$. In all plots, the error bars represent the standard error of the mean.

as a function of both cluster-centric distance and local galaxy density, in low-redshift clusters, obtaining clear trends of the same kind, representing a star-formation-density relation.

Remarkably, A2151 shows clearly higher values than the other two clusters in these left column plots, and even a slight enhancement at very high local densities. We have already shown above that A2151 hosts active SF galaxies in its very central parts, where the local density is also highest, a characteristic feature proper to its early stage of development (see Section 2.1 and Figure 2.4) that we have discussed further in Chapter 3 (Section 3.11).

Although this general behavior is dominated by the fact that early-type galaxies are dominant in the center of the clusters (Dressler 1980), Lewis et al. (2002) have argued that the star-formation-density relation is not a mere expression of the morphology-density relation, as galaxies in dense regions show lower SFRs than field galaxies of the same morphological type. To disentangle from the general trend the effect of the environment on the present SFR, only SF galaxies should be considered. In this context, Reverte (2008) have shown that the distributions of the $EW(\mathrm{H}\alpha)$ between cluster and field SF galaxies are different (see Figure 2.12) and Gavazzi et al. (2002) have found a clear drop of the mean $EW(\mathrm{H}\alpha)$ for luminous SF galaxies in the Virgo cluster. Thus, dense environments should suppress the SFR of galaxies, and this has been attributed to the effect of gas removal, principally due to RPS (and starvation, see Lewis et al. 2002).

In this context, in the right column of Figure 4.4 we explore the average log $EW(\mathrm{H}\alpha)$ only for actively SF galaxies. The interesting feature is the lack of actively SF galaxies (with $EW(\mathrm{H}\alpha){>}2$ Å) in the regions of the smaller cluster-centric distance and of the higher galaxy density for A2152 and A2147, in contrast to A2151 that host SF galaxies right in the center. The active SF population (with $EW(\mathrm{H}\alpha){>}2$ Å) of all three clusters is dominated by low-mass galaxies to a 70%, and this could explain why we do not observe any significant dependence, within the errors, neither on cluster-centric distance (top) nor on local galaxy density (bottom). Gavazzi et al. (2002) did neither find a radial trend of the SFR in Virgo, when only low-luminosity galaxies where taken into account; these authors concluded that this is consistent with the picture of ongoing infall of low-mass galaxies onto rich clusters.

These findings are reproduced in Figures 4.5, 4.6, and 4.7, where we show the 2D color $g-i$ maps (left) and the log $EW(\mathrm{H}\alpha)$ maps (right) of the 1.6×1.6 deg^2 region around A2151, A2152, and A2147 cluster center, as indicated in Figure 4.1. In the upper panels we include all the assigned galaxies for each cluster and in the lower panels just the low-mass population ($\log(M_\star/M_\odot) < 10.$). The maps have been produced performing a grid of 22 kpc pixel size over the 1.6×1.6 deg^2 regions ($\sim 4.4 \times 4.4$ Mpc^2), and kriging interpolation. Thus galaxy data (color and $EW(\mathrm{H}\alpha)$) as well as their spatial variance determine trends which are applied to the grid points. Finally it has been applied a smoothing in radius of 250 kpc.

The color map of A2151 (upper left panel of Figure 4.5) illustrates nicely the clumpiness of A2151 in the direction East-West, following its X-ray morphology showed in Figure 2.8 and the results of Bird et al. (1995). The color map of the low-mass galaxies (lower left) shows that the fraction of blue low-mass galaxies even within the R_{200} region of A2151 is elevated.

An interesting feature unraveled in the 2D $EW(\mathrm{H}\alpha)$ map of A2151 (upper right panel of Figure 4.5) is the presence of a blue “stream” entering into the cluster from the North, indicating the presence of a filament of galaxies with high $EW(\mathrm{H}\alpha)$ entering the cluster environment and reaching up to the cluster center. Bird et al. (1995) also suggested an infall of galaxies from the North, as they found that a subgroup identified in the North, on the basis of the velocity distribution of A2151, did not show X-ray emission. They interpreted this result as this feature not being a physically distinct substructure, yet an infall population along a filament. The lower right panel suggests that this northern filamentary structure is dominated by low-mass galaxies, for which it appears to be more spatially expanded.

A2152 and A2147 color maps show a lack of blue galaxies inside the clusters’ R_{200} radius, resembling more virilized structures. South-East of A2147 there appears to be a filamentary structure with relative higher fraction of blue low-mass galaxies with high EWs, entering to the cluster’s R_{200} region, possibly indicating an area of infall of low-mass galaxies.

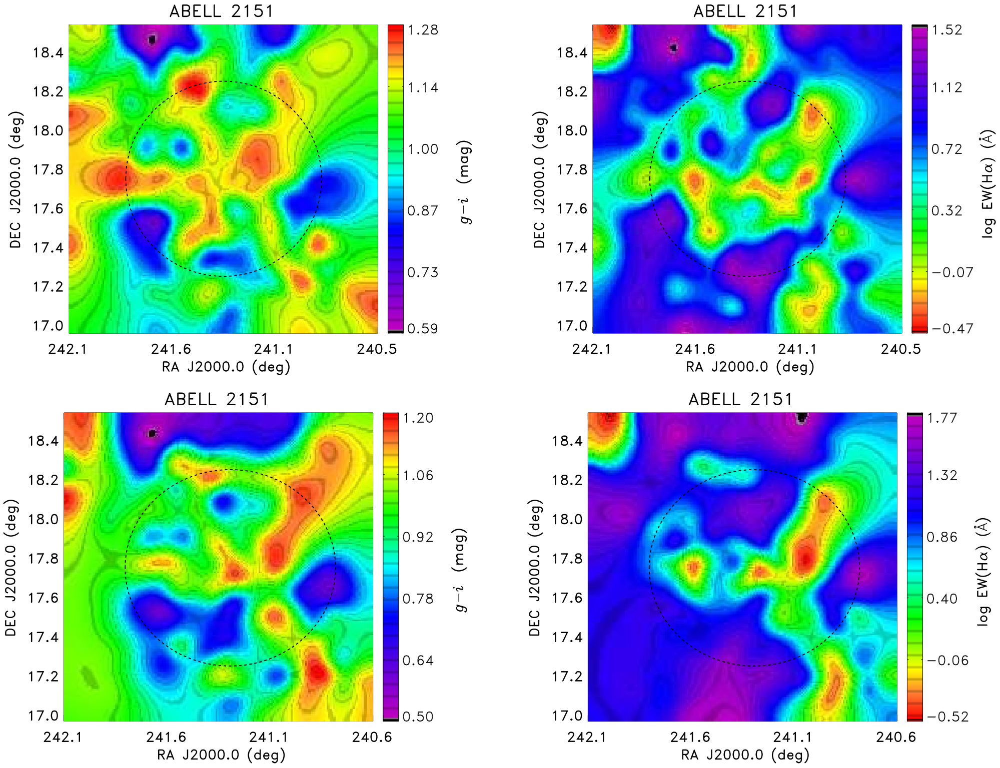

Figure 4.5: 2D color $g-i$ map (left) and log EW(Hα) map (right) in a region of 2.56 deg^2 around A2151, including all galaxies (upper panels) and only low-mass galaxies ($\log(M_\star/M_\odot) < 10.$) in the lower panels. The cluster radius R_{200} is indicated by a dotted circle.

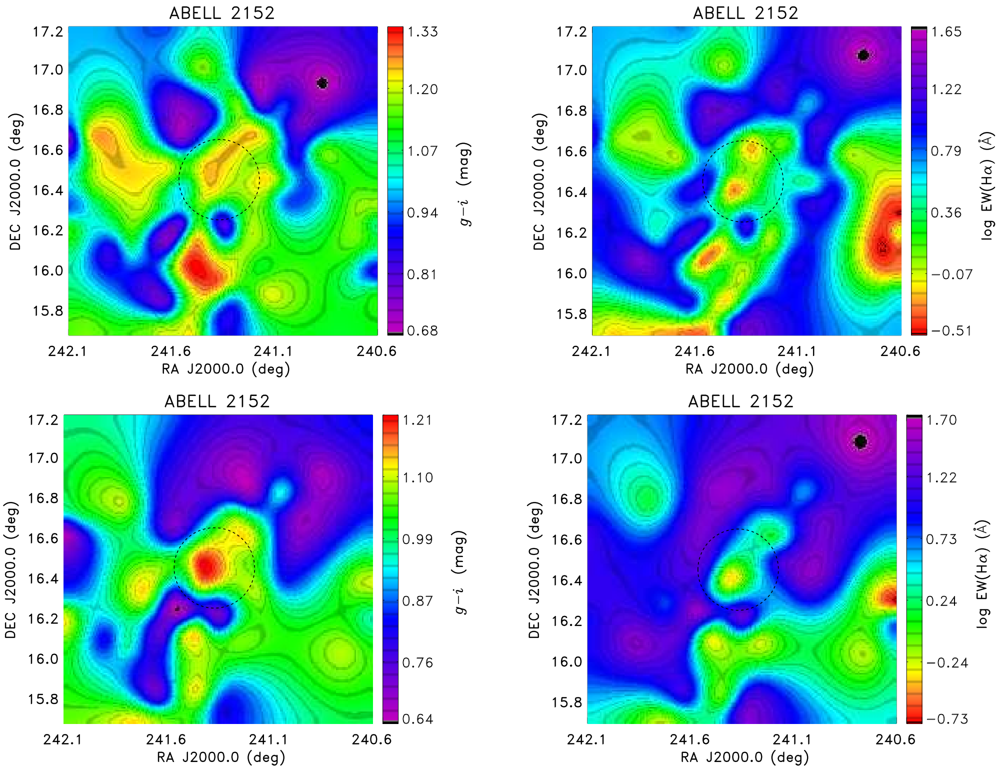

Figure 4.6: The same as in Figure 4.5 for A2152.

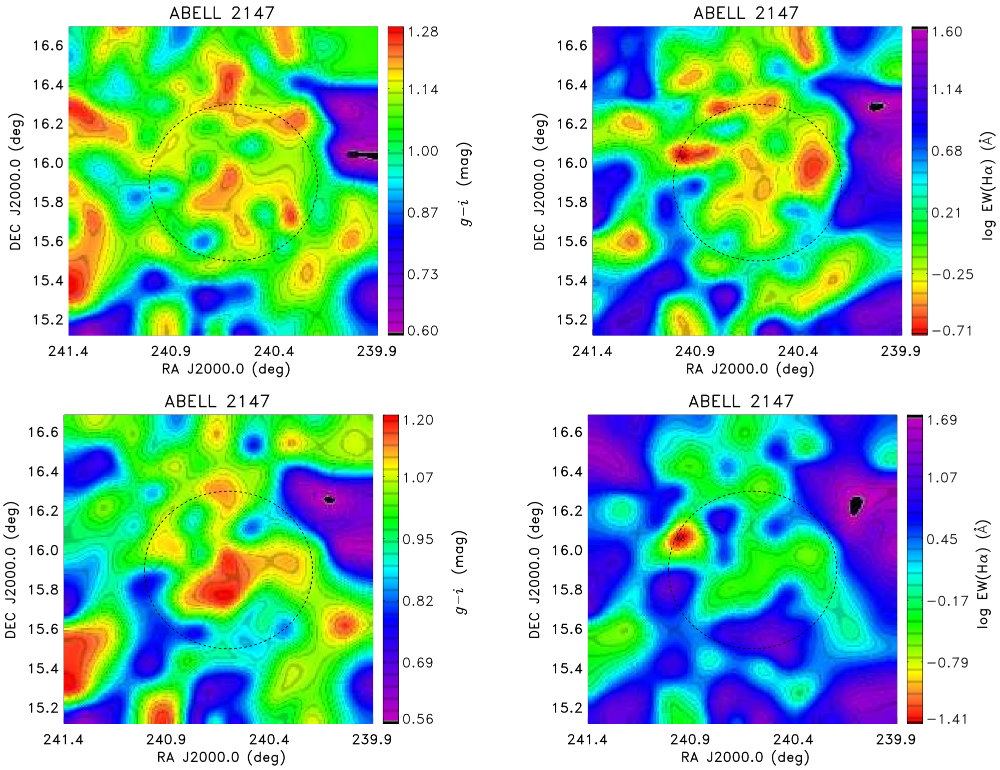

Figure 4.7: The same as in Figure 4.5 for A2147.

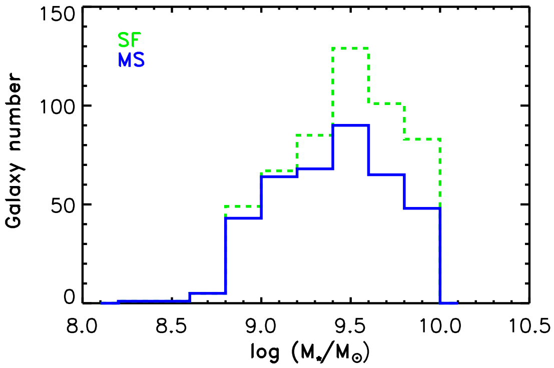

Figure 4.8: The distribution of low-mass SF galaxies selected using SDSS BPT flag (green line) and the “metallicity sample” (MS) of low-mass SF galaxies, selected using a S/N criterion on the emission lines (blue line).

4.4 Chemical history of low-mass galaxies in the Hercules Supercluster

4.4.1 Spectroscopic properties

We study here the spectroscopic and chemical properties of SF galaxies in the HSC. We focus our attention only to low-mass galaxies ($\log(M/M_{\odot}) < 10$). The reason of this selection is to avoid aperture biases in the galaxy metallicity estimates, that could be introduced by the 3-arcsec SDSS fiber spectroscopy (e.g. Kewley et al. 2005), since it is established that spiral galaxies show important radial metallicity gradients (e.g., Vílchez et al. 1988; Kennicutt et al. 2003; Pilyugin et al. 2004; Magrini et al. 2007; Bresolin et al. 2009), while in lower mass galaxies, spatial variations in metallicity are not expected to be important (Kobulnicky & Skillman 1997; van Zee & Haynes 2006; van Zee et al. 2006). In Chapter 3 we have also found that the nuclear and disk parts of spiral galaxies in A2151 show relevant differences regarding their spectroscopic properties, oxygen abundances and the N/O ratios. At the HSC distance, 3 arcsec represent ∼2.5 kpc, thus fiber spectroscopy gives a sufficient radial sampling for low-mass galaxies.

For the reliable derivation of spectroscopic properties and galaxy metallicities, we impose the condition that S/N> 3 for the emission lines Hα, Hβ, [OIII]λ5007, [NII]λ6584, [SII]$\lambda\lambda$6717,6731, and [OII]λ3727. This is a more restrictive criterion for SF galaxies than the one considered in the previous section, e.g. galaxies with SDSS BPT class=1 and 2. We refer to this S/N selected sample as the metallicity sample (MS) of low-mass galaxies, and we find 91/29/61/204 galaxies fullfilling our S/N restriction in A2151/A2152/A2147/DISP respectively. In Figure 4.8 we show the difference between the two sample selections for low-mass SF galaxies. We see that the MS includes almost all galaxies at the lower bins of mass, while at higher mass bins we note a relative incompleteness.

As an example, in Figure 4.9 we present the SDSS images and spectra of four galaxies of our MS galaxies, sampling the higher (the upper two galaxies) and the lower (the lower two galaxies) mass bins, and showing a variety of morphologies and spectral properties. Figure 4.10 shows the relative error (ε) of the emission lines used in the following to derive spectroscopic properties and metallicities. We see that εHα, εHβ, ε[NII]λ6584, and ε[SII]$\lambda\lambda$6717,6731 are typically less than 10%. The bulk of objects show relative error less than 10% in the oxygen lines [OII]λ3727 and [OIII]λ5007, while for a very small fraction of objects the errors can reach 25% to 30%.

We use the Balmer emission lines Hα, Hβ, Hγ (and where the S/N permits also Hδ) to derive the reddening coefficients c(Hβ) for our MS galaxies, using Case B approximation (Osterbrock 1989) (assuming low density and $T_e = 10^4$ K), adopting the Cardelli et al. (1989) extinction law, and taking into account the error in the emission line measurements. We note that we find the DR8 measures of Balmer emission lines such as Hγ and Hδ, significantly improved as compared to DR7 spectroscopic data. We also remind that DR8 data are corrected for the underlying stellar population, something very important for this kind of analysis as we discussed in Section 3.5.

The spectral properties of extragalactic HII regions have been extensively studied in the last four decades (e.g. Searle 1971; Shields 1974; Pagel et al. 1979; Alloin et al. 1979; Edmunds & Pagel 1984; McCall et al. 1985; Vilchez & Pagel 1988; Pérez-Montero & Díaz 2003) and well defined correlations have been found among line ratios such as [OIII]λ5007/Hβ (which represents the excitation), R_{23}, [NII]λ6584/[OII]λ3727, [NII]λ6584/Hα [NII]λ6584/[SII]$\lambda\lambda$6717,6731, among others. These correlations provide clues on the chemical composition (oxygen, nitrogen, and sulfur abundances) and the ionization conditions (e.g. the distribution of stellar effective temperature, the ionization parameter) of the nebulae and are generally independent of the host galaxy type (McCall et al. (1985), but see Pérez-Montero & Vílchez (2009)).

We have used the reddening corrected line fluxes of the MS galaxies to compute five standard optical line ratios, that we show in Figure 4.11, combined into four commonly used diagnostic diagrams. We plot in gray all the MS galaxies, and in colors the galaxies that are located within the cluster's core $R \leq R_{200}$ (blue: A2151, yellow: A2152, and red: A2147). Our sample galaxies show tight correlations on these diagrams, covering the typical ranges of normal SF galaxies. Additionally, the galaxies located at $R \leq R_{200}$ span the whole range of values in all diagrams, suggesting that the observed spectroscopic properties of our MS galaxies are independent of the location in the cluster.

Figure 4.12 shows the excitation as measured by [OIII]λ5007/Hβ vs. EW(Hα) (left) and the [OIII]λ5007/[OII]λ3727 (which is related both to excitation and ionization parameter) vs. EW(Hα) (right). We derive EW(Hα) from the stellar absorption corrected Hα flux and the adjacent continuum provided in DR8. Colored symbols represent again galaxies to distances $R \leq R_{200}$ and we see that neither the excitation conditions observed seem to vary with respect to the environment in the

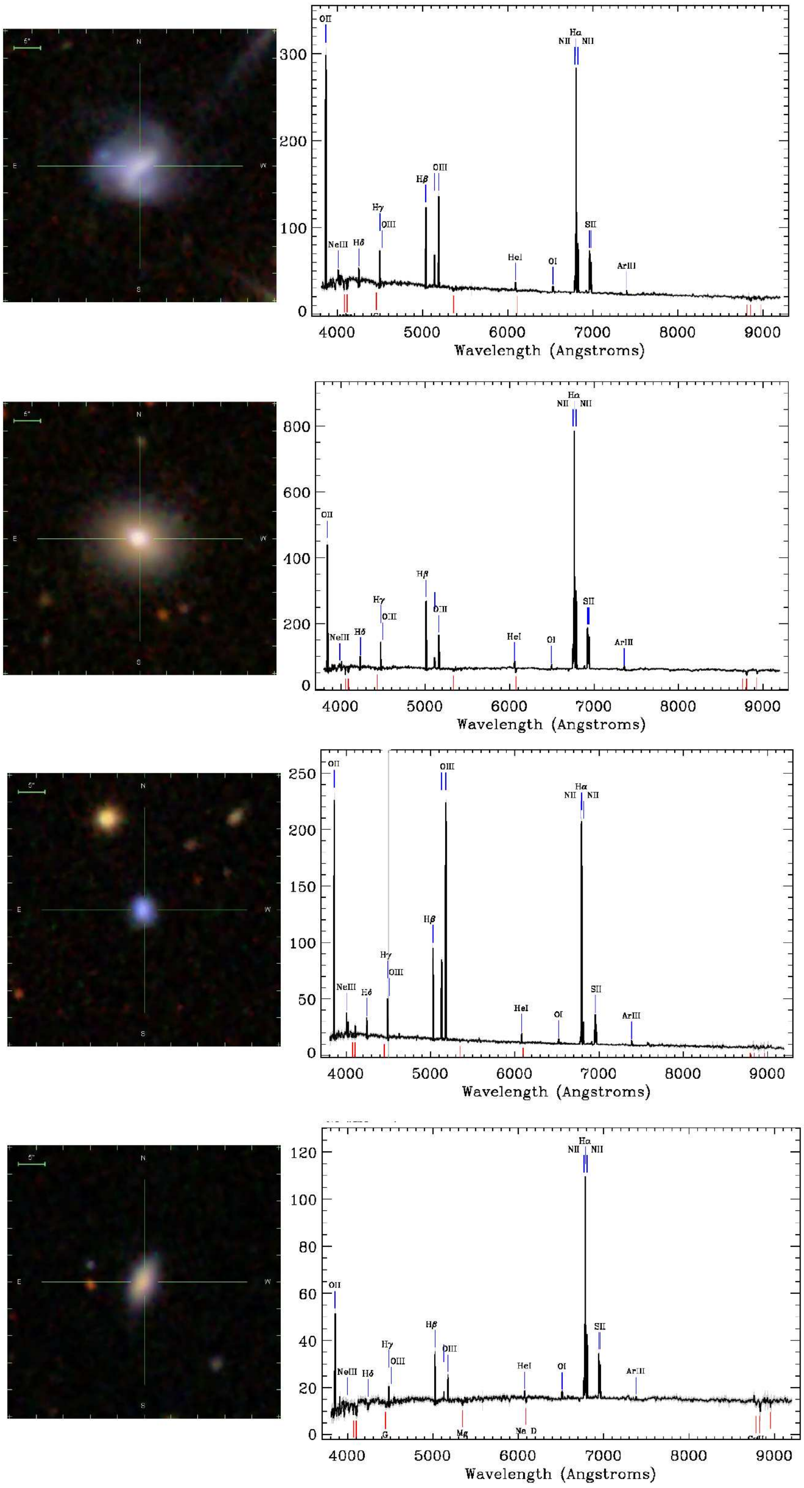

Figure 4.9: The SDSS image (left) and spectrum (right) of four galaxies of our MS sample, belonging to the higher (the upper two) and the lower (the lower two) mass bins sampled in this work.

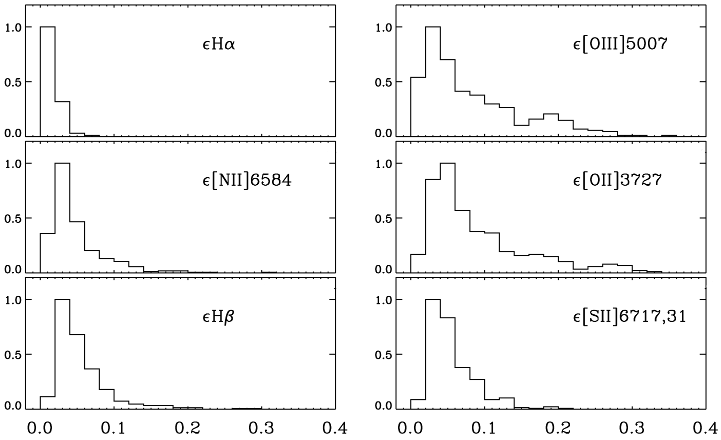

Figure 4.10: The normalized histograms of the relative error ε of the emission lines used in this work.

cluster.

4.4.2 Chemical abundance derivation

As we already discussed in Sections 1.3.1 and 3.6.3, the commonly used methods to determine oxygen abundances in HII regions are either the direct method, based on measurements of the electron temperature, or using empirical or model calibrations. The electron temperature can be derived for seven galaxies of our sample, using [OIII]λ4363 measurements; this very low rate of detection is normal given the intrinsically faint nature of these lines and the distance of HSC. For these seven galaxies we derive the electron temperatures and the oxygen abundances and in Figure 4.13 we compare the result with the values derived using the c-method (see below), and we find a very good agreement.

On the basis of the arguments presented in Section 3.6.3, in this work we use empirical calibrations to derive oxygen abundances and N/O ratios. Very recently, Pilyugin et al. (2012) presented a new way to determine abundances and electron temperatures from the strong emission lines [OII]λ3727, [OIII]λ5007, [NII]λ6584, and [SII]$\lambda\lambda$6717,6731, called "counterpart" method (or c-method). This method is based on the standard assumption that HII regions with similar emission line intensities have similar physical properties and abundances. Thus, for every HII region, there can be found a "counterpart" from a reference sample of HII regions, with well determined abundance (e.g. measured using the "direct" method). Using the c-method we derive electron temperatures, O/H, and N/O for our MS galaxies. Pilyugin et al. (2012) quote that the errors of the calibration are less than 0.1 dex when the emission line errors are less than 10%.

As already mentioned in Sections 1.3.1 and 3.6.3, the use of N2=log([NII]λ6584/ Hα) to derive gas-phase metallicities has two important advantages: the relation between N2 and the oxygen abundance is single-valued and the emission lines involved

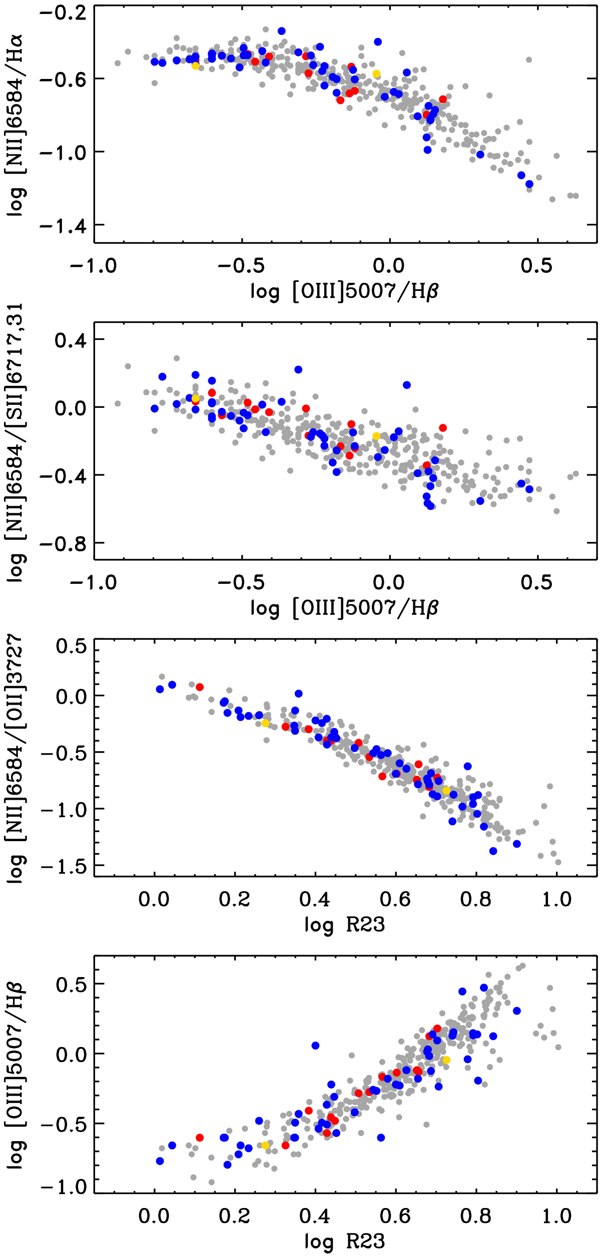

Figure 4.11: Five line ratios combined into four generally used diagnostic diagrams for our MS galaxies in the HSC region. The galaxies inside the cluster core ($R \leq R_{200}$) of each cluster are indicated with blue (A2151), yellow (A2152) and red (A2147).

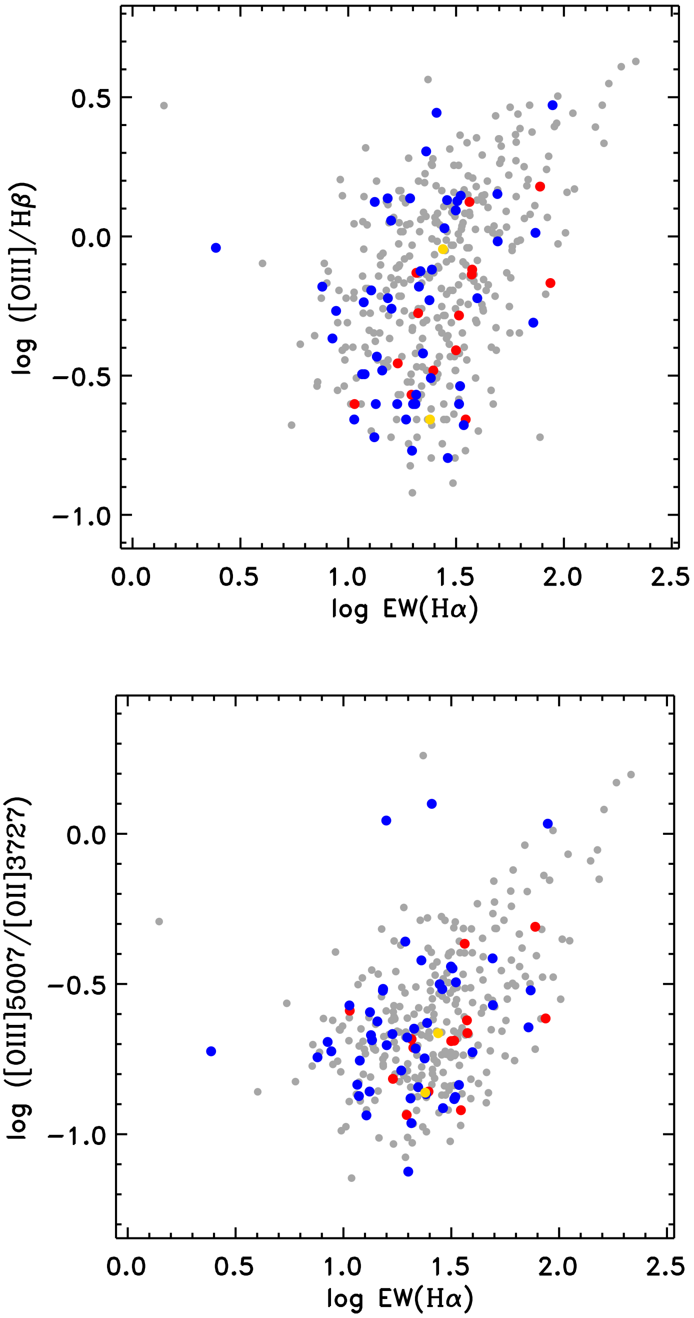

Figure 4.12: [OIII]λ5007/Hβ and [OIII]λ5007/[OII]λ3727 vs. EW(Hα) for our MS galaxies in the HSC. The galaxies inside the cluster core ($R \leq R_{200}$) of each cluster are indicated with blue (A2151), yellow (A2152) and red (A2147) points.

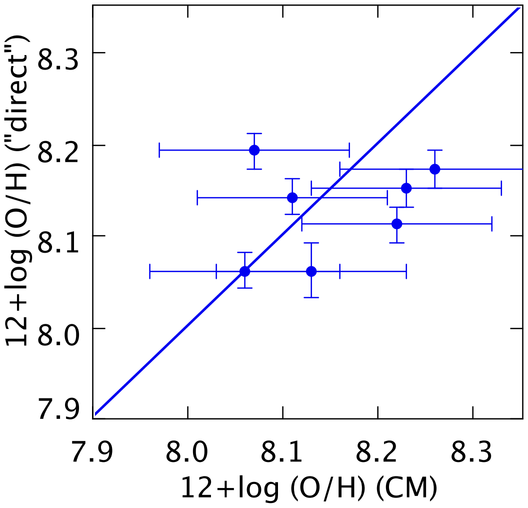

Figure 4.13: 12+log (O/H) derived using the electron temperature ("direct") method vs. the value derived using the c-method (CM) of Pilyugin et al. (2012).

are very close in wavelength, so the N2 parameter is almost free of uncertainties introduced by reddening correction or flux calibration. As in Chapter 3, we use the N2 calibration given by PMC09 to derive O/H and their calibration based on N2S2 to derive the N/O ratio (see Section 3.6.3). PMC09 quotes that the rms of the N2 calibration for O/H, and of the N2S2 calibration for N/O, is ~ 0.3 dex.

Another very useful index to derive oxygen abundances is O3N2, defined as O3N2=log{([O III]λ5007/Hβ)/([N II]λ6584/Hα)} (Alloin et al. 1979), which shows a relatively tight and linear relationship with 12+log(O/H) (Pettini & Pagel 2004, from now on PP04) for O3N2$\lesssim 2$. For our MS sample of galaxies always O3N2 < 2, and we adopt the O3N2 calibration of PP04 to derive a third estimate of the oxygen abundances. The error of the O3N2 calibration is 0.14 dex. Finally, we also derive the oxygen abundances using a model calibration, based on the diagnostic diagram [O III]λ5007/[O II]λ3727 vs. [N II]λ6584/[O II]λ3727, given by Dors et al. (2011). We find that these models systematically underestimate metallicities for 12+log(O/H)<8.3, thus we only take into account the values 12+log(O/H)$>$ 8.3.

Figure 4.14 shows the differences between O/H estimates given by the four calibrations that we have used. PMC09 and PP04 empirical calibrations show very good agreement, and almost +0.2 dex difference with the c-method of Pilyugin et al. (2012). Dors et al. (2011) models, for galaxies with 12+log(O/H)>8.3, show +0.1 dex difference with the c-method. Following the same argument of Section 3.6.3, the PMC09 and PP04 abundances are considered an upper estimate of the O/H, while the values derived by the c-method a lower estimate and, being conservative, here we derive the mean of the three, weighted to the respective calibration error. We note that for the galaxies in common with the previous chapter, the metallicities

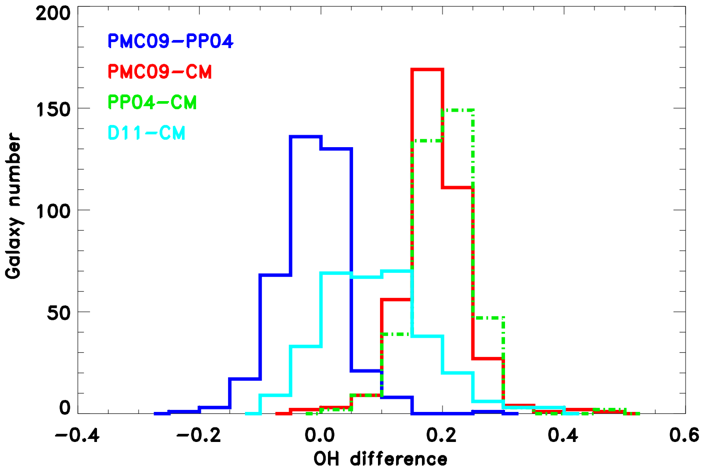

Figure 4.14: Differences between O/H estimates given by the four calibrations that we have used: the c-method (CM) of Pilyugin et al. (2012), the N2 calibration of PMC09, the O3N2 calibration of PP04, and the models of Dors et al. (2011) for the MS galaxies in HSC.

derived now are generally in good agreement with the previously derived values.

In Figure 4.15 we represent each one of the three estimates of O/H vs. the mean value. We note first that the weighted mean value for all MS galaxies is consistent with all three calibrations, within their respective statistical error. The second point is that, despite their differences, the used calibrations show linear correlations, this implying that the mean value bears only a zero-point difference. This is important, given that in the following sections, the relative differences of the chemical abundances are investigated, between galaxies inside and outside the cluster cores, and a zero-point shift would not introduce any bias. Thus, here we adopt the weighted mean value of 12+log(O/H), considering an error of 0.1 dex. Accordingly, for the N/O ratio we see that the values derived using the c-method and the PMC09 N2S2 calibration show a linear correlation with a zero-point difference, and thus we adopt the mean value and an error of 0.1 dex.

In Appendix B we quote the derived values of O/H and N/O, the adopted values, as well as all the physical properties discussed in this work, for all MS galaxies in the three clusters and DISP (A2151: Table B.1, A2152: Table B.2, A2147: Table B.3, and DISP: Table B.4).

4.4.3 The luminosity-metallicity relation

It has long been observed that galaxy metallicity correlates with luminosity (Lequeux et al. 1979; Skillman et al. 1989; Zaritsky et al. 1994; Lamareille et al. 2004; Tremonti et al. 2004; van Zee & Haynes 2006; van Zee et al. 2006; Lee et al. 2006), and this LZR has been interprated in the basis of the more fundamental

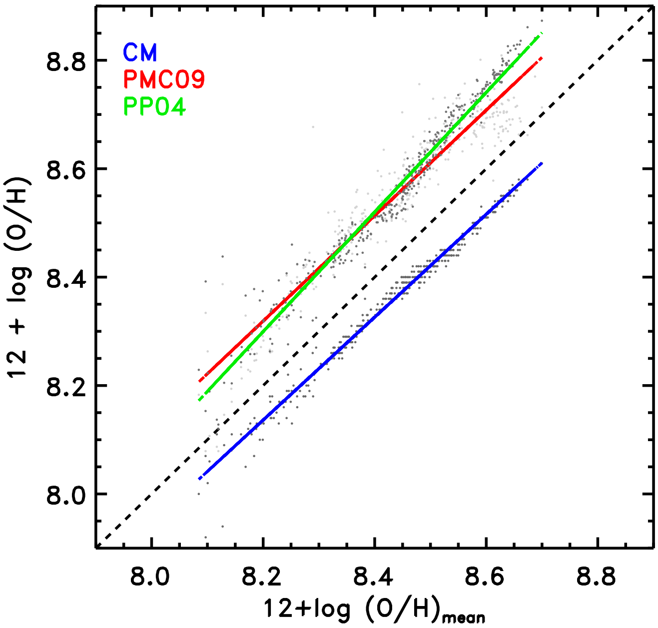

Figure 4.15: 12+log(O/H) derived by the c-method (CM), PMC09, and PP04 calibrations, vs. the weighted mean value. The grey points (of different tones) correspond to the three 12+log(O/H) estimates for each galaxy, and the linear fits to the values derived using the same calibration are ploted with solid lines (blue: CM estimates, red: PMC09, and blue: PP04).

MZR. Optical LZR has been found to show larger scatter than the MZR, attributed to variations in the stellar-mass-to-light ratios, produced by variations in galaxy SFRs (Bell & de Jong 2001).

In Figure 4.16 we plot the 12+log(O/H) vs. the $M_{\rm B}$ absolute magnitude for the MS galaxies, color-coded to their color $g-i$. We derive $M_{\rm B}$ from the SDSS g magnitude, adopting, for the clusters, their distance modulus $m-M$ given in NED (36.0/36.23/35.91 mag for A2151/A2152/A2147 respectively). For DISP, we separate galaxies in three velocity bins of 2000 km s^{-1} (our total velocity range is 6000 km s^{-1}, see Section 4.2) and we assign to galaxies in each velocity bin the $m-M$ of the cluster to the corresponding velocity range. We also adopt the conversion formula $g-{\rm B}=-0.21$ for magellanic-type irregulars (Fukugita et al. 1995), since our MS sample contains low-mass SF galaxies. We add in Figure 4.16 the samples of field dIrr of Lee et al. (2006) and van Zee & Haynes (2006).

We observe in Figure 4.16 that the MS galaxies show an interesting feature: in the same bin of magnitude, e.g. $-18.5 < M_{\rm B} < -17.5$, MS galaxies span a wide range in metallicity, showing a clear color segregation, where more metal rich galaxies appear to be redder in color $g-i$. Figure 4.17 shows clear correlations between the chemical abundances O/H and N/O and the $g-i$ color for the MS

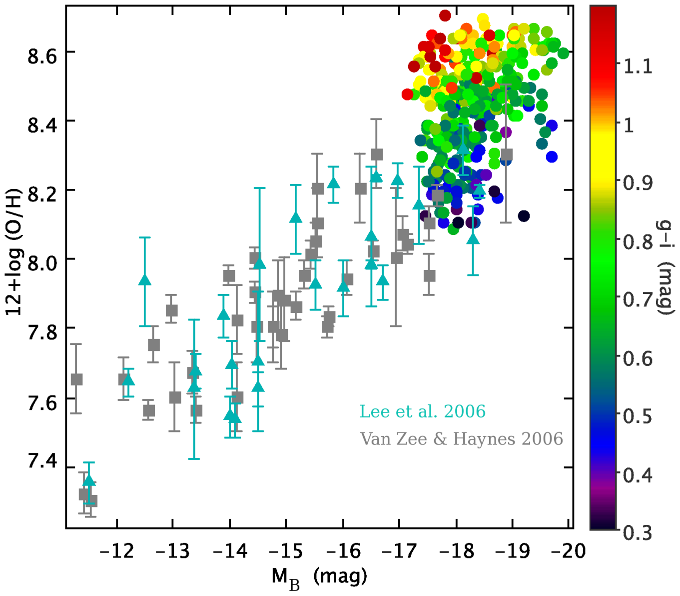

Figure 4.16: 12+log(O/H) vs. $M_{\rm B}$ magnitude for the MS galaxies (points, color coded to the galaxy $g-i$ color), and the samples of nearby dIrr of Lee et al. (2006) (cyan triangles) and van Zee & Haynes (2006) (gray squares).

galaxies. In Figure 4.16, the redder and more metallic MS galaxies produce a large dispersion at $-18.5 < M_{\rm B} < -17.5$ and appear to be shifted upwards compared to the general LZR defined by field dIrr.

Before considering a color evolution scenario for the dispersion on the LZR of our MS galaxies, we should investigate possible biases in the $g-i$ color. For example, while in the wavelength range of SDSS i band (centered at $\sim$ 7700Å) there are not bright emission lines, in g band (centered at $\sim$ 4400Å) are included the Hβ and [O III]$\lambda\lambda$4959,5007 lines, which could produce a bias for galaxies with high SFRs toward bluer colors. The excess in g magnitude, due to these nebular emission lines, is equal to their total EW divided by the FWHM of the g filter. We have checked that, for our sample of MS galaxies, an excess in g magnitude due to gas emission should be typically less than 0.02 mag, that is within the error of SDSS g magnitude.

Another relevant parameter to take into account is the reddening. In the previous section we derived the c(Hβ) using the Balmer emission lines for our sample of galaxies. Figure 4.18 (left) shows that c(Hβ) correlates with galaxy $g-i$ color, increasing from $\sim 0.0-1.0$ as galaxy $g-i$ color goes from $\sim 0.2-1.2$. Adopting the extinction law of Cardelli et al. (1989) with $R_{\rm V}=3.1$, $A_{\rm V}=2.14c({\rm H}\beta)$; thus the redder galaxies of our sample could suffer up to 2 mag higher extinction in the V band. This effect would affect more importantly the higher metallicity galaxies, as c(Hβ) correlates with metallicity too (Figure 4.18, right).

We adopt the simple picture where stellar population and ionized gas suffer the

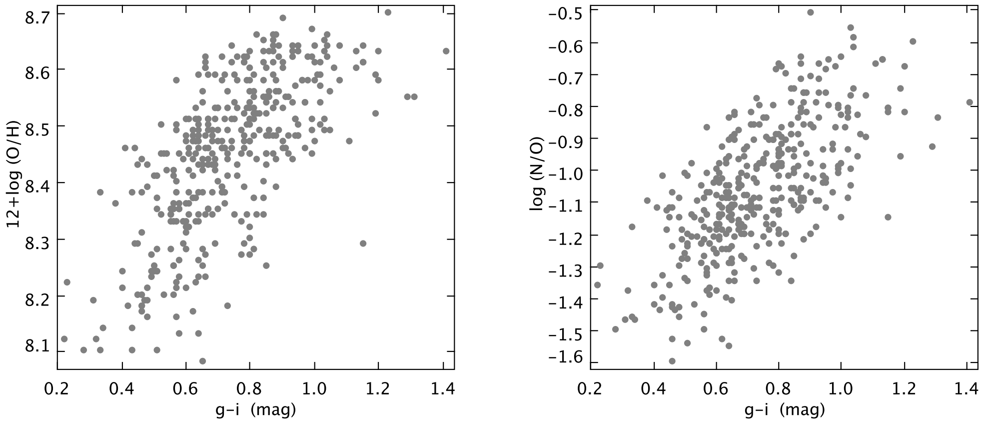

Figure 4.17: 12+log(O/H) (left) and log(N/O) (right) vs. $g-i$ for the MS galaxies.

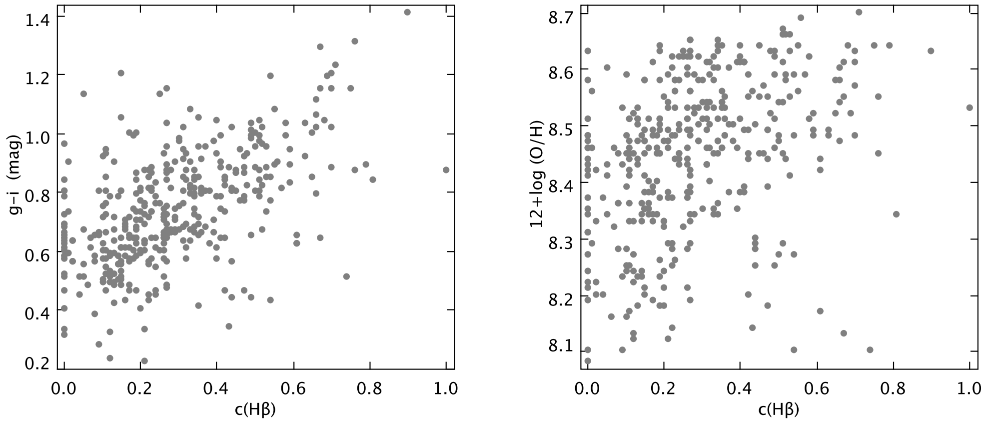

Figure 4.18: Galaxy $g-i$ color (left) and 12+log(O/H) (right) vs. $c(H\beta)$ for the MS galaxies.

same extinction[2], and the extinction law of Cardelli et al. (1989) with $R_V = 3.1$, and we correct for extinction both M_B magnitude and $g-i$ color, obtaining $M_{B,cor}$ the $(g-i)_{cor}$.

In Figure 4.19 we plot the oxygen abundance (upper panel) and N/O ratio (lower panel) vs. $M_{B,cor}$ magnitude, corrected for extinction. The points are color coded to the galaxy $(g-i)_{cor}$ color (also corrected for extinction). We see that galaxies are clearly separated in color in the plane of the LZR and the luminosity vs. N/O. Thus, large part of the dispersion observed in these plots is intrinsically related to galaxy evolution: in the same bin of M_B, redder galaxies would host a more evolved stellar

---

[2] Calzetti et al. (1994) have argued that stars may suffer less extinction than the gas, and we have found that this might be true for A2151 galaxies (see Figure 3.12). We have checked that considering a factor of 0.8 and 0.5 would not have changed the following considerations.

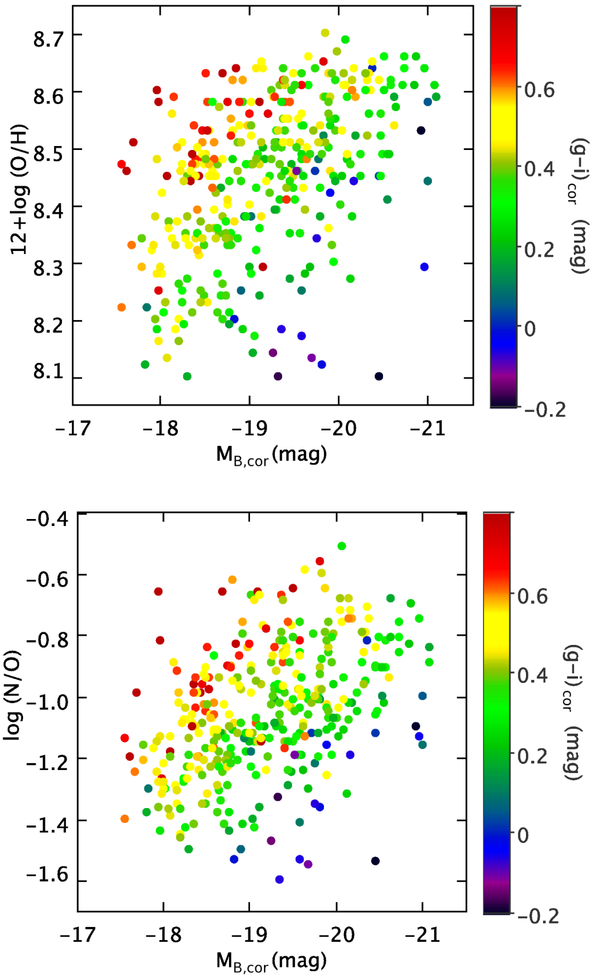

Figure 4.19: 12+log(O/H) (upper panel) and log(N/O) (lower panel) vs. $M_{\mathrm{B,cor}}$ magnitude, corrected for extinction. The points are color coded to the galaxy $(g-i)_{\mathrm{cor}}$ color.

population, indicating an older mass-weighted stellar age, that would be consistent with the higher metallicity and N/O ratio of these galaxies.

In Figure 4.20 we present the same relations of Figure 4.19, but now we explore the effect of the SFR. We plot in color the $EW(\mathrm{H}\alpha)$[3] and we do not find any clear trend. It has been claimed that the SFR can explain large part of the scatter of the MZR (Mannucci et al. 2010), and this can be understood by the correlated behavior of gas-phase metallicity and SFR after a gas infall event (we discuss this further in the following chapter, in Section 5.5). The LZR of our MS galaxies, though, does not reveal this kind of effect.

In Figure 4.21 we plot again the oxygen abundance vs. $M_{\mathrm{B,cor}}$ magnitude, corrected for extinction and using points color coded to the galaxy $(g-i)_{\mathrm{cor}}$ color (also

---

[3] We remind that Hα emission has been corrected for the underlying absorption.

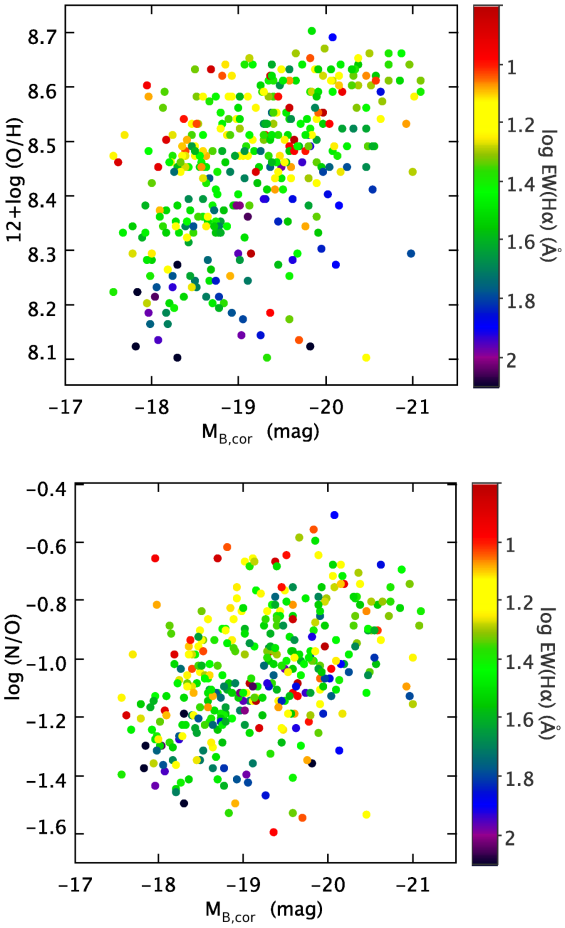

Figure 4.20: 12+log(O/H) (upper panel) and log(N/O) (lower panel) vs. $M_{\mathrm{B,cor}}$ magnitude, corrected for extinction.The points are color coded to the galaxy logEWHα.

corrected for extinction); this is the same as Figure 4.19 upepr panel, but now we add the field samples of dIrr. We see that the MS galaxies follow a well defined LZR relation, matching the LZR observed for field dIrr galaxies. The dispersion observed in the LZR of the MS galaxies, after correcting for extinction, is of the same order of that observed in the field samples of Lee et al. (2006) and van Zee & Haynes (2006). Our large sample of galaxies has permitted to clearly identify a second parameter correlation in this LZR with galaxy color, i.e. with the mass-weighted age of the stellar populations.

In the following section we analyze the MZR, which is not expected to be affected by galaxy color evolution, as the mass estimates have been derived using spectral fitting based on population synthesis models (see Kauffmann et al. 2003); then we explore the effect of the environment on the MZR for our MS galaxies.

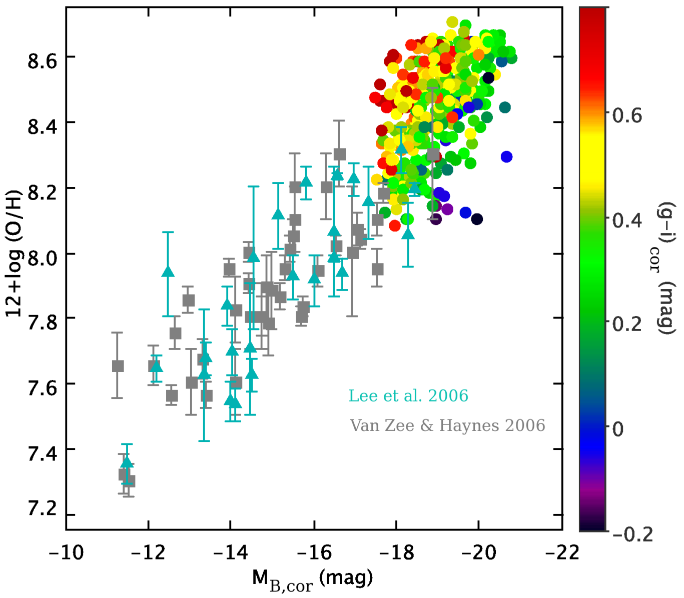

Figure 4.21: The same as in Figure 4.16 using $M_{\mathrm{B,cor}}$ magnitude and $(g-i)_{\mathrm{cor}}$ color, corrected for extinction.

4.4.4 The mass-metallicity relation

In Figure 4.22 we plot the oxygen abundance vs. the galaxy stellar mass for all our MS galaxies and we mark with colors galaxies located at the clusters' cores ($R \leq R_{200}$): blue (A2151), yellow (A2152), and red (A2147). We see that our MS galaxies follow a well defined MZR. We perform a linear fit to all MS galaxies and we find 12+log(O/H)=(5.64 ± 0.14)+(0.30 ± 0.02)log($M_\star/M_\odot$). The linear fit is indicated in Figure 4.22 with a black solid line.

Lee et al. (2006) have derived the MZR for 25 nearby dwarf irregular galaxies ($10^6 < M < 10^9 M_\odot$), extending the well-known SDSS MZR (Tremonti et al. 2004) to the lower mass range. Lee et al. (2006) have found a very tight correlation, over the whole stellar mass range, with slope 0.30 ± 0.03 and zero point 5.65 ± 0.23 in absolute agreement with our findings here. In Figure 4.22 we plot Lee et al. (2006) dataset and their linear fit to the MZR. It is worth noting that for the dIrrs of Lee et al. (2006) sample, the oxygen abundances have been derived using the direct method. Therefore, the matching we find in the MZR fit between our sample and that of Lee et al. (2006), both in terms of the slope and the zero point, suggests that the metallicities we derive here using empirical calibrations are consistent with the metallicities derived using the T_e. Furthermore, as we discuss in Chapter 7, the derived slope for the MZR is in agreement with the predictions of recent hydrodynamic simulations (Davé et al. 2011), that use momentum driven winds and an "equilibrium" picture of gas infall and outflows (Finlator & Davé 2008) to explain the MZR.

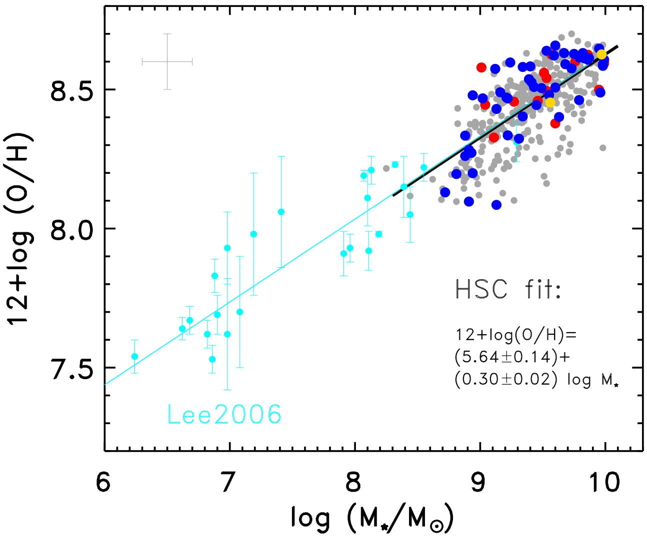

Figure 4.22: 12 +log(O/H) vs. galaxy stellar mass for our MS galaxies. The black solid line indicates the linear fit to all MS galaxies. Galaxies at distances $R \leq R_{200}$ in each cluster are marked with colors: A2151 (blue), A2152 (yellow), A2147 (red). The error bars in the upper left corner indicate the adopted errors of 0.1 dex in metallicity and 0.2 dex in mass. Cyan points represent Lee et al. (2006) sample of local Volume dIrr galaxies and the cyan line is the fit given by Lee et al. (2006).

In order to explore the possible imprint of the cluster environment on the MZR for the three clusters of the HSC, in Figure 4.23 we give the residuals log(O/H)-log(O/H)$_{\rm fit}$ from the MZR fit for all MS galaxies as a function of local galaxy density ($\Sigma_{4,5}$, upper panel) and galaxy stellar mass (lower panel). We mark the galaxies in the cluster cores with blue (A2151), yellow (A2152), and red (A2147) colors. In these two plots we see that galaxies inside $R \leq R_{200}$ regions show higher local densities (as expected), span the whole range of masses, and we find more of these core galaxies in the part of the positive residuals. We also observe higher positive residuals with decreasing stellar mass for A2151 and A2147 cluster core galaxies. For A2152 there are only two galaxies in our MS sample with $R \leq R_{200}$ and have metallicities very close to the general MZR fit.

A2151 having enough MS galaxies located at distances $R \leq R_{200}$ (the blue points in Figure 4.23), permits to explore the differences in metallicity as a function of cluster-centric distance and local galaxy density. In the upper panel of Figure 4.24, we plot the mean difference log(O/H)-log(O/H)$_{\rm fit}$ as a function of the distance from the cluster center for the A2151 MS galaxies, in bins[4] of $0.2R_{200}$, and the error bars represent the standard error of the mean. The point sizes are proportional to the number of galaxies included in each bin, and we observe that at $\sim R_{200}$

---

[4] The last bin at $R > 1.6R_{200}$ is a bit wider, to increase statistics.

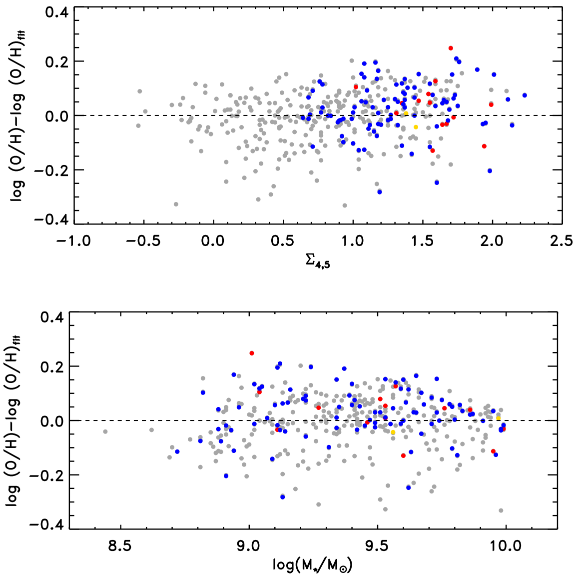

Figure 4.23: The residuals log(O/H)-log(O/H)$_{\rm fit}$ from the MZR fit for all MS galaxies as a function of local galaxy density ($\Sigma_{4,5}$, upper panel) and galaxy stellar mass (lower panel). We mark the galaxies in the cluster cores with blue (A2151), yellow (A2152), and red (A2147) colors.

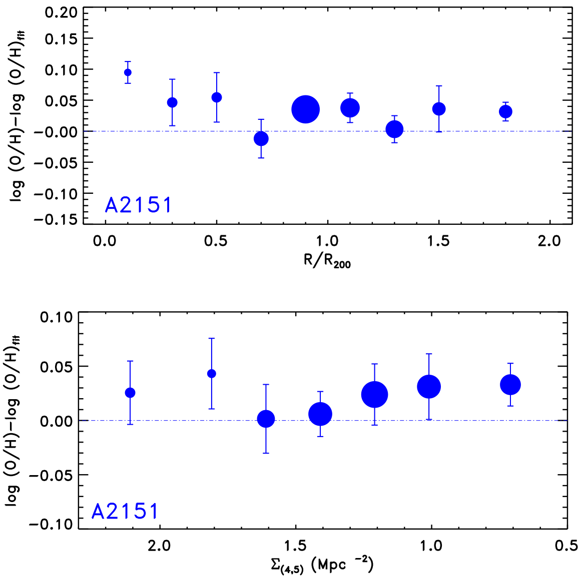

Figure 4.24: Upper panel: the mean log(O/H)-log(O/H)$_{\rm fit}$ as a function of the distance from the cluster center in bins of $0.2R_{200}$ for A2151 MS galaxies. Lower panel: the same as a function of local galaxy density $\Sigma_{4,5}$. The error bars represent the standard error of the mean value and the point sizes are proportional to the number of galaxies included in each bin.

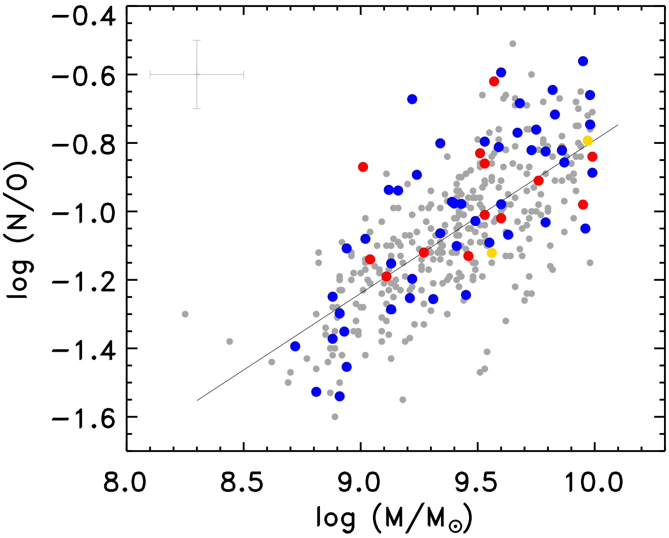

Figure 4.25: Log (N/O) vs. galaxy stellar mass for the MS galaxies in the HSC. Galaxies at $R \leq R_{200}$ are marked with colors: A2151 (blue), A2152 (yellow), A2147 (red).

there is an increment in the number of galaxies observed, reflecting the population of "newcomers" in the cluster environment, that we have already discussed in the previous sections and in Chapter 3.

At distances $R \leq R_{200}$ we observe a marginal trend of increasing O/H compared to the expected values from the MZR fit, as we move toward the cluster core. At the lowest distances to the cluster center $R \leq 0.2R_{200}$, the mean O/H increment reaches $\sim$ 0.1 dex. This is in agreement with the result obtained in Section 3.8, where we have found that dwarf/irregular galaxies located at the highest densities inside the cluster R_{200} region, were located at the upper part of the general MZR.

In the lower panel of Figure 4.24, we plot the mean O/H-O/H$_{\rm fit}$ as a function of local galaxy density, in bins[5] of 0.2 dex in log $\Sigma_{4,5}$. Here again the error bars represent the standard error of the mean and the point sizes are proportional to the number of galaxies included in each bin. We see that there appears to be a marginal average increment in galaxy metallicity at local galaxy densities log $\Sigma_{4,5} > 1.8$ (see also Section 3.7), but there does not appear a clear general trend.

It is known that galaxy N/O ratio shows a complex behavior, due to the primary/secondary nature of nitrogen (see Section 1.3.1) and its delayed delivery to the ISM $\gtrsim$ 250 Myr, as compared to oxygen, which is typically released after ~10 Myr in Type II SNe. Additionally, the N/O ratio has a different response than O/H in effects of gas interchange with the environment, e.g. gas infall and outflows

---

[5] The first and last density bin are slightly wider to include all A2151 MS galaxies and increase statistics.

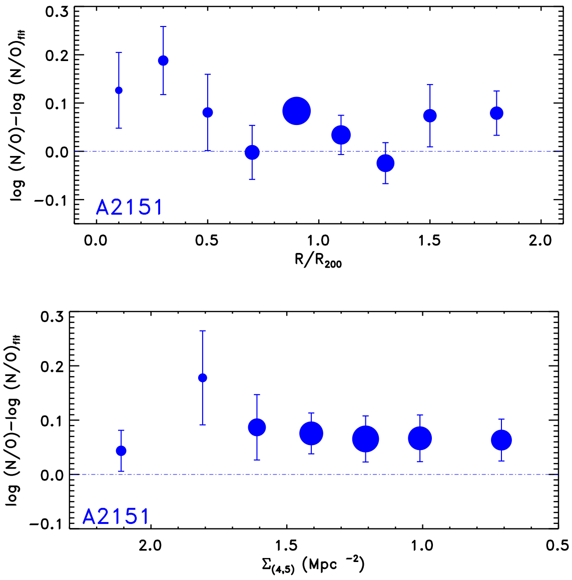

Figure 4.26: Upper panel: the mean log(N/O)-log$(N/O)_{\rm fit}$ as a function of the distance from the cluster center in bins of $0.2R_{200}$ for A2151 MS galaxies. Lower panel: the same as a function of local galaxy density $\Sigma_{4,5}$. The error bars represent the standard error of the mean and the point sizes are proportional to the number of galaxies included in each bin.

(Edmunds 1990; Köppen & Hensler 2005; van Zee & Haynes 2006; Pérez-Montero & Contini 2009). Therefore, tracing the N/O ratio in galaxies can give an important piece of information regarding galaxy chemical evolution.

In Figure 4.25 we plot the N/O ratio vs. galaxy stellar mass, finding a well defined correlation. The points in colors represent galaxies in the cluster cores as previously, and we see that these cluster core galaxies do not show any evident trend on this plane. We perform a linear fit to the plot in Figure 4.25, and in Figure 4.26 and we explore the residuals from the fit for A2151 MS galaxies, as we did previously for the MZR. We plot the mean of the difference log(N/O)-log$(N/O)_{\rm fit}$ as a function of the distance to the cluster center (top) and as a function of local galaxy density (bottom). We observe the same trends as in Figure 4.24; a slight enhancement of the N/O ratio in galaxies in the more central parts of the cluster, as compared to the expected value form the fit. This enhancement is also verified at local galaxy densities $\Sigma_{4,5} \sim 1.8$.

The trends observed in O/H and N/O in A2151 low-mass SF galaxies could be interpreted by the galaxy "surviving" scenario proposed in Chapter 3 (Section 3.7): only the more massive (and thus more metallic) of these galaxies have been able to "survive" (as SF galaxies) until reaching the cluster core. The star formation of the lower-mass galaxies would get faster switched off by the cluster environment, before the crossing of the cluster center. In Chapter 7 we will discuss another possible explanation, in terms of an accelerated SFH in the fillaments, during the infall of these galaxies toward the cluster.

4.5 Summary

In this chapter we study the star formation and chemical history in the HSC. We take advantage of the SDSS DR8 to construct a large spectroscopic sample of galaxies in this region.

Based on this large sample we first investigate the large-scale structure of the HSC. We derive new parameters for the clusters, as the mean cluster velocity v_{clus} and velocity dispersion σ_v. We derive a lower value for the velocity dispersion of A2152 than previously quoted, in agreement with the low X-ray luminosity of this cluster.

We investigate the relative population of SF galaxies and low-mass galaxies in each cluster and DISP, finding interesting differences among them. DISP is dominated by low-mass SF galaxies. A2151 shows a relatively elevated ratio of SF galaxies, accented by its very high ratio of low-mass SF galaxies, even inside the R_{200} region. A2147 shows the lowest ratio of SF galaxies among the three clusters.

The $EW(\mathrm{H}\alpha)$ shows a clear drop with cluster-centric distance for all three clusters, showing higher average values in A2151. When only actively SF galaxies are considered (with $EW(\mathrm{H}\alpha){>}2$) the radial trend disappears. This indicates that the population of actively SF galaxies, which are predominantly low-mass galaxies, should have been incorporated recently to the cluster.

These results are reproduced by the 2D color $g-i$ and $EW(\mathrm{H}\alpha)$ maps of the clusters. We find that A2151 hosts an elevated population of blue low-mass SF galaxies inside the R_{200} region, illustrating the early stage of formation of the cluster. We also observe the presence of a filament, mainly of low-mass galaxies, to the North of A2151, that reaches down to the cluster core. The $g-i$ and $EW(\mathrm{H}\alpha)$ maps of the other two clusters indicate more virialized structures; nonetheless, we identify a filamentary structure dominated by blue low-mass SF galaxies entering in A2147 R_{200} region from South-East.

We define a subsample of low-mass galaxies in the HSC region, selected on the basis of the S/N of their emission lines, to study their chemical enrichment. Considering the low-mass galaxies, we avoid the aperture bias effects of SDSS fiber spectroscopy, as chemical abundance gradients are not expected to be important for these galaxies.

First we derive the spectroscopic properties of these galaxies and we find that emission line ratios span the typical ranges in standard diagnostic diagrams and are independent of the position of the galaxies in the HSC. We then derive their chemical abundances using three empirical calibrations.

We find that the low-mass SF galaxies in the HSC follow a well defined LZR and N/O vs. mass relation. These relations have been found to show an intrinsic dispersion that correlates with galaxy color. For the derivation of these relations we have corrected our galaxies for extinction, that has been found to affect predominantly the higher metallicity galaxies, introducing an important bias to the LZR.

Finally, we build the MZR and the N/O ratio vs. stellar mass relation and we find well defined sequences. The derived slope of the MZR is in absolute agreement with the value derived for local dIrr galaxies. We study the effect of the environment on the MZR and the low-mass SF galaxies in the core of A2151 appear to show, on average, slightly higher metallicities and N/O ratios.

Chapter 5

The metal enrichment of low-mass galaxies in four nearby clusters

---

Contents

5.1 Introduction

In accordance to the current cosmological paradigm (e.g., Springel et al. 2005), clusters at $z \sim 0$ have been found to accrete late-type galaxies along the filamentary structures that compose the cosmic web (e.g., Smith et al. 2012). Mahajan et al. (2011) have found that post-starburst dwarfs are preferentially located in the infall regions of Coma and A1367, suggesting that these galaxies experience a sudden quenching of star formation due to the interaction with the ICM. Moreover, before the gas gets totally stripped off, dwarf galaxies could experience an enhancement of star formation, either during their infall into the cluster along the filaments (Mahajan et al. 2010; Porter et al. 2008), or in the first stages of their encounter with the hot ICM (pressure triggered star formation, Abramson et al. 2011; Sun et al. 2007; Gavazzi et al. 2001). Thus SF dwarf galaxies are excellent probes to test the influence of the environment on the process of star formation and galaxy evolution.

According to previous works on the gas metallicity of SF dwarf galaxies in local Universe clusters, the effect of the environment seems to be relevant. In Virgo dIrr, the gas metallicity has not been found to show a clear trend with the environment (Vilchez 1995; Lee et al. 2003; Vaduvescu et al. 2007); however, Lee et al. (2003) have found that five of these dIrr are gas deficient with respect to field dIrr at comparable oxygen abundances, and this gas deficiency correlates with the X-ray surface brightness of the ICM. Some SF dwarfs in Hydra cluster (Duc et al. 2001) have been found metal-rich for their luminosities and Vaduvescu et al. (2011), comparing the MZR of SF dwarfs in Hydra, Fornax and Virgo, have suggested that differences in the MZR seem to exist for galaxies in such different environments. Furthermore, in Chapters 3 and 4 we have been able to observe low-mass galaxies, located in A2151 cluster core, showing higher metallicities for their mass.

In this chapter we extend these previous works, studying the chemical history of a large sample of SF dwarf galaxies in four local Universe clusters: Coma (A1656), A1367, A779, and A634. Coma and A1367 are among the nearest very rich galaxy clusters, and both belong to the large structure called the Coma supercluster. Recent insightful evidences on the assembly history and the SFH of the low-mass galaxy population in the Coma supercluster (Smith et al. 2012; Mahajan et al. 2011, 2010) seem to indicate that it provides exemplary conditions for searching the potential imprints of the cluster environment on galaxy chemical enrichment. A779 and A634, in turn, are two lower mass clusters, permiting to investigate whether the mass of the host cluster could play a significant role in the chemical evolution of SF dwarf galaxies.

In the same manner as in the previous chapter, we take advantage of the latest spectroscopic release SDSS DR8, where new emission line measures have been provided, after correcting the spectra for the underlying stellar population. This is an important issue when deriving gas-phase metallicities, reducing biases that previous works could have been suffering. We study the chemical properties of SF dwarf galaxies in the central region (up to $\sim 3R_{200}$) of our sample of clusters. We note that three out of these four clusters were not included in releases previous to DR7.

Kewley et al. (2005) argued that using the 3-arcsec diameter aperture of the SDSS spectra to estimate SFRs and metallicities of late type galaxies located at $z < 0.04$ could introduce systematic biases. This is due to the significant radial metallicity gradients that can be found in SF spiral galaxies (see also Section 4.4.1). However, in this work we focus our attention to dwarf/irregular galaxies, where spatial metallicity gradients are not expected to be important (Kobulnicky & Skillman 1997; van Zee & Haynes 2006; van Zee et al. 2006). Thus, taking into account the smaller diameter of dwarfs, we do not expect aperture biases to be important for the galaxies of the present sample .

5.2 The galaxy sample

Cluster galaxies were selected using spectroscopic redshift information. In Figure 5.1 we plot the velocity histograms of all galaxies with SDSS spectroscopic data in the areas considered. We perform a Gaussian fitting to the velocity distribution of each cluster. The central velocity obtained by the fitting is in good agreement with the mean cluster velocity given by NED, indicated in Figure 5.1. We consider as cluster galaxies all the galaxies with velocities $v_{\mathrm{clus}} \pm 3\sigma_v$, where v_{clus} is the mean cluster velocity and σ_v is the dispersion given by the fit. In Table 5.1 we give details on the surveyed regions, the velocity range considered for each cluster, and the total

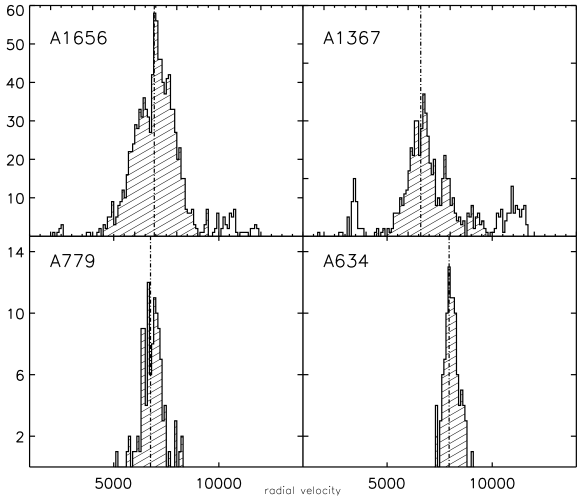

Figure 5.1: Histogram of the radial velocity for all galaxies with SDSS DR8 spectroscopic data within $3R_{200}$ from the center of each cluster. The velocity bin is 100 km s^{-1}. The dashed line represents the mean cluster radial velocity as given in NED (Coma: $cz = 6930$ km s^{-1}; A1367: $cz = 6600$ km s^{-1}; A779: $cz = 6750$ km s^{-1}; A634: $cz = 7950$ km s^{-1}). The dashed region indicates the adopted velocity range at $\pm 3\sigma_v$ around the mean cluster velocity.

number of galaxies with SDSS spectroscopic data found within the area considered and within the respective velocity range.

To select the dwarf galaxies, as the four clusters are located at similar distances ($m - M \sim 35.0$ mag), we adopt the criterion used by Mahajan et al. (2010, 2011): $M_z \geq 15$, which results in a selection of $\sim (M^\star + 2) < M_z <\sim (M^\star + 4)$, assuming $M_z^\star = -22.32$ (from Blanton et al. 2001) and the SDSS upper magnitude limit $r = 17.77$. This criterion yields to a sample of galaxies of log mass range $\sim 8.0 - 10.0$ $\mathrm{M}_\odot$, the upper mass limit being consistent with the adopted in Chapter 4 for low-mass galaxies in HSC.

From this sample we select the SF dwarf galaxies adopting the criteria: SDSS BPT class=1 (classification as SF, based on the BPT diagram, Baldwin et al. 1981), and S/N> 3 for the lines [O III]λ5007, [N II]λ6584, Hα, Hβ, and [S II]λλ6717,6731. Finally, we have taken special care to include to our final sample of SF dwarf galaxies one spectrum per galaxy (a few galaxies have multiple observations), as well as to exclude spectra that correspond to distinct H II regions of some parts of galaxies, because these spectra provide substantially underestimated mass values (see Section 5.3). The number of SF dwarf galaxies for each cluster is given in Table 5.1. The coordinates as well all the physical parameters derived and discussed in the following of this chapter, for all SF dwarf galaxies in the four clusters, are given in Tables C.1, C.2, C.3 and C.4 in Appendix C. For these galaxies we calculate the distance R from the cluster center given in units of the R_{200}. In Table 5.1 we also give the number of SF dwarf galaxies located in the cluster core, at distance $R \leq R_{200}$, and

Table 5.1: **Cluster regions considered**

Cluster	Area deg^2	z	Total	Dwarf	SF	Dwarf SF	Dwarf R_{200}	Dwarf SF R_{200}
A1656	5.7×5.7	0.015-0.0323	1017	616	194	148	293	25
A1367	5.2×5.2	0.015-0.0323	564	356	238	191	107	41
A779	2×2	0.0189-0.0275	106	66	32	31	26	7
A634	2×2	0.0246-0.0293	97	60	34	26	24	10

Note. Column 1: Cluster; Column 2: Square area studied in deg^2; Column 3: The redshift range considered for each cluster; Column 4: Total number of galaxies in the considered area and velocity range; Column 5: Number of dwarf (with SDSS $z > 15$) galaxies; Column 6: Number of SF galaxies; Column 7: Number of SF dwarf galaxies; Column 8: Number of dwarf galaxies at distances $R \leq R_{200}$ from the cluster center; Column 9: Number of SF dwarf galaxies at distances $R \leq R_{200}$ from the cluster center.

the total number of dwarf galaxies at $R \leq R_{200}$ for each cluster.

We note that there are more SF dwarf galaxies showing low S/N emission lines (the galaxies with BPT class=2 in SDSS) in the areas of the clusters of our sample, specially of Coma. These galaxies could be suffering the quenching effect of the cluster environment, illustrated well in studies based on the Hα equivalent widths (EWs) of SF galaxies (e.g., Balogh et al. 2004; Rines et al. 2005). In the present work, given that a high S/N emission line spectrum is required to derive properly spectroscopic properties (e.g., reddening coefficients) and gas metallicities, we do not include in our galaxy sample the low S/N SF population (we call them class 2 population). By doing this, we probably consider the more recently accreted galaxies to the cluster environment, and as a consequence the potential suppression of their star formation could be observed in an early stage. As we will discuss in Section 5.5, the behavior of class 2 population would not change the conclusions of this work.

Based on a large sample of clusters, sampling the whole mass range from groups to massive clusters, Poggianti et al. (2006) have been able to show that the fraction of SF galaxies depends on galaxy mass, both for clusters at high-z and low-z. These authors found that about 20% of the galaxies in clusters at $z \simeq 0$ with $\sigma > 500$ km s^{-1} are SF. Due to the S/N restrictions, and the SDSS spectroscopic data incompleteness (specially in clusters, due to constraints in the fiber placement, see Blanton et al. 2005a,b), our galaxy sample is not a complete sample of the SF galaxies in these clusters. Thus, we should not compare our data with the rates found by Poggianti et al. (2006). However, the goal of this work is to investigate the imprint of the cluster environment on the chemical evolution of SF galaxies in clusters, the general quenching effect in clusters being well established by several previous works.

Figure 5.2 shows the color $g - i$ histogram of dwarf galaxies (green line), SF dwarf galaxies (blue line), and SF dwarf galaxies to $R \leq R_{200}$ for each cluster (note that logarithmic scale has been used for Coma). It is well illustrated that the dwarf galaxy population in these clusters (as well as in the clusters of HSC as shown in Figure 4.3 right), is composed by two main populations, red and blue, producing two maxima in the color histogram at $g - i \sim 0.6$ and $g - i \sim 1.1$, following the general bimodal distribution of the galaxy population (Strateva et al. 2001; Baldry et al. 2004). Coma, has a larger fraction of red-sequence over blue SF dwarfs, in agreement with its low fraction of spiral galaxies (Dressler 1980). The dynamically younger cluster A1367, in turn, hosts an almost equivalent blue and red dwarf population, as well as a larger number of SF dwarfs inside R_{200}.

These differences are in agreement with previous findings on the color magnitude diagrams of these clusters (e.g., Mouhcine et al. 2011; Terlevich et al. 2001). We note that in all clusters there are some SF galaxies with red colors and that the SF dwarfs at $R \leq R_{200}$ span the whole color range. We have performed KS tests which have shown that the SF dwarf galaxies to distances $R \leq R_{200}$ and those to distances $R_{200} < R < 3R_{200}$ are statistically indistinguishable with respect to their $g - i$ color for Coma, with a probability of 89%. Smaller probabilities have been found for the three remaining clusters.

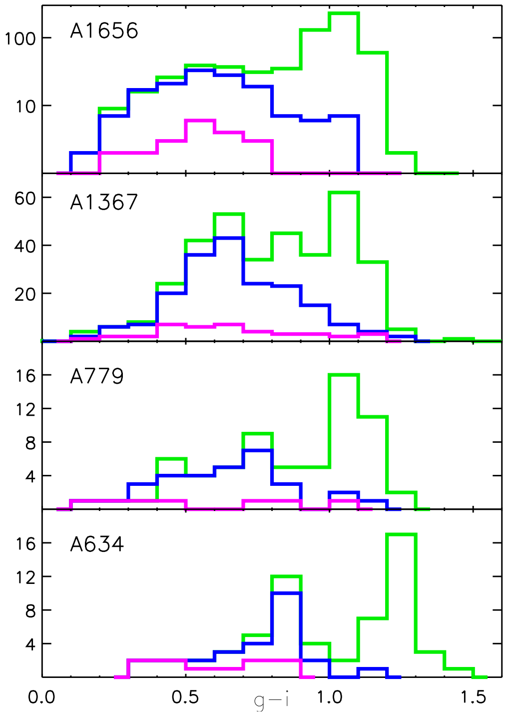

Figure 5.2: Color $g-i$ histogram of dwarf galaxies (green line), SF dwarf galaxies (blue line), and SF dwarf galaxies to $R \leq R_{200}$ (magenta line) for our clusters sample. Logarithmic scale is used for Coma (A1656). No correction has been performed for the galactic extinction, and the shift observed for A634 toward redder colors is consistent with the slightly higher galactic extinction suffered by this cluster.

5.3 Spectroscopic properties

In the following we use the emission line measures (Tremonti et al. 2004; Brinchmann et al. 2004), the BPT (Baldwin et al. 1981) diagram classification and the median estimate of the total stellar mass of the galaxies (Kauffmann et al. 2003), as given in SDSS DR8, as we did in Chapter 4. In the same manner as in Section 4.4.1, we use the Balmer emission lines Hα, Hβ, Hγ (and where the S/N permits also Hδ) to derive the reddening coefficients c(Hβ) for our sample of SF galaxies, using Case B approximation (Osterbrock 1989), adopting the Cardelli et al. (1989) extinction law, and taking into account the line measurements error. Mahajan et al. (2010) provide Spitzer MIPS 24μm flux for a sample of Coma cluster galaxies. From this sample, 25 galaxies belong to our sample of SF dwarfs. For these 25 galaxies we find that the derived reddening coefficient c(Hβ) shows a tight correlation with their flux at 24μm, in the line of Relaño et al. (2010), who suggest that the dust responsible for the Balmer extinction should be emitting at 24 μm.

The presence of both singly and doubly ionized oxygen line transitions in the optical wavelengths has permitted to develop an efficient metallicity calibration (Pagel et al. 1979) based on the indicator R_{23}=([O II]λ3727+[O III]$\lambda\lambda$4959,5007)/Hβ.

Table 5.2: **Galaxies with [OII]λ3727measures**

Cluster	DR8	New	Total	All
A1656	35	52	87	149
A1367	42	48	90	194

Obtaining the [OII]λ3727 line measures from DR8, however, resulted problematic. Although some spectra present high S/N [OII]λ3727 line, no measure is provided by DR8. For those galaxies no [OII]λ3727 line measures in SDSS, but [OII]λ3727 is detectable in the spectrum with S/N$>$ 3, we measure the [OII]λ3727 integrated flux. We have verified that our measures and DR8 give consistent emission line fluxes for several emission lines (e.g. [NII]λ6584/Hα and [NII]λ6584/[OII]λ3727, when there is [OII]λ3727). Table 5.2 presents the number of galaxies for which we have SDSS [OII]λ3727 measures, the number of galaxies for which we measure [OII]λ3727, the total number of galaxies with [OII]λ3727 measure and the total number of SF dwarf galaxies for Coma and A1367 (with S/N$>$3 in all cases).

Despite this effort, we could not obtain [OII]λ3727 for all galaxies belonging to the four clusters of $z \sim 0.023$. This is because [OII]λ3727, redshifted to this velocity, lie at the edge of the wavelength range covered by SDSS spectroscopy. We have performed KS tests and have verified that the subsample of galaxies with [OII]λ3727 measured (by DR8 or this work) and the whole sample of SF dwarf galaxies are statistically indistinguishable in their properties: M_z, metallicity (by PMC09, see Section 5.4) and mass. We conclude that the lack of [OII]λ3727 measures is a random effect, due to the radial velocity of each galaxy for the cluster velocity dispersion, and does not correlate with any of the fundamental galaxy properties. The relative errors (ε) of the remaining emission lines, used in the following to derive spectroscopic properties and metallicities, are shown in Figure 5.3. We see that εHα, εHβ, ε[NII]λ6584, and ε[SII]$\lambda\lambda$6717,6731 are almost always less than 10%, while [OIII]λ5007 presents relatively higher errors.

We have used the reddening corrected line fluxes for our sample of galaxies to compute five standard optical line ratios, that we show in Figure 5.4, combined into three commonly used diagnostic diagrams (see also Section 4.4.1). Our sample galaxies show typical line ratios of normal SF dwarf galaxies, spanning the same ranges as in Figure 4.11, and again here we find that galaxies located at $R \leq R_{200}$ span the whole range of values in all diagrams. Figure 5.5 shows the excitation as measured by [OIII]λ5007/Hβ vs. EW(Hα) (that we derived from the stellar absorption corrected Hα flux and the adjacent continuum as provided in DR8) for the SF dwarf galaxies in Coma (left) and A1367 (right). Filled symbols represent galaxies to distances $R \leq R_{200}$ and we see that the galaxies in the cluster core are not different from the rest regarding excitation.

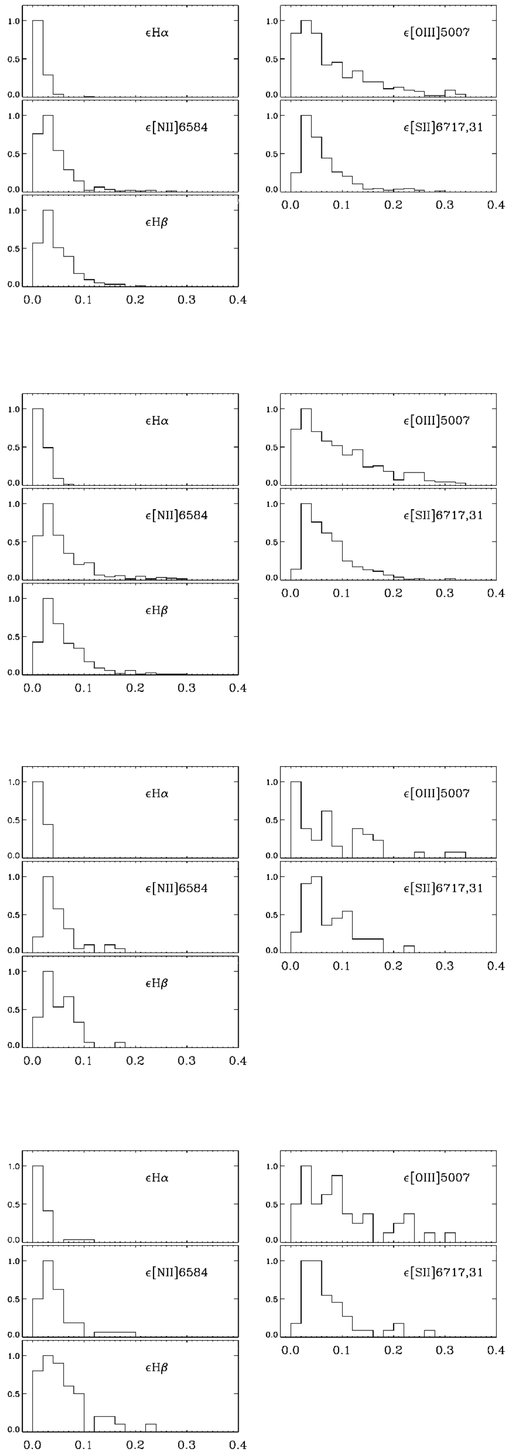

Figure 5.3: The relative errors of the emission lines used in this work, for the clusters, from top to bottom: A1656, A1367, A779, and A634.

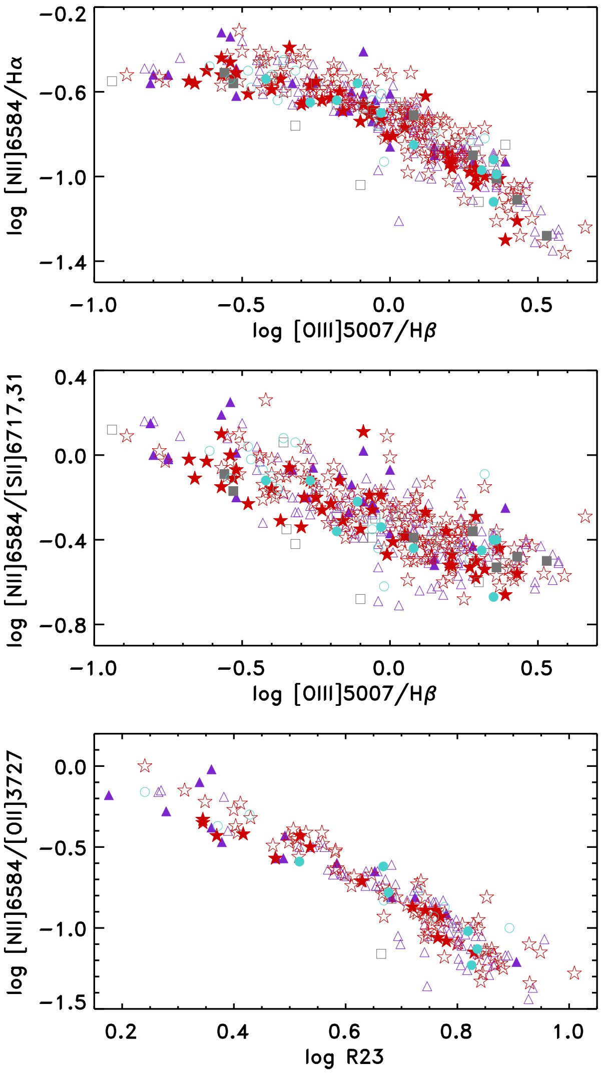

Figure 5.4: Five line ratios combined into three generally used diagnostic diagrams for SF dwarf galaxies in Coma (triangles), A1367 (stars), A779 (squares), and A634 (circles). Filled symbols correspond to galaxies at $R \leq R_{200}$. Our sample galaxies show values typical of normal HII galaxies.

5.4 Oxygen abundances

In this chapter we use the same empirical calibrations as in Chapters 3 and 4 to derive metallicities. We use for the whole sample of galaxies the N2 calibration of PMC09, and O3N2 calibration of PP04 (see Sections 3.6.3 and 4.4.2). We note that for our sample of galaxies always O3N2 < 2, lying in the valid range of PP04 calibration. For galaxies with [OII]λ3727 measurements (see Section 5.3) we also use the multiparametric calibration of P10 (which is a function of P, R_2, R_3, S_2, N_2, see Section 3.6.3) and the model of Dors et al. (2011), based on the diagnostic

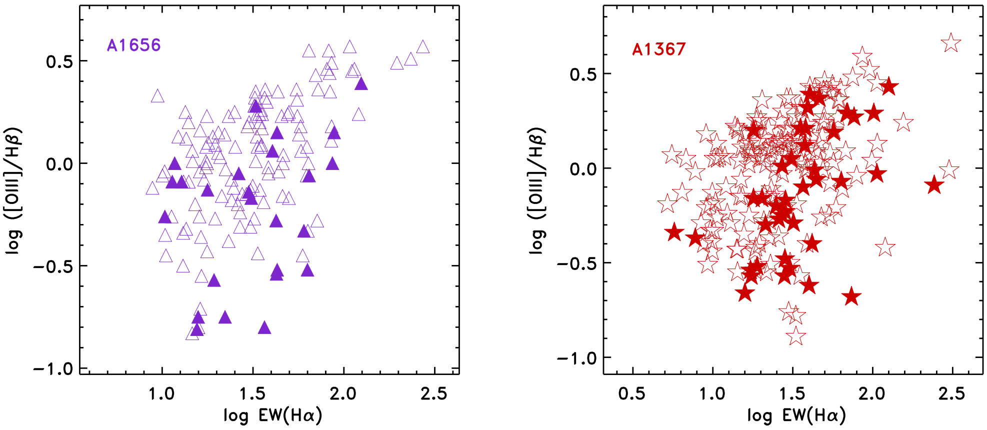

Figure 5.5: [O$\,$III]λ5007/Hβ vs. EW(Hα) for SF dwarf galaxies in Coma (A1656, triangles) and A1367 (stars). Filled symbols represent galaxies at $R \leq R_{200}$.

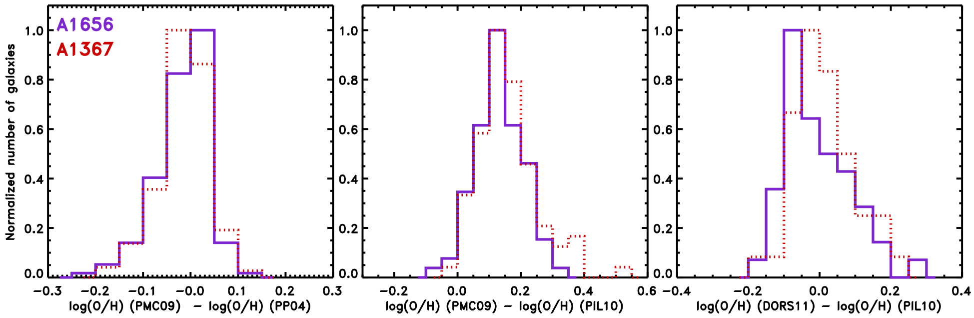

Figure 5.6: Left: The difference of 12+log(O/H) derived using PMC09 and PP04 calibrations. A1656: continuous, A1367: dashed line. Middle: The same between PMC09 and PIL10 calibrations, for galaxies with [O$\,$II]λ3727measured. Right: The same using Dors et al. (2011) models and PIL10 calibration (for galaxies with [O$\,$II]λ3727 measured and 12+log(O/H)$_{\mathrm{DORS11}}$ >8.2).

diagram [O$\,$III]λ5007/[O$\,$II]λ3727 vs. [N$\,$II]λ6584/[O$\,$II]λ3727. In Figure 5.6 (left) we compare the oxygen abundances derived using the PMC09 and PP04 calibrations for the galaxies in the two most populated clusters of our sample, and we can see a very good agreement. In Figure 5.6 (middle) we compare the oxygen abundances derived using the P10 and PMC09 calibration, for those galaxies with [O$\,$II]λ3727 measured. We see that the PMC09 calibration yields slightly higher metallicities ($\sim$ 0.1dex) than P10 calibration, in agreement with our previous considerations in Chapter 3. We find that Dors et al. (2011) models systematically underestimate metallicities for 12+log(O/H)<8.2. On the contrary, for 12+log(O/H)$\gtrsim$8.2, we find a good agreement with the empirical P10 estimates (see Figure 5.6, right).

In order to avoid limiting our sample only to galaxies with [O$\,$II]λ3727 measures, in the following we use the PMC09 calibration of the galaxy oxygen abundance.

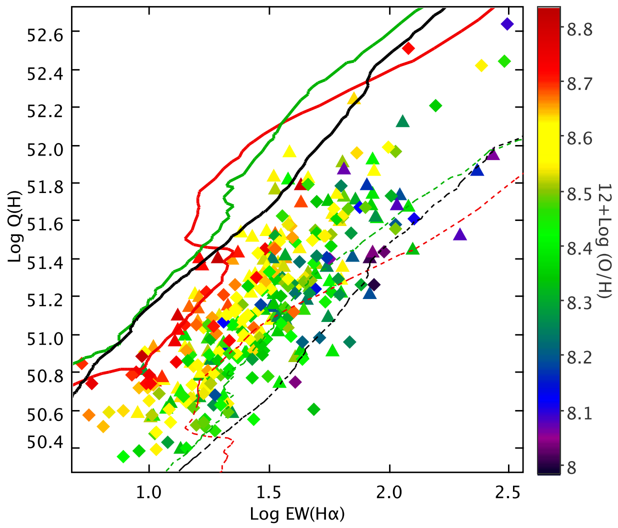

Figure 5.7: Number of ionized photons Q(H), as measured by the Hα flux of the SF region covered by the SDSS fiber, for our sample of SF dwarf galaxies in Coma (triangles) and A1367 (diamonds), vs. the EW(Hα), color coded to the derived galaxy metallicity. Lines represent the Starburst99 models Leitherer et al. (1999) for instantaneous bursts of total mass in massive stars $M_\star = 10^7 M_\odot$ (continuous) and $M_\star = 10^6 M_\odot$ (dashed) and metallicities $Z = 0.02$ (in red), $Z = 0.008$ (green), and $Z = 0.004$ (black).

We are aware that PMC09 could slightly overestimate ($\sim$ 0.1dex) the galaxy O/H abundance, but as discussed later on, we do not expect this to affect our discussion, as this analysis is based on the relative comparison of galaxy metallicities; thus no relevant effect is expected from the derivation of absolute abundances. Following Chapters 3 and 4, here we use again N2S2 calibration of PMC09 to derive N/O ratios for our SF dwarf galaxies.

In order to illustrate the properties of our galaxies, in Figure 5.7 we plot the Hα flux of the SF region covered by the SDSS fiber, for the SF dwarf galaxies in Coma (triangles) and A1367 (diamonds), vs. the EW(Hα). The Hα fluxes have been corrected for extinction (from the derived c(Hβ), see Section 5.3), and have been transformed to an equivalent number of ionizing photons $Q(H) = 7.35 \times 10^{11} \times L(\mathrm{H}\alpha)$, under the assumption that no ionizing photons escape the galaxies (Osterbrock 1989). The points are color coded to the derived galaxy metallicity. Then we add the loci of Starburst99 models (Leitherer et al. 1999) for instantaneous bursts of total mass $M_\star = 10^7 M_\odot$ (continuous lines) and $M_\star = 10^6 M_\odot$ (dashed lines) in massive stars for metallicities $Z = 0.02$ (in red), $Z = 0.008$ (green), and $Z = 0.004$ (black). According to these models, and assuming single bursts, the SF regions studied would span a mass range of $\sim 10^6 - 10^7 M_\odot$.

5.5 The mass-metallicity relation

In Figures 5.8 and 5.9 we plot the galaxy metallicity, as measured by 12+log(O/H), vs. galaxy stellar mass, for the SF dwarf galaxies in Coma (A1656, triangles), A1367 (stars), A779 (squares), and A634 (circles). Filled symbols correspond to galaxies to a distance $R \leq R_{200}$ from the cluster center. We see that the SF dwarf galaxies follow well defined sequences on these plots. Having a look at the MZR of Coma and A1367, we observe that at low galaxy masses ($10^8 M_\odot < M_\star < 10^9 M_\odot$), the derived metallicities cover a range of ~ 0.4 dex, while at higher masses ($10^9 M_\odot < M_\star < 10^{10} M_\odot$) the relation becomes tighter, appearing to shape a triangle instead of a simple linear correlation. Additionally, we observe that, for the same bin of mass, galaxies at $R \leq R_{200}$ are preferentially located at the upper part of the global sequences. For the two clusters (A779, A634) of lower mass, we do not verify neither of these two features, as we discuss in the following.

We first note that the behavior observed seems independent of the abundance calibration used. When we use the PP04 calibration of O3N2, we obtain the same mass-metallicity sequences and the SF dwarf galaxies in the core of Coma and A1367 still crowd the upper part of the MZR (we cannot do the same using P10 calibration because we do not have enough galaxies with measured [O II]λ3727 inside R_{200}). As a consequence, the effect observed seems to be significant, despite the intrinsic errors of the N2 and O3N2 calibrations.

Second, in Section 5.3 we have verified that our sample galaxies do not show any systematic differences regarding excitation, as a function of their location in the cluster (in or out R_{200}). Thus, the higher metallicities derived for galaxies at $R \leq R_{200}$, with higher [N II]λ6584/Hα, are not biased by excitation effects (see Berg et al. 2011, for a thorough discussion on this effect).

The third sanity check has been to test whether the position of the SF dwarfs at $R \leq R_{200}$ on the MZR, is the result of some bias in the mass estimate. We have found that galaxy stellar mass, vs. other galaxy properties, such as broad-band colors and excitation, do not show any correlated dependance of the cluster-centric distance of the galaxies. After all these tests, we assume that the shift observed toward higher metallicities, for galaxies at $R \leq R_{200}$, mainly in Coma, should not be the result of some bias in the abundance and/or mass estimates.

In order to explore further the trends that appear in Figures 5.8 and 5.9, we have performed a linear fit to the MZR of each cluster, considering first the galaxies at $R \leq R_{200}$, second the galaxies at $R > R_{200}$, and third all the galaxies together. In Table 5.3 we present the obtained slopes and the corresponding errors from the dispersion around the linear fit. We observe that the MZR fits for galaxies at $R > R_{200}$ have slopes ~ 0.3 for all the clusters of our sample, in agreement with our findings for low-mass galaxies in HSC (Section 4.4.4) and with Lee et al. (2006) result. As we discuss further in Chapter 7 this value of the slope is supported by the semi-analytic models and hydrodynamic simulations of Finlator & Davé (2008) and Davé et al. (2011) where momentum-driven wind scalings are introduced to explain the MZR.

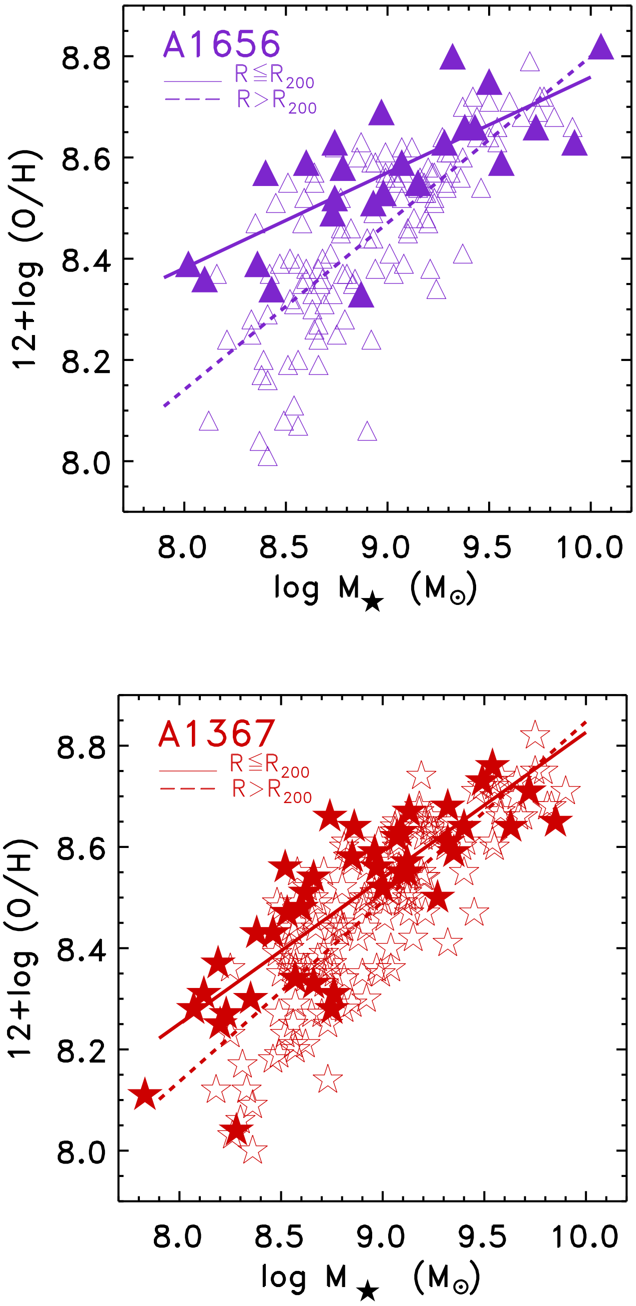

Figure 5.8: The oxygen abundance 12+log(O/H) versus stellar mass for SF dwarf galaxies in Coma (A1656, triangles) and A1367 (stars). Filled symbols correspond to galaxies at $R \leq R_{200}$. The continuous line is the linear fit for galaxies at $R \leq R_{200}$ and the dashed line the fit for galaxies at $R > R_{200}$.

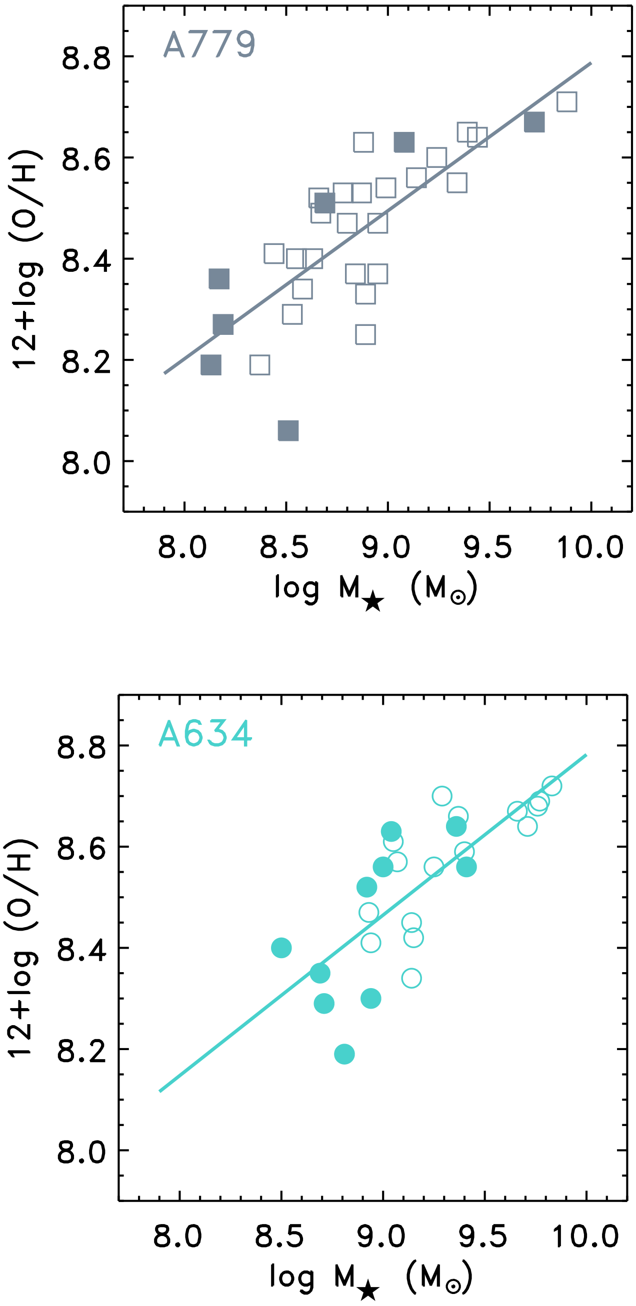

Figure 5.9: The oxygen abundance 12+log(O/H) versus stellar mass for SF dwarf galaxies in A779 (squares) and A634 (circles). Filled symbols correspond to galaxies at $R \leq R_{200}$. The continuous line is the linear fit considering all galaxies.

Table 5.3: **Slope of MZR fit**

Cluster	$R \leq R_{200}$	$R > R_{200}$	All
A1656	0.19 ± 0.03	0.33 ± 0.03	0.30 ± 0.02
A1367	0.28 ± 0.03	0.36 ± 0.02	0.33 ± 0.02
A779	0.30 ± 0.11	0.28 ± 0.05	0.29 ± 0.04
A634	0.37 ± 0.15	0.29 ± 0.07	0.32 ± 0.05

For Coma, and to less extent for A1367, a flattening of the MZR is observed when considering galaxies inside R_{200}, with the fits showing clearly smaller slopes, within the quoted errors (see Table 5.3). This is made evident in Figure 5.8, where we plot with a continuous line the linear fit for galaxies at $R \leq R_{200}$ and with dashed line the fit corresponding to galaxies at $R > R_{200}$.[1] For A779 and A634, considering the large errors (due to the reduced number of SF dwarf galaxies in these clusters), we do not appreciate any difference in the slope inside and outside the cluster core. In Figure 5.9 we plot the overall fit to the MZR for A779 and A634.

In Figures 5.10 and 5.11 we plot the N/O ratio vs. galaxy stellar mass, and again we find a good correlation, even tighter than the MZR, for all our clusters. Again, filled symbols correspond to galaxies to a distance $R \leq R_{200}$ from the cluster center. As before, galaxies in the cluster core of Coma and A1367 tend to crowd the upper part of the global sequence. Oxygen, produced in Type II SNe, is typically released after $\sim$10 Myr, while the bulk of nitrogen is produced and released over a substantially longer period, $\gtrsim$ 250 Myr. This is an important piece of information to take into account when one attempts to identify the mechanisms relevant for the chemical evolution of cluster galaxies. As we will discuss further in Chapter 7, this chemical "clock" seems to imply that if there is an environmental effect driving the observed difference in the abundance ratio, this should be acting since at least 10^8 yr ago.

Observing the triangular shape of the MZR of Coma and A1367 in Figure 5.8, we investigate whether there could be a physical cause for the galaxies showing lower metallicity for the same bin of mass. The MZR has been found to show a second parameter dependence on SFR (Ellison et al. 2008; Amorín et al. 2010; Mannucci et al. 2010; Lara-López et al. 2010; Cresci et al. 2012). This can easily be understood by the correlated behavior of gas-phase metallicity and SFR after a gas infall event: when a galaxy accretes metal-poor gas, its metallicity is diluted to values typical of lower mass galaxies, while its final mass increases, and consequently the galaxy moves below the MZR. In the same time, the presence of large amount of gas stimulates star formation, and this is the reason why galaxies with higher SFR have lower metallicities at a given stellar mass. This should be a transient phase,

---

[1] We note here that the class 2 population referred to in Section 5.2, span the higher mass range, where we have seen that the MZR becomes tighter, and had it been included, would not have significantly changed the derived slopes.

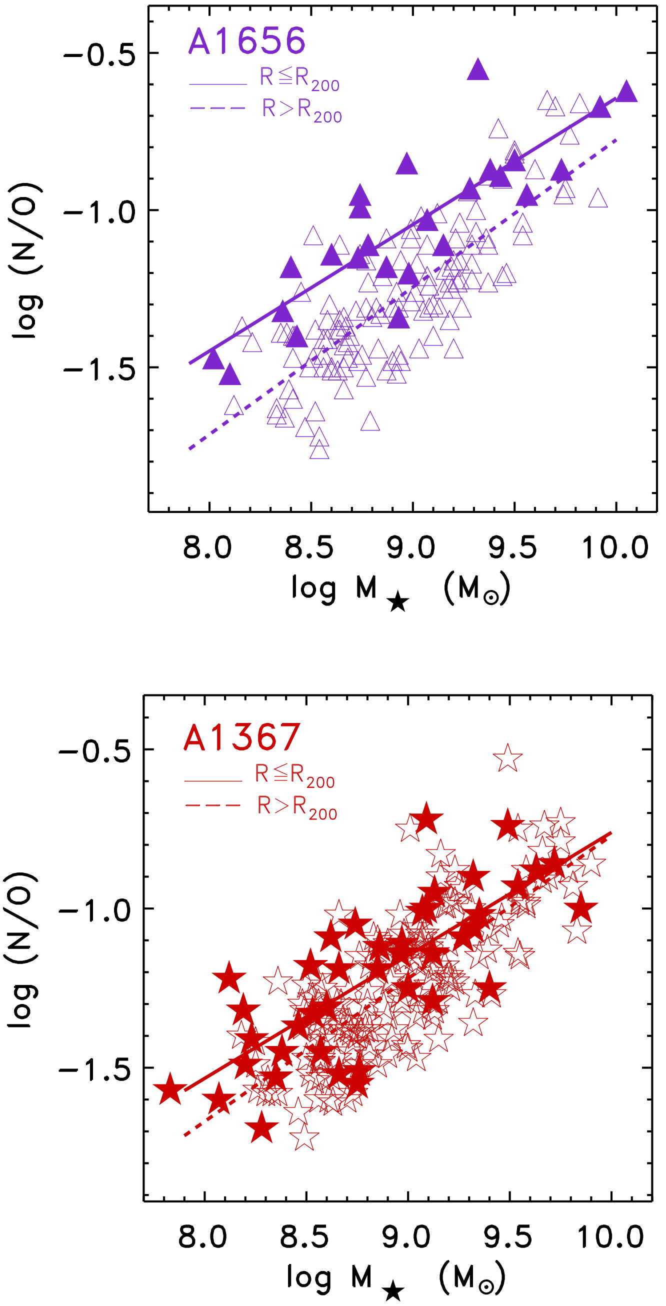

Figure 5.10: N/O versus stellar mass for dwarf SF galaxies in Coma (triangles) and A1367 (stars). Filled symbols correspond to galaxies inside R_{200}. The continuous line is the linear fit for galaxies at $R \leq R_{200}$ and the dashed line the fit for galaxies at $R > R_{200}$.

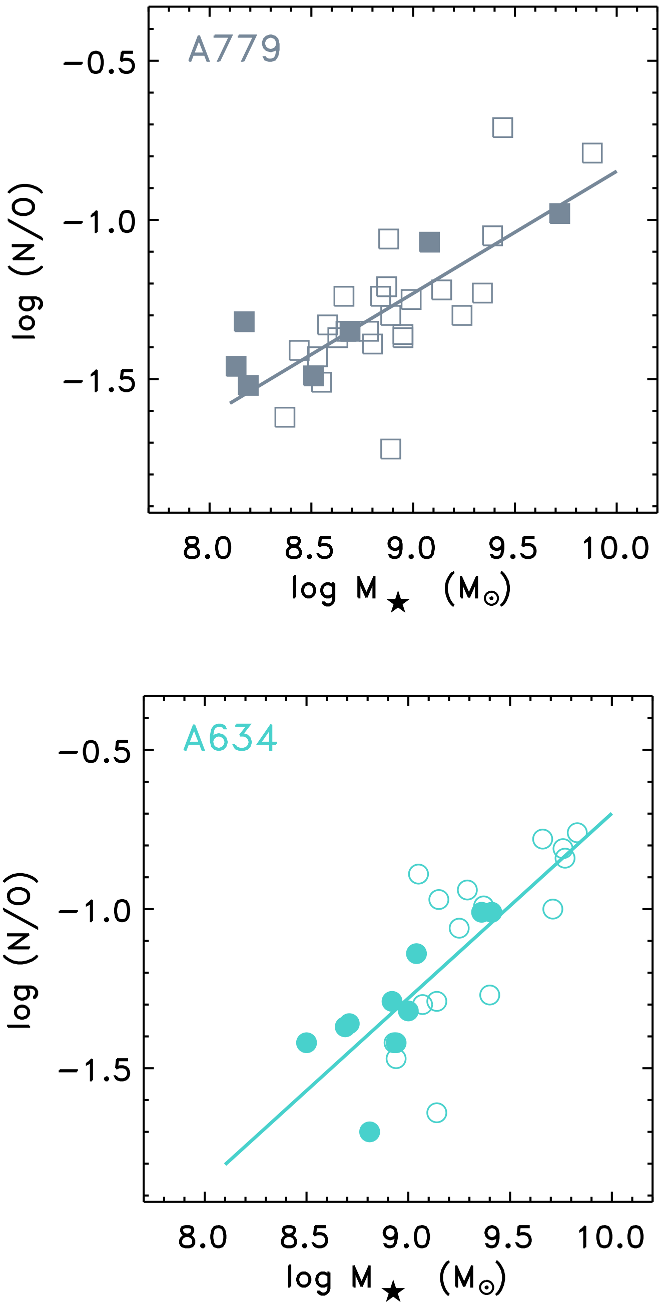

Figure 5.11: N/O versus stellar mass for dwarf SF galaxies in A779 (squares) and A634 (circles). Filled symbols correspond to galaxies inside R_{200}. The continuous line is the linear fit considering all galaxies.

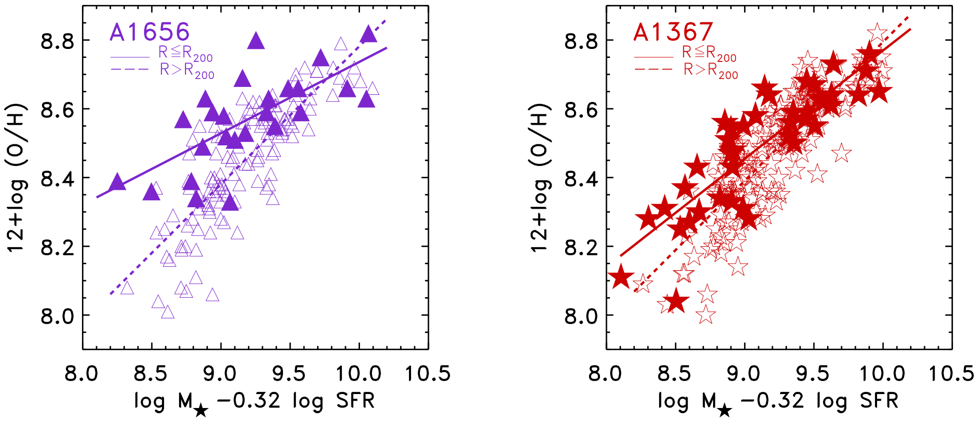

Figure 5.12: The oxygen abundance 12+log(O/H) versus the quantity $\mu = \log M_\star - 0.32\log(\mathrm{SFR})$ for SF dwarf galaxies in Coma (A1656, triangles) and A1367 (stars). Filled symbols correspond to galaxies at $R \leq R_{200}$. The continuous line is the linear fit for galaxies at $R \leq R_{200}$ and the dashed line the fit for galaxies at $R > R_{200}$.

and when the galaxy will consume the gas, producing the new metals, will return to the mean MZR (Davé et al. 2011; Dalcanton 2007).

Mannucci et al. (2010) claimed that the MZR is the projection in the two-dimentional (2D) space of a more fundamental 3D relation between stellar mass, gas metallicity and SFR and proposed the quantity $\mu = \log M_\star - 0.32\log(\mathrm{SFR})$ which defines a projection of the MZR that minimizes the scatter of local galaxies. We have used the median estimate of the total SFR provided by DR8 (Brinchmann et al. 2004) to explore whether the quantity μ could decrease the scatter observed in Figure 5.8. The SDSS SFR estimates have been derived by combining emission line measurements of the fiber spectrum and applying aperture corrections by fitting models to the photometry outside the fiber (as in Gallazzi et al. 2005; Salim et al. 2007). In Figure 5.12 we plot the oxygen abundance 12+log(O/H) vs. μ for the SF dwarfs in Coma and A1367, and we see that the scatter drops for the galaxies at lower metallicities for the same bin of mass (the Spearman's correlation coefficient increases from 0.73 in Figure 5.8 to 0.77 in Figure 5.12 for Coma, and from 0.80 to 0.83 for A1367). However, the separation we observe in the MZR between galaxies inside and outside R_{200} is kept equally.

Moreover, in this metal dilution scenario, the N/O ratio should not be affected (e.g., the "green pea" galaxies show normal N/O ratios for their mass, Amorín et al. 2010), and the relation between N/O vs. stellar mass should not show correlated scatter. However, as Figure 5.10 shows, the N/O ratio segregates galaxies inside R_{200}, these galaxies also showing higher N/O ratios for the same bin of mass. The effect of infalling gas is expected to be more relevant for galaxies at high redshift (e.g. Cresci et al. 2010; Tacconi et al. 2010; Dekel et al. 2009), thus the fundamental metallicity relation introduced by Mannucci et al. (2010) considerably accounts for the evolution of the MZR with redshift (Erb et al. 2006; Maiolino et al. 2008; Mannucci et al. 2009). But in the local Universe, where our clusters are located, different mechanisms should be invoked to explain the trends observed.

The question arises now as to whether the galaxies inside R_{200} have evolved in a different way than the other cluster galaxies, rendering them chemically more enriched than the galaxies at $R > R_{200}$, or alternatively whether less metallic galaxies, for the same bin of mass, are more vulnerable to the quenching effect of the cluster environment, and this could be the reason we do not observe them preferentially in the cluster core. To investigate the second idea we searched whether there is any observable trend with the distance from the cluster center of the morphological type of our sample of SF galaxies.

We have calculated the standard concentration index $C = R90/R50$, where $R90$ and $R50$ are the radii enclosing 90% and 50% of the Petrosian r-band luminosity of the galaxy. We have found that our sample galaxies show typical C values as related to late-type galaxies ($\sim 2.3-2.5$, see e.g., Shimasaku et al. 2001; Strateva et al. 2001) and we see no trend of the C value in and out R_{200}. We have additionally checked that galaxies in the same bin of mass do not show any concentration-metallicity correlation. A more detailed morphological study could be of interest here; Penny et al. (2011) found remarkably smooth structures of dwarf galaxies in the Perseus cluster, and suggest that dwarfs in cluster cores should be highly dark matter dominated to prevent their tidal disruption by the cluster potential. In the present study we cannot verify the hypothesis that SF galaxies inside R_{200} are more concentrated/compact, and consequently more resistant to the hostile cluster environment. Thus, morphology does not seem to explain their relative position in the upper part of the MZR; this should be the result of some different evolution.

To investigate whether the scatter observed in the MZR could be related to differences in the underlying stellar population, we have obtained for all our cluster galaxies the spectral index D_n (4000) (Balogh et al. 1999), after correction for emission lines, as given by SDSS DR8. All our SF dwarfs show $D_n(4000) < 1.4$, which corresponds to typical ages < 1 Gyr. Additionally, we have seen that the gas-phase metallicity does not show any correlated behavior with the age of the underlying population. In Section 5.3 we have shown that SF dwarfs at $R \leq R_{200}$ in Coma do not show any observable difference in the $g - i$ color distribution as compared to the galaxies at $R > R_{200}$. Thus, the more metallic SF dwarf galaxies found in the cluster core, specially of Coma, are neither older nor redder than the rest of SF galaxies.

To quantify the effect observed in the MZR for Coma and A1367, in the upper panel of Figure 5.13 we plot the mean difference of the derived 12+log(O/H) abundance for each galaxy with respect to the 12+log(O/H) given by the linear fit, as a function of the cluster-centric radial distance, sampled in a bin of 0.5 R_{200}. The errors correspond to the standard deviation from the mean value of log(O/H)-log$(\mathrm{O/H})_{\mathrm{fit}}$. In the lower panel we plot the same for the log(N/O) ratio. We observe that in Coma, the mean difference in 12+log(O/H), in the closest bin to the cluster core, is positive and above the rms error (i.e. positive for all objects), and can reach

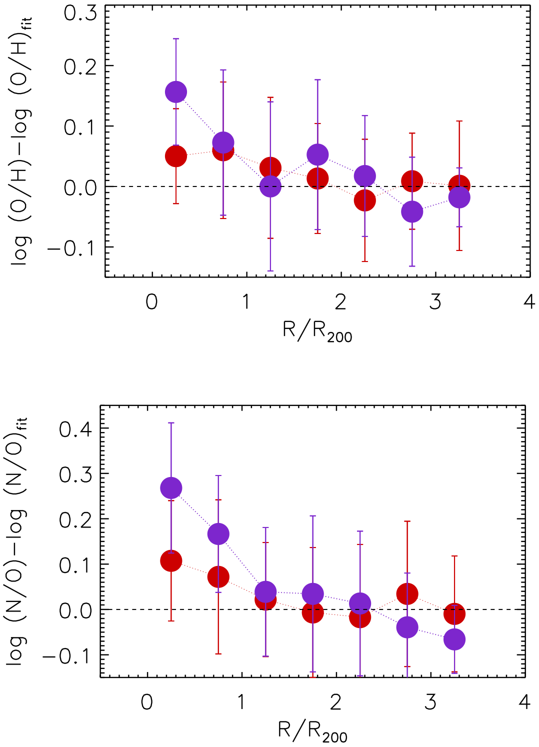

Figure 5.13: Upper panel: the difference of the derived oxygen abundance 12+log(O/H), for each galaxy, with the oxygen abundance given by the linear fit 12+log(O/H)$_{\rm fit}$, as a function of the cluster-centric radial distance R/R_{200}, in a bin of 0.5 R_{200}. Lower panel: the same for log(N/O). The blue points correspond to Coma and the red points to A1367. The errors indicate the rms of the mean value in each bin.

above $\sim$ 0.15 dex. The same is found for the log(N/O) ratio, which can get up to $\sim$ 0.27 dex difference in the cluster core. In A1367 smaller differences are obtained, of $\sim$ 0.05 dex in log(O/H) and $\sim$ 0.1 dex in log(N/O). This divergence, combined to the fact that for the low-mass clusters of our sample, this trend has not been revealed at all, seem to indicate that the cluster mass is a most relevant parameter. As it will be discussed in Chapter 7, what seems to drive the disparate evolution of SF dwarf galaxies in Coma appears to be related to the properties of the forceful ICM of this cluster.

We explore the dependence of the trend observed for our cluster galaxies as a function of the local galaxy density, using the density estimator $\Sigma_{4,5}$, defined as the logarithm of the density obtained to the average of the projected distances to the fourth and fifth nearest neighbors, including all galaxies with SDSS spectra, within the cluster region (used in the previous Chapters, formula 3.2). In the upper panel of Figure 5.14 we plot the mean difference of the derived 12+log(O/H) for each galaxy with respect to the 12+log(O/H) given by the linear fit, as a function of

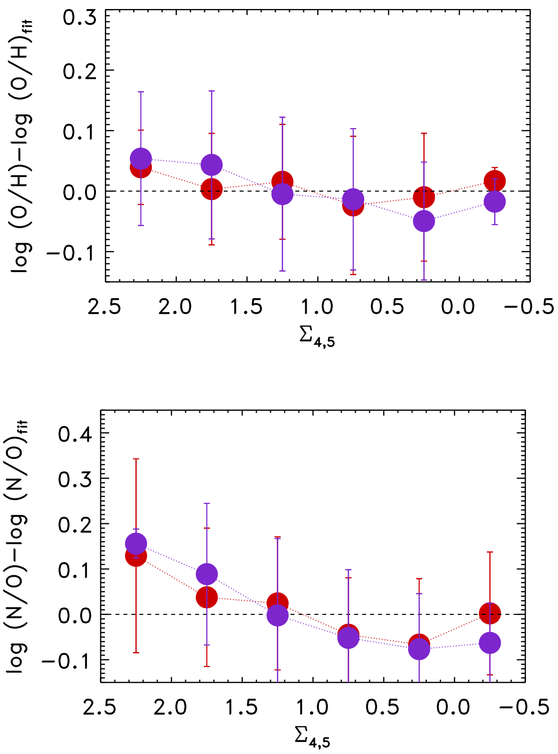

Figure 5.14: Same as in Figure 5.13, as a function of the local galaxy density $\Sigma_{4,5}$ in a bin of 0.5 dex.

$\Sigma_{4,5}$, in a bin of 0.5 dex. The errors correspond to the standard deviation from the mean value of log(O/H)-log(O/H)$_{\rm fit}$. In the lower panel we plot the same difference for the log(N/O) ratio. In the highest local density bin we find a mean difference in log(O/H) of ~ 0.05 dex for both Coma and A1367, in agreement with the previous findings (e.g. Ellison et al. 2009). Finally, log(N/O) presents a measured difference of ~ 0.15 dex for both clusters.

We note here that estimating the local galaxy density for clusters with large velocity dispersions as in Coma (σ_v ∼1000 km s^{-1}) and A1367, bears significant hazards. Allowing neighbors to have velocity differences of the order of σ_v, could result in counting out galaxies in the cluster core, and thus underestimating density. Conversely, allowing velocity differences of $2\sigma_v$ or $3\sigma_v$ could introduce a severe bias to relatively isolated objects, overestimating their density. In Figure 5.14 we use $\Sigma_{4,5}$ derived permitting neighbors to have velocity differences of 2000 km s^{-1}, but we have checked that the behavior does not change using velocity difference of σ_v, $2\sigma_v$, and $3\sigma_v$.

Previous works have pointed out the effect of the environment on the gas-phase metallicity of galaxies (Mouhcine et al. 2007; Cooper et al. 2008; Ellison et al. 2009) and have found that galaxies within dense environments show statistically higher metallicities of ~ 0.05 dex at the same bin of galaxy mass. These works, however, have related this behavior to local galaxy density. Specially Ellison et al. (2009) have discussed the importance of cluster membership, and although they have found that enhanced metallicities are present at distances $R < R_{200}$ from the cluster center, they have concluded that the enhancement observed is driven by local overdensity and does not depend on cluster properties such as R_{200}, σ_v, or cluster mass.

There is a general good relation between the cluster-centric distance and the local galaxy density, within the cluster virial radius (e.g., Rines et al. 2005), so the metallicity enhancement of the cluster core galaxies is expected to appear as a function of the local galaxy density as well. However, in the present work we find that the enhancement of the gas-phase metallicity is sensitive to the cluster mass, and appears to be more prominent if we consider the R_{200} region of a massive cluster such as Coma. This evidence points towards a possible connection of the chemical enrichment of cluster galaxies with their ICM properties.

5.6 Chemical enrichment versus HI mass

In clusters, the gas interchange of a galaxy with its environment is expected to be very relevant. Evidences of ongoing gas stripping, both in low and high luminosity galaxies, have turned out to be frequent in local Universe clusters, such as the Virgo cluster (Abramson et al. 2011; Kenney & Koopmann 1999), A1367 (Gavazzi et al. 2001), and A3627 (Sun et al. 2007). In the Coma cluster core several galaxies have been observed showing Hα or ultraviolet tails (Yagi et al. 2010; Smith et al. 2010), clear sign of ongoing gas stripping. Another evidence suggesting gas stripping in clusters are the observed truncated ionized gas disks (Koopmann & Kenney 2004; Koopmann et al. 2006; Cedrés et al. 2009).

Recently, Jaffé et al. (2011), based in a large sample of emission line galaxies from the EDisCS[2] sample at intermediate redshifts ($0.4 < z < 1$), found that the fraction of kinematically disturbed galaxies increases with cluster velocity dispersion and decreases with distance from the cluster center, but remains constant with projected galaxy density. In addition, disturbed gas kinematics does not co-occur with morphological distortions as traced by optical (*Hubble Space Telescope*) imaging, suggesting the mechanism that affects most the gas of cluster galaxies has to be linked with the ICM.

The atomic gas is expected to be the first to suffer the RPS in the cluster environment. HI deficiency and disturbed HI morphologies of cluster galaxies have long been observed in several nearby clusters (e.g. Cayatte et al. 1990; Bravo-Alfaro et al. 2000; Vollmer et al. 2001; Kenney et al. 2004; Vollmer et al. 2004; Balkowski & Chemin 2005; Chung et al. 2009). Additionally, because of the shallower gravitational potentials, dwarfs can be extremely fragile to RPS (Solanes et al. 2001).

An interesting method to check for modulations of the HI content of SF galaxies is through comparing the galaxy chemical enrichment with the theoretical values

---

[2] European Southern Observatory Distant Cluster Survey

predicted by the "closed-box" model (Edmunds 1990). According to this model, the mass fraction of metals should be a direct function of the gas mass fraction:

$$\mu = M_{gas}/(M_{gas} + M_{\star})$$

Here, the gas mass is considered to be the mass of HI ($M_{\rm HI}$) with a correction for neutral helium $M_{gas} = 1.32 M_{\rm HI}$. We neglect the contribution due to molecular hydrogen, as this seems to be small and difficult to evaluate. According to Israel (1997), for Magellanic type irregular galaxies, the H_2/HI mass ratio is 0.2, which would mean an increase of 0.08 dex in the M_{gas} estimate. However, the CO to H_2 conversion relation is not well known for low metallicity systems and the H_2 fraction might be even higher (e.g. Keres et al. 2003).

Comparing with chemical evolution models is actually possible only when information on the HI mass of a galaxy is available. Two of our sample clusters have recently published HI data. Cortese et al. (2008b) have presented 21 cm HI line observations of the central part of A1367, as part of the Arecibo Galaxy Environment Survey (AGES). This sample covers $\sim 20\%$ of the total region covered by our sample and $\sim 70\%$ of the region with $R \leq R_{200}$ and their HI lower mass limit, at A1367 distance, is $6 \times 10^8 \rm M_{\odot}$. They have detected 57 galaxies that belong to A1367 cluster, out of which 17 also belong to our sample of SF dwarf galaxies. Haynes et al. (2011) have recently released a catalog with 21 cm HI line sources, covering $\sim 40\%$ of the final ALFALFA[3] survey area. This release includes $\sim 50\%$ of the area of Coma covered by the present work, also $\sim 50\%$ of the area with $R \leq R_{200}$, and their low HI mass limit at the Coma cluster distance, is $\sim 4 \times 10^8 \rm M_{\odot}$ ($M_{\rm HI} > 10^7 M_{\odot}$ at the Virgo cluster distance, Giovanelli et al. 2005). We have found 31 objects in common with our sample of SF dwarf galaxies.[4]

In Figure 5.15 (left) we plot the oxygen abundance vs. the gas mass fraction (in the form $\log \ln 1/\mu$) for Coma (triangles) and A1367 (stars) for the galaxies we have HI data (filled symbols mean $R \leq R_{200}$). In Figure 5.15 (right) we plot the gas mass fraction μ vs. the stellar mass. We add (with smaller points) all the SF dwarf galaxies of our sample that do not have HI measurements, but they are located within the regions mapped by AGES and ALFALFA (up to the present release). We assign to these galaxies the HI mass detection limit of each survey, this being an upper limit of the HI mass of these galaxies (the arrows indicate the direction to which these upper limits could be displaced). Again, open and filled small symbols mean outside and inside the cluster R_{200} respectively.

We observe that Coma dwarf galaxies located to distances $R \leq R_{200}$ (filled triangles), all except one, have been assigned an upper limit. In contrast, inside R_{200} of A1367 we have both upper limits and detections. This could be an evidence of the stronger and more effective ram-pressure exerted by the ICM of Coma than that of A1367. Tecce et al. (2010) have found that at low-z, the mean ram-pressure

---

[3] Arecibo Legacy Fast Arecibo L-band Feed Array (ALFALFA).

[4] We have derived the $M_{\rm HI}$ using the standard formula $M_{\rm HI} = 2.36 \times 10^5 D^2 F_{\rm HI}$ (Haynes et al. 2011) and adopting the same mean distance D for all cluster galaxies.

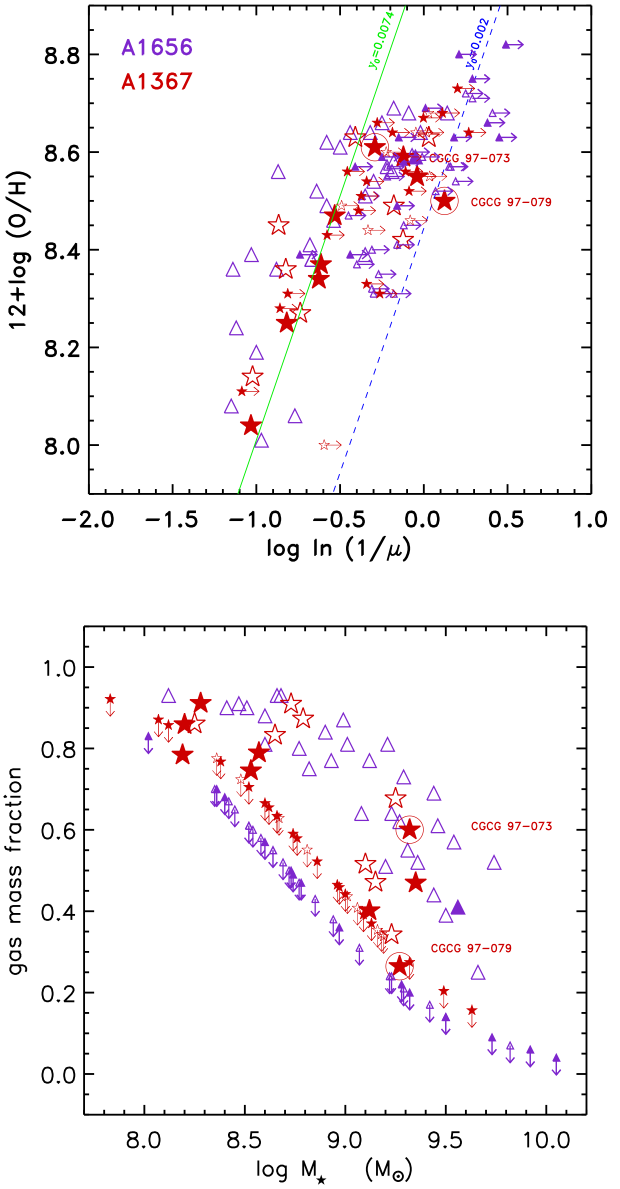

Figure 5.15: Upper panel: the oxygen abundance vs. the gas mass fraction for Coma (triangles) and A1367 (stars, filled symbols mean $R \leq R_{200}$), for the galaxies within the covered regions by AGES and ALFALFA. The green continuous line indicates the theoretical yield $y_o = 0.0074$, and the blue dashed line corresponds to a lower yield $y_o = 0.002$. Lower panel: the gas mass fraction μ vs. the stellar mass. Small points in both plots represent HI mass upper limits for the galaxies included in the surveyed regions but not having HI measurements. The arrows indicate the direction to which these upper limits could be displaced.

is $\sim 10^{-11}h^2$ dyn cm^{-2} in clusters with virial masses $\sim 10^{15}M_\odot$, while in lower mass clusters of $\sim 10^{14}M_\odot$, the mean ram pressure is approximately one order of magnitude lower. At distances $R > R_{200}$ (open triangles), there are measured HI masses as well as upper limits for both clusters. Theoretical models have started to investigate the effects of the ICM turbulence, substructure and shocks during groups infall, finding that RPS can be effective even at the cluster outskirts and filaments, as well as during tidal interactions (e.g., Tonnesen & Bryan 2008; Kapferer et al. 2008).

We then compare the position of our galaxies in the left plot of Figure 5.15, with model predictions for the yield. The green continuous line indicates the model value $y_o = 0.0074$, that is the theoretical yield of oxygen expected for a Salpeter IMF and constant star formation rate, for stars with rotation following Meynet & Maeder (2002) models (van Zee & Haynes 2006). Both, infall and outflow of well-mixed material will result in effective yields that are less than the true yield, as the enriched material is either diluted or lost from the system. The blue dashed line corresponds to a lower yield $y_o = 0.002$, almost $1/4$ of the model prediction, which is the effective yield found for a fraction of the sample of isolated dI galaxies of van Zee & Haynes (2006).

Some of the SF dwarf galaxies located at cluster-centric distances $R > R_{200}$ in both clusters, and a fraction of the SF dwarfs in A1367 cluster core ($R \leq R_{200}$), appear to follow the theoretical "closed-box" model predictions (considering our metallicity typical uncertainty ~ 0.1 dex, see Section 5.4). These galaxies in the core of A1367 could be "newcomers" (as those identidied in A2151, see Section 3.11), observed before the action of RPS lowers significantly their atomic gas content, shifting them towards lower effective yield values.

We also observe a tendency to lower effective yields as metallicity increases, suggesting that these galaxies host lower HI mass than the expected by the "closed-box model". A similar behavior was found for A2151 SF galaxies in Section 3.22. The atomic gas deficiency is confirmed when we compare the HI content of our sample galaxies (measurements or upper limits) with the $M_{\rm HI}$ of field counterparts of the same absolute magnitude, as calculated following Toribio et al. (2011). Two representative examples are the dwarf galaxies CGCG 97-073 and CGCG 97-079 (marked on the plot) that have been investigated before (Iglesias-Páramo et al. 2002; Gavazzi et al. 2001), showing long (Hα) tails that reveal their recent interaction with the ICM. The HI content of CGCG 97-079 appears to be severely affected: this galaxy has the lower HI mass detected and lays below $y = 0.002$ in the left panel of Figure 5.15. CGCG 97-073 in turn does not appear to have lost a large amount of HI yet.

We conclude that, to the distance of Coma and A1367, given the detection limit of the HI data, we observe the atomic gas of galaxies that still contain a substantial fraction of their HI mass. The almost absolute lack of detections in the central part of Coma, indicates that galaxies there have been severely affected by the cluster environment, and the RPS has partly or completely removed their atomic gas content, rendering them undetectable in 21 cm HI line. In turn, in the central part of A1367 there are some SF dwarf galaxies still with detectable HI mass (i.e. possible "newcomers").

5.7 Summary and conclusions

In this work we have studied the chemical history of low-mass SF galaxies in four clusters in the local Universe. The sample clusters belong to a semi-spheric shell of the local Universe ($\delta \gtrsim$ -25 deg and $0.02 < z < 0.03$) and span a mass range from 10^{13} to $10^{15} M_{\odot}$. The regions studied cover the clusters' core up to $3R_{200}$. We have been searching for the potential imprints of the cluster environment on the galaxy chemical enrichment.

We have used the latest SDSS spectroscopic release DR8. SF galaxies have been selected on the basis of their SDSS emission line fluxes, and a limit in magnitude has been applied to select dwarf galaxies. Considering low-mass galaxies, aperture biases are not expected to be important. We note that DR8 spectroscopic data have been corrected for the underlying stellar continuum; this being an important improvement when studying nebular gas properties. We have found that our SF dwarf galaxies show typical line ratios of normal HII galaxies.

Gas-phase metallicities of the O/H and N/O ratio, have been derived carefully using different empirical and model calibrations. The accurate mass estimates provided by SDSS DR8 have been used, to derive the MZR of the cluster galaxies. Well defined sequences have been found in the MZ plane, and we have observed a decrease of the scatter when the correction for the SFR has been applied. The value derived for the slope of the MZR is in agreement with the predictions of hydrodynamic models, which use momentum-driven winds to reproduce the MZR. Well defined sequences have also been derived in the N/O vs. mass plane.

For the more massive clusters of this sample, Coma and A1367, the galaxies located at cluster-centric distances $R \leq R_{200}$, are preferentially located at the upper part of the global sequences of O/H and N/O vs. mass. This increase in metallicity is mass dependent, being higher at the lower mass bins, and in the core of Coma reaches on average ~ 0.15 dex in O/H. This effect yields the flattening of the MZR for SF dwarf galaxies within the core of these massive clusters.

The metal enhancement of SF dwarfs in the cluster core has been found to be more important when considering the R_{200} region of the most massive cluster Coma ($M \simeq 10^{15} M_{\odot}$). Despite the general good relation of local galaxy density with cluster-centric distance, this effect appears diluted in terms of local galaxy density, suggesting that the relevant parameter able to affect the chemical evolution of SF dwarf galaxies should be the presence of a dense ICM.

Finally, we have related the metallicity of our SF dwarf galaxies, with their HI mass content, derived using available 21 cm data. We then have compared with the predictions of the so-called "closed-box" model and the normal HI content of isolated counterparts, and we have found that SF dwarf galaxies in the cores of A1367 and Coma should be suffering an important RPS.

CHAPTER 6

Future Work

Contents

6.1 3D spectroscopy of a ram-pressure stripped galaxy in A1367

6.1.1 Introduction

CGCG097-73 is an Irr ($M_g = -19.1$ mag) galaxy located at 98 Mpc, in the A1367 cluster[1] (Figure 6.1, left). It shows a total Hα luminosity $L_{H\alpha} = 1.45 \times 10^{41}$ ergs s^{-1}, derived using the Hα total flux given by Iglesias-Páramo et al. (2002), considering H_0=73 km s^{-1} Mpc^{-1}, correcting for extinction using the derived c(Hβ) from Chapter 5, and for the [NII]λ6584 contribution, using Equation 3.3. This $L_{H\alpha}$ is converted to SFR $\sim 1.2 M_{\odot}$/yr using Kennicutt (1998) calibration.

Its SF regions form a bright arc on the side of the galaxy facing the cluster center. The galaxy is quite anemic on the opposite side, forming a "jelly-fish" morphology (Figure 6.1, right), highlighted by that side long Hα tail, extending ~75 kpc (Figure 1.6, Gavazzi et al. 2001). Similar morphologies have been observed in SF galaxies in local Universe clusters (e.g. Sun et al. 2007; Yagi et al. 2010) and are associated with the interaction with the ICM. The "bow-shock" morphology with the large scale gaseous tail and the chain of ongoing massive starbursts indicate that CGCG097-73 is in the course of its first infall toward the dense cluster region.

---

[1] We attribute to the galaxy the distance of cluster A1367, not the distance derived from its own radial velocity.

Significant infall of late-type galaxies into dense cluster regions is taking place along the filamentary structures that compose the cosmic web. RPS has been invoked as the responsible process for the gas ablation and the eventual truncation of star formation. Before this fateful "switching off", galaxies may experience a burst of pressure-triggered star formation (see Section 1.2.1). The characteristics of such a starburst event are the subject of this study. We analyze the stellar and gaseous physical properties of CGCG097-73 searching for the imprints of its interaction with the X-ray emitting ICM.

6.1.2 PPAK 3D spectroscopy

We have obtained PMAS/PPAK spectroscopy at CAHA 3.5m telescope on 26 Mar 2009. PMAS (Potsdam MultiAperture Spectrophotometer) is an integral field unit (IFU) which is used to obtain spatially resolved spectroscopy, usually called 3D spectroscopy. Figure 6.2 illustrates the basic concept of the integral field spectroscopy, consisting in the use of fibers in order to obtain simultaneously spectra in a two-dimensional field. PPAK is a hexagonal configuration with a field of view 74×65 arcsec^2. It consists of 382 fibers (331 for object, 36 for sky, and 15 for calibration) with a spatial sampling of 2.7 arcsec per fiber. The characteristics of the observations we obtained are shown in Table 6.1.

The PPAK data reduction and the cube analysis are in progress, using IRAF, R3D and E3D routines. We reduce the images in a standard way, with following the steps: bias correction, extraction of 1D spectra, lambda calibration, dispersion cor-

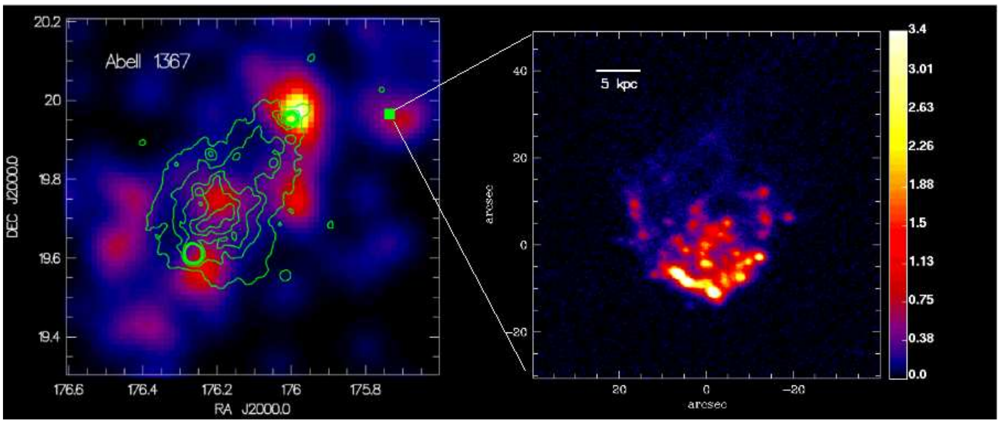

Figure 6.1: Left: Galaxy density map of A1367 ($\sim 0.7 R_{200}$) using SDSS DR8 spectroscopic data. Cluster membership is defined combining velocity and position information as in Chapter 5. Green contours represent the ROSAT-PSPC X-ray emission. The clumpy structure of both the density map and the X-ray emission highlight that A1367 is a merging cluster. The green point represents the position of CGCG097-73. Right: Hα image of CGCG097-73 from the deep Hα survey of A1367 (Iglesias-Páramo et al. 2002) in units 10^{15} erg s^{-1} cm^{2} Å^{-1}. we can disintegrate individual starburst "knots".

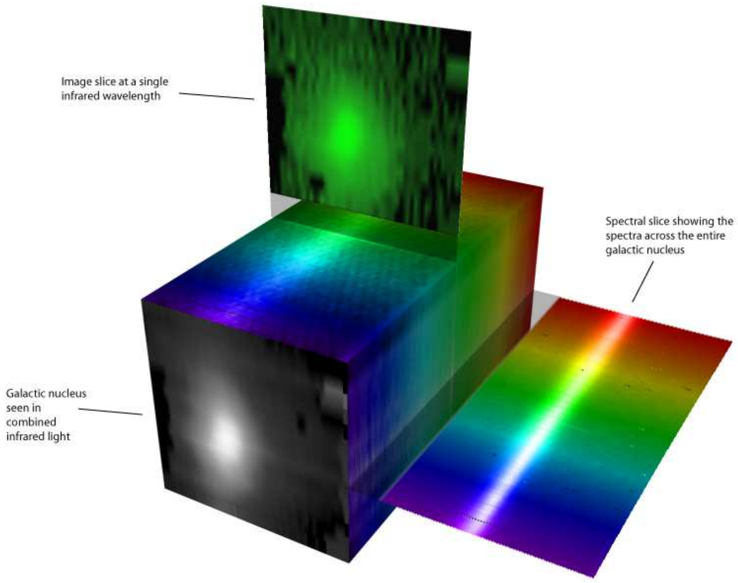

Figure 6.2: An illustration of the data obtained with an IFU. Image credit: Stephen Todd, ROE and Douglas Pierce-Price, JAC.

Table 6.1: **PMAS/PPAK spectroscopy on 26 Mar 2009**

Grating:	R600
Spectral range:	$\sim$5300-6950 Å
Dispersion:	0.75 Å pix^{-1}
Dithering:	3 positions with: $\Delta\alpha = -1.56$”, $\Delta\delta = \pm 0.78$”
Exposure time:	1200 sec
Airmass:	$\sim$1.05

rection, flat field correction, sky subtraction, and flux calibration. Then, we obtain the cube by combining the 3 dithered exposures. On each one of the 1D spectra we extract for the whole 2D surface of the galaxy, we apply Gaussian fits to measure emission lines: Hα, [NII]$\lambda\lambda$6548,6584, [SII]$\lambda\lambda$6717,6731, [OI]λ6300, HeIλ5876. As an example in Figure 6.3 we show to the left the 2D map of Hα and to the right the 1D-spectra of three starburst regions: they appear to be objects of relatively low metallicity and their densities could show mild variations.

In Figure 6.4 we show some preliminary results. In the left plot we present the 2D velocity map ΔV of the galaxy, with respect to the central galaxy velocity $V_{\rm gal}$=7280 km s^{-1}. We can see a clear velocity gradient and the observed 2D pattern may suggest the presence of a distorted rotating disk, with an approximate max velocity difference larger than the rotation velocity derived for M33 (V_{rot}= 100 km s^{-1}, $M_{\rm B} = -18.94$ mag) and NGC300 (V_{rot}= 90 km s^{-1}, $M_{\rm B} = -18.13$ mag, the rotation velocities and absolute magnitudes for these two galaxies are driven from

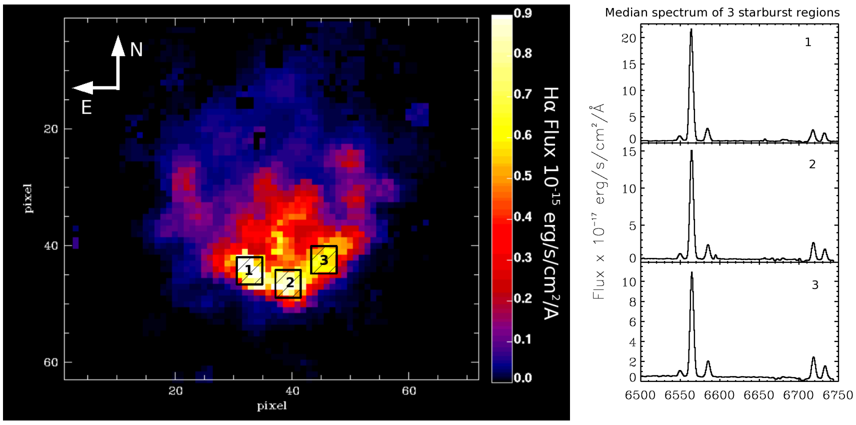

Figure 6.3: Left: Hα emission in 2D derived by the PPAK cube. Gaussian fits have been applied for the line measurements in each spectrum of the cube. Right: The emission-line spectra of the three indicated starburst regions. The main lines used in our analysis are visible: Hα, [NII]$\lambda\lambda$6548,6584, [SII]$\lambda\lambda$6717,6731.

HyperLeda catalog). The velocity gradient is strikingly asymmetric, reproducing the head of "jellyfish" morphology of the Hα. The 2D kinematic information reveals how the velocity field of the gas at the leading edge of the galaxy is being distorted, while entering through the intracluster medium at high pressure. The infall direction, as suggested by the direction of the tail (Figure 1.6) is North to South, while the left plot of Figure 6.4 shows that the max velocity gradient is rather oriented towards the South West, thus projection effects should be considered carefully.

In Figure 6.4, right we derive the RS2=[SII]λ6717/[SII]λ6731 index map, which gives information on the gas density. Curiously, it seems to indicate that the ionized gas at the heading starburst knots appears systematically less dense than that of the opposite side of the galaxy, thus further investigation of the gas origin and its physical conditions is underway. Additionally we are currently producing the 2D maps of [NII]λ6584/Hα and HeIλ5876 in order to study the ionization state of the gas, and the [OI]λ6300 to study possible shock effects in the diffuse gas.

6.1.3 Work in progress

We will investigate further the impact of the cluster environment on the galaxy evolution, specially during the first encounter with the hot ICM, using our multifrequency photometry of CGCG097-73 to derive the physical properties (e.g. mass, age, SFR) of the individual starburst "knots". Hα and broad-band r imaging have been obtained with INT2.5m and WHT4.2m, under excellent seeing conditions (0."85) providing high resolution images. Additional narrow band [OIII]λ5007 and adjacent continuum images have been obtained with ALFOSC at NOT2.5m. NIR imaging has been obtained with NICS at TNG3.6m. Finally, GALEX-UV and SDSS photometry are also available. We plan to use SED-fitting to these photometric data, using the European Virtual Observatory tool VOSA, where the libraries of PopStar

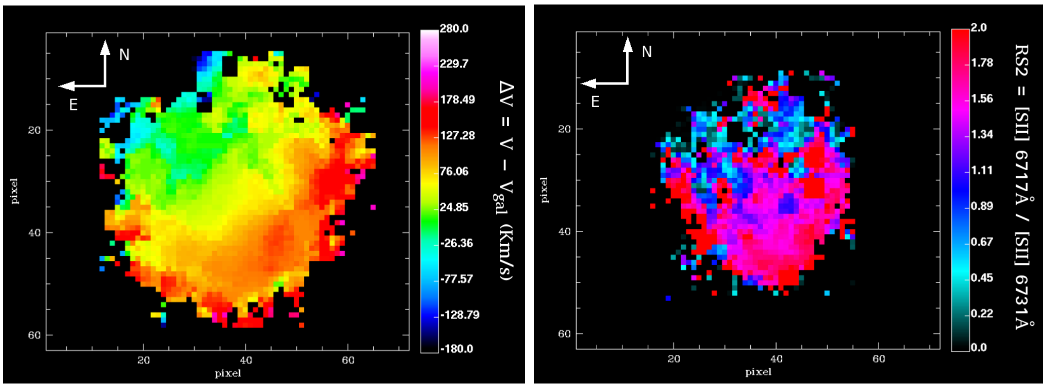

Figure 6.4: Left: Velocity map ΔV, with respect to the central galaxy velocity $V_{\rm gal}$=7280 km s^{-1}. The velocities have been derived using the central wavelength of the Gaussian fitting on Hα. Right: The RS2=[S II]λ6717/[S II]λ6731 index map gives 2D information on the gas density.

(Mollá et al. 2009) have been introduced.

The goal is to derive the properties of the very young stellar objects formed in the observed starburst event, and give observational constraints on the effect of ram-pressure triggered star formation predicted by hydrodynamical simulations (Kronberger et al. 2008; Kapferer et al. 2009).

6.2 Multifiber spectroscopy of star-forming galaxies in nearby clusters

6.2.1 Introduction

Reverte (2008) presented a wide field deep Hα survey of galaxies in nearby clusters ($z \sim 0.02$, also see Chapter 2). For each cluster a field of ($\approx 1° \times 1°$) was observed. This work resulted in an exhaustive catalog of Hα emitting sources in clusters, down to a luminosity of L(Hα)$\approx 10^{39}$ erg s^{-1}, comparable to the luminosity of the large SF complexes in nearby spiral galaxies.

Three out of the five clusters of Reverte (2008) sample have never before been observed spectroscopically: A539, A400, A2666. Thus, we have started the spectroscopic follow-up of the new sample of emission-line galaxies in these three clusters, taking new observations with the multiobject spectrograph WYFFOS at the WHT4.2m. WYFFOS is ideal for our purposes, offering simultaneous observations of a large number of objects. This spectroscopic information will permit to obtain a precise measurement of the redshift of the galaxies, apart from their physical and chemical properties. Moreover, the effects of the environment on the chemical history of these SF galaxies will be investigated, focusing on the study of the mass-metallicity and luminosity-metallicity relations, and the comparison of these relations with those of field galaxies and the predictions of chemical evolution models.

Important emphasis will be given in the study of the low-luminosity SF galaxies. Reverte (2008) work unveiled a significant population of these low-luminosity emission line galaxies in each cluster, and derived their 2D spatial distribution. Figure 6.5, for example, shows the spatial distribution of the number density of all the SF galaxies detected in A539 (upper panel), and of the bright (down to the left) and the faint population (down to the right) separately. The contours correspond to the galaxy number density derived with 2MASS data. We see that the spatial distribution of faint SF galaxies does not follow so well the 2MASS density contours, forming a secondary maximum to the West of the maximum of the total galaxy number density. We take advantage of this rich spatial information to design properly our observations, including both the central and West parts of A539. WYFFOS spectroscopy suffers the same aperture bias effects as SDSS spectroscopy (see Section 4.4.1). However, focusing to the low-luminosity galaxies, where spatial variations in metallicity are not expected to be important, we circumvent this problem.

In Chapter 5 we discuss the environmental effects on the chemical evolution of low-mass SF galaxies in four nearby clusters and we have found that the effect of the environment appears to depend on the cluster mass. This work will take further our previous investigation, increasing the sample of studied clusters to cover the intermediate range of cluster X-ray luminosities (see Figure 2.13). The immediate goal is answering the question: does the metal enhancement of low-mass cluster galaxies that we observed e.g. in Coma occur as a continuous function of the ICM density or is there a density threshold above which the chemical evolution of cluster galaxies gets affected? This will deepen our understanding on the mechanisms that mostly affect the chemical evolution of cluster galaxies.

6.2.2 WYFFOS Multifiber Spectroscopy

We took observations with the Wide Field Fibre Optical Spectrograph (WYFFOS) at WHT4.2m at ORM in Spain and we are currently reducing the data. WYFFOS contains 150 science fibres each of 1.6 arcsec diameter, and 10 fiducial bundles for acquisition and guiding. The fibres are placed onto a field plate by the robot positioner Autofib2 (AF2). To this goal, it was mandatory to prepare beforehand the observations configurations files, which would do the maching between the objects that would be observed during a WYFFOS exposure and the fibers that would observe them. For the preparation of these configuration files, we used the available program af2_configure. This program uses an algorithm to achieve the optimal fiber placement, which includes position angle scanning, and the final result is to maximize the number of fibers placed and their statistical weight. This program provided us with a plot of the fiber placement (Figure 6.6) over which we had the possibility of manual editing of the configuration. Following this procedure, we created configuration files for the three clusters of our sample: A539, A400, and A2666. For A539 we obtained configurations for two different pointings, one on the central part of the cluster and one to the West (where the maximum density of

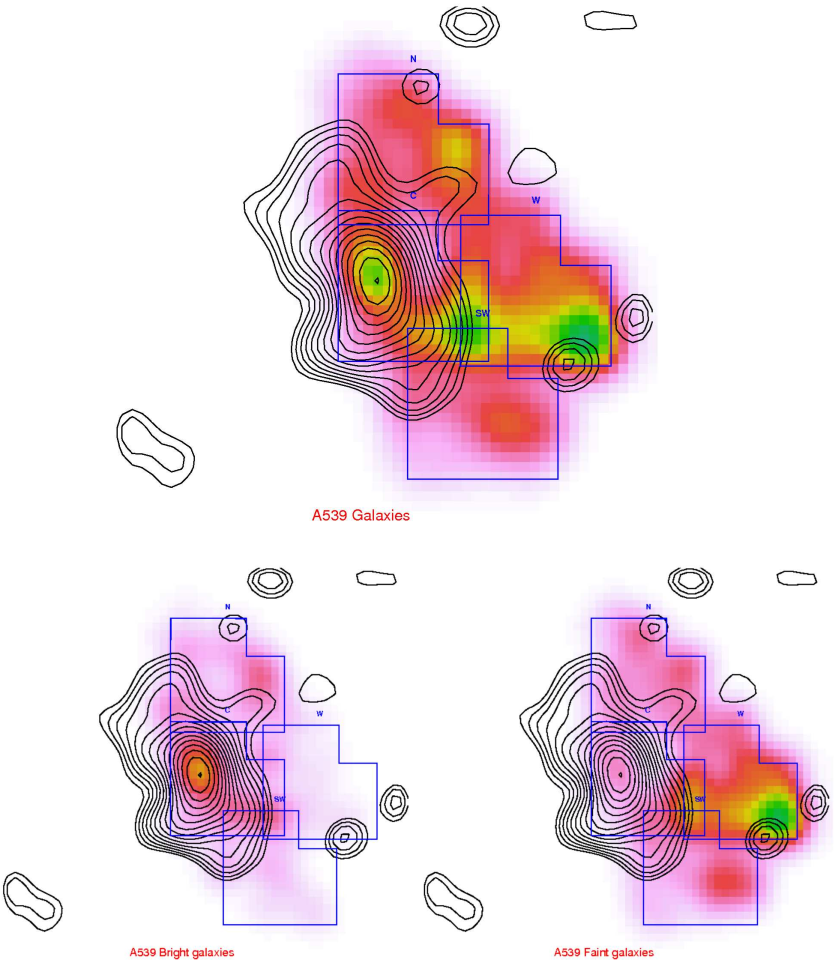

Figure 6.5: Up: The spatial distribution of number density of SF galaxies detected in A539 (Reverte 2008). Down: The spatial distribution of number density of the bright (left) and the faint population (right). The contours correspond to the galaxy number density derived using 2MASS data.

low-luminosity SF galaxies where found as shown in Figure 6.5).

The observations were performed during two nights, 21 and 22 November 2009. We performed two pointings on A539 (on the center and to the West), one pointing on A400 and one on A2666 (we note that part of the observing time was lost due to bad weather). For the observations we used the R300B grating, giving a nominal dispersion of 1.6Å pix^{-1} and total spectral coverage of ~6000Å. The spectral resolution is 8.8Å at a blaze wavelength 4000Å. This instrumental set-up is ideal for the purpose of this work, since it provides the spectral coverage necessary to include emission lines from [O II]λ3727, up to the [S III]$\lambda\lambda$9069,9532 in the far red; including all the optical lines necessary to derive physical conditions and abundances. In Table 6.2 we give further information on the pointings during the two nights of ob-

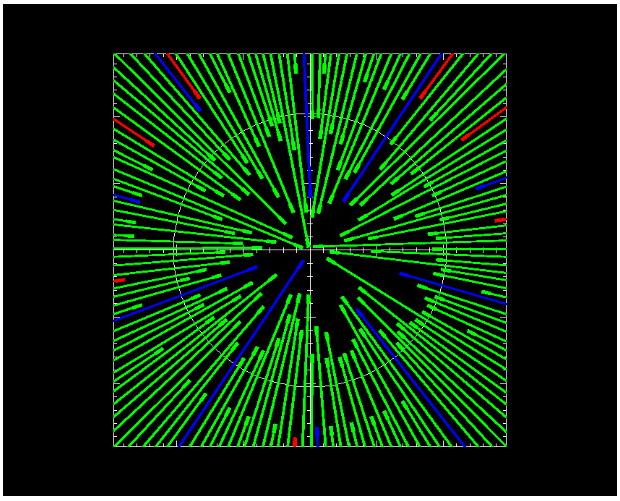

Figure 6.6: The configuration algorithm *af2_configure* places the fibers in such a way to maximize the number of fibers placed on science objects and their statistical weight. Green fibers correspond to science objects, blue to fiducial objects for acquisition and guiding, and the disabled/dead fibers are plotted in red. The output can be edited manually on this interactive PGPLOT device. The field shown here is the A539W, to the West of the cluster center, where a maximum of low-mass SF galaxies has been identified by Reverte (2008).

Table 6.2: **Observations with WYFFOS at WHT**

Cluster (1)	R.A. J2000.0 hh mm ss (2)	DEC. J2000.0 dd mm ss (3)	P.A. deg (4)	Fibers Obj (5)	Exp sec (6)
A539C	05 15 30	+06 28 00	288	106	5400
A539W	05 15 00	+06 20 00	144	116	5900
A400	02 58 00	+06 02 09	72	84	5400
A2666	23 50 40	+27 15 00	180	78	5400

servation. In the first column is given the name of the cluster, in column 2 and 3 are given the coordinates of the center of WYFFOS field, column 4 gives the position angle defined by AF2 algorithm in order to optimize the fiber placement, column 5 gives the number of fibers placed on science objects, and column 6 the exposure time in seconds.

Chapter 7

General Discussion & Conclusions

It is well established that dense environments, such as cluster cores, present larger fractions of passive galaxies than the field (e.g., Dressler 1980; Poggianti et al. 1999; Treu et al. 2003; Finn et al. 2005; Poggianti et al. 2006). This confirms the important influence of the environment on galaxy evolution. Although the big debate on nature vs. nurture remains open, accumulated evidence seems to indicate that, in the particular case of dwarf galaxies, environment is a fundamental driver of their evolution (Mahajan et al. 2010; Haines et al. 2007, 2006).

It has been found (Smith et al. 2012; Porter et al. 2008) that significant infall of low-mass SF galaxies exists along the filamentary structures onto the densest clusters. Reaching cluster cores, dwarf galaxies can experience a starburst event, induced by their first interaction with the ICM (pressure-triggered star formation, Kronberger et al. 2008; Kapferer et al. 2009). Low-mass galaxies with the characteristic morphologies produced by this effect have been observed in several nearby clusters (e.g. Gavazzi et al. 2001; Sun et al. 2007; Levy et al. 2007; Yoshida et al. 2008; Yagi et al. 2010; Smith et al. 2010). Then, RPS is expected to be very efficient (e.g., Tonnesen et al. 2007) and it could strip the gas of a dwarf galaxy in very short timescales ($\sim 10^9$yr) converting a large fraction of dwarf galaxies, first into post-starburst as those observed in Coma (Mahajan et al. 2011; Poggianti et al. 2004), and finally into passive galaxies.

Despite the fateful "switching off" of star formation predicted by the models of RPS, we have found quite a number of SF galaxies in our sample of clusters. The selection of our galaxy sample to have strong emission lines means that they do still contain ionized gas. However, as we show in Sections 3.9 and 5.6, a large fraction of these galaxies do not contain the amount of HI mass expected by the closed-box model, indicating that they should be suffering RPS which has first affected their neutral gas content.

The simulations of Tecce et al. (2010) predict that inside the virial radius (R_{vir}) of a cluster at $z \sim 0$, over 50% of the galaxies should have experienced important ram-pressure effects. The pressures predicted by their models appear to have a strong effect on the cold gas content: these authors found that 70% of the simulated galaxies within R_{vir} have been completely depleted of cold gas. Additionally, Tecce et al. (2010) models suggest that the rate at which the cold gas of a galaxy is stripped, depends on the halo virial mass of the host cluster; thus less massive galaxies within massive clusters are the most affected.

Within this framework, in this thesis we have investigated the chemical history of SF galaxies in a sample of seven nearby clusters, and we have focused our attention to the low-mass SF population, being the most suitable to probe the environmental impact. The chemical abundances of the ionized interstellar medium have been derived for a total of 781 low-mass SF galaxies, for which the behavior of the MZR and LZR has been studied as a function of their environment. The environment has been quantified as a function of cluster-centric distance and also as a function of the local galaxy density.

The MZR of galaxies is well established (e.g., Tremonti et al. 2004; Lee et al. 2006). There exist a variety of chemical evolution models and hydrodynamical simulations advocating different physical mechanisms to explain this relation. For example, the ejection of metal-enriched gas by galactic outflows, triggered by e.g., (multiple) supernovae explosions, could be more efficient in systems with shallower potential wells (e.g., Larson 1974; Marconi et al. 1994; De Lucia et al. 2004). A variable efficiency of star formation, increasing with galactic mass (often named "downsizing"), could also be invoked to reproduce the MZR (e.g., Matteucci 1994; Tissera et al. 2005; de Rossi et al. 2007; Calura et al. 2009). For dwarf galaxies, where supernova winds are expected to be more important, a combination of downsizing and winds could affect the shape and slope of the MZR (Tassis et al. 2008; Spitoni et al. 2010). Other mechanisms, such as dilution caused by infall and variations in the IMF have also been proposed, however they show problems reconciling dwarf SFRs and metallicities (see the review by Tolstoy et al. 2009).

Recently it has been found that hydrodynamic simulations that incorporate momentum-driven wind scaling provide among the most successful overall fits to a wide range of observed galaxy properties (Finlator & Davé 2008; Oppenheimer et al. 2010; Davé et al. 2011). Finlator & Davé (2008) developed a simple analytic model to understand the MZR, where the gas-phase metallicity of a galaxy is set by a balance between inflow and outflow, plus star formation. In this "equilibrium" model the mass outflow rate (η, i.e., the balance between inflow and outflow) scales inversely with circular velocity, and this naturally reproduces a slope of the MZR $Z \propto M_{\star}^{0.3}$ at $M_{\star} < 10^{10.5} M_{\odot}$. Lee et al. (2006) observationally obtained this slope of the MZR for a sample of nearby dIrr galaxies, with a remarkably small dispersion. This value of the slope is in agreement with the slope given by the linear fit of our sample of low-mass galaxies in the HSC (Section 4.4.4), in the low-mass clusters A779 and A634, and at the outer regions of Coma and A1367 (Section 5.5),.

Davé et al. (2011) discuss the effect of SFR and of environment on the MZR, and find that the overall trends are consistent with the expectations from the "equilibrium" model. We have shown that the scatter observed in the MZR of Coma and A1367 low-mass SF galaxies, does not correlate with the SFR (Section 5.5), and neither does the dispersion of the LZR of the HSC low-mass SF galaxies (Section 4.4.3). Thus we can not advocate metal dilution suffered by the galaxies showing lower metallicities at the same bin of mass to explain the observed trends.

Regarding environment, Davé et al. (2011) hydrodynamic simulations reproduce low mass galaxies in dense environments showing higher metallicities for the same bin of mass than galaxies at lower densities. The authors suggest that this should not be the result of galaxies processing more gas into stars, but rather the consequence of the environmental dependence of wind recycling. Much of the material entering into the galaxies' ISM at $z = 0$ is recycled winds (Oppenheimer et al. 2010), that is the reaccretion of the wind material when the wind velocity does not exceed the galaxy escape velocity (see also Bekki et al. 2009). This mechanism accounts for the fact that metallicity differences seem to disappear for high-mass galaxies: at high galaxy mass, wind recycling is so effective that metallicity approaches the theoretical yield regardless of environment. Instead, at low masses, most ejected material could normally escape the galaxy (Oppenheimer et al. 2010), unless the galaxy resides in a dense environment, with a hot gaseous halo that could significantly slow winds.

In Section 4.4.4 we have found that low-mass galaxies populating the densest regions in A2151 cluster core show slightly higher average metallicity for their mass (in agreement with our findings in Section 3.8). Additionally, in Section 5.5 we have seen that SF dwarf galaxies in the Coma cluster core, and to less extend in A1367, show higher metallicities for the same bin of mass than galaxies outside R_{200}. This results in the flattening of the derived MZR of the dwarfs located to distances $R \leq R_{200}$ in the core of these two clusters. The amount of this flattening appears to be related to cluster mass, with the less massive clusters of our sample not showing at all this behavior.

This observed trend matches well the above wind recycling scenario. Models suggest that at high density environments (i.e. in cluster cores) galactic winds can be suppressed by the high pressure of the ICM (Schindler et al. 2005; Kapferer et al. 2006, 2009). Accordingly this could cause faster recycling and thus preventing galaxies from losing their metals. The suppression to take place needs ICM pressures $\gtrsim 10^{-12}$ dyn cm^{-2} (Schindler & Diaferio 2008). Tecce et al. (2011) have found that on the outskirts of clusters as (or more) massive as Coma ($> 10^{15} M_{\odot}$) the ram-pressure reaches $\sim 5 \times 10^{-12} h^2$ dyn cm^{-2}, the same order of magnitude as in the core of clusters of virial mass $\sim 10^{14} M_{\odot}$. In turn, the ram-pressure in the core of massive clusters is expected to be ~ 100 times higher. Consequently, as we go to clusters of higher X-ray luminosity, higher would be the pressure exerted and the wind suppression is expected to be more effective. The wind suppression in the cluster cores could approximate the no-wind case depicted at Davé et al. (2011) hydrodynamic simulations, where the slope of the MZR is found to be flatter than when considering wind scaling.

The important role of the density of the ICM can be supported by Poggianti et al. (2009a,b) findings. These authors have found that the fraction of post-starburst galaxies depends on cluster mass, and the fraction of spiral galaxies in clusters in the local Universe is anticorrelated with L_X (whereas no trend is observed with cluster velocity dispersion). Now it seems to turn up that it is not only to the quenching efficiency, but also to the chemical evolution of low-mass cluster galaxies that the properties of the ICM could play an important role.

Another possibility that emerges from the "equilibrium" model scenario is that galaxies in denser regions could result having higher metallicities as a consequence of curtailed inflow, due to gas stripping and/or strangulation. The relation $Z \propto M_{\star}^{0.3}$ is the result of the balance between inflow and outflow processes. If gas accretion is truncated by some sort of environmental suppression, then the galaxy consumes its gas to form metals along the locus of $Z \propto M_\star$ and will move above the mean MZR (Davé et al. 2011). If accretion does not restart, the galaxy will end up exhausting all the available gas for star formation and finally be transformed to a passive galaxy. Accordingly, our SF dwarf galaxies that lie above the MZR could be in this particular phase of environmental quenching, where enhanced metal enrichment precedes the switching off of star formation. As we show in Section 5.6 the majority of galaxies inside R_{200} seem to have suffered important gas removal, specially in Coma.

The above picture could describe well what is happening to the galaxies in the Coma cluster core, where SF dwarfs show on average ~ 0.15 dex higher metallicities than the overall MZR. By reaching the outskirts of this massive cluster, the ISM-ICM interaction can produce starburst events, that accelerate gas depletion in cluster dwarf galaxies, as compared to their isolated counterparts. In the same time, galactic winds should have started to get suppressed, preventing metal lost from the low-mass galaxies, that otherwise would have been expected to be very efficient. As RPS gets shearing the gas content (starting from the halo gas reservoir and the HI disk), the infall of pristine gas gets truncated, and the chemical enrichment follows a steeper path on the mass-metallicity plane. By the end of their star formation, the low-mass galaxies could have experienced a significant metallicity enhancement. Considering that this shutting-off in Coma could take $\sim 10^9$ yr (the crossing-time of this cluster), there is enough time also for nitrogen to get delivered to the ISM, yielding the observed trend in the N/O ratio. In Figure 7.1 we give a schematic representation of this scenario.

Moreover, low-mass galaxies could reach clusters already chemically enhanced up to some degree. Recent works (Mahajan et al. 2010; Porter et al. 2008) have found an increased star formation in galaxies falling into clusters along supercluster-scale filaments. Additionally, simulations (e.g., Bekki 2009) suggest that even moderately strong ram pressure, such as in group-like environments, could strip the hot gas halos of galaxies, with efficiency increasing at the low-mass regimes. Consequently, low-mass galaxies, could suffer gas exhaustion by both gas depletion through star formation and some stripping process such as strangulation, *also* in their ways *toward* clusters. Both mechanisms would lead to chemical enhancement (product of the increased star formation as compared to isolated dwarf galaxies in the first case, and of the lulled infall in the second). This scenario could explain the trends observed for the oxygen abundance and N/O ratio even in A2151 and A1367 (clusters of $M_\star \sim 10^{14} M_\odot$), as well as the elevated metallicities observed for some galaxies at $R > R_{200}$ in Coma and A1367, as well as in the HSC region.

Carter et al. (2002) have invoked pressure confinement by the intracluster medium to explain the cluster-centric radial gradient of the stellar metallicity for a sample of passive galaxies in Coma. Smith et al. (2009), however, have argued that the observed gradient should be interpreted as a trend in age rather than metallicity. Younger passively evolving dwarfs could have arisen by the transformation of infalling field late-type galaxies, indicating that the buildup of the passive population is an ongoing process in the outskirts of the cluster, related to environment-driven

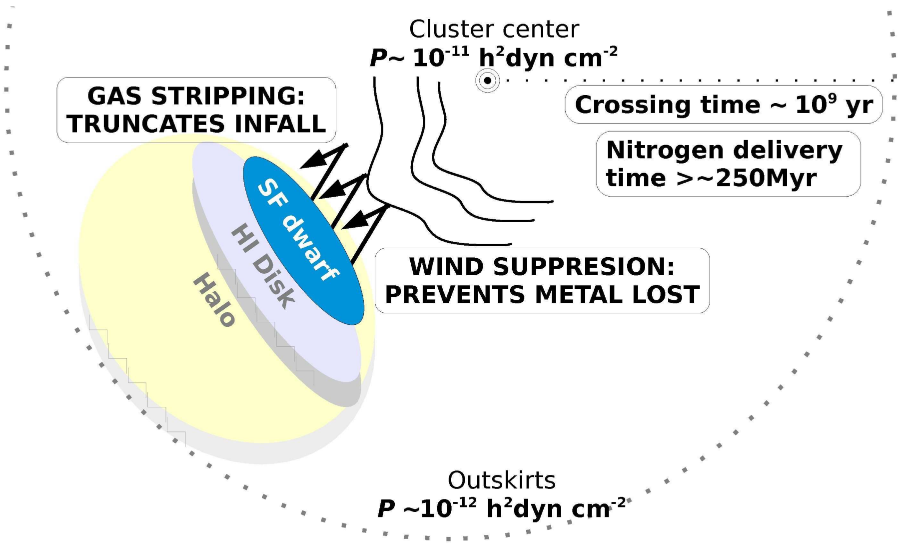

Figure 7.1: Schematic view of the main mechanisms that could affect the chemical evolution of a low-mass galaxy in a massive cluster like Coma. As this galaxy enters the cluster environment, the ISM-ICM interaction produces starburst events, accelerating gas depletion as compared to its isolated counterparts. The pressure of the ICM (depicted as pleats), in the region inside R_{200} is high enough to produce wind suppression, and the reaccretion of the wind material (the returning arrows) prevents dwarf galaxies from losing the produced metals. Additionally, the accretion rate of pristine gas becomes truncated, as the HI disk and the hot halo reservoir of the dwarf galaxies are effectively stripped in that region.

processes (regarding the infalling galaxy population in Coma, see also Aguerri et al. 2004).

In a subsequent work, Smith et al. (2012) have found that the cluster-centric age gradient for the red-sequence dwarfs in Coma is a global trend, and is not driven by the ongoing merger of the NGC4839 group to the south west of Coma. These authors have compared their results with the predictions from simulated cluster assembly histories (the Millenium Simulation, Springel et al. 2005) and have argued that in order to reproduce the strength of the age gradient observed for the red-sequence dwarfs in Coma, either a dominant burst or a gradual decline in the SFR has to be invoked; models with very abrupt quenching would lead to shallower age trend. These findings support the scenario proposed here: recent star formation, within a massive cluster like Coma, could yield the chemical enhancement of dwarf cluster galaxies.

Finally, a mechanism for the chemical enrichment of cluster galaxies to be considered could be the presence of enriched inflows. Historically it has been thought that there was a remarkable uniformity in the metal abundance of the ICM ($\sim 0.5Z_{\odot}$) as a function of cluster mass, ranging from cooling-core to noncooling-core clusters (see Werner et al. (2008) for a review on the chemical enrichment in the ICM, and

Schindler & Diaferio (2008) for a review on the processes proposed to explain this enrichment). However, recently, the spatially resolved analysis of the chemical composition of the ICM has revealed that this is not uniformly enriched in metals. ICM abundance gradients are common in clusters, showing a peak in the central region and a decline outwards (e.g. De Grandi et al. 2004; Leccardi & Molendi 2008; Lovisari et al. 2011). The central metallicity of the ICM can reach even over solar values, associated with the presence of the brightest cluster galaxy (RPS could also play a role in the metallicity enhancement in cluster centers). The question arises as to whether infall of enriched material of the ICM could affect the metallicity of cluster galaxies. However, detailed modeling would be needed, regarding the cooling of the ICM and the accretion mechanisms, which is beyond the scope of the present work.

In the following we summarize the conclusions reached in this thesis.

Main conclusions of this thesis

The aim of this thesis is to investigate the influence of environment on the chemical history of SF galaxies in a sample of local Universe clusters. We have achieved this goal through the study of the fundamental relations between the metallicity of galaxies and their main physical properties, such as stellar mass, luminosity, gas content, star formation activity and structure.

In order to carry out this study, we have obtained new optical long-slit spectroscopy of the A2151 cluster with the telescopes INT2.5m and WHT4.2m at the ORM. Additionally an extensive spectroscopic database has been extracted from the SDSS DR8, for a large sample of 781 low-mass SF galaxies in the clusters: A1656 (Coma), A1367, A779 A634 as well as in A2147, A2151, A2152 of the Hercules supercluster.

We have derived the chemical abundances of the ionized interstellar medium of our sample galaxies, for which we have studied the behavior of the MZR and LZR as a function of their environment. The environment has been quantified as a function of cluster-centric distance and also as a function of the local density of galaxies. The main conclusion of this work can be summarized as follows:

- Overall, our sample of SF galaxies exhibits well defined sequences of stellar mass and metallicity (as parametrized by O/H, and the N/O ratio), following the well known general behavior for SF galaxies. Notably outside the cores of more massive clusters, the derived slope of the MZR is in agreement with the predictions of state-of-the-art hydrodynamic models.

- Besides this global behavior, we have found that dwarf/irregular galaxies populating the densest regions in the A2151 cluster show higher metallicity for their mass and crowd the upper part of the MZR and N/O vs. stellar mass relations.

- Furthermore, low-mass SF galaxies located at cluster-centric distances $R \leq R_{200}$ in Coma (especially) and A1367, appear preferentially located at the upper side of the derived MZR global relations of O/H and N/O vs. mass. This observed enhancement in metallicity appears to be dependent of galaxy stellar mass, being higher for the lower mass bins, thus flattening the MZR slope in the core of these massive clusters.

This observed behavior reveals that the imprint of the cluster environment on the chemical evolution of SF galaxies shows up in a mass-dependent way, being both, galaxy mass and cluster mass, relevant parameters. This result suggests the important role that ICM properties could play in the chemical evolution of cluster galaxies. A physical scenario has been proposed to explain the metal enhancement of low-mass SF galaxies in clusters, in the light of the predictions of recent hydrodynamic simulations for galaxy evolution in clusters. Within this framework, this thesis aims at motivating further efforts in theoretical modelling of chemical evolution in dense environments.

Additional specific conclusions obtained in the present work are the following:

- The Hercules SF spirals present oxygen abundances close to solar and shallow oxygen abundance gradients, a result suggesting possible gas infall at their centers. For the N/O ratio, even oversolar values have been obtained for the central parts of some galaxies and a significant spatial variation has been observed.

- A clear trend was found for the gas-phase metallicity of Hercules galaxies, gradually approaching the stellar metallicity as the latter increases from $Z_{\odot}/2$ to $Z_{\odot}$. The outliers of this trend (less chemically evolved systems with approximately equal gas-phase and stellar metallicity) are identifiable with "newcomers" in the cluster environment.

- An overall positive trend has been found in the gas-phase oxygen abundance vs. the mass-weighted stellar age $\tau_{\star,M}$, which becomes more prominent in the case of the N/O ratio.

- The 2D color $g-i$ and $EW(\mathrm{H}\alpha)$ maps of the Hercules cluster have revealed the presence of a filament, mainly of low-mass SF galaxies, to the North of A2151, that reaches down to the cluster core. The $g-i$ and $EW(\mathrm{H}\alpha)$ maps of A2152 ans A2147 indicate more virialized structures; nonetheless, a filamentary structure dominated by blue low-mass SF galaxies has been identified entering in A2147 R_{200} region from South-East.

- The LZR and N/O ratio vs. stellar mass relation of the HSC low-mass SF galaxies have been found to show an intrinsic dispersion that correlates with galaxy color.

- In the clusters with available HI measurements we have found that most of the dwarf galaxies with available HI mass are either located outside the cluster core or have been recently accreted to the cluster environment and appear consistent with the predictions of the "closed box" model. In the cores of these clusters, HI detections are scarce, thus SF dwarf galaxies should be suffering an important RPS.

- The metal enhancement of SF dwarfs in the cluster core has been found to be more important when considering the R_{200} region of the most massive cluster Coma ($M_{\star} \simeq 10^{15} M_{\odot}$). Despite the general good relation of local galaxy density with cluster-centric distance, this effect appears diluted in terms of local galaxy density, suggesting that the relevant parameter able to affect the chemical evolution of SF dwarf galaxies should be the presence of an ICM.

Finally, specific operational achievements towards the realization of this work are briefly summarized:

- We performed a study of the morphological and structural properties of the SF galaxies in the Hercules cluster. This work allowed a careful spectroscopic follow-up of these galaxies with long-slit spectroscopy.
- We derived galaxy stellar masses using SED fitting on SDSS broad-band photometry. The fundamental parameters of the underlying stellar component, such as mean metallicity and age were derived via spectral fitting using the population synthesis code STARLIGHT.

Appendix A

Details on A2151 star-forming galaxies

A.1 2D morphological study

From our 2D morphological study of Hercules galaxies presented in Section 3.3 we derive color $(g - i)$ map (left) and $EW(\mathrm{H}\alpha)$ map (right), for all the galaxies of our spectroscopic follow-up that show rich spatial structure. The position of the long-slit is overposed to the images, and additional information on the galaxies are given.

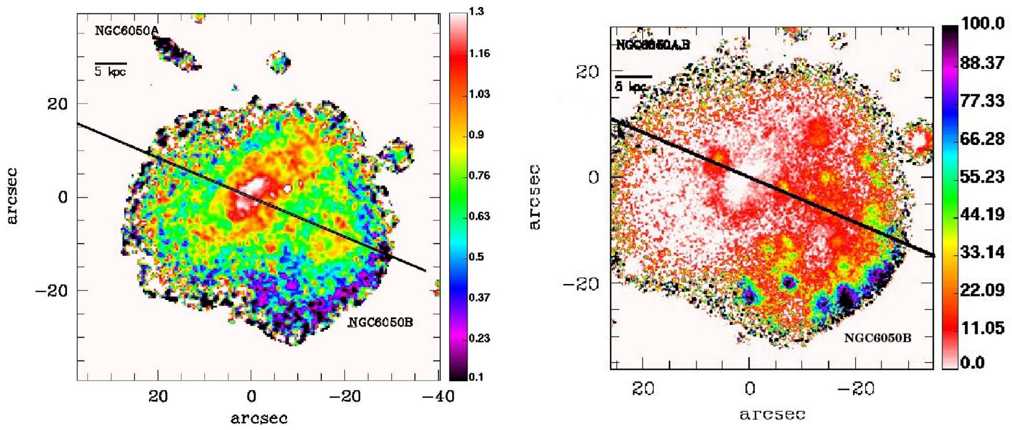

Figure A.1: NGC6050: It has long been considered as a collision between two spiral galaxies (NGC6050A and NGC6050B). From our long-slit spectrum (see Figure 3.8) we found that these two galaxies show important velocity difference ($\sim$ 1600 km s^{-1}) suggesting that they might be just a chance galaxy alignment. On the other hand, to the North of the system we have identified another galaxy, on the basis of its underlying stellar component (clearly seen in the 2MASS imaging) and its SDSS spectrum. This galaxy is probably in interaction with NGC6050A. Dickey (1997) quotes an HI mass for the NGC6050 system. We attributed the HI mass exclusively to NGC6050B because NGC6050A is out of the velocity cutoff of the spectrometer used by Dickey (1997). The HI distribution is centered on NGC6050B.

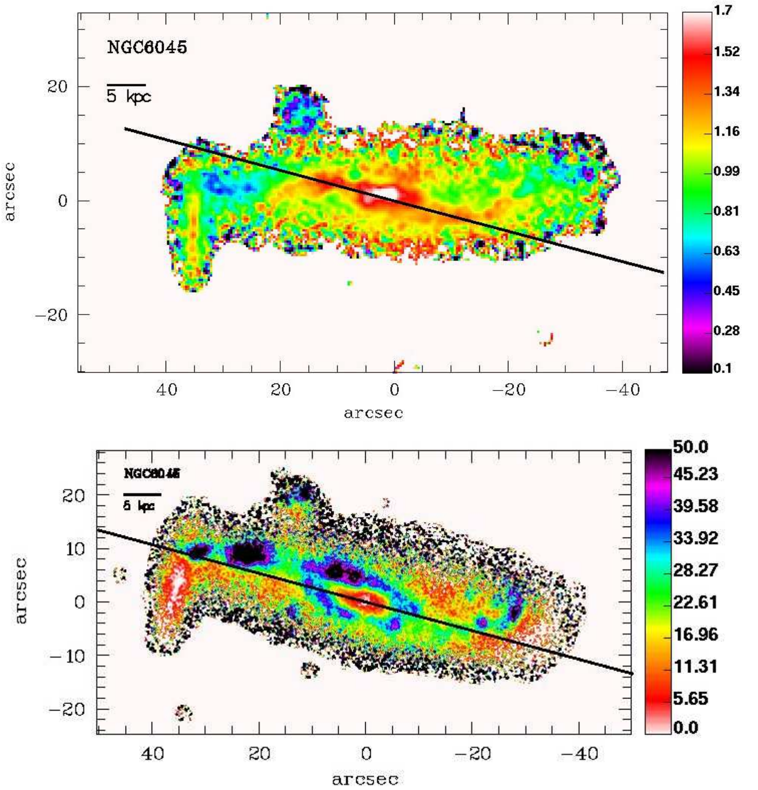

Figure A.2: NGC6045: This edge-on spiral could be interacting with a smaller spiral companion located at the East of it. On its Hα map we can see intense starburst activity on the East part of the galaxy disk, probably triggered by this interaction. Huang & Sarazin (1996) suggested a possible interaction of NGC6045 with the radio galaxy NGC6047 which is about $1'.6$ (~ 74 kpc) to the South. Dickey (1997) reports that in HI only half of the disk is visible. From our long-slit spectroscopy we find a large large velocity gradient along the disk of the galaxy (see Figure 3.8) and half of the disk shows velocity out of the cut-off of the spectrometer used by Dickey (1997).

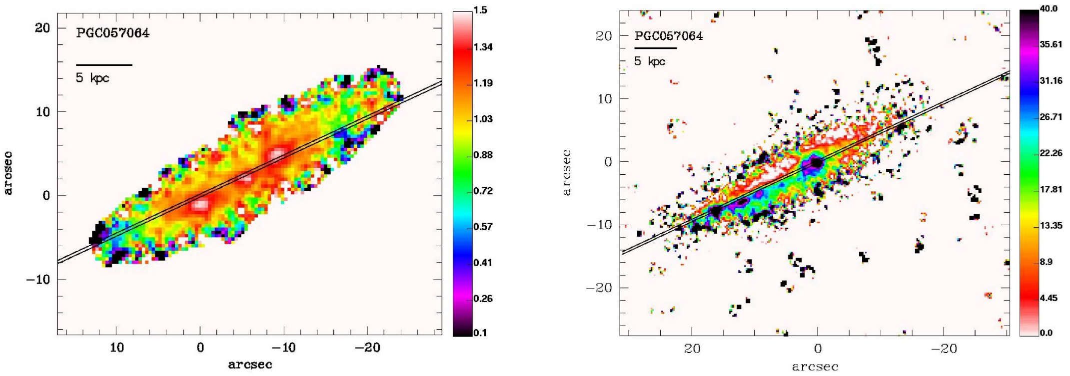

Figure A.3: PGC057064: This peculiar galaxy, until now considered as one galaxy, has turned out to be a merger of two galaxies, which on our long-slit spectrum show different rotation velocities (see Figure 3.8). We have considered the corresponding 2D spectrum parts separately. The 1D spectrum part (a) corresponds to the North-West galaxy and (b) to the South-East. The two dwarf galaxies comprising this merger do not show any significant chemical variation.

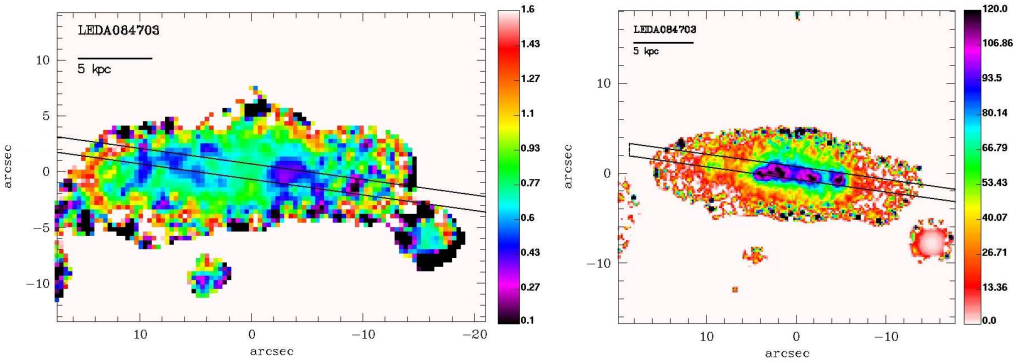

Figure A.3: LEDA084703: This is one of the two galaxies of this sample situated in the substructure almost 1 Abell radius South-West from the cluster center. It is a quite blue galaxy, classified Sd/Irr and it is situated almost one Abell radius away from the cluster center. There has been a SN explosion reported by Zwicky et al. (1969) in the East part of this irregular galaxy. There is a long plume extending towards South-East detected in the optical images as well as in HI by Dickey (1997). The West part of the disk hosts a very intense starburst activity as can be seen in its $EW(\mathrm{H}\alpha)$ map.

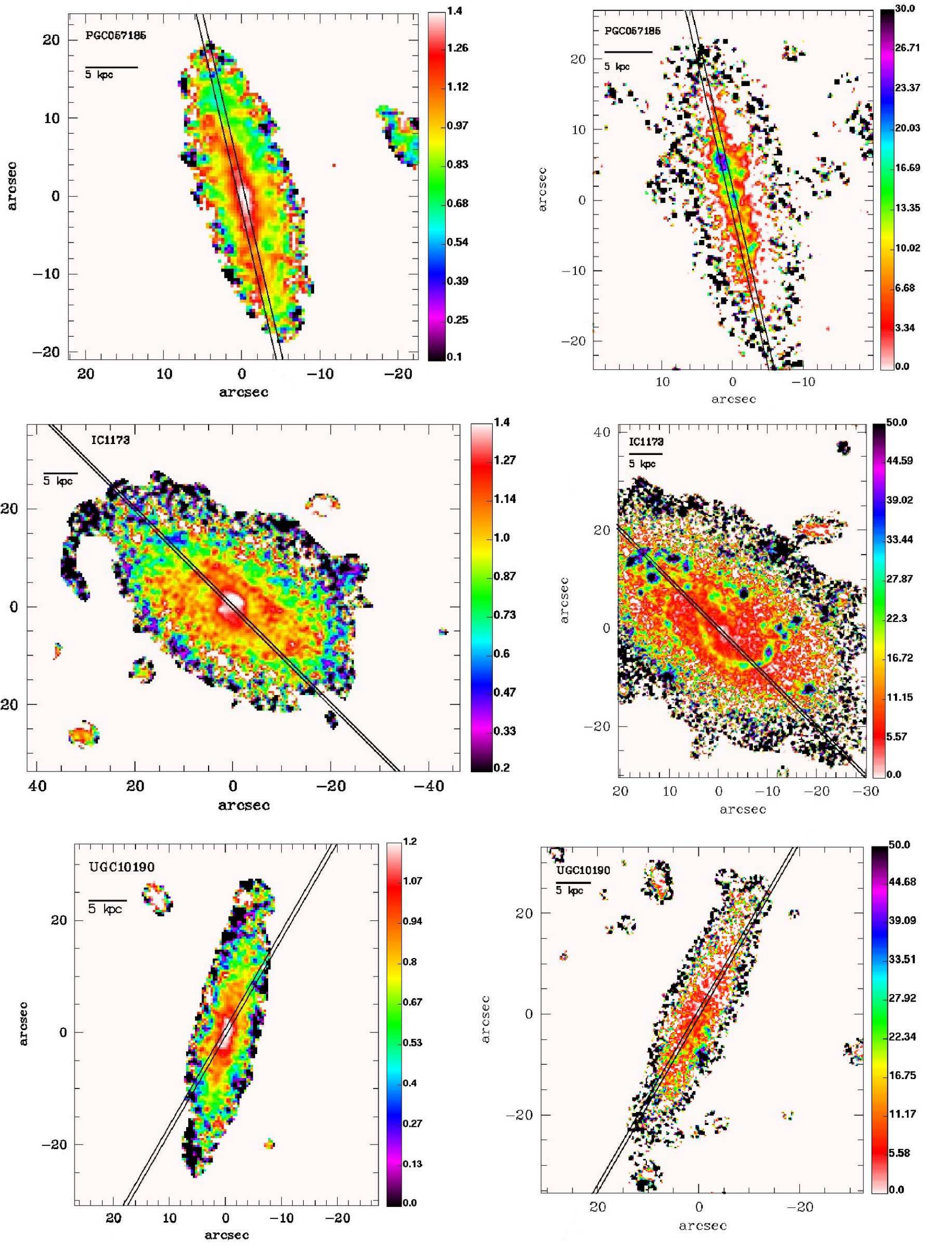

Figure A.4: Color $(g - i)$ map (left) and the $EW(\mathrm{H}\alpha)$ map (right) for PGC057185 (upper) IC1173 (middle) and UGC10190 (lower panel).

A.2 Peculiar galaxies

- *SDSSJ160520.58+175210.6* appears to be embedded into the HI structure assigned to the galaxy [D97]ce-200 (SDSSJ160520.64+175201.5); Dickey (1997) reports that this system looks like the Magellanic Clouds and the Magellanic Stream. However these two galaxies have a velocity difference of 1300 km s^{-1} a fact that renders unlikely an actual interaction of them. The velocity of the HI cloud is very similar to the velocity of the galaxy [D97]ce-200.

- *SDSSJ160524.27+175329.3*: It has typical Hα morphology and colors of a blue compact galaxy. This compact starburst, located close to the X-ray maximum in the center of the Hercules cluster could have resulted from the compression of the interstellar gas of a dwarf galaxy when entering the cluster core. Similar compact starburst galaxies have been found in the cores of other nearby clusters by Reverte et al. (2007).

- *SDSS J160556.98+174304.1* The Hα map of this dwarf galaxy shows an off-center starburst. Additionally this galaxy is located close to the edge of the primary X-ray maximum in the cluster center and presents a large velocity difference with NGC6041A. These evidences could suggest that the starburst has been triggered by the effect of the hot ICM. (Dickey 1997) have not detected molecular gas for this galaxy, suggesting that the ram-pressure stripping could have already taken off its molecular gas.

- *LEDA084724* presents an extended knotty Hα structure North-West, in the direction towards the X-ray cluster center. This morphology could be suggestive of a starburst triggered by the ICM. (Dickey 1997) have not detected molecular gas for this galaxy.

- *SDSSJ160304.20+171126.7* is one of the two SF galaxies of this spectroscopic sample situated in the substructure almost 1 Abell radius South-West from the cluster center. This galaxy has a close companion, the galaxy SDSSJ160305.24+171136.1. The disturbed Hα structure of both could suggest a possible interaction.

- *SDSSJ160523.66+174832.3* is located very close to the faint galaxy SDSSJ-160523.67+174828.8 (#22 and #23 in C09). The Hα map as well as the $g-i$ color map of SDSSJ160523.66+174832.3 seem to reveal a disturbed morphology. There could be the possibility that the two galaxies are interacting, although SDSSJ160523.67+174828.8 does not have spectroscopic data and SDSS provide a photo-z estimate of $z = 0.15 \pm 0.02$, nominally not consistent with the velocity range of Hercules cluster.

- *[DKP87]160310.21+175956.7* is projected close to a faint galaxy located South-East. The EWHα map of [DKP87]160310.21+175956.7 shows an intense starburst event towards that direction. However the close companion galaxy has no spectroscopic data and the photo-z estimate provided by SDSS $z = 0.25 \pm 0.06$ is not consistent with the velocity range of Hercules cluster.

- *SDSSJ160547.17+173501.6*: It has turned out to be a background galaxy with $z = 0.12 \pm 0.01$. The various SDSS photo-z estimates were 0.06 ± 0.01, 0.06 ± 0.05 and 0.10 ± 0.04, thus the criteria adopted by C09 for cluster membership were fulfilled.

Appendix B

Galaxy properties in the Hercules Supercluster

We quote the coordinates, the metallicities derived, and the physical properties discussed in Chapter 4, for the MS galaxies in the three clusters and the dispersed component (Table B.1: A2151, Table B.2: A2152, Table B.3: A2147, Table B.4: dispersed component). Galaxies are sorted to increasing R.A.

Table B.1: **MS galaxies in A2151**

# (1)	R.A. J2000 hh mm ss (2)	DEC J2000 dd mm ss (3)	z (4)	R/R_{200} (5)	$\Sigma_{4,5}$ Mpc^{-2} (6)	g mag (7)	i mag (8)	$M_\star$ $M_\odot$ (9)	$c(\mathrm{H}\beta)$ (10)	OH CM (11)	OH PP04 (12)	OH PMC09 (13)	OH D11 (14)	OH ADOP (15)	NO CM (16)	NO PMC09 (17)	NO ADOP (18)
01	16 02 30.55	17 00 35.64	0.0329	1.99	0.78	17.82	16.69	9.62	0.25	8.55	8.76	8.72	8.73	8.63	-0.65	-0.67	-0.66
02	16 02 31.25	17 39 06.12	0.0355	1.32	0.71	18.03	17.15	9.22	0.70	8.41	8.61	8.59	8.09	8.48	-1.27	-1.18	-1.22
03	16 02 54.74	17 44 03.84	0.0351	1.12	0.91	17.99	17.20	9.11	0.34	8.29	8.43	8.45	8.40	8.34	-1.04	-1.15	-1.10
04	16 03 04.20	17 11 26.88	0.0361	1.54	1.67	18.42	17.50	9.35	0.63	8.41	8.60	8.60	8.40	8.48	-1.06	-1.13	-1.10
05	16 03 05.73	17 10 20.28	0.0336	1.56	1.60	17.10	16.30	9.62	0.50	8.19	8.39	8.38	8.03	8.27	-1.28	-1.35	-1.32
06	16 03 11.18	17 33 52.56	0.0386	1.05	1.09	18.30	17.67	8.96	0.21	8.28	8.50	8.53	8.34	8.37	-1.11	-1.30	-1.20
07	16 03 12.26	17 15 20.88	0.0434	1.40	0.68	18.10	17.49	9.02	0.07	8.26	8.42	8.44	8.35	8.32	-1.08	-1.26	-1.17
08	16 03 21.00	17 43 26.04	0.0300	0.91	0.71	18.06	17.48	8.72	0.12	8.09	8.21	8.15	7.87	8.13	-1.33	-1.46	-1.39
09	16 03 22.32	17 35 07.08	0.0362	0.96	1.06	16.85	16.22	9.43	0.13	8.41	8.66	8.69	8.55	8.51	-0.87	-1.09	-0.98
10	16 03 34.39	17 28 17.76	0.0380	0.98	1.35	17.65	17.09	8.94	0.02	8.10	8.37	8.29	7.84	8.20	-1.34	-1.57	-1.45
11	16 03 44.62	17 28 26.40	0.0370	0.91	1.15	18.34	17.52	9.22	0.33	8.27	8.44	8.46	8.31	8.34	-1.14	-1.25	-1.20
12	16 03 49.34	18 29 40.56	0.0370	1.65	0.76	18.54	17.74	9.05	0.11	8.39	8.60	8.57	8.42	8.47	-1.03	-1.24	-1.14
13	16 03 51.19	18 17 43.08	0.0349	1.28	1.08	17.49	16.49	9.57	0.19	8.54	8.81	8.73	8.70	8.64	-0.76	-0.89	-0.83
14	16 03 59.04	18 27 16.20	0.0365	1.54	0.99	16.41	15.68	9.71	0.23	8.42	8.71	8.69	8.52	8.53	-0.92	-1.15	-1.04
15	16 04 01.56	17 37 13.08	0.0369	0.64	1.19	17.83	17.18	9.13	0.00	8.00	8.23	8.18	8.30	8.08	-1.15	-1.42	-1.29
16	16 04 03.86	18 28 16.32	0.0371	1.56	0.93	16.58	15.96	9.59	0.21	8.42	8.61	8.61	8.54	8.49	-0.92	-0.93	-0.93
17	16 04 07.56	17 12 24.84	0.0350	1.22	1.44	18.29	17.68	8.82	0.15	8.30	8.50	8.52	8.36	8.38	-1.08	-1.22	-1.15
18	16 04 21.82	18 08 19.68	0.0363	0.89	1.00	16.78	15.87	9.79	0.31	8.38	8.60	8.59	8.54	8.46	-0.88	-1.18	-1.03
19	16 04 21.98	18 18 02.16	0.0371	1.19	1.37	18.08	17.14	9.40	0.31	8.42	8.65	8.60	8.51	8.51	-0.95	-1.08	-1.02
20	16 04 24.14	17 41 19.32	0.0320	0.42	1.89	18.01	17.35	8.94	0.36	8.41	8.60	8.57	8.39	8.48	-1.07	-1.15	-1.11
21	16 04 28.44	17 13 19.92	0.0346	1.13	1.35	17.92	17.25	9.04	0.16	8.39	8.57	8.55	8.50	8.46	-0.95	-1.17	-1.06
22	16 04 28.58	18 12 33.48	0.0341	0.99	1.18	17.14	15.95	9.98	0.54	8.49	8.74	8.80	8.71	8.59	-0.67	-0.82	-0.75
23	16 04 32.55	17 14 57.48	0.0352	1.06	1.30	17.04	16.06	9.78	0.49	8.54	8.77	8.67	8.78	8.62	-0.59	-0.78	-0.68
24	16 04 34.37	18 18 53.28	0.0361	1.18	1.14	16.97	16.23	9.51	0.26	8.43	8.64	8.64	8.51	8.51	-0.94	-1.02	-0.98
25	16 04 38.98	18 02 09.60	0.0372	0.64	1.10	17.51	16.76	9.39	0.21	8.44	8.70	8.67	8.55	8.54	-0.90	-1.04	-0.97
26	16 04 39.02	17 21 00.00	0.0354	0.85	1.22	16.68	15.81	9.82	0.27	8.55	8.78	8.70	8.76	8.63	-0.62	-0.67	-0.65
27	16 04 39.48	17 36 58.68	0.0352	0.39	1.73	17.73	16.86	9.41	1.00	8.43	8.67	8.73	8.34	8.53	-1.14	-1.06	-1.10
28	16 04 40.25	16 59 07.44	0.0307	1.56	0.77	17.42	16.40	9.53	0.44	8.42	8.61	8.69	8.33	8.50	-1.13	-1.05	-1.09
29	16 04 42.70	17 45 53.64	0.0313	0.26	1.76	17.60	16.80	9.24	0.37	8.51	8.75	8.68	8.61	8.60	-0.86	-0.93	-0.89
30	16 04 47.55	17 20 52.08	0.0354	0.84	1.25	16.17	15.33	9.99	0.51	8.52	8.76	8.70	8.59	8.61	-0.88	-0.89	-0.89
31	16 04 51.17	17 16 16.32	0.0330	0.98	1.31	17.98	17.15	9.16	0.24	8.40	8.63	8.65	8.65	8.49	-0.78	-1.10	-0.94
32	16 04 55.58	18 00 22.32	0.0381	0.54	1.17	18.30	17.30	9.40	0.65	8.48	8.76	8.68	8.49	8.58	-1.01	-0.94	-0.98
33	16 04 56.95	17 14 52.08	0.0344	1.02	1.18	17.32	16.42	9.65	0.56	8.60	8.84	8.77	8.83	8.69	-0.51	-0.50	-0.51

Table B.1: **MS galaxies in A2151**

# (1)	R.A. J2000 hh mm ss (2)	DEC J2000 dd mm ss (3)	z (4)	R/R_{200} (5)	$\Sigma_{4,5}$ Mpc^{-2} (6)	g mag (7)	i mag (8)	$M_\star$ $M_\odot$ (9)	$c(\mathrm{H}\beta)$ (10)	OH CM (11)	OH PP04 (12)	OH PMC09 (13)	OH D11 (14)	OH ADOP (15)	NO CM (16)	NO PMC09 (17)	NO ADOP (18)
34	16 04 58.44	18 11 12.48	0.0377	0.89	1.08	17.11	16.08	9.96	0.63	8.42	8.59	8.63	8.40	8.49	-1.05	-1.05	-1.05
35	16 05 02.93	17 07 43.68	0.0407	1.25	0.84	17.38	16.32	9.91	0.66	8.51	8.75	8.70	8.57	8.60	-0.91	-0.88	-0.89
36	16 05 04.15	17 49 03.36	0.0332	0.16	2.01	17.60	16.56	9.60	0.51	8.58	8.81	8.66	8.81	8.66	-0.55	-0.64	-0.59
37	16 05 04.22	17 34 49.80	0.0434	0.35	0.93	17.43	16.83	9.31	0.25	8.25	8.44	8.43	8.30	8.32	-1.16	-1.35	-1.26
38	16 05 06.98	17 05 16.08	0.0364	1.34	0.92	18.29	17.66	8.89	0.02	8.14	8.35	8.34	7.87	8.22	-1.32	-1.48	-1.40
39	16 05 07.06	17 38 57.84	0.0339	0.21	1.59	16.74	15.71	9.95	0.27	8.57	8.79	8.69	8.84	8.65	-0.50	-0.62	-0.56
40	16 05 10.46	17 51 16.20	0.0330	0.21	1.98	17.45	16.94	8.91	0.74	7.92	8.39	8.33	0.00	8.10	-1.54	-1.54	-1.54
41	16 05 12.41	17 35 56.04	0.0354	0.30	1.72	17.10	16.62	9.13	0.13	8.38	8.51	8.52	8.34	8.43	-1.12	-1.18	-1.15
42	16 05 13.22	17 21 14.40	0.0360	0.80	1.32	18.10	17.44	8.93	0.00	8.18	8.42	8.42	8.32	8.27	-1.11	-1.59	-1.35
43	16 05 16.08	17 19 40.80	0.0351	0.85	1.27	17.35	16.48	9.55	0.22	8.38	8.62	8.76	8.44	8.48	-0.95	-1.23	-1.09
44	16 05 19.32	17 20 38.40	0.0336	0.82	1.37	18.13	17.43	9.02	0.20	8.40	8.57	8.59	8.44	8.47	-1.01	-1.15	-1.08
45	16 05 21.69	17 57 27.36	0.0398	0.42	1.95	17.95	17.11	9.34	0.32	8.34	8.50	8.53	8.37	8.40	-1.08	-1.05	-1.06
46	16 05 22.23	17 45 15.12	0.0368	0.06	2.79	16.24	15.50	9.87	0.41	8.52	8.78	8.70	8.68	8.61	-0.78	-0.93	-0.86
47	16 05 24.24	18 08 53.88	0.0377	0.81	1.93	18.14	17.56	8.88	0.19	8.16	8.42	8.42	7.94	8.26	-1.29	-1.45	-1.37
48	16 05 25.66	17 58 00.12	0.0333	0.45	1.74	18.45	17.51	9.12	0.46	8.49	8.72	8.65	8.56	8.57	-0.91	-0.96	-0.94
49	16 05 26.30	17 41 48.48	0.0370	0.14	2.14	16.69	15.73	9.98	0.00	8.50	8.72	8.72	8.79	8.58	-0.48	-0.84	-0.66
50	16 05 27.02	16 58 02.28	0.0362	1.58	0.78	17.08	16.24	9.65	0.42	8.47	8.69	8.68	8.59	8.55	-0.86	-0.87	-0.86
51	16 05 28.90	17 13 13.44	0.0336	1.07	1.06	17.98	16.75	9.73	0.71	8.61	8.87	8.71	8.76	8.70	-0.63	-0.56	-0.60
52	16 05 31.85	17 48 26.28	0.0317	0.18	2.23	18.66	17.55	9.22	0.66	8.42	8.53	8.62	8.81	8.47	-0.65	-0.69	-0.67
53	16 05 34.15	17 46 12.00	0.0341	0.16	2.11	16.79	15.98	9.68	0.57	8.53	8.69	8.71	8.67	8.59	-0.79	-0.58	-0.68
54	16 05 35.69	17 22 33.24	0.0354	0.77	1.47	17.03	16.29	9.53	0.34	8.54	8.83	8.67	8.72	8.64	-0.72	-0.87	-0.80
55	16 05 38.28	18 04 00.12	0.0377	0.67	1.68	18.07	17.47	8.91	0.10	8.19	8.43	8.45	8.14	8.28	-1.21	-1.39	-1.30
56	16 05 43.78	17 36 55.80	0.0390	0.36	1.71	18.35	17.39	9.34	0.52	8.49	8.73	8.70	8.73	8.58	-0.68	-0.92	-0.80
57	16 05 45.14	17 55 34.32	0.0395	0.43	1.39	17.70	16.67	9.67	0.49	8.54	8.80	8.67	8.72	8.63	-0.70	-0.84	-0.77
58	16 05 47.02	17 18 27.00	0.0364	0.93	1.55	16.29	15.72	9.63	0.18	8.33	8.51	8.54	8.38	8.40	-1.05	-1.09	-1.07
59	16 05 47.28	18 23 04.20	0.0402	1.30	1.42	17.73	17.13	9.09	0.20	8.14	8.34	8.31	7.95	8.21	-1.29	-1.46	-1.38
60	16 05 49.03	18 07 12.72	0.0366	0.80	1.69	17.10	16.08	9.86	0.31	8.52	8.75	8.73	8.69	8.61	-0.74	-0.90	-0.82
61	16 05 52.34	18 27 53.64	0.0389	1.47	1.27	17.05	16.42	9.47	0.21	8.40	8.58	8.60	8.42	8.47	-1.03	-1.15	-1.09
62	16 05 54.02	17 20 27.60	0.0343	0.88	1.75	16.65	15.78	9.83	0.32	8.52	8.77	8.70	8.77	8.61	-0.60	-0.83	-0.72
63	16 05 57.89	18 24 42.84	0.0389	1.38	1.44	18.23	17.41	9.15	0.42	8.38	8.53	8.53	8.32	8.44	-1.16	-1.24	-1.20
64	16 06 08.88	17 52 36.12	0.0358	0.50	1.37	17.40	16.78	9.21	0.38	8.39	8.60	8.60	8.15	8.47	-1.23	-1.28	-1.25
65	16 06 10.35	17 42 07.92	0.0352	0.46	1.55	17.49	16.50	9.59	0.58	8.54	8.78	8.66	8.71	8.62	-0.74	-0.88	-0.81
66	16 06 13.03	17 19 10.56	0.0390	0.99	1.37	18.25	17.05	9.73	0.15	8.48	8.74	8.70	8.73	8.58	-0.62	-1.02	-0.82

Table B.1: **MS galaxies in A2151**

# (1)	R.A. J2000 hh mm ss (2)	DEC J2000 dd mm ss (3)	z (4)	R/R_{200} (5)	$\Sigma_{4,5}$ Mpc^{-2} (6)	g mag (7)	i mag (8)	$M_\star$ $M_\odot$ (9)	$c(\mathrm{H}\beta)$ (10)	OH CM (11)	OH PP04 (12)	OH PMC09 (13)	OH D11 (14)	OH ADOP (15)	NO CM (16)	NO PMC09 (17)	NO ADOP (18)
67	16 06 13.78	17 57 15.12	0.0386	0.63	1.32	16.06	15.40	9.79	0.39	8.53	8.77	8.68	8.64	8.61	-0.83	-0.82	-0.83
68	16 06 14.18	18 31 33.60	0.0368	1.63	1.20	17.84	17.28	9.42	0.02	8.36	8.53	8.47	8.35	8.42	-1.12	-1.33	-1.22
69	16 06 17.18	18 11 00.24	0.0384	1.01	1.65	17.48	16.94	9.10	0.11	8.36	8.50	8.51	8.33	8.42	-1.14	-1.28	-1.21
70	16 06 21.79	17 17 11.40	0.0398	1.08	1.12	17.88	17.28	9.12	0.20	8.26	8.43	8.48	8.34	8.33	-1.09	-1.26	-1.17
71	16 06 22.44	18 11 17.88	0.0393	1.04	1.64	17.73	16.80	9.56	0.32	8.45	8.68	8.72	8.66	8.54	-0.76	-0.92	-0.84
72	16 06 28.58	17 32 12.84	0.0405	0.73	1.17	18.17	17.71	8.81	0.42	8.13	8.31	8.27	0.00	8.20	-1.50	-1.55	-1.53
73	16 06 35.13	16 59 54.96	0.0393	1.65	1.00	18.23	17.35	9.34	0.47	8.39	8.52	8.54	8.38	8.44	-1.07	-1.12	-1.09
74	16 06 37.82	18 23 53.52	0.0369	1.47	1.18	16.91	16.53	9.07	0.08	8.31	8.43	8.46	8.34	8.36	-1.11	-1.09	-1.10
75	16 06 38.38	17 51 00.72	0.0397	0.70	1.57	17.25	16.32	9.75	0.48	8.54	8.79	8.68	8.71	8.63	-0.73	-0.79	-0.76
76	16 06 39.74	17 55 46.20	0.0386	0.77	1.36	18.21	17.62	8.88	0.12	8.26	8.45	8.48	8.29	8.33	-1.16	-1.34	-1.25
77	16 06 43.87	17 26 30.12	0.0360	0.95	0.90	17.26	16.53	9.45	0.23	8.37	8.57	8.53	8.34	8.44	-1.14	-1.35	-1.24
78	16 06 44.62	18 14 43.80	0.0387	1.23	1.60	17.62	17.03	9.14	0.20	8.26	8.45	8.43	8.17	8.33	-1.21	-1.36	-1.29
79	16 06 57.00	17 51 24.84	0.0384	0.85	1.44	16.81	16.06	9.60	0.30	8.42	8.65	8.65	8.53	8.51	-0.91	-1.05	-0.98
80	16 07 00.67	17 34 00.48	0.0395	0.93	1.01	16.88	16.21	9.49	0.19	8.43	8.63	8.63	8.47	8.51	-0.99	-1.07	-1.03
81	16 07 05.30	18 06 55.08	0.0371	1.15	1.16	18.44	17.58	9.11	0.27	8.47	8.70	8.68	8.57	8.56	-0.88	-0.90	-0.89
82	16 07 07.87	18 26 01.68	0.0386	1.65	1.11	17.38	16.76	9.67	0.10	8.41	8.59	8.60	8.49	8.48	-0.96	-1.10	-1.03
83	16 07 13.41	18 11 54.60	0.0374	1.31	1.25	17.17	16.31	9.64	0.45	8.44	8.74	8.68	8.39	8.55	-1.08	-1.07	-1.07
84	16 07 20.21	17 19 41.52	0.0394	1.32	0.64	18.12	17.12	9.49	0.50	8.39	8.59	8.59	8.40	8.47	-1.06	-1.23	-1.15
85	16 07 22.18	18 19 26.40	0.0370	1.54	1.08	17.83	16.97	9.37	0.19	8.54	8.80	8.67	8.66	8.63	-0.81	-0.88	-0.84
86	16 07 23.04	17 06 52.92	0.0361	1.64	0.69	17.15	16.13	9.80	0.70	8.49	8.70	8.73	8.59	8.57	-0.85	-0.76	-0.81
87	16 07 25.25	18 30 14.40	0.0372	1.84	1.36	17.35	16.56	9.71	0.33	8.54	8.76	8.77	8.72	8.62	-0.68	-0.70	-0.69
88	16 07 27.17	17 59 17.88	0.0353	1.16	0.89	17.64	16.79	9.49	0.42	8.39	8.54	8.57	8.43	8.45	-1.01	-1.11	-1.06
89	16 07 39.60	17 32 08.16	0.0398	1.24	0.68	17.77	16.79	9.61	0.30	8.50	8.71	8.67	8.70	8.58	-0.74	-0.99	-0.87
90	16 08 21.02	18 17 08.16	0.0362	1.84	1.04	16.28	15.61	9.81	0.52	8.37	8.56	8.58	8.31	8.44	-1.18	-1.13	-1.16
91	16 08 24.53	18 07 59.52	0.0370	1.70	0.82	18.16	16.87	9.74	0.67	8.45	8.71	8.69	8.56	8.55	-0.88	-0.99	-0.93

Note: Column 1: order number for our sample of A2151 MS galaxies; column 2: right ascension in hours, minutes, and seconds; column 3: declination, in degrees, arcminutes, and arcseconds; column 4: redshift as given in SDSS; column 5: R/R_{200} distance from the cluster center in R_{200} units; column 6: log $\Sigma_{4,5}$ the logarithm of the density to the average of the projected distances to the fourth and fifth nearest neighbors in Mpc^{-2}; column 7: observed g magnitude given in SDSS; column 8: observed i magnitude given in SDSS; column 9: log$M_\star$ logarithm of the stellar mass given in SDSS; column 10: c(Hβ); column 11: log+12(O/H) derived using c-method (CM) calibration of Pilyugin et al. (2012); column 13: log+12(O/H) derived by PP04 calibration; column 13: log+12(O/H) derived by PMC09 calibration of N2; column 14: log+12(O/H) derived using Dors et al. (2011) models; column 15: the adopted value for log+12(O/H); column 16: log(N/O) derived using c-method (CM) calibration; column 17: log(N/O) derived by PMC09 calibration; column 18: the adopted value of log(N/O).

Table B.2: **MS galaxies in A2152**

# (1)	R.A. J2000 hh mm ss (2)	DEC J2000 dd mm ss (3)	z (4)	R/R_{200} (5)	$\Sigma_{4,5}$ Mpc^{-2} (6)	g mag (7)	i mag (8)	$M_\star$ $M_\odot$ (9)	$c(\mathrm{H}\beta)$ (10)	OH CM (11)	OH PP04 (12)	OH PMC09 (13)	OH D11 (14)	OH ADOP (15)	NO CM (16)	NO PMC09 (17)	NO ADOP (18)
01	16 02 12.00	16 13 12.36	0.0432	4.00	1.03	17.91	17.02	9.62	0.79	8.55	8.82	8.68	8.68	8.64	-0.81	-0.83	-0.82
02	16 02 55.92	17 03 48.24	0.0461	4.26	0.38	18.06	17.28	9.35	0.47	8.33	8.47	8.50	8.33	8.39	-1.13	-1.08	-1.10
03	16 03 16.27	16 55 09.84	0.0443	3.46	0.32	17.59	16.97	9.28	0.00	8.35	8.51	8.54	8.47	8.41	-0.96	-1.28	-1.12
04	16 03 35.16	16 25 03.00	0.0463	2.15	0.60	18.06	17.21	9.44	0.65	8.45	8.65	8.63	8.45	8.52	-1.02	-0.99	-1.01
05	16 03 38.98	16 42 27.00	0.0467	2.44	0.88	16.33	15.68	9.89	0.27	8.46	8.72	8.69	8.59	8.56	-0.85	-0.95	-0.90
06	16 03 57.19	16 45 15.48	0.0453	2.29	0.98	16.90	16.11	9.80	0.66	8.48	8.76	8.71	8.45	8.58	-1.07	-0.93	-1.00
07	16 04 02.16	16 48 33.48	0.0459	2.42	0.85	17.65	16.50	9.98	0.27	8.18	8.42	8.68	8.36	8.29	-0.96	-1.34	-1.15
08	16 04 03.77	16 22 18.84	0.0454	1.62	0.90	17.12	16.32	9.76	0.31	8.45	8.68	8.65	8.51	8.54	-0.96	-1.00	-0.98
09	16 04 33.91	16 48 11.16	0.0443	2.03	1.16	17.74	17.16	9.19	0.16	8.28	8.47	8.48	8.33	8.35	-1.11	-1.28	-1.19
10	16 04 44.28	16 54 20.16	0.0431	2.42	0.72	17.88	17.27	9.15	0.16	8.28	8.48	8.49	8.32	8.36	-1.14	-1.30	-1.22
11	16 05 10.10	16 11 54.24	0.0431	1.29	1.29	16.72	16.09	9.69	0.33	8.40	8.52	8.55	8.42	8.45	-1.03	-1.07	-1.05
12	16 05 18.22	16 09 34.20	0.0434	1.47	1.33	17.46	16.85	9.30	0.00	8.37	8.50	8.50	8.72	8.42	-0.66	-1.29	-0.98
13	16 05 21.43	15 45 20.16	0.0432	3.51	1.22	17.53	16.75	9.52	0.41	8.53	8.78	8.58	8.58	8.61	-0.95	-1.03	-0.99
14	16 05 24.19	16 46 30.00	0.0409	1.64	0.98	17.80	17.02	9.37	0.51	8.21	8.43	8.41	8.05	8.29	-1.27	-1.32	-1.30
15	16 05 26.62	16 14 25.44	0.0427	1.06	1.30	17.70	17.12	9.19	0.08	8.40	8.54	8.58	8.39	8.45	-1.05	-1.09	-1.07
16	16 05 58.13	16 27 52.20	0.0430	0.74	1.45	17.74	16.87	9.56	0.76	8.38	8.56	8.62	8.32	8.45	-1.17	-1.07	-1.12
17	16 06 00.00	16 13 56.64	0.0415	1.34	1.50	17.61	17.28	8.97	0.21	8.31	8.49	8.48	8.31	8.38	-1.16	-1.19	-1.18
18	16 06 02.93	16 24 24.48	0.0435	0.86	1.38	16.65	15.81	9.97	0.34	8.55	8.77	8.65	8.69	8.63	-0.79	-0.80	-0.79
19	16 06 03.41	16 51 41.76	0.0454	2.24	0.36	17.82	17.06	9.43	0.21	8.44	8.68	8.65	8.56	8.53	-0.89	-1.01	-0.95
20	16 06 08.31	16 37 58.44	0.0432	1.32	0.90	17.48	16.87	9.31	0.24	8.39	8.56	8.51	8.38	8.45	-1.08	-1.20	-1.14
21	16 06 10.20	16 11 01.68	0.0426	1.66	1.26	16.33	15.62	9.90	0.22	8.53	8.77	8.71	8.59	8.62	-0.89	-0.83	-0.86
22	16 06 16.75	16 19 29.28	0.0434	1.28	1.61	17.69	16.93	9.42	0.24	8.50	8.73	8.66	8.57	8.58	-0.91	-0.89	-0.90
23	16 06 20.64	15 49 32.52	0.0430	3.37	1.15	17.60	17.14	9.09	0.00	8.24	8.43	8.45	8.32	8.31	-1.12	-1.36	-1.24
24	16 06 22.71	16 06 34.92	0.0447	2.12	0.91	17.88	17.30	9.12	0.14	8.29	8.47	8.50	8.19	8.36	-1.20	-1.25	-1.23
25	16 06 27.36	16 52 04.80	0.0410	2.49	0.82	16.99	16.19	9.66	0.00	8.53	8.80	8.72	8.88	8.63	-0.41	-0.92	-0.67
26	16 06 47.74	15 56 26.16	0.0420	3.11	0.81	18.36	17.58	9.17	0.34	8.39	8.59	8.57	8.41	8.47	-1.04	-1.21	-1.13
27	16 07 23.40	16 05 07.44	0.0413	3.07	0.73	18.18	17.51	9.08	0.33	8.29	8.45	8.49	8.31	8.35	-1.14	-1.21	-1.17
28	16 08 10.94	16 39 43.20	0.0436	3.58	0.23	17.78	17.21	9.47	0.32	8.41	8.65	8.61	8.34	8.50	-1.16	-1.12	-1.14
29	16 08 13.34	16 18 09.36	0.0410	3.55	0.39	16.50	15.65	9.99	0.22	8.52	8.73	8.74	8.70	8.60	-0.71	-0.78	-0.75

Note: The columns are the same as in Table B.1

Table B.3: **MS galaxies in A2147**

# (1)	R.A. J2000 hh mm ss (2)	DEC J2000 dd mm ss (3)	z (4)	R/R_{200} (5)	$\Sigma_{4,5}$ Mpc^{-2} (6)	g mag (7)	i mag (8)	$M_\star$ $M_\odot$ (9)	$c(\mathrm{H}\beta)$ (10)	OH CM (11)	OH PP04 (12)	OH PMC09 (13)	OH D11 (14)	OH ADOP (15)	NO CM (16)	NO PMC09 (17)	NO ADOP (18)
01	15 59 30.65	15 59 45.96	0.0377	1.67	0.60	18.09	17.53	8.98	0.22	8.19	8.33	8.37	8.16	8.25	-1.21	-1.32	-1.27
02	15 59 37.71	15 18 41.76	0.0381	2.15	0.30	16.16	15.56	9.72	0.21	8.41	8.57	8.57	8.40	8.47	-1.05	-1.10	-1.08
03	15 59 40.42	16 22 35.76	0.0367	1.95	0.70	17.59	16.88	9.25	0.17	8.34	8.48	8.47	8.33	8.39	-1.15	-1.08	-1.11
04	16 00 00.55	16 07 38.28	0.0368	1.46	1.08	17.33	16.60	9.41	0.42	8.39	8.65	8.64	8.40	8.49	-1.06	-1.18	-1.12
05	16 00 12.74	16 24 41.04	0.0349	1.76	0.65	16.28	15.38	9.99	0.33	8.51	8.76	8.74	8.75	8.60	-0.62	-0.79	-0.71
06	16 00 15.31	16 14 36.60	0.0327	1.47	0.70	16.96	16.50	9.13	0.11	8.12	8.27	8.23	7.81	8.17	-1.34	-1.53	-1.43
07	16 00 16.15	16 08 36.24	0.0338	1.34	1.14	16.68	15.95	9.75	0.53	8.34	8.51	8.59	8.45	8.41	-0.98	-1.01	-1.00
08	16 00 17.76	16 01 21.36	0.0369	1.22	1.19	17.69	17.23	8.89	0.47	8.07	8.38	8.32	0.00	8.18	-1.59	-1.61	-1.60
09	16 00 21.82	16 01 42.60	0.0361	1.18	1.15	18.27	17.12	9.62	0.67	8.52	8.75	8.72	8.65	8.61	-0.81	-0.82	-0.82
10	16 00 23.90	15 13 22.44	0.0335	2.02	0.82	17.99	16.97	9.48	0.66	8.45	8.68	8.64	8.54	8.54	-0.91	-0.97	-0.94
11	16 00 26.52	16 04 30.00	0.0384	1.18	1.10	17.30	16.67	9.37	0.31	8.44	8.68	8.62	8.55	8.53	-0.91	-1.03	-0.97
12	16 00 36.43	16 21 10.08	0.0315	1.50	0.57	17.80	17.18	8.92	0.19	8.31	8.47	8.50	8.38	8.37	-1.05	-1.13	-1.09
13	16 00 38.04	16 39 10.08	0.0326	2.10	1.30	17.96	17.09	9.24	0.28	8.43	8.71	8.62	8.50	8.53	-0.99	-1.12	-1.06
14	16 01 02.35	16 22 40.80	0.0355	1.39	0.92	18.06	17.50	8.91	0.44	8.20	8.34	8.36	0.00	8.25	-1.50	-1.50	-1.50
15	16 01 07.15	15 12 52.20	0.0343	1.83	0.79	17.43	16.63	9.41	0.38	8.43	8.61	8.60	8.46	8.50	-1.00	-1.05	-1.02
16	16 01 11.57	16 25 10.92	0.0352	1.44	1.11	17.25	16.37	9.81	0.41	8.32	8.49	8.55	8.35	8.39	-1.09	-1.11	-1.10
17	16 01 15.07	16 26 39.12	0.0401	1.48	1.15	17.56	16.95	9.22	0.40	8.44	8.63	8.62	8.47	8.51	-1.01	-1.00	-1.01
18	16 01 18.60	15 35 32.64	0.0329	0.96	1.30	16.38	15.81	9.53	0.17	8.41	8.64	8.62	8.51	8.49	-0.94	-1.08	-1.01
19	16 01 28.10	15 36 48.60	0.0315	0.86	1.14	17.71	16.66	9.51	0.35	8.47	8.71	8.69	8.68	8.56	-0.76	-0.90	-0.83
20	16 01 32.52	15 28 20.64	0.0384	1.15	1.44	17.13	16.33	9.69	0.51	8.39	8.56	8.53	8.39	8.45	-1.06	-1.19	-1.13
21	16 01 33.46	15 46 44.40	0.0384	0.52	1.47	17.56	16.68	9.53	0.50	8.46	8.67	8.69	8.59	8.54	-0.85	-0.88	-0.86
22	16 01 43.49	15 26 16.44	0.0363	1.19	1.51	17.48	16.58	9.56	0.41	8.53	8.77	8.67	8.66	8.61	-0.81	-0.90	-0.86
23	16 01 45.94	16 29 51.36	0.0379	1.51	1.35	17.68	17.34	8.70	0.43	8.08	8.26	8.19	7.62	8.14	-1.41	-1.53	-1.47
24	16 01 55.61	15 42 23.04	0.0347	0.52	1.85	15.96	15.30	9.86	0.29	8.54	8.78	8.68	8.67	8.62	-0.81	-0.82	-0.82
25	16 01 57.48	16 05 49.56	0.0420	0.52	1.08	16.98	16.57	9.27	0.35	8.40	8.55	8.50	8.39	8.46	-1.09	-1.15	-1.12
26	16 02 03.67	15 11 13.92	0.0354	1.77	0.82	18.05	17.20	9.29	0.34	8.39	8.56	8.57	8.40	8.45	-1.04	-1.17	-1.11
27	16 02 09.38	15 30 05.40	0.0359	0.99	1.72	17.15	16.44	9.46	0.35	8.40	8.56	8.54	8.37	8.46	-1.10	-1.16	-1.13
28	16 02 13.63	15 06 56.52	0.0341	1.94	0.90	17.85	17.28	8.90	0.11	8.25	8.46	8.43	8.24	8.33	-1.20	-1.42	-1.31
29	16 02 16.61	16 04 36.48	0.0330	0.44	1.58	16.78	16.26	9.95	0.13	8.43	8.60	8.65	8.48	8.50	-0.98	-0.99	-0.98
30	16 02 45.55	16 13 21.36	0.0378	0.85	1.38	17.77	17.20	9.01	0.23	8.50	8.71	8.67	8.59	8.58	-0.87	-0.87	-0.87
31	16 02 46.01	15 16 57.36	0.0305	1.56	0.30	16.18	15.63	9.47	0.14	8.27	8.40	8.52	8.40	8.33	-1.01	-1.09	-1.05
32	16 02 49.58	16 23 19.32	0.0354	1.25	1.54	17.48	16.67	9.43	0.20	8.46	8.71	8.65	8.60	8.55	-0.85	-0.96	-0.90
33	16 02 50.98	15 57 39.60	0.0352	0.37	1.38	16.00	15.57	9.60	0.16	8.33	8.45	8.51	8.42	8.38	-1.03	-1.02	-1.02

Table B.3: **MS galaxies in A2147**

#	R.A. J2000 hh mm ss	DEC J2000 dd mm ss	z	R/R_{200}	$\Sigma_{4,5}$ Mpc^{-2}	g mag	i mag	$M_\star$ $M_\odot$	$c(\mathrm{H}\beta)$	OH CM	OH PP04	OH PMC09	OH D11	OH ADOP	NO CM	NO PMC09	NO ADOP
(1)	(2)	(3)	(4)	(5)	(6)	(7)	(8)	(9)	(10)	(11)	(12)	(13)	(14)	(15)	(16)	(17)	(18)
34	16 02 53.62	15 35 30.84	0.0364	0.85	0.98	17.73	17.21	9.04	0.11	8.38	8.56	8.53	8.40	8.45	-1.05	-1.22	-1.14
35	16 02 56.62	15 07 44.76	0.0374	1.95	0.87	17.87	17.42	8.85	0.04	8.13	8.32	8.28	8.00	8.20	-1.28	-1.44	-1.36
36	16 03 00.57	16 07 16.68	0.0341	0.70	1.25	17.69	17.05	9.11	0.27	8.26	8.44	8.44	8.35	8.33	-1.09	-1.29	-1.19
37	16 03 03.07	15 12 36.72	0.0345	1.77	1.45	16.69	15.69	9.94	0.17	8.52	8.77	8.75	8.78	8.61	-0.56	-0.73	-0.65
38	16 03 05.21	15 11 20.76	0.0335	1.83	1.31	18.05	17.47	9.21	0.14	8.17	8.34	8.33	7.90	8.23	-1.32	-1.42	-1.37
39	16 03 07.92	16 11 09.24	0.0396	0.87	1.58	18.04	17.00	9.57	0.40	8.54	8.77	8.70	8.83	8.62	-0.48	-0.76	-0.62
40	16 03 12.74	15 50 58.20	0.0388	0.57	1.27	15.81	15.17	9.99	0.42	8.51	8.73	8.70	8.61	8.59	-0.84	-0.83	-0.84
41	16 03 34.56	15 52 30.00	0.0338	0.77	1.31	16.16	15.50	9.76	0.34	8.51	8.76	8.69	8.58	8.60	-0.89	-0.92	-0.91
42	16 03 40.94	16 17 54.60	0.0326	1.29	1.56	17.72	17.27	8.82	0.24	8.38	8.52	8.51	8.40	8.43	-1.06	-1.18	-1.12
43	16 03 44.49	16 19 18.84	0.0316	1.36	1.47	16.63	15.92	9.56	0.26	8.51	8.74	8.68	8.60	8.59	-0.87	-0.95	-0.91
44	16 03 45.74	15 23 50.28	0.0399	1.53	0.56	18.33	17.78	9.06	0.14	8.28	8.43	8.45	8.33	8.34	-1.12	-1.20	-1.16
45	16 03 49.13	16 31 24.60	0.0415	1.79	1.03	17.19	16.71	9.22	0.27	8.33	8.48	8.50	8.35	8.39	-1.10	-1.08	-1.09
46	16 03 53.83	16 18 46.44	0.0320	1.40	1.60	17.49	16.68	9.34	0.28	8.43	8.67	8.65	8.52	8.52	-0.93	-1.05	-0.99
47	16 03 54.96	16 07 24.96	0.0323	1.12	1.01	16.90	16.22	9.44	0.31	8.43	8.60	8.60	8.47	8.49	-1.00	-1.01	-1.01
48	16 04 06.84	15 48 48.60	0.0339	1.11	1.16	17.81	17.13	9.08	0.37	8.31	8.50	8.51	8.32	8.38	-1.15	-1.20	-1.18
49	16 04 13.80	16 21 30.96	0.0317	1.62	1.02	17.64	16.98	9.04	0.28	8.27	8.44	8.48	8.31	8.34	-1.15	-1.26	-1.21
50	16 04 16.53	15 13 33.60	0.0342	2.05	0.41	16.79	16.11	9.48	0.31	8.37	8.52	8.53	8.34	8.43	-1.13	-1.26	-1.20
51	16 04 37.92	16 28 14.52	0.0390	1.99	1.00	16.13	15.53	9.70	0.11	8.27	8.50	8.52	8.25	8.36	-1.17	-1.35	-1.26
52	16 04 39.50	16 41 25.08	0.0316	2.41	1.11	16.69	15.65	9.93	0.68	8.56	8.79	8.69	8.69	8.64	-0.79	-0.71	-0.75
53	16 04 46.08	15 57 07.20	0.0384	1.49	0.60	17.61	16.81	9.42	0.15	8.49	8.73	8.69	8.56	8.58	-0.91	-0.97	-0.94
54	16 04 47.59	16 21 17.28	0.0411	1.87	0.94	17.20	16.37	9.72	0.59	8.45	8.64	8.63	8.42	8.52	-1.05	-1.00	-1.02
55	16 04 56.09	15 13 58.08	0.0395	2.29	0.96	18.35	17.40	9.33	0.37	8.40	8.67	8.60	8.43	8.50	-1.04	-1.20	-1.12
56	16 04 58.78	16 20 18.96	0.0314	1.94	0.80	17.92	17.23	8.97	0.00	8.36	8.56	8.55	8.40	8.44	-1.04	-1.32	-1.18
57	16 05 04.46	16 34 30.36	0.0389	2.35	0.95	18.24	17.27	9.42	0.39	8.39	8.57	8.59	8.48	8.46	-0.97	-1.18	-1.07
58	16 05 06.12	15 10 41.52	0.0403	2.46	0.94	17.90	17.39	9.00	0.00	8.14	8.41	8.40	8.31	8.24	-1.14	-1.43	-1.28
59	16 05 07.54	15 12 28.08	0.0400	2.41	1.11	17.88	16.93	9.57	0.50	8.42	8.57	8.58	8.42	8.48	-1.03	-1.03	-1.03
60	16 05 12.72	16 31 04.08	0.0399	2.32	0.95	17.61	16.74	9.58	0.45	8.55	8.79	8.67	8.66	8.64	-0.83	-0.81	-0.82
61	16 05 22.23	15 39 54.36	0.0411	1.93	1.32	17.46	16.93	9.18	0.12	8.39	8.55	8.54	8.36	8.45	-1.10	-1.21	-1.15

Note: The columns are the same as in Table B.1

Table B.4: **MS galaxies in the dispersed component**

# (1)	R.A. J2000 hh mm ss (2)	DEC J2000 dd mm ss (3)	z (4)	$\Sigma_{4,5}$ Mpc^{-2} (5)	$\Sigma_{4,5}$ Mpc^{-2} (6)	g mag (7)	i mag (8)	$M_\star$ $M_\odot$ (9)	$c(\mathrm{H}\beta)$ (10)	OH CM (11)	OH PP04 (12)	OH PMC09 (13)	OH D11 (14)	OH ADOP (15)	NO CM (16)	NO PMC09 (17)	NO ADOP (18)
001	15 56 00.86	17 20 51.72	0.0463	-0.22	-0.22	17.70	17.01	9.46	0.35	8.45	8.66	8.65	8.48	8.53	-0.98	-0.94	-0.96
002	15 56 05.59	16 48 02.88	0.0470	-0.49	-0.49	17.91	17.20	9.39	0.26	8.40	8.57	8.55	8.38	8.46	-1.08	-1.17	-1.12
003	15 56 11.43	19 08 46.32	0.0373	-0.53	-0.81	18.23	17.26	9.41	0.51	8.45	8.70	8.65	8.60	8.54	-0.84	-0.99	-0.92
004	15 56 20.69	16 57 41.04	0.0457	-0.10	-0.32	16.76	16.22	9.54	0.24	8.39	8.55	8.54	8.41	8.45	-1.04	-1.16	-1.10
005	15 56 20.78	18 19 37.92	0.0461	0.42	0.42	17.12	16.45	9.62	0.27	8.41	8.63	8.57	8.48	8.49	-1.00	-1.11	-1.06
006	15 56 36.53	18 30 01.44	0.0332	-0.09	-0.09	17.44	16.78	9.11	0.09	8.17	8.32	8.34	8.04	8.23	-1.26	-1.38	-1.32
007	15 56 41.04	17 45 22.68	0.0345	0.10	0.10	16.08	15.23	9.92	0.35	8.44	8.70	8.69	8.56	8.54	-0.87	-1.00	-0.94
008	15 56 41.83	15 58 00.12	0.0399	0.33	0.23	16.59	15.82	9.83	0.47	8.42	8.59	8.65	8.52	8.49	-0.92	-0.89	-0.91
009	15 56 49.80	17 11 44.16	0.0456	-0.04	-0.04	16.94	16.44	9.42	0.15	8.33	8.51	8.60	8.45	8.41	-0.98	-1.03	-1.01
010	15 56 55.99	19 03 58.68	0.0461	0.09	0.09	17.33	16.53	9.72	0.44	8.24	8.40	8.42	8.30	8.30	-1.18	-1.19	-1.19
011	15 57 00.05	16 24 18.72	0.0359	0.77	0.77	17.93	17.44	8.88	0.13	8.17	8.33	8.31	8.30	8.23	-1.20	-1.35	-1.28
012	15 57 05.06	18 09 55.44	0.0319	0.19	0.19	17.22	16.76	8.96	0.17	8.36	8.42	8.42	8.32	8.38	-1.17	-1.07	-1.12
013	15 57 08.52	19 06 07.20	0.0458	0.12	0.12	16.98	16.11	9.86	0.51	8.57	8.84	8.69	8.65	8.66	-0.86	-0.75	-0.81
014	15 57 16.75	18 10 20.64	0.0450	1.13	1.13	18.33	17.55	9.26	0.00	8.37	8.62	8.53	8.47	8.46	-1.01	-1.34	-1.17
015	15 57 22.25	16 04 09.12	0.0368	0.90	0.90	18.18	17.55	8.88	0.02	8.26	8.44	8.46	8.30	8.33	-1.16	-1.34	-1.25
016	15 57 22.34	19 01 37.20	0.0465	0.32	0.32	18.02	17.34	9.30	0.00	8.40	8.61	8.65	8.50	8.48	-0.94	-1.17	-1.05
017	15 57 31.75	18 05 20.40	0.0312	0.20	0.12	17.43	16.93	8.85	0.14	8.16	8.36	8.36	8.03	8.24	-1.26	-1.41	-1.34
018	15 57 40.75	16 07 34.32	0.0373	1.20	1.20	16.16	15.38	9.93	0.24	8.54	8.76	8.64	8.68	8.62	-0.80	-0.80	-0.80
019	15 57 40.94	16 23 13.20	0.0360	1.35	1.35	16.86	16.07	9.71	0.36	8.45	8.67	8.66	8.63	8.53	-0.82	-0.95	-0.89
020	15 57 41.98	17 47 55.68	0.0470	0.55	0.55	17.40	16.47	9.85	0.26	8.52	8.77	8.77	8.75	8.62	-0.59	-0.74	-0.67
021	15 57 52.97	16 43 46.92	0.0402	0.51	0.12	17.23	16.67	9.30	0.27	8.34	8.51	8.55	8.36	8.41	-1.09	-1.09	-1.09
022	15 57 54.14	18 27 37.44	0.0308	0.10	0.07	17.48	16.92	9.00	0.15	8.29	8.44	8.46	8.33	8.35	-1.14	-1.22	-1.18
023	15 57 59.66	16 02 53.16	0.0380	1.01	1.01	17.25	16.40	9.68	0.54	8.41	8.59	8.57	8.38	8.48	-1.08	-1.15	-1.11
024	15 57 59.88	16 05 44.16	0.0353	1.18	1.18	17.62	16.82	9.36	0.00	8.42	8.65	8.62	8.61	8.51	-0.83	-1.07	-0.95
025	15 58 05.21	18 31 03.72	0.0465	0.53	0.53	17.89	17.18	9.22	0.10	8.34	8.48	8.48	8.38	8.39	-1.07	-1.33	-1.20
026	15 58 08.11	18 51 42.12	0.0347	0.06	-0.15	17.16	16.46	9.35	0.16	8.32	8.51	8.54	8.36	8.40	-1.08	-1.16	-1.12
027	15 58 09.84	18 23 04.56	0.0458	0.63	0.62	17.58	16.80	9.53	0.12	8.44	8.66	8.68	8.56	8.52	-0.84	-0.98	-0.91
028	15 58 12.02	16 30 03.96	0.0367	0.88	0.88	16.41	15.59	9.93	0.52	8.56	8.83	8.72	8.74	8.66	-0.67	-0.74	-0.70
029	15 58 18.02	16 17 30.12	0.0353	1.43	1.43	16.89	16.03	9.80	0.47	8.42	8.61	8.62	8.52	8.49	-0.94	-1.03	-0.99
030	15 58 18.60	16 32 16.08	0.0365	0.70	0.70	17.02	16.13	9.77	0.55	8.48	8.70	8.66	8.54	8.56	-0.93	-0.96	-0.95
031	15 58 21.65	17 27 51.84	0.0369	0.45	0.14	17.72	16.77	9.59	0.53	8.55	8.78	8.71	8.69	8.63	-0.78	-0.74	-0.76
032	15 58 22.42	16 06 09.36	0.0386	0.91	0.91	16.92	16.03	9.91	0.59	8.42	8.59	8.62	8.46	8.49	-1.00	-1.04	-1.02
033	15 58 28.15	17 30 12.24	0.0442	0.40	0.40	17.99	17.07	9.59	0.47	8.47	8.67	8.73	8.63	8.55	-0.79	-0.78	-0.79

Table B.4: **MS galaxies in the dispersed component**

# (1)	R.A. J2000 hh mm ss (2)	DEC J2000 dd mm ss (3)	z (4)	$\Sigma_{4,5}$ Mpc^{-2} (5)	$\Sigma_{4,5}$ Mpc^{-2} (6)	g mag (7)	i mag (8)	$M_\star$ $M_\odot$ (9)	c(Hβ) (10)	OH CM (11)	OH PP04 (12)	OH PMC09 (13)	OH D11 (14)	OH ADOP (15)	NO CM (16)	NO PMC09 (17)	NO ADOP (18)
034	15 58 28.61	18 11 10.68	0.0417	1.20	0.98	17.30	16.64	9.45	0.26	8.51	8.75	8.68	8.60	8.60	-0.86	-0.92	-0.89
035	15 58 42.48	17 21 37.44	0.0368	0.30	0.03	16.58	16.36	8.99	0.21	8.12	8.13	8.08	7.75	8.12	-1.37	-1.36	-1.36
036	15 58 44.86	17 56 23.64	0.0365	0.67	-0.11	17.64	16.92	9.28	0.11	8.42	8.66	8.65	8.48	8.51	-0.97	-1.09	-1.03
037	15 59 02.33	14 36 20.88	0.0338	0.47	0.47	18.30	17.61	8.90	0.21	8.22	8.40	8.39	8.32	8.29	-1.13	-1.42	-1.28
038	15 59 05.30	17 20 02.40	0.0350	0.24	0.19	17.32	16.86	8.88	0.19	8.11	8.30	8.27	7.82	8.18	-1.33	-1.52	-1.42
039	15 59 12.24	14 22 20.64	0.0350	0.36	0.36	17.04	16.40	9.56	0.26	8.38	8.51	8.51	8.36	8.43	-1.10	-1.20	-1.15
040	15 59 13.39	18 04 20.28	0.0471	1.34	1.34	16.93	16.11	9.91	0.48	8.44	8.64	8.66	8.56	8.52	-0.88	-0.94	-0.91
041	15 59 20.62	18 40 25.68	0.0466	0.44	0.44	17.98	17.46	9.04	0.00	8.25	8.47	8.51	8.36	8.34	-1.06	-1.36	-1.21
042	15 59 21.15	15 08 21.48	0.0427	0.68	0.49	16.59	15.81	9.86	0.40	8.52	8.78	8.72	8.59	8.61	-0.89	-0.94	-0.91
043	15 59 21.58	19 16 23.52	0.0289	-0.05	-0.09	16.78	15.79	9.77	0.41	8.41	8.63	8.65	8.50	8.49	-0.95	-1.08	-1.01
044	15 59 22.08	19 12 48.60	0.0461	0.26	0.26	17.55	16.94	9.34	0.32	8.40	8.56	8.54	8.37	8.46	-1.09	-1.14	-1.11
045	15 59 38.95	19 05 04.92	0.0317	0.35	0.28	18.26	17.42	9.09	0.81	8.26	8.45	8.49	7.71	8.34	-1.37	-1.32	-1.35
046	15 59 39.38	17 44 42.36	0.0433	0.77	0.64	18.44	17.36	9.55	0.55	8.55	8.79	8.70	8.71	8.64	-0.71	-0.82	-0.77
047	15 59 40.03	15 42 46.44	0.0429	0.31	-0.13	17.57	17.08	9.15	0.10	8.22	8.28	8.32	8.30	8.24	-1.19	-1.25	-1.22
048	15 59 44.43	18 44 00.96	0.0295	0.27	0.19	17.26	16.68	9.01	0.00	8.27	8.47	8.47	8.31	8.35	-1.14	-1.31	-1.23
049	15 59 46.87	18 54 36.36	0.0461	0.51	0.51	18.11	17.34	9.30	0.54	8.20	8.38	8.37	8.07	8.27	-1.26	-1.31	-1.29
050	15 59 47.76	18 11 43.80	0.0319	0.58	-0.10	18.11	17.38	8.97	0.20	8.14	8.26	8.25	8.01	8.18	-1.27	-1.43	-1.35
051	15 59 50.76	14 41 23.64	0.0367	0.63	0.63	17.76	17.12	9.14	0.23	8.18	8.39	8.40	8.30	8.26	-1.16	-1.34	-1.25
052	15 59 57.77	18 18 45.00	0.0318	0.49	0.08	17.79	17.07	9.16	0.00	8.37	8.60	8.59	8.50	8.46	-0.95	-1.23	-1.09
053	16 00 18.94	16 04 17.04	0.0435	0.83	0.16	18.04	17.42	9.13	0.26	8.31	8.47	8.49	8.34	8.37	-1.12	-1.16	-1.14
054	16 00 19.01	14 32 47.04	0.0364	0.88	0.88	17.27	16.51	9.48	0.31	8.37	8.52	8.54	8.38	8.43	-1.06	-1.24	-1.15
055	16 00 21.65	15 03 06.12	0.0348	0.80	0.80	18.21	17.98	8.25	0.12	8.18	8.28	8.26	8.05	8.22	-1.28	-1.31	-1.30
056	16 00 29.71	14 30 11.16	0.0362	0.65	0.65	17.52	16.99	9.02	0.15	8.13	8.32	8.30	7.86	8.20	-1.33	-1.51	-1.42
057	16 00 41.43	18 07 33.96	0.0301	0.58	-0.36	17.66	16.97	9.03	0.00	8.37	8.53	8.50	8.36	8.43	-1.11	-1.29	-1.20
058	16 00 52.01	18 59 13.92	0.0320	0.63	0.46	17.69	16.98	9.13	0.13	8.39	8.59	8.59	8.45	8.47	-0.99	-1.21	-1.10
059	16 00 57.00	16 50 22.56	0.0344	1.10	1.10	17.72	17.21	8.91	0.15	8.27	8.48	8.47	8.35	8.35	-1.09	-1.30	-1.20
060	16 00 57.39	16 20 24.36	0.0435	0.93	0.56	17.96	17.45	9.02	0.04	8.31	8.44	8.56	8.41	8.37	-1.00	-1.04	-1.02
061	16 00 58.49	17 04 22.08	0.0372	0.89	0.89	17.35	16.68	9.29	0.05	8.36	8.53	8.52	8.39	8.43	-1.06	-1.29	-1.17
062	16 00 59.97	18 18 22.32	0.0298	0.59	-0.12	16.72	15.86	9.62	0.23	8.40	8.62	8.64	8.40	8.48	-1.03	-1.22	-1.13
063	16 01 13.34	18 47 59.64	0.0320	0.69	0.64	17.25	16.40	9.48	0.53	8.44	8.72	8.73	8.54	8.55	-0.90	-1.02	-0.96
064	16 01 16.68	16 47 23.28	0.0444	0.38	0.25	17.82	17.01	9.47	0.22	8.29	8.48	8.53	8.43	8.37	-0.99	-1.19	-1.09
065	16 01 26.04	17 03 06.48	0.0343	1.10	1.10	18.09	17.14	9.36	0.27	8.39	8.62	8.63	8.52	8.48	-0.92	-1.16	-1.04
066	16 01 33.02	17 41 36.24	0.0439	0.47	0.47	17.87	17.00	9.61	0.34	8.56	8.82	8.71	8.76	8.65	-0.61	-0.73	-0.67

Table B.4: **MS galaxies in the dispersed component**

# (1)	R.A. J2000 hh mm ss (2)	DEC J2000 dd mm ss (3)	z (4)	$\Sigma_{4,5}$ Mpc^{-2} (5)	$\Sigma_{4,5}$ Mpc^{-2} (6)	g mag (7)	i mag (8)	$M_\star$ $M_\odot$ (9)	$c(\mathrm{H}\beta)$ (10)	OH CM (11)	OH PP04 (12)	OH PMC09 (13)	OH D11 (14)	OH ADOP (15)	NO CM (16)	NO PMC09 (17)	NO ADOP (18)
067	16 01 34.39	17 06 56.52	0.0444	0.09	0.02	18.20	17.52	9.11	0.16	8.26	8.46	8.46	8.30	8.34	-1.15	-1.38	-1.27
068	16 01 45.22	19 03 44.64	0.0315	0.33	0.33	17.68	16.75	9.43	0.11	8.36	8.57	8.55	8.51	8.44	-0.92	-1.27	-1.10
069	16 01 49.44	17 38 26.16	0.0358	0.33	0.33	16.05	15.29	9.82	0.25	8.53	8.78	8.71	8.68	8.62	-0.79	-0.90	-0.84
070	16 01 51.86	18 03 55.44	0.0471	0.83	0.71	17.87	16.97	9.62	0.13	8.43	8.69	8.65	8.55	8.53	-0.90	-1.06	-0.98
071	16 01 53.69	16 51 29.52	0.0359	1.27	1.21	18.00	17.31	9.14	0.16	8.42	8.65	8.65	8.43	8.51	-1.02	-1.13	-1.08
072	16 01 58.90	14 30 40.32	0.0356	0.80	0.80	18.04	17.23	9.21	0.44	8.20	8.41	8.43	8.31	8.28	-1.15	-1.30	-1.23
073	16 02 00.62	18 31 31.08	0.0453	0.52	0.42	16.84	16.04	9.87	0.45	8.40	8.53	8.58	8.39	8.45	-1.06	-1.07	-1.06
074	16 02 01.73	16 45 27.72	0.0318	1.37	0.93	16.66	15.99	9.47	0.28	8.51	8.74	8.68	8.59	8.59	-0.87	-0.90	-0.88
075	16 02 05.42	16 48 51.48	0.0344	1.56	1.56	17.86	17.31	8.91	0.15	8.27	8.47	8.48	8.30	8.35	-1.15	-1.30	-1.23
076	16 02 07.23	18 45 29.52	0.0318	0.30	0.30	18.11	17.21	9.22	0.01	8.38	8.60	8.57	8.36	8.46	-1.10	-1.30	-1.20
077	16 02 08.71	14 25 22.44	0.0374	0.81	0.42	17.60	16.82	9.36	0.14	8.39	8.63	8.60	8.52	8.48	-0.92	-1.20	-1.06
078	16 02 11.85	16 43 06.60	0.0344	1.20	1.20	18.11	17.69	8.62	0.13	8.13	8.26	8.23	7.66	8.18	-1.40	-1.48	-1.44
079	16 02 30.79	14 29 13.20	0.0336	1.00	0.60	18.07	17.28	9.14	0.19	8.42	8.62	8.73	8.47	8.50	-0.96	-1.01	-0.99
080	16 02 36.05	18 17 33.00	0.0464	0.68	0.63	18.23	17.31	9.42	0.10	8.37	8.59	8.59	8.41	8.45	-1.03	-1.33	-1.18
081	16 02 40.68	14 51 30.60	0.0412	1.05	-0.25	17.93	17.37	9.13	0.08	8.28	8.48	8.51	8.39	8.36	-1.03	-1.23	-1.13
082	16 02 42.96	19 19 01.56	0.0463	0.46	0.45	17.72	17.16	9.66	0.17	8.27	8.42	8.40	8.31	8.33	-1.17	-1.28	-1.22
083	16 02 43.90	14 31 57.36	0.0357	0.84	0.84	16.96	16.32	9.41	0.24	8.41	8.65	8.63	8.49	8.50	-0.96	-1.13	-1.05
084	16 02 55.44	14 58 18.84	0.0354	0.96	0.90	17.78	17.23	8.92	0.22	8.20	8.40	8.42	8.32	8.28	-1.14	-1.31	-1.23
085	16 03 00.07	14 56 24.36	0.0357	1.09	0.95	16.51	16.05	9.32	0.24	8.39	8.52	8.53	8.40	8.44	-1.05	-1.09	-1.07
086	16 03 06.19	14 48 28.08	0.0344	1.14	1.12	18.03	17.31	9.09	0.34	8.28	8.50	8.44	8.08	8.36	-1.27	-1.36	-1.31
087	16 03 09.50	18 08 54.60	0.0457	0.30	0.23	18.27	17.50	9.26	0.20	8.26	8.43	8.45	8.30	8.33	-1.16	-1.31	-1.23
088	16 03 21.00	19 07 43.68	0.0404	1.25	-0.20	17.75	16.94	9.63	0.36	8.41	8.60	8.61	8.53	8.48	-0.92	-0.98	-0.95
089	16 03 21.50	14 41 37.68	0.0408	1.04	0.11	18.10	17.53	8.98	0.10	8.11	8.24	8.23	8.12	8.16	-1.23	-1.41	-1.32
090	16 03 21.67	14 39 52.92	0.0339	1.12	1.12	17.46	16.85	9.13	0.17	8.26	8.47	8.47	8.35	8.34	-1.09	-1.34	-1.21
091	16 03 32.40	19 15 56.88	0.0383	-0.18	-0.31	17.76	17.08	9.49	0.19	8.37	8.58	8.58	8.39	8.45	-1.05	-1.28	-1.17
092	16 03 35.73	16 58 41.88	0.0479	0.48	0.34	17.97	16.77	9.92	0.70	8.54	8.76	8.81	8.72	8.63	-0.68	-0.69	-0.68
093	16 03 36.50	16 54 10.08	0.0353	0.99	0.99	18.24	17.37	9.20	0.21	8.51	8.74	8.65	8.64	8.59	-0.81	-1.04	-0.92
094	16 03 41.83	14 33 32.76	0.0420	1.46	0.00	17.65	16.84	9.53	0.33	8.45	8.66	8.66	8.55	8.53	-0.90	-0.94	-0.92
095	16 03 48.17	14 31 29.28	0.0362	1.34	1.20	17.39	16.96	8.87	0.22	8.11	8.20	8.17	7.82	8.14	-1.34	-1.47	-1.40
096	16 03 53.38	14 36 38.52	0.0368	1.24	1.14	16.87	16.06	9.72	0.23	8.46	8.72	8.76	8.70	8.56	-0.70	-1.05	-0.87
097	16 03 54.77	14 35 27.24	0.0347	1.12	1.12	17.92	17.44	8.77	0.17	8.10	8.36	8.29	7.90	8.19	-1.31	-1.55	-1.43
098	16 04 13.92	18 34 36.48	0.0470	-0.06	-0.07	18.01	17.37	9.16	0.07	8.39	8.57	8.61	8.40	8.46	-1.03	-1.16	-1.09
099	16 04 23.88	18 59 20.76	0.0357	0.28	0.25	18.04	17.45	9.31	0.01	8.22	8.41	8.38	8.41	8.29	-0.99	-1.44	-1.21

Table B.4: **MS galaxies in the dispersed component**

# (1)	R.A. J2000 hh mm ss (2)	DEC J2000 dd mm ss (3)	z (4)	$\Sigma_{4,5}$ Mpc^{-2} (5)	$\Sigma_{4,5}$ Mpc^{-2} (6)	g mag (7)	i mag (8)	$M_\star$ $M_\odot$ (9)	$c(\mathrm{H}\beta)$ (10)	OH CM (11)	OH PP04 (12)	OH PMC09 (13)	OH D11 (14)	OH ADOP (15)	NO CM (16)	NO PMC09 (17)	NO ADOP (18)
100	16 04 26.43	14 53 03.12	0.0377	1.18	1.18	18.41	17.47	9.26	0.11	8.43	8.67	8.57	8.69	8.51	-0.75	-1.24	-0.99
101	16 04 35.47	16 45 35.64	0.0301	0.91	0.87	17.74	17.25	8.91	0.12	8.23	8.33	8.34	8.31	8.27	-1.19	-1.19	-1.19
102	16 04 44.71	18 42 24.48	0.0356	0.38	0.38	17.64	16.75	9.71	0.27	8.54	8.76	8.70	8.71	8.62	-0.72	-0.79	-0.76
103	16 04 58.32	14 43 00.12	0.0373	0.94	0.71	17.87	17.07	9.29	0.15	8.40	8.60	8.59	8.55	8.47	-0.90	-1.07	-0.99
104	16 05 05.33	14 51 23.40	0.0422	0.90	0.58	17.23	16.35	9.72	0.23	8.49	8.74	8.73	8.72	8.58	-0.66	-0.86	-0.76
105	16 05 14.26	16 45 39.96	0.0396	1.37	0.87	16.74	16.14	9.60	0.26	8.43	8.65	8.60	8.50	8.51	-0.97	-1.03	-1.00
106	16 05 21.34	16 55 17.76	0.0365	0.97	0.72	17.99	16.91	9.56	0.33	8.50	8.72	8.66	8.69	8.58	-0.78	-1.02	-0.90
107	16 05 26.02	18 46 53.40	0.0373	0.70	0.70	18.27	17.55	9.34	0.27	8.31	8.50	8.50	8.36	8.38	-1.09	-1.19	-1.14
108	16 05 39.07	15 54 36.72	0.0378	1.25	1.17	18.32	17.68	8.96	0.17	8.40	8.61	8.57	8.41	8.48	-1.04	-1.23	-1.13
109	16 05 41.71	14 57 28.80	0.0394	0.55	0.55	17.35	16.66	9.37	0.27	8.36	8.52	8.51	8.33	8.42	-1.13	-1.28	-1.20
110	16 05 46.37	16 11 48.84	0.0401	1.68	1.35	17.21	16.57	9.41	0.19	8.43	8.64	8.63	8.53	8.51	-0.93	-0.99	-0.96
111	16 05 48.31	14 37 16.32	0.0411	1.01	1.01	18.28	17.31	9.41	0.30	8.44	8.71	8.70	8.59	8.54	-0.84	-1.04	-0.94
112	16 05 49.37	18 59 30.48	0.0465	-0.27	-0.32	18.00	17.52	9.53	0.06	8.10	8.27	8.21	7.85	8.16	-1.34	-1.57	-1.46
113	16 05 50.81	18 35 25.44	0.0387	1.25	1.25	17.77	17.11	9.51	0.11	8.38	8.60	8.55	8.50	8.46	-0.95	-1.22	-1.09
114	16 05 56.50	15 38 27.96	0.0418	1.63	1.61	18.18	17.38	9.30	0.36	8.42	8.65	8.63	8.63	8.51	-0.81	-1.06	-0.94
115	16 06 14.49	16 45 15.12	0.0390	0.91	0.67	16.82	16.12	9.58	0.26	8.45	8.65	8.64	8.44	8.53	-1.03	-1.01	-1.02
116	16 06 15.65	14 39 40.32	0.0391	0.70	0.70	18.07	17.17	9.41	0.29	8.40	8.59	8.59	8.48	8.47	-0.97	-1.16	-1.07
117	16 06 22.08	15 33 05.76	0.0388	1.54	1.45	16.58	15.70	9.98	0.53	8.57	8.83	8.69	8.70	8.66	-0.77	-0.76	-0.76
118	16 06 29.45	15 05 40.92	0.0401	0.72	0.72	17.80	17.20	9.09	0.18	8.42	8.58	8.58	8.47	8.48	-1.00	-1.06	-1.03
119	16 06 39.70	18 44 26.88	0.0387	0.95	0.95	17.66	17.22	9.52	0.49	8.39	8.56	8.57	8.32	8.46	-1.19	-1.19	-1.19
120	16 06 41.33	15 50 21.12	0.0387	1.31	1.27	16.73	16.12	9.53	0.15	8.40	8.52	8.54	8.45	8.45	-1.01	-1.07	-1.04
121	16 06 42.14	15 43 01.92	0.0363	1.75	1.56	17.27	16.28	9.78	0.51	8.58	8.86	8.66	8.71	8.67	-0.76	-0.83	-0.80
122	16 06 50.50	15 03 11.88	0.0414	0.90	0.37	18.28	17.13	9.66	0.70	8.53	8.75	8.70	8.67	8.61	-0.80	-0.83	-0.81
123	16 06 51.38	15 21 37.44	0.0391	0.75	0.75	17.76	17.48	8.69	0.09	8.06	8.19	8.11	7.46	8.10	-1.44	-1.56	-1.50
124	16 06 54.22	15 48 15.84	0.0391	1.25	1.25	17.22	16.52	9.47	0.29	8.45	8.65	8.66	8.47	8.53	-1.00	-0.98	-0.99
125	16 06 58.63	15 00 44.28	0.0376	0.90	0.81	17.46	16.76	9.38	0.39	8.29	8.43	8.48	8.33	8.35	-1.11	-1.18	-1.15
126	16 07 00.12	15 29 52.44	0.0394	1.01	1.01	18.19	17.71	8.81	0.15	8.18	8.26	8.27	8.02	8.21	-1.28	-1.32	-1.30
127	16 07 01.78	14 46 28.92	0.0383	0.67	0.58	17.68	17.04	9.12	0.18	8.25	8.49	8.51	8.21	8.34	-1.17	-1.41	-1.29
128	16 07 06.69	19 09 38.88	0.0398	0.01	-0.02	17.87	17.17	9.52	0.19	8.42	8.61	8.63	8.56	8.49	-0.88	-0.98	-0.93
129	16 07 09.31	16 56 53.52	0.0399	0.89	0.86	16.62	15.93	9.71	0.32	8.51	8.75	8.64	8.58	8.59	-0.90	-0.98	-0.94
130	16 07 12.72	15 21 33.84	0.0407	0.71	0.71	17.84	17.13	9.30	0.26	8.31	8.49	8.52	8.36	8.38	-1.06	-1.18	-1.12
131	16 07 16.61	15 09 56.52	0.0378	0.77	0.70	17.77	17.20	9.19	0.26	8.14	8.34	8.31	7.92	8.21	-1.30	-1.46	-1.38
132	16 07 28.85	15 58 07.32	0.0310	0.37	-0.18	17.06	16.41	9.26	0.17	8.31	8.48	8.50	8.33	8.38	-1.12	-1.16	-1.14

Table B.4: **MS galaxies in the dispersed component**

# (1)	R.A. J2000 hh mm ss (2)	DEC J2000 dd mm ss (3)	z (4)	$\Sigma_{4,5}$ Mpc^{-2} (5)	$\Sigma_{4,5}$ Mpc^{-2} (6)	g mag (7)	i mag (8)	$M_\star$ $M_\odot$ (9)	$c(\mathrm{H}\beta)$ (10)	OH CM (11)	OH PP04 (12)	OH PMC09 (13)	OH D11 (14)	OH ADOP (15)	NO CM (16)	NO PMC09 (17)	NO ADOP (18)
133	16 07 36.34	14 54 10.44	0.0341	0.75	-0.30	17.10	16.59	9.17	0.05	8.35	8.50	8.46	8.35	8.41	-1.11	-1.34	-1.23
134	16 07 42.50	14 52 13.44	0.0366	0.69	0.67	17.08	16.23	9.70	0.31	8.36	8.52	8.59	8.51	8.43	-0.90	-1.11	-1.00
135	16 07 43.03	14 59 43.80	0.0374	0.90	0.73	17.43	16.44	9.73	0.49	8.42	8.67	8.64	8.53	8.51	-0.91	-1.08	-1.00
136	16 08 00.65	15 42 38.88	0.0369	1.04	1.00	18.08	17.34	9.16	0.18	8.39	8.58	8.60	8.45	8.46	-1.00	-1.18	-1.09
137	16 08 21.48	16 55 52.32	0.0396	0.44	0.26	17.99	17.42	9.02	0.40	8.32	8.47	8.49	8.34	8.38	-1.15	-1.12	-1.14
138	16 08 36.86	16 09 06.12	0.0436	0.79	0.79	17.17	16.33	9.79	0.19	8.50	8.72	8.66	8.62	8.58	-0.82	-0.95	-0.89
139	16 08 37.29	15 52 36.84	0.0310	0.18	-0.49	17.87	17.25	8.87	0.61	8.05	8.37	8.33	0.00	8.17	-1.59	-1.48	-1.53
140	16 08 57.26	18 48 37.44	0.0363	0.74	0.74	17.61	16.96	9.54	0.49	8.13	8.46	8.39	7.87	8.25	-1.36	-1.46	-1.41
141	16 08 58.80	17 30 24.48	0.0347	0.17	0.02	16.77	15.97	9.64	0.23	8.48	8.69	8.63	8.50	8.56	-0.99	-0.98	-0.98
142	16 09 08.31	16 39 37.08	0.0359	0.77	0.24	17.90	16.96	9.42	0.59	8.42	8.56	8.60	8.38	8.48	-1.08	-1.00	-1.04
143	16 09 10.10	18 35 01.32	0.0365	0.52	0.52	18.07	16.66	9.50	0.90	8.54	8.78	8.73	8.70	8.63	-0.75	-0.82	-0.79
144	16 09 10.78	16 20 07.44	0.0412	0.72	0.63	17.37	16.35	9.94	0.52	8.51	8.73	8.70	8.62	8.59	-0.83	-0.86	-0.84
145	16 09 11.18	15 40 37.20	0.0459	0.62	0.54	17.73	16.96	9.43	0.46	8.38	8.56	8.61	8.12	8.45	-1.23	-1.14	-1.19
146	16 09 17.33	19 12 12.96	0.0362	0.16	0.16	17.14	16.26	9.78	0.43	8.47	8.69	8.71	8.68	8.56	-0.75	-0.82	-0.79
147	16 09 27.26	15 41 53.88	0.0459	0.58	0.58	18.11	17.12	9.61	0.18	8.37	8.58	8.61	8.57	8.45	-0.82	-1.17	-0.99
148	16 09 27.98	16 30 22.32	0.0417	0.62	0.40	17.12	16.47	9.45	0.35	8.44	8.70	8.64	8.36	8.54	-1.14	-1.07	-1.11
149	16 09 28.03	16 45 37.80	0.0358	0.47	0.27	17.17	16.53	9.33	0.41	8.32	8.47	8.52	8.32	8.38	-1.13	-1.11	-1.12
150	16 09 30.12	15 02 07.80	0.0464	0.22	0.13	16.31	15.87	9.64	0.44	8.26	8.32	8.41	8.32	8.29	-1.16	-1.10	-1.13
151	16 09 34.56	18 18 10.08	0.0364	0.56	0.56	17.09	16.44	9.73	0.26	8.36	8.56	8.57	8.31	8.44	-1.14	-1.35	-1.24
152	16 09 36.10	18 38 27.24	0.0461	-0.54	-0.97	17.96	17.32	9.60	0.15	8.39	8.58	8.66	8.57	8.47	-0.85	-0.98	-0.91
153	16 09 36.82	14 40 12.00	0.0317	-0.16	-0.23	17.79	17.15	8.99	0.19	8.13	8.39	8.35	8.10	8.23	-1.23	-1.46	-1.35
154	16 09 46.82	14 25 07.32	0.0426	-0.23	-0.36	17.02	16.39	9.53	0.00	8.39	8.61	8.55	8.53	8.47	-0.93	-1.20	-1.07
155	16 09 47.69	17 46 06.24	0.0372	0.27	0.22	17.45	16.81	9.21	0.26	8.42	8.60	8.64	8.40	8.49	-1.04	-1.09	-1.07
156	16 09 56.47	18 45 19.08	0.0355	0.77	0.77	18.09	17.34	9.35	0.27	8.28	8.43	8.45	8.30	8.34	-1.17	-1.24	-1.21
157	16 10 00.26	17 12 05.04	0.0445	0.12	0.03	16.99	16.06	9.97	0.40	8.55	8.80	8.73	8.71	8.64	-0.72	-0.72	-0.72
158	16 10 03.50	15 15 28.80	0.0455	0.23	0.23	18.36	17.51	9.27	0.11	8.17	8.37	8.39	8.30	8.25	-1.16	-1.38	-1.27
159	16 10 13.01	15 41 19.68	0.0463	0.36	0.36	17.48	17.08	9.12	0.20	8.19	8.33	8.33	7.83	8.24	-1.35	-1.38	-1.36
160	16 10 19.17	14 28 11.28	0.0324	-0.16	-0.16	18.07	17.23	9.17	0.00	8.30	8.46	8.56	8.48	8.37	-0.90	-1.31	-1.10
161	16 10 30.79	16 58 10.20	0.0439	0.46	0.46	17.87	17.22	9.26	0.61	8.34	8.52	8.64	8.01	8.42	-1.26	-1.07	-1.16
162	16 10 37.20	18 04 55.92	0.0334	0.32	0.29	17.92	17.49	9.27	0.54	8.02	8.22	8.26	8.37	8.10	-1.02	-1.63	-1.33
163	16 10 40.18	17 32 48.84	0.0381	0.23	0.01	17.79	17.32	8.86	0.27	8.13	8.29	8.26	7.70	8.19	-1.39	-1.48	-1.44
164	16 10 42.07	14 58 48.00	0.0460	0.17	0.17	17.59	16.97	9.38	0.61	8.37	8.53	8.59	8.07	8.44	-1.25	-1.13	-1.19
165	16 10 42.72	14 55 26.76	0.0452	0.06	0.06	17.96	17.01	9.66	0.35	8.55	8.80	8.69	8.78	8.64	-0.59	-0.79	-0.69

Table B.4: **MS galaxies in the dispersed component**

#	R.A. J2000 hh mm ss	DEC J2000 dd mm ss	z	$\Sigma_{4,5}$ Mpc^{-2}	$\Sigma_{4,5}$ Mpc^{-2}	g mag	i mag	$M_\star$ $M_\odot$	$c(\mathrm{H}\beta)$	OH CM	OH PP04	OH PMC09	OH D11	OH ADOP	NO CM	NO PMC09	NO ADOP
(1)	(2)	(3)	(4)	(5)	(6)	(7)	(8)	(9)	(10)	(11)	(12)	(13)	(14)	(15)	(16)	(17)	(18)
166	16 10 44.90	16 16 22.80	0.0460	0.12	-0.06	18.17	17.44	9.16	0.19	8.36	8.57	8.70	8.52	8.45	-0.88	-1.11	-0.99
167	16 10 51.53	16 45 42.48	0.0448	0.34	0.14	18.76	17.45	9.92	0.76	8.45	8.71	8.74	8.69	8.55	-0.71	-0.97	-0.84
168	16 10 52.39	18 30 43.20	0.0363	0.47	0.47	17.65	17.05	9.48	0.00	8.24	8.43	8.43	8.39	8.31	-1.04	-1.35	-1.19
169	16 10 54.38	18 59 03.12	0.0363	0.41	0.41	17.11	16.80	9.51	0.00	8.12	8.31	8.25	7.74	8.19	-1.37	-1.57	-1.47
170	16 11 04.44	14 23 59.28	0.0328	-0.06	-0.06	17.84	16.83	9.51	0.49	8.51	8.73	8.68	8.67	8.59	-0.79	-0.96	-0.87
171	16 11 06.72	18 17 27.60	0.0333	0.43	0.40	16.83	16.32	9.71	0.26	8.21	8.38	8.39	8.20	8.28	-1.21	-1.27	-1.24
172	16 11 12.89	16 57 30.60	0.0337	0.48	0.48	17.00	16.33	9.38	0.30	8.29	8.45	8.49	8.29	8.35	-1.18	-1.20	-1.19
173	16 11 17.52	16 53 57.84	0.0444	0.53	0.53	18.10	17.29	9.45	0.34	8.43	8.65	8.66	8.51	8.51	-0.94	-1.01	-0.98
174	16 11 20.81	14 21 44.28	0.0302	-0.13	-0.13	17.89	16.76	9.52	0.05	8.51	8.76	8.69	8.81	8.60	-0.49	-0.84	-0.66
175	16 11 22.49	17 41 01.32	0.0377	0.22	0.20	16.19	15.35	9.92	0.27	8.55	8.83	8.73	8.70	8.65	-0.73	-0.76	-0.75
176	16 11 27.53	15 21 17.64	0.0471	0.18	0.18	17.53	16.89	9.46	0.00	8.39	8.63	8.65	8.50	8.48	-0.93	-1.18	-1.05
177	16 11 31.30	17 03 29.16	0.0436	0.33	0.33	17.65	17.20	9.02	0.22	8.27	8.33	8.38	8.30	8.29	-1.19	-1.11	-1.15
178	16 11 46.59	15 57 19.08	0.0329	-0.30	-0.30	17.71	17.16	8.91	0.05	8.26	8.46	8.47	8.14	8.34	-1.19	-1.38	-1.29
179	16 11 48.74	19 00 45.00	0.0359	0.34	0.34	18.26	17.69	9.23	0.00	8.15	8.35	8.31	8.07	8.22	-1.26	-1.40	-1.33
180	16 11 51.69	16 59 21.12	0.0356	0.51	0.51	17.43	17.03	8.92	0.00	8.17	8.29	8.26	7.64	8.21	-1.42	-1.42	-1.42
181	16 11 52.32	17 53 08.52	0.0361	0.23	0.23	18.17	17.14	9.42	0.58	8.43	8.65	8.65	8.49	8.51	-0.97	-1.03	-1.00
182	16 11 54.50	16 45 00.36	0.0337	0.47	0.47	16.64	15.97	9.51	0.29	8.43	8.62	8.58	8.47	8.50	-1.01	-1.06	-1.04
183	16 12 04.27	16 26 55.68	0.0420	-0.11	-0.30	18.30	17.65	9.01	0.08	8.18	8.43	8.42	8.21	8.28	-1.20	-1.36	-1.28
184	16 12 16.82	16 59 05.28	0.0349	0.48	0.48	18.23	17.91	8.44	0.12	8.11	8.14	8.09	7.74	8.12	-1.38	-1.39	-1.38
185	16 12 16.90	15 08 60.00	0.0325	0.14	0.14	17.55	17.04	8.89	0.12	8.17	8.35	8.36	7.95	8.24	-1.29	-1.40	-1.35
186	16 12 39.79	14 47 34.08	0.0462	0.02	0.02	18.03	17.35	9.27	0.34	8.41	8.56	8.53	8.35	8.47	-1.13	-1.12	-1.12
187	16 12 43.13	15 23 39.48	0.0306	0.40	0.40	17.77	16.72	9.49	0.15	8.40	8.63	8.67	8.57	8.49	-0.84	-1.08	-0.96
188	16 12 44.76	19 19 27.48	0.0359	0.08	-0.04	17.43	16.52	9.68	0.36	8.46	8.69	8.69	8.63	8.55	-0.82	-0.91	-0.87
189	16 12 46.32	15 18 44.28	0.0474	1.17	1.17	18.25	17.61	9.18	0.67	7.94	8.44	8.39	0.00	8.13	-1.64	-1.45	-1.55
190	16 12 57.82	15 17 35.16	0.0473	1.44	1.44	16.96	16.25	9.76	0.29	8.50	8.70	8.68	8.60	8.58	-0.85	-0.80	-0.82
191	16 13 01.68	15 30 52.56	0.0312	0.09	0.09	17.43	17.10	8.81	0.00	8.07	8.15	8.08	7.58	8.10	-1.41	-1.51	-1.46
192	16 13 02.18	18 25 18.84	0.0308	0.75	-0.51	17.35	16.16	9.66	0.69	8.45	8.63	8.64	8.48	8.52	-0.99	-0.93	-0.96
193	16 13 03.41	18 54 18.72	0.0359	0.44	0.44	16.62	15.89	9.86	0.01	8.47	8.70	8.72	8.73	8.56	-0.63	-0.94	-0.78
194	16 13 04.44	19 16 14.88	0.0357	0.13	0.00	16.79	16.04	9.88	0.10	8.51	8.73	8.70	8.67	8.59	-0.79	-0.89	-0.84
195	16 13 07.87	18 24 01.08	0.0352	0.70	0.50	17.63	17.13	9.44	0.10	8.19	8.35	8.36	8.15	8.25	-1.23	-1.29	-1.26
196	16 13 15.07	18 36 48.96	0.0370	0.65	0.58	17.90	17.31	9.42	0.13	8.39	8.51	8.55	8.44	8.44	-1.01	-1.07	-1.04
197	16 13 21.07	18 44 56.40	0.0361	0.74	0.74	17.96	17.16	9.41	0.20	8.23	8.44	8.52	8.35	8.32	-1.03	-1.37	-1.20
198	16 13 25.25	18 40 52.68	0.0355	0.54	0.54	16.69	15.93	9.82	0.11	8.35	8.51	8.56	8.38	8.41	-1.05	-1.29	-1.17

Table B.4: **MS galaxies in the dispersed component**

# (1)	R.A. J2000 hh mm ss (2)	DEC J2000 dd mm ss (3)	z (4)	$\Sigma_{4,5}$ Mpc^{-2} (5)	$\Sigma_{4,5}$ Mpc^{-2} (6)	g mag (7)	i mag (8)	$M_\star$ $M_\odot$ (9)	$c(\mathrm{H}\beta)$ (10)	OH CM (11)	OH PP04 (12)	OH PMC09 (13)	OH D11 (14)	OH ADOP (15)	NO CM (16)	NO PMC09 (17)	NO ADOP (18)
199	16 13 33.63	17 07 26.76	0.0431	-0.24	-0.33	17.81	17.07	9.34	0.29	8.39	8.59	8.61	8.39	8.47	-1.06	-1.19	-1.12
200	16 13 43.34	19 16 01.20	0.0359	-0.02	-0.14	16.78	16.11	9.87	0.13	8.43	8.65	8.64	8.54	8.51	-0.91	-1.02	-0.97
201	16 13 49.87	15 28 13.44	0.0309	-0.15	-0.15	17.12	15.97	9.94	0.75	8.55	8.79	8.71	8.64	8.64	-0.84	-0.77	-0.81
202	16 13 57.31	16 59 56.76	0.0344	-0.17	-0.17	16.87	16.15	9.51	0.21	8.40	8.53	8.63	8.59	8.46	-0.84	-0.88	-0.86
203	16 14 12.89	14 27 33.84	0.0465	-0.17	-0.17	17.69	17.04	9.40	0.09	8.36	8.53	8.56	8.46	8.43	-0.98	-1.27	-1.12
204	16 14 14.47	15 02 12.12	0.0462	0.16	0.16	17.82	17.02	9.51	0.09	8.44	8.70	8.63	8.59	8.53	-0.86	-1.06	-0.96

Note: The columns are the same as in Table B.1, exept for columns 5 and 6. Here in column 5 we quote the log $\Sigma_{4,5}$ the logarithm of the density to the average of the projected distances to the fourth and fifth nearest neighbors allowing a velocity difference of 2000 km s^{-1} and in column 6 we give the same as in column 5 with velocity difference of 1000 km s^{-1}

Appendix C

Galaxy properties in A1656, A1367, A1779, and A634

We quote the coordinates, the metallicities derived, and the physical properties discussed in Chapter 5, for the SF dwarf galaxies in the four clusters: Table C.1: A1656, Table C.2: A1367, Table C.3: A779, Table C.4: A634. Galaxies are sorted to increasing R.A.

Table C.1: **Our sample of SF low-mass galaxies in Coma**

# (1)	R.A. J2000 hh mm ss (2)	DEC J2000 dd mm ss (3)	z (4)	R/R_{200} (5)	$\Sigma_{4,5}$ Mpc^{-2} (6)	g mag (7)	i mag (8)	$M_\star$ $M_\odot$ (9)	$M_{\rm HI}$ $M_\odot$ (10)	OH PMC09 (11)	OH PP04 (12)	OH P10 (13)	OH DORS (14)	NO PMC09 (15)
001	12 48 24.87	28 18 24.84	0.0228	2.66	0.19	17.24	16.73	8.68	...	8.40	8.41	8.16	8.06	-1.47
002	12 48 30.24	29 15 36.72	0.0250	2.92	1.09	17.28	16.58	9.08	...	8.57	8.56	8.43	8.31	-1.24
003	12 48 32.95	26 06 55.80	0.0214	3.31	-0.03	16.08	15.48	9.29	9.60	8.61	8.61	...	...	-1.11
004	12 48 34.87	28 50 49.20	0.0224	2.74	0.47	16.44	16.06	8.84	...	8.36	8.33	8.19	8.01	-1.33
005	12 48 38.38	29 11 25.08	0.0238	2.86	0.95	16.86	16.30	9.04	...	8.56	8.50	8.41	8.32	-1.02
006	12 48 42.74	29 14 21.48	0.0233	2.87	1.15	16.45	15.91	9.13	...	8.48	8.50	8.30	7.98	-1.31
007	12 48 59.30	27 22 31.80	0.0209	2.61	1.55	16.01	15.45	9.21	9.73	8.38	8.38	...	...	-1.09
008	12 49 01.49	27 10 44.76	0.0199	2.66	1.25	15.83	15.44	9.01	9.53	8.41	8.42	...	...	-1.26
009	12 49 15.72	28 29 51.00	0.0244	2.50	0.35	17.49	17.24	8.41	...	8.29	8.31	8.13	7.92	-1.47
010	12 49 23.76	29 19 16.68	0.0250	2.77	1.02	16.72	16.18	9.10	...	8.46	8.44	8.20	8.03	-1.40
011	12 49 41.50	30 45 08.64	0.0163	3.71	-0.65	16.37	15.74	8.93	...	8.44	8.43	...	...	-1.46
012	12 49 44.38	27 40 10.92	0.0254	2.37	1.17	17.56	16.70	9.22	...	8.57	8.53	8.46	8.46	-1.23
013	12 50 09.91	29 40 34.32	0.0238	2.84	0.20	17.91	17.46	8.39	...	8.20	8.29	8.10	7.59	-1.57
014	12 50 20.21	26 44 59.64	0.0237	2.57	1.67	16.38	15.69	9.36	9.29	8.56	8.57	8.44	8.32	-1.09
015	12 50 31.66	27 18 50.40	0.0267	2.28	1.73	16.58	15.80	9.46	9.53	8.54	8.56	8.48	8.42	-1.20
016	12 50 51.98	25 15 32.76	0.0145	3.57	-0.50	17.05	16.45	8.60	9.10	8.38	8.38	...	...	-1.50
017	12 51 06.58	29 11 48.48	0.0221	2.37	0.44	17.61	16.78	9.07	...	8.62	8.60	8.44	8.36	-1.11
018	12 51 25.70	28 07 14.88	0.0243	1.95	0.93	18.21	17.34	8.92	...	8.59	8.67	8.51	8.34	-1.26
019	12 51 44.93	27 01 06.24	0.0213	2.14	1.51	16.08	15.37	9.44	9.22	8.68	8.71	...	...	-0.90
020	12 51 53.47	27 58 40.80	0.0232	1.84	1.09	17.76	17.27	8.52	...	8.32	8.38	...	...	-1.64
021	12 51 55.01	26 33 29.88	0.0265	2.39	0.95	18.19	17.21	9.07	...	8.52	8.52	...	...	-1.21
022	12 52 05.52	26 11 54.96	0.0262	2.61	0.68	17.72	17.25	8.66	9.65	8.24	8.32	8.12	7.68	-1.57
023	12 52 36.77	30 25 00.48	0.0231	3.04	0.22	16.66	15.91	9.31	...	8.61	8.57	...	...	-1.00
024	12 52 41.85	28 57 34.20	0.0327	1.93	-0.12	16.45	15.67	9.77	...	8.72	8.76	8.58	8.73	-0.76
025	12 52 56.33	26 35 40.92	0.0243	2.18	1.29	17.51	16.93	8.77	...	8.45	8.45	8.30	7.92	-1.31
026	12 52 56.71	28 48 43.56	0.0206	1.81	0.51	17.87	17.23	8.58	...	8.47	8.47	...	...	-1.35
027	12 52 58.25	30 09 07.56	0.0244	2.77	0.11	17.57	16.83	9.02	...	8.57	8.59	...	...	-1.17
028	12 53 07.51	28 14 28.68	0.0234	1.57	1.03	17.15	16.80	8.56	...	8.20	8.24	...	...	-1.50
029	12 53 17.61	26 20 21.48	0.0231	2.31	1.22	18.10	17.45	8.64	...	8.55	8.62	...	...	-1.11
030	12 53 23.11	27 02 00.60	0.0235	1.80	1.32	16.58	15.72	9.50	...	8.71	8.73	...	...	-0.81
031	12 53 31.03	30 43 24.60	0.0265	3.22	0.48	16.97	16.58	8.83	...	8.35	8.38	8.16	8.02	-1.44
032	12 53 44.47	27 49 17.40	0.0164	1.42	1.13	17.85	17.27	8.35	...	8.47	8.50	...	...	-1.39
033	12 53 46.85	27 29 15.36	0.0169	1.50	1.00	17.54	17.00	8.45	...	8.51	8.50	...	...	-1.26

Table C.1: **Our sample of SF low-mass galaxies in Coma**

#	R.A. J2000 hh mm ss	DEC J2000 dd mm ss	z	R/R_{200}	$\Sigma_{4,5}$ Mpc^{-2}	g mag	i mag	$M_\star$ $M_\odot$	$M_{\rm HI}$ $M_\odot$	OH PMC09	OH PP04	OH P10	OH DORS	NO PMC09
(1)	(2)	(3)	(4)	(5)	(6)	(7)	(8)	(9)	(10)	(11)	(12)	(13)	(14)	(15)
034	12 54 24.74	27 21 50.40	0.0261	1.42	1.64	16.39	15.39	9.82	...	8.68	8.84	8.67	8.77	-0.66
035	12 54 42.07	27 38 20.40	0.0287	1.24	1.41	17.98	17.69	8.41	9.24	8.01	8.12	8.00	7.50	-1.60
036	12 54 57.86	30 42 29.16	0.0263	3.07	0.61	16.57	15.48	9.91	...	8.66	8.68	8.50	8.52	-0.96
037	12 55 00.84	27 29 00.24	0.0232	1.23	1.81	16.75	15.74	9.66	9.07	8.68	8.83	8.65	8.74	-0.65
038	12 55 16.78	25 57 24.48	0.0316	2.38	-0.02	17.44	16.73	9.23	...	8.57	8.59	8.49	8.44	-1.22
039	12 55 20.45	26 47 59.64	0.0228	1.63	1.21	17.72	16.99	8.85	...	8.60	8.63	8.47	8.38	-1.21
040	12 55 44.30	28 45 16.56	0.0275	1.24	0.70	17.21	16.91	8.66	...	8.19	8.23	8.11	7.62	-1.43
041	12 55 52.37	25 10 58.44	0.0229	3.09	-0.46	16.62	16.00	9.31	9.28	8.57	8.53	8.44	8.38	-1.07
042	12 56 04.20	27 17 07.80	0.0224	1.14	1.58	18.03	17.32	8.64	...	8.57	8.57	...	...	-1.35
043	12 56 11.57	29 23 53.88	0.0241	1.71	0.87	18.08	17.41	8.67	...	8.35	8.33	8.15	8.30	-1.37
044	12 56 27.58	30 25 59.88	0.0253	2.69	0.75	17.67	17.30	8.49	...	8.08	8.15	8.10	...	-1.50
045	12 56 28.73	29 08 13.56	0.0316	1.44	0.82	17.03	16.46	9.18	...	8.53	8.49	8.37	8.32	-1.23
046	12 56 40.35	28 13 04.08	0.0277	0.77	1.52	17.53	16.82	9.07	...	8.59	8.58	8.51	8.61	-1.03
047	12 56 54.70	30 40 35.40	0.0241	2.91	1.82	16.05	15.29	9.60	...	8.71	8.71	8.50	8.52	-0.87
048	12 57 04.54	27 46 22.80	0.0251	0.67	2.09	16.39	15.32	9.92	...	8.63	8.81	8.65	8.71	-0.67
049	12 57 04.85	28 12 34.92	0.0172	0.68	1.73	17.93	17.50	8.10	...	8.36	8.39	...	...	-1.52
050	12 57 05.69	30 39 54.36	0.0245	2.89	1.49	16.74	16.12	9.16	...	8.56	8.62	8.50	8.41	-1.19
051	12 57 26.11	27 39 33.84	0.0169	0.65	1.80	17.59	17.07	8.36	...	8.39	8.45	...	...	-1.32
052	12 57 43.70	29 00 11.52	0.0231	1.18	1.61	17.66	17.33	8.33	...	8.25	8.32	8.13	...	-1.63
053	12 57 49.78	28 37 27.48	0.0250	0.82	1.39	17.56	17.01	8.74	...	8.52	8.56	8.42	8.51	-0.99
054	12 57 50.23	28 10 13.44	0.0231	0.50	1.86	17.18	16.97	8.43	...	8.34	8.34	8.21	7.57	-1.40
055	12 57 56.23	27 34 53.04	0.0166	0.60	1.62	16.03	15.71	8.73	...	8.49	8.51	...	...	-1.15
056	12 57 56.71	27 26 33.36	0.0257	0.71	2.32	17.85	17.23	8.78	...	8.58	8.70	8.57	8.55	-1.11
057	12 57 56.78	27 59 30.48	0.0152	0.43	1.62	17.18	17.04	8.02	...	8.39	8.41	...	...	-1.47
058	12 58 07.08	26 47 13.56	0.0240	1.32	1.46	17.37	16.37	9.42	...	8.72	8.82	8.61	8.71	-0.74
059	12 58 09.27	26 39 50.76	0.0243	1.44	1.15	16.74	16.11	9.20	9.10	8.58	8.57	8.40	...	-1.16
060	12 58 15.07	28 31 18.48	0.0230	0.67	1.32	16.72	16.19	8.98	...	8.53	8.56	8.35	8.33	-1.20
061	12 58 18.60	30 32 16.80	0.0252	2.72	0.53	16.85	16.25	9.10	...	8.45	8.45	8.32	8.09	-1.30
062	12 58 18.63	27 18 38.88	0.0247	0.79	1.53	16.52	15.77	9.56	9.28	8.59	8.53	8.45	8.46	-0.95
063	12 58 25.54	28 07 44.04	0.0274	0.36	2.18	16.09	15.40	9.38	...	8.66	8.82	8.63	8.65	-0.87
064	12 58 27.10	27 01 24.60	0.0252	1.06	1.82	17.44	17.01	8.69	...	8.31	8.31	8.21	7.75	-1.40
065	12 58 30.84	26 59 41.64	0.0249	1.08	1.69	17.81	17.63	8.12	9.15	8.08	8.17	8.13	...	-1.62
066	12 58 37.82	27 27 50.40	0.0209	0.61	1.74	16.50	15.64	9.73	...	8.66	8.80	...	...	-0.87

Table C.1: **Our sample of SF low-mass galaxies in Coma**

#	R.A. J2000 hh mm ss	DEC J2000 dd mm ss	z	R/R_{200}	$\Sigma_{4,5}$ Mpc^{-2}	g mag	i mag	$M_\star$ $M_\odot$	$M_{\rm HI}$ $M_\odot$	OH PMC09	OH PP04	OH P10	OH DORS	NO PMC09
(1)	(2)	(3)	(4)	(5)	(6)	(7)	(8)	(9)	(10)	(11)	(12)	(13)	(14)	(15)
067	12 58 38.69	27 00 47.88	0.0234	1.05	1.64	17.45	16.75	8.94	...	8.59	8.62	8.48	8.36	-1.16
068	12 58 39.96	26 45 34.20	0.0249	1.31	1.38	16.45	16.11	8.90	9.52	8.06	8.14	8.02	7.74	-1.48
069	12 58 56.62	27 49 19.20	0.0290	0.26	2.15	17.28	16.34	9.50	...	8.75	8.63	8.57	8.86	-0.84
070	12 59 10.20	26 43 13.44	0.0245	1.34	1.34	17.74	17.14	8.72	...	8.41	8.42	...	...	-1.32
071	12 59 16.68	27 06 21.96	0.0280	0.93	1.25	16.89	15.69	10.05	...	8.82	8.81	8.56	8.74	-0.62
072	12 59 18.55	27 35 36.96	0.0174	0.42	1.87	17.00	16.49	8.60	...	8.59	8.57	...	...	-1.14
073	12 59 22.80	29 53 16.44	0.0247	2.01	0.59	16.87	15.80	9.75	...	8.72	8.70	8.50	8.55	-0.93
074	12 59 23.16	28 29 18.96	0.0233	0.54	1.75	16.26	15.56	9.43	...	8.66	8.80	8.61	8.58	-0.89
075	12 59 39.81	27 34 35.40	0.0167	0.43	1.72	16.12	15.58	8.97	...	8.69	8.74	...	...	-0.85
076	12 59 40.42	30 14 49.20	0.0254	2.39	0.54	17.23	16.84	8.79	...	8.28	8.38	8.07	7.73	-1.67
077	12 59 49.25	26 58 27.48	0.0235	1.06	1.53	17.32	16.79	8.77	9.24	8.52	8.56	8.46	8.32	-1.16
078	12 59 56.11	27 44 46.68	0.0298	0.25	2.26	16.49	16.00	9.28	...	8.63	8.63	8.49	8.47	-0.93
079	13 00 09.14	27 51 59.40	0.0177	0.15	1.96	15.92	15.25	9.32	...	8.80	8.79	...	...	-0.55
080	13 00 31.20	28 57 01.80	0.0233	1.04	1.39	17.22	16.56	8.99	...	8.57	8.58	8.44	8.34	-1.29
081	13 00 33.55	27 30 14.76	0.0186	0.53	1.81	16.36	16.02	8.74	...	8.63	8.65	...	...	-0.95
082	13 00 37.15	28 39 50.76	0.0236	0.75	1.22	17.12	16.37	9.15	...	8.55	8.61	8.52	8.50	-1.11
083	13 01 11.95	29 39 50.76	0.0239	1.80	0.61	17.67	16.73	9.18	...	8.55	8.55	8.47	8.42	-1.35
084	13 01 14.95	28 31 18.48	0.0281	0.66	1.15	17.42	16.91	8.87	...	8.33	8.31	8.30	8.39	-1.18
085	13 01 21.75	26 47 47.76	0.0284	1.30	0.80	18.13	17.65	8.54	...	8.31	8.43	8.01	7.79	-1.72
086	13 01 47.07	29 04 36.12	0.0231	1.24	1.78	17.80	17.43	8.33	...	8.28	8.36	8.07	8.00	-1.65
087	13 02 11.37	28 10 20.64	0.0299	0.59	1.55	17.21	16.97	8.93	...	8.51	8.48	8.16	8.21	-1.34
088	13 02 17.78	26 08 33.36	0.0215	2.02	0.32	17.00	16.47	8.82	9.18	8.46	8.46	...	...	-1.31
089	13 02 25.66	28 51 29.16	0.0223	1.11	1.08	16.72	16.42	8.64	...	8.26	8.25	8.18	7.79	-1.38
090	13 02 32.59	27 23 36.60	0.0182	0.89	1.23	17.46	17.02	8.40	...	8.57	8.54	...	...	-1.18
091	13 02 39.38	25 23 00.96	0.0242	2.82	0.08	16.12	15.47	9.50	9.18	8.64	8.65	8.50	8.54	-0.82
092	13 03 05.73	25 28 30.00	0.0243	2.75	0.28	16.41	15.85	9.23	9.36	8.51	8.50	8.41	8.33	-1.04
093	13 03 17.42	26 03 36.36	0.0249	2.18	0.45	17.15	16.51	9.08	9.21	8.39	8.40	...	...	-1.31
094	13 03 23.45	27 18 25.20	0.0186	1.10	0.97	17.73	17.24	8.42	...	8.37	8.37	...	...	-1.40
095	13 03 27.91	28 33 51.12	0.0159	1.05	0.98	16.51	15.92	8.77	...	8.46	8.50	...	...	-1.53
096	13 03 54.43	28 18 37.80	0.0268	1.01	1.46	17.04	16.63	8.80	...	8.37	8.33	8.15	8.32	-1.34
097	13 03 57.14	26 43 46.20	0.0220	1.64	0.76	17.50	17.13	8.47	9.37	8.39	8.40	...	...	-1.69
098	13 04 07.32	25 43 30.72	0.0242	2.59	0.58	17.33	17.01	8.51	9.37	8.19	8.23	8.11	7.70	-1.47
099	13 04 13.13	28 32 33.00	0.0271	1.18	1.56	17.54	17.29	8.37	...	8.04	8.16	8.01	7.56	-1.66

Table C.1: **Our sample of SF low-mass galaxies in Coma**

# (1)	R.A. J2000 hh mm ss (2)	DEC J2000 dd mm ss (3)	z (4)	R/R_{200} (5)	$\Sigma_{4,5}$ Mpc^{-2} (6)	g mag (7)	i mag (8)	$M_\star$ $M_\odot$ (9)	M_{HI} $M_\odot$ (10)	OH PMC09 (11)	OH PP04 (12)	OH P10 (13)	OH DORS (14)	NO PMC09 (15)
100	13 04 14.83	26 06 58.32	0.0249	2.23	0.66	16.94	16.43	8.93	9.34	8.49	8.48	8.33	8.33	-1.31
101	13 04 15.77	28 32 43.44	0.0279	1.19	1.55	18.21	17.35	8.99	...	8.61	8.66	8.54	8.61	-1.09
102	13 04 16.99	26 28 31.44	0.0251	1.90	0.68	17.62	17.19	8.58	...	8.35	8.37	8.14	7.79	-1.41
103	13 04 26.54	27 18 15.48	0.0184	1.30	0.86	15.56	15.13	8.99	9.72	8.56	8.54	...	...	-1.06
104	13 04 26.78	30 25 04.80	0.0331	2.78	0.41	17.52	16.92	9.05	...	8.55	8.56	8.46	8.37	-1.32
105	13 04 31.34	28 18 06.84	0.0263	1.15	1.75	17.76	17.45	8.38	...	8.17	8.22	8.04	7.95	-1.39
106	13 04 35.76	28 37 39.72	0.0224	1.30	1.52	16.02	15.44	9.29	...	8.55	8.52	...	...	-1.17
107	13 04 37.06	29 08 48.12	0.0194	1.65	1.73	17.75	17.14	8.59	...	8.52	8.51	...	...	-1.30
108	13 04 38.79	28 58 21.72	0.0253	1.53	1.46	16.95	16.46	8.92	...	8.24	8.29	...	...	-1.52
109	13 04 47.95	29 36 53.64	0.0199	2.07	0.97	18.16	17.27	8.74	...	8.62	8.54	...	...	-1.14
110	13 05 06.62	28 38 28.32	0.0182	1.41	0.88	17.31	16.83	8.41	...	8.16	8.20	...	...	-1.40
111	13 05 15.38	28 37 35.04	0.0219	1.43	1.55	17.26	16.61	8.90	...	8.44	8.39	...	...	-1.31
112	13 05 16.46	29 35 15.36	0.0237	2.11	1.30	17.16	16.64	8.78	...	8.37	8.37	...	...	-1.23
113	13 05 18.89	30 16 38.28	0.0332	2.72	0.41	16.07	15.67	9.37	...	8.41	8.37	8.33	8.24	-1.23
114	13 05 26.88	25 11 28.32	0.0237	3.23	0.66	16.85	15.94	9.44	9.68	8.64	8.66	8.49	8.39	-1.21
115	13 05 36.24	30 47 26.52	0.0222	3.24	-0.12	17.31	16.77	8.73	...	8.33	8.36	...	...	-1.48
116	13 05 39.12	26 06 23.76	0.0211	2.41	0.63	15.89	15.32	9.27	9.37	8.64	8.70	...	...	-0.94
117	13 05 44.62	25 23 06.00	0.0246	3.08	1.04	16.82	15.81	9.74	9.66	8.69	8.63	8.45	8.45	-0.95
118	13 05 45.36	28 52 16.68	0.0266	1.66	1.01	17.01	16.56	8.75	...	8.25	8.28	8.13	7.98	-1.46
119	13 06 03.86	29 42 34.92	0.0203	2.32	1.24	17.10	16.40	9.19	...	8.48	8.47	...	...	-1.18
120	13 06 08.35	30 12 33.48	0.0161	2.76	0.05	16.14	15.46	9.15	...	8.54	8.49	...	...	-1.25
121	13 06 13.61	29 08 29.40	0.0232	1.92	1.40	17.54	17.03	8.63	...	8.33	8.35	...	...	-1.51
122	13 06 15.12	29 21 58.32	0.0245	2.08	1.49	17.97	17.48	8.56	...	8.39	8.37	8.21	7.98	-1.41
123	13 06 25.97	25 14 16.80	0.0249	3.29	0.94	17.87	17.31	8.60	9.33	8.36	8.37	...	...	-1.51
124	13 06 33.02	29 21 56.16	0.0243	2.13	1.18	16.36	15.79	9.20	...	8.47	8.48	...	...	-1.44
125	13 06 36.41	25 25 46.56	0.0240	3.14	1.06	16.08	15.37	9.54	9.55	8.66	8.65	...	...	-1.08
126	13 06 37.06	28 14 05.28	0.0213	1.60	1.22	18.21	17.57	8.51	...	8.55	8.50	...	...	-1.08
127	13 07 08.21	28 04 50.16	0.0165	1.71	1.02	17.86	17.44	8.16	...	8.37	8.37	...	...	-1.37
128	13 07 08.98	30 23 35.52	0.0229	3.04	0.12	17.76	17.13	8.66	...	8.27	8.33	...	...	-1.50
129	13 07 14.09	28 15 29.88	0.0214	1.75	1.47	17.69	17.10	8.66	...	8.38	8.37	...	...	-1.34
130	13 07 15.00	28 20 35.52	0.0187	1.77	1.57	16.73	16.10	8.87	...	8.63	8.57	...	...	-1.09
131	13 07 22.99	29 24 04.32	0.0175	2.29	0.56	16.72	16.38	8.56	...	8.07	8.15	...	...	-1.46
132	13 07 31.10	25 30 18.00	0.0256	3.19	0.55	16.93	16.23	9.29	...	8.54	8.53	8.46	...	-1.22

Table C.1: **Our sample of SF low-mass galaxies in Coma**

#	R.A. J2000 hh mm ss	DEC J2000 dd mm ss	z	R/R_{200}	$\Sigma_{4,5}$ Mpc^{-2}	g mag	i mag	$M_\star$ $M_\odot$	$M_{\rm HI}$ $M_\odot$	OH PMC09	OH PP04	OH P10	OH DORS	NO PMC09
(1)	(2)	(3)	(4)	(5)	(6)	(7)	(8)	(9)	(10)	(11)	(12)	(13)	(14)	(15)
133	13 07 37.61	29 55 36.48	0.0254	2.72	0.46	17.62	17.01	8.87	...	8.33	8.39	8.11	7.96	-1.51
134	13 08 02.57	27 18 39.96	0.0196	2.05	0.54	16.10	15.56	9.12	9.53	8.62	8.60	...	...	-1.01
135	13 08 03.96	28 59 53.88	0.0241	2.18	0.99	16.88	16.33	8.94	...	8.38	8.39	8.19	7.71	-1.48
136	13 08 15.17	29 01 22.80	0.0205	2.23	1.04	17.84	17.49	8.21	...	8.24	8.28	...	...	-1.42
137	13 08 26.37	29 45 16.20	0.0230	2.72	0.39	17.75	17.27	8.54	...	8.11	8.33	7.94	...	-1.76
138	13 08 27.60	28 21 02.52	0.0238	2.04	1.40	17.54	16.77	9.03	...	8.37	8.42	8.10	7.65	-1.44
139	13 08 30.14	27 52 45.48	0.0204	2.03	0.85	17.79	17.21	8.52	...	8.40	8.39	...	...	-1.38
140	13 08 32.76	30 44 53.52	0.0235	3.52	0.06	15.84	15.39	9.24	...	8.34	8.34	8.28	8.08	-1.31
141	13 08 51.55	28 37 45.48	0.0227	2.20	1.18	16.18	15.43	9.54	...	8.63	8.63	8.47	8.42	-1.04
142	13 08 57.17	28 16 49.80	0.0195	2.15	1.62	15.82	15.18	9.37	...	8.70	8.66	...	...	-0.89
143	13 09 07.27	29 49 51.60	0.0231	2.89	0.41	17.29	16.30	9.37	...	8.60	8.64	8.49	8.41	-1.11
144	13 09 07.32	28 40 06.60	0.0187	2.27	1.15	16.98	16.57	9.19	...	8.53	8.57	...	...	-1.25
145	13 09 37.51	26 09 32.76	0.0212	3.01	-0.30	17.13	16.68	8.68	9.69	8.36	8.39	...	...	-1.42
146	13 09 45.77	28 37 16.32	0.0226	2.40	1.06	16.55	15.52	9.70	...	8.79	8.77	8.55	8.71	-0.67
147	13 10 27.86	30 44 24.36	0.0281	3.78	-0.34	17.98	17.46	8.63	...	8.30	8.32	8.07	8.20	-1.38
148	13 11 04.56	30 28 58.80	0.0210	3.67	-0.17	16.44	15.81	9.23	...	8.52	8.47	8.39	8.32	-1.16

Note: Column 1: order number for our sample of A1656 SF galaxies; column 2: right ascension in hours, minutes, and seconds; column 3: declination, in degrees, arcminutes, and arcseconds; column 4: redshift as given in SDSS; column 5: R/R_{200} distance from the cluster center in R_{200} units; column 6: log $\Sigma_{4,5}$ the logarithm of the density to the average of the projected distances to the fourth and fifth nearest neighbors in Mpc^{-2}; column 7: observed g magnitude given in SDSS; column 8: observed i magnitude given in SDSS; column 9: log$M_\star$ log stellar mass given in SDSS; column 10: log$M_{\rm HI}$ logarithm of the HI mass, as derived by ALFALFA data (Haynes et al. 2011); column 11: log+12(O/H) derived by PMC09 calibration of N2; column 12: log+12(O/H) derived by PP04 calibration; column 13: log+12(O/H) derived by P10 calibration for the galaxies that have [OII]λ3727 measurements (new or derived in this work); column 14: log+12(O/H) derived by Dors et al. (2011) model calibration for the galaxies that have [OII]λ3727 measurements; column 15: log(N/O) derived by PMC09 calibration.

Table C.2: **Our sample of SF low-mass galaxies in A1367**

# (1)	R.A. J2000 hh mm ss (2)	DEC J2000 dd mm ss (3)	z (4)	R/R_{200} (5)	$\Sigma_{4,5}$ (6)	g (7)	i (8)	$M_\star$ $M_\odot$ (9)	$M_{\rm HI}$ $M_\odot$ (10)	OH PMC09 (11)	OH PP04 (12)	OH P10 (13)	OH DORS (14)	NO PMC09 (15)
001	11 34 17.28	20 23 53.16	0.0322	2.84	1.26	17.92	17.28	8.96	...	8.59	8.62	8.50	8.50	-1.02
002	11 34 26.95	21 21 07.92	0.0212	3.22	0.06	16.80	15.85	9.45	...	8.47	8.38	...	...	-1.05
003	11 34 46.01	20 12 17.28	0.0319	2.67	1.29	17.38	16.80	9.10	9.05	8.49	8.43	8.36	8.35	-1.24
004	11 35 04.27	20 38 06.72	0.0239	2.71	1.26	16.58	16.04	9.04	...	8.36	8.40	8.13	7.83	-1.47
005	11 35 05.76	22 26 05.28	0.0272	3.91	0.52	17.77	17.55	8.26	...	8.03	8.14	8.01	7.50	-1.57
006	11 35 07.61	21 37 53.76	0.0295	3.26	1.15	16.71	15.69	9.90	...	8.71	8.72	8.52	8.56	-0.86
007	11 35 11.16	20 30 49.68	0.0224	2.64	1.46	17.91	17.53	8.25	...	8.23	8.27	...	...	-1.49
008	11 35 19.94	17 24 30.60	0.0272	3.78	-0.36	16.66	15.72	9.75	...	8.75	8.76	8.55	8.68	-0.79
009	11 35 19.94	21 27 29.16	0.0230	3.09	0.96	17.39	16.70	8.97	...	8.36	8.38	8.29	7.74	-1.29
010	11 35 21.69	20 38 40.56	0.0214	2.64	1.27	16.66	16.04	9.04	...	8.57	8.61	...	...	-1.06
011	11 35 23.62	21 30 06.84	0.0297	3.11	0.91	16.97	16.12	9.58	...	8.67	8.68	8.51	8.55	-0.98
012	11 35 25.58	22 25 26.04	0.0304	3.84	0.66	16.77	15.80	9.81	...	8.68	8.63	8.48	8.56	-0.93
013	11 35 27.84	20 00 03.24	0.0319	2.46	0.72	17.93	17.12	9.15	9.02	8.42	8.47	...	...	-1.41
014	11 35 38.79	22 18 56.52	0.0237	3.71	0.56	18.24	17.51	8.72	...	8.36	8.38	8.18	7.74	-1.45
015	11 35 40.99	20 31 59.88	0.0210	2.51	1.26	17.38	16.45	9.16	...	8.65	8.81	...	...	-0.83
016	11 36 32.18	22 01 36.84	0.0299	3.31	1.00	18.06	17.54	8.68	...	8.49	8.46	8.16	8.45	-1.38
017	11 36 34.32	20 21 51.48	0.0209	2.23	1.13	16.81	16.11	9.08	...	8.56	8.56	...	...	-1.17
018	11 36 39.70	20 17 24.00	0.0319	2.19	0.81	17.67	16.95	9.18	...	8.68	8.68	8.51	8.56	-0.99
019	11 36 42.10	22 02 47.04	0.0308	3.30	1.16	16.99	15.96	9.79	...	8.75	8.74	8.55	8.71	-0.88
020	11 36 49.63	20 09 40.68	0.0210	2.11	1.21	17.97	17.46	8.36	...	8.00	8.11	...	...	-1.58
021	11 36 54.00	19 55 34.68	0.0208	2.06	2.01	16.15	15.86	9.01	...	8.46	8.49	...	...	-0.75
022	11 37 09.84	20 01 31.08	0.0202	2.00	1.75	17.19	16.68	8.67	...	8.44	8.42	...	...	-1.30
023	11 37 10.32	19 58 19.20	0.0212	1.99	2.05	17.17	16.34	9.16	...	8.64	8.80	...	...	-0.90
024	11 37 11.95	21 13 06.96	0.0231	2.53	0.32	18.19	17.33	8.71	...	8.33	8.35	...	...	-1.26
025	11 37 16.03	19 37 10.20	0.0205	1.98	0.75	16.98	16.12	9.19	...	8.55	8.56	...	...	-1.22
026	11 37 24.17	19 13 15.24	0.0298	2.06	0.02	17.09	16.67	8.92	...	8.30	8.33	8.09	8.10	-1.41
027	11 37 28.30	21 58 36.48	0.0311	3.10	1.87	16.94	15.95	9.75	...	8.82	8.79	8.58	8.79	-0.73
028	11 37 30.72	19 02 33.36	0.0295	2.12	0.02	16.10	15.48	9.55	...	8.70	8.64	8.49	8.61	-1.15
029	11 37 38.33	21 58 19.20	0.0288	3.07	2.16	18.35	17.42	9.06	...	8.63	8.69	8.52	8.53	-1.08
030	11 37 51.82	20 27 28.80	0.0298	1.93	1.26	17.81	17.02	9.14	...	8.55	8.54	8.48	8.43	-1.18
031	11 38 03.82	19 51 42.12	0.0207	1.75	0.98	16.33	15.64	9.25	9.50	8.63	8.64	...	...	-0.93
032	11 38 05.59	20 41 55.32	0.0222	1.99	1.13	16.92	16.26	9.07	...	8.65	8.60	...	...	-1.32
033	11 38 16.18	21 37 16.68	0.0310	2.65	1.36	17.92	17.25	9.04	...	8.51	8.49	8.38	8.36	-1.17

Table C.2: **Our sample of SF low-mass galaxies in A1367**

# (1)	R.A. J2000 hh mm ss (2)	DEC J2000 dd mm ss (3)	z (4)	R/R_{200} (5)	$\Sigma_{4,5}$ (6)	g (7)	i (8)	$M_\star$ $M_\odot$ (9)	$M_{\rm HI}$ $M_\odot$ (10)	OH PMC09 (11)	OH PP04 (12)	OH P10 (13)	OH DORS (14)	NO PMC09 (15)
034	11 38 17.81	22 28 45.84	0.0303	3.47	0.37	17.88	17.02	9.20	…	8.62	8.57	8.47	8.55	-1.11
035	11 38 25.68	20 39 55.44	0.0223	1.90	1.37	17.08	16.54	8.63	…	8.52	8.49	…	…	-1.33
036	11 38 28.15	19 58 50.16	0.0233	1.64	0.80	16.41	15.77	9.23	8.87	8.63	8.59	8.43	8.38	-1.23
037	11 38 35.04	21 41 45.96	0.0315	2.67	1.15	17.72	16.57	9.66	…	8.70	8.68	8.56	8.75	-0.82
038	11 38 42.14	19 54 36.36	0.0226	1.58	0.64	18.11	17.09	9.06	…	8.64	8.68	…	…	-1.11
039	11 38 52.97	21 46 19.56	0.0228	2.69	0.59	17.59	17.10	8.62	…	8.21	8.25	…	…	-1.53
040	11 38 59.23	20 33 37.44	0.0219	1.71	1.35	17.61	16.90	8.80	…	8.52	8.49	…	…	-1.30
041	11 39 06.60	22 01 15.60	0.0214	2.90	0.37	18.19	17.59	8.50	…	8.48	8.45	…	…	-1.24
042	11 39 37.01	17 26 20.76	0.0211	3.08	0.19	18.28	17.41	8.58	…	8.55	8.50	…	…	-1.25
043	11 39 48.86	22 24 42.84	0.0310	3.23	0.22	17.99	17.60	8.56	…	8.25	8.25	8.14	7.89	-1.38
044	11 39 52.44	17 19 03.72	0.0221	3.18	0.21	16.65	15.89	9.32	…	8.41	8.39	…	…	-1.36
045	11 39 56.52	20 50 13.92	0.0233	1.69	0.71	17.27	16.47	9.13	…	8.47	8.48	8.09	8.18	-1.32
046	11 40 01.73	18 33 57.96	0.0269	1.91	0.25	16.15	15.39	9.58	…	8.74	8.72	8.50	8.58	-0.88
047	11 40 05.64	20 16 22.44	0.0216	1.29	1.19	18.19	17.29	8.81	…	8.60	8.61	…	…	-1.18
048	11 40 10.25	20 47 38.40	0.0296	1.61	0.57	17.83	17.13	8.99	…	8.35	8.37	8.14	7.89	-1.43
049	11 40 34.06	18 51 06.84	0.0271	1.57	0.41	17.99	17.40	8.70	…	8.27	8.34	8.18	…	-1.60
050	11 40 39.00	19 54 38.52	0.0261	1.05	0.81	17.49	17.04	8.65	9.27	8.27	8.31	8.16	7.57	-1.47
051	11 40 46.51	17 16 04.80	0.0221	3.14	0.41	16.34	15.55	9.41	…	8.61	8.60	…	…	-1.27
052	11 40 59.71	21 00 35.28	0.0218	1.65	0.60	16.39	15.40	9.67	…	8.66	8.85	…	…	-0.74
053	11 41 06.77	20 30 30.60	0.0240	1.20	0.97	18.09	17.28	8.82	…	8.61	8.63	…	…	-1.15
054	11 41 10.56	20 11 18.60	0.0236	0.99	1.22	17.99	17.38	8.62	…	8.51	8.53	8.38	8.20	-1.09
055	11 41 17.04	18 49 14.88	0.0269	1.47	0.56	17.75	17.39	8.54	…	8.40	8.39	8.29	…	-1.54
056	11 41 17.71	20 09 43.56	0.0195	0.94	1.21	18.09	17.18	8.97	…	8.56	8.61	…	…	-1.11
057	11 41 25.37	17 25 32.16	0.0208	2.91	0.42	17.12	16.67	8.62	…	8.34	8.35	…	…	-1.41
058	11 41 41.23	20 02 31.92	0.0284	0.80	1.32	17.74	17.29	8.66	…	8.33	8.36	8.13	7.97	-1.52
059	11 41 42.60	20 00 56.16	0.0284	0.78	1.35	17.76	17.21	8.76	…	8.31	8.36	8.14	7.92	-1.51
060	11 41 49.82	19 46 04.44	0.0261	0.73	0.93	17.91	17.64	8.28	9.22	8.04	8.19	8.09	…	-1.69
061	11 41 54.31	20 20 35.16	0.0198	0.91	1.35	16.80	15.69	9.54	…	8.76	8.71	…	…	-0.93
062	11 42 03.48	21 20 24.72	0.0255	1.85	0.72	17.96	17.03	9.12	…	8.51	8.48	8.15	8.28	-1.34
063	11 42 11.21	18 41 08.52	0.0282	1.47	0.66	17.82	17.37	8.57	…	8.20	8.23	8.15	7.65	-1.48
064	11 42 15.62	20 02 55.32	0.0204	0.65	1.93	15.94	15.30	9.35	9.22	8.59	8.59	…	…	-1.02
065	11 42 18.34	20 27 08.64	0.0198	0.92	1.27	16.94	16.35	8.85	…	8.58	8.49	…	…	-1.19
066	11 42 31.42	21 49 3…	0.0235	2.36	0.48	17.53	16.99	8.81	…	8.34	8.39	…	…	-1.46

Table C.2: **Our sample of SF low-mass galaxies in A1367**

# (1)	R.A. J2000 hh mm ss (2)	DEC J2000 dd mm ss (3)	z (4)	R/R_{200} (5)	$\Sigma_{4,5}$ (6)	g (7)	i (8)	$M_\star$ $M_\odot$ (9)	$M_{\rm HI}$ $M_\odot$ (10)	OH PMC09 (11)	OH PP04 (12)	OH P10 (13)	OH DORS (14)	NO PMC09 (15)
067	11 42 39.31	19 58 08.40	0.0245	0.52	2.03	17.43	16.95	8.66	...	8.54	8.53	8.36	8.19	-1.19
068	11 42 50.09	19 16 19.56	0.0175	0.80	0.88	17.60	16.98	8.52	...	8.56	8.60	...	...	-1.18
069	11 42 50.98	20 26 31.92	0.0190	0.83	1.39	16.34	15.64	9.07	...	8.62	8.64	...	...	-1.01
070	11 42 56.45	19 57 58.32	0.0243	0.45	2.24	15.92	15.29	9.32	9.42	8.61	8.67	8.50	8.37	-1.06
071	11 42 59.04	22 27 25.56	0.0238	3.05	0.30	17.82	17.24	8.58	...	8.49	8.45	8.22	8.06	-1.41
072	11 43 03.26	18 27 42.84	0.0245	1.64	0.71	17.50	16.96	8.77	...	8.48	8.46	...	...	-1.39
073	11 43 13.06	19 36 47.16	0.0208	0.43	1.80	17.76	17.43	8.20	8.91	8.25	8.30	...	...	-1.49
074	11 43 13.10	20 00 17.28	0.0234	0.40	1.96	15.94	15.48	9.27	8.75	8.50	8.51	8.38	8.30	-1.09
075	11 43 13.20	22 00 23.40	0.0227	2.53	0.54	18.13	17.59	8.46	...	8.18	8.25	...	...	-1.64
076	11 43 15.29	17 22 06.96	0.0225	2.88	0.27	16.10	15.48	9.33	...	8.65	8.63	...	...	-1.27
077	11 43 22.39	18 32 48.12	0.0167	1.52	0.59	16.55	16.00	8.73	...	8.25	8.27	...	...	-1.42
078	11 43 34.03	20 30 38.16	0.0242	0.82	1.23	18.11	17.10	9.09	...	8.63	8.77	8.59	8.56	-1.00
079	11 43 41.54	20 01 37.20	0.0217	0.31	1.93	17.60	17.06	8.60	...	8.48	8.53	...	...	-1.31
080	11 43 48.91	20 14 54.24	0.0204	0.51	2.04	16.41	15.84	9.09	...	8.55	8.55	...	...	-0.72
081	11 44 05.06	21 15 36.72	0.0263	1.65	0.85	17.97	17.40	8.63	...	8.36	8.39	...	...	-1.61
082	11 44 07.01	22 26 01.32	0.0310	3.00	1.38	17.73	17.24	8.76	...	8.44	8.44	8.12	8.30	-1.38
083	11 44 13.92	19 20 11.40	0.0194	0.59	1.10	17.57	17.27	8.07	...	8.28	8.32	...	...	-1.60
084	11 44 23.98	22 25 26.76	0.0310	2.99	1.24	17.54	17.01	8.88	...	8.42	8.39	8.31	8.20	-1.31
085	11 44 24.31	21 17 24.36	0.0257	1.68	1.01	17.48	16.74	9.10	...	8.49	8.47	...	...	-1.12
086	11 44 32.61	22 09 35.28	0.0237	2.68	0.66	17.43	16.73	8.98	...	8.61	8.61	...	...	-1.08
087	11 44 33.50	19 37 36.12	0.0241	0.25	1.75	17.53	16.39	9.49	...	8.73	8.77	8.54	8.55	-0.74
088	11 44 40.35	20 28 37.92	0.0203	0.74	1.34	17.06	16.21	9.12	...	8.57	8.59	...	...	-1.14
089	11 44 47.81	19 46 24.24	0.0282	0.11	1.94	15.79	15.18	9.63	...	8.64	8.77	8.60	8.61	-0.88
090	11 44 48.46	22 05 56.04	0.0232	2.61	0.69	16.57	15.96	9.20	...	8.54	8.51	8.40	8.08	-1.21
091	11 44 53.38	20 41 12.84	0.0205	0.99	1.21	18.10	17.65	8.23	...	8.27	8.29	...	...	-1.41
092	11 44 54.58	20 01 01.56	0.0243	0.24	1.54	16.65	15.92	9.32	...	8.68	8.77	8.58	8.63	-0.90
093	11 45 04.49	20 36 27.36	0.0200	0.90	1.25	16.85	15.84	9.40	...	8.64	8.67	...	...	-1.25
094	11 45 15.51	21 12 15.12	0.0237	1.59	1.39	17.53	16.89	8.90	...	8.49	8.51	...	...	-1.11
095	11 45 18.82	20 17 33.36	0.0235	0.57	2.16	17.57	16.77	9.00	...	8.52	8.56	8.31	8.08	-1.25
096	11 45 19.11	19 23 39.12	0.0185	0.56	1.86	17.73	16.93	8.74	...	8.66	8.75	...	...	-1.05
097	11 45 19.90	21 20 22.20	0.0258	1.75	1.60	16.17	15.47	9.55	...	8.60	8.60	8.48	8.45	-0.98
098	11 45 20.42	19 32 58.20	0.0160	0.41	1.95	17.38	17.05	8.12	...	8.31	8.33	...	...	-1.22
099	11 45 25.44	20 36 36.72	0.0264	0.93	1.37	16.54	15.42	9.85	...	8.65	8.73	8.56	8.57	-1.00

Table C.2: **Our sample of SF low-mass galaxies in A1367**

# (1)	R.A. J2000 hh mm ss (2)	DEC J2000 dd mm ss (3)	z (4)	R/R_{200} (5)	$\Sigma_{4,5}$ (6)	g (7)	i (8)	$M_\star$ $M_\odot$ (9)	$M_{\rm HI}$ $M_\odot$ (10)	OH PMC09 (11)	OH PP04 (12)	OH P10 (13)	OH DORS (14)	NO PMC09 (15)
100	11 45 28.66	20 05 36.96	0.0249	0.40	1.27	17.63	16.81	8.96	...	8.59	8.69	8.54	8.48	-1.14
101	11 45 29.01	18 33 48.60	0.0268	1.50	0.18	18.12	17.60	8.53	...	8.37	8.36	8.30	8.23	-1.28
102	11 45 33.05	20 19 55.56	0.0231	0.64	2.23	19.83	17.75	8.35	...	8.30	8.33	...	...	-1.53
103	11 45 33.34	19 30 28.08	0.0150	0.48	1.86	17.38	17.22	7.83	...	8.11	8.20	...	...	-1.57
104	11 45 34.03	20 00 30.96	0.0228	0.35	1.41	17.84	17.41	8.38	...	8.43	8.47	...	...	-1.45
105	11 45 35.62	21 18 17.64	0.0233	1.72	1.40	16.91	15.94	9.54	...	8.61	8.59	...	...	-1.14
106	11 45 36.38	18 49 49.44	0.0152	1.20	0.65	17.69	17.10	8.30	...	8.06	8.18	...	...	-1.58
107	11 45 37.77	21 09 12.60	0.0224	1.55	1.32	17.91	17.24	8.71	...	8.39	8.42	...	...	-1.38
108	11 45 45.26	19 41 30.84	0.0205	0.38	2.10	17.97	17.02	9.12	8.87	8.55	8.61	...	...	-1.29
109	11 45 51.50	22 13 31.80	0.0214	2.78	0.80	17.31	16.03	9.66	...	8.73	8.70	...	...	-0.91
110	11 46 01.66	20 36 59.76	0.0261	0.99	1.33	17.63	17.10	8.75	...	8.28	8.31	8.17	7.80	-1.55
111	11 46 07.75	21 39 36.72	0.0270	2.15	0.69	17.23	16.85	8.72	...	8.35	8.32	8.16	8.33	-1.39
112	11 46 09.00	20 26 51.00	0.0238	0.83	1.13	16.15	15.26	9.72	...	8.71	8.76	8.54	8.51	-0.86
113	11 46 21.94	22 08 03.84	0.0278	2.70	0.60	18.36	17.52	8.91	...	8.50	8.47	8.35	8.32	-1.23
114	11 46 36.48	19 48 34.20	0.0180	0.58	1.60	18.07	17.61	8.19	8.67	8.37	8.39	...	...	-1.32
115	11 46 38.23	21 05 19.68	0.0226	1.56	1.20	17.44	16.42	9.39	...	8.60	8.68	...	...	-1.13
116	11 46 40.10	21 22 51.24	0.0248	1.88	0.88	17.14	16.60	8.90	...	8.35	8.40	8.10	7.99	-1.46
117	11 46 42.36	20 38 55.32	0.0222	1.11	1.40	17.95	17.22	8.66	...	8.50	8.46	...	...	-1.02
118	11 46 47.86	21 01 54.84	0.0256	1.51	1.04	17.39	16.53	9.23	...	8.66	8.57	8.39	8.32	-0.88
119	11 46 50.38	17 48 50.76	0.0206	2.43	0.01	17.25	16.61	8.76	...	8.40	8.44	...	...	-1.49
120	11 46 53.76	20 19 53.76	0.0219	0.87	0.97	18.13	17.59	8.46	...	8.43	8.47	...	...	-1.37
121	11 47 00.82	19 27 30.24	0.0180	0.82	1.14	17.04	16.13	9.13	...	8.67	8.74	...	...	-0.95
122	11 47 04.56	22 14 27.96	0.0215	2.86	0.51	17.17	16.39	9.07	...	8.60	8.65	...	...	-1.09
123	11 47 08.18	19 42 06.84	0.0207	0.74	1.25	17.51	16.78	8.86	...	8.64	8.64	...	...	-1.12
124	11 47 10.37	20 36 06.84	0.0234	1.14	1.31	17.80	17.18	8.71	...	8.55	8.57	8.02	8.33	-1.36
125	11 47 25.08	19 23 31.56	0.0196	0.95	1.05	17.15	16.67	8.57	9.07	8.34	8.37	...	...	-1.45
126	11 47 30.12	21 49 15.96	0.0277	2.43	0.71	17.54	16.71	9.19	...	8.74	8.69	8.52	8.71	-0.99
127	11 47 32.28	21 41 06.00	0.0262	2.28	0.86	17.45	16.85	8.90	...	8.48	8.47	8.12	8.31	-1.34
128	11 47 37.56	20 09 00.72	0.0177	0.92	0.85	17.51	16.89	8.53	8.92	8.47	8.47	...	...	-1.33
129	11 47 38.18	20 33 55.80	0.0224	1.20	0.96	16.59	15.63	9.58	...	8.66	8.74	...	...	-0.99
130	11 47 46.97	19 04 55.20	0.0201	1.25	1.10	16.42	15.43	9.55	...	8.72	8.70	...	...	-0.97
131	11 48 05.45	21 49 45.48	0.0268	2.49	0.56	16.18	16.35	8.36	...	8.09	8.12	...	...	-1.23
132	11 48 13.03	21 29 40.20	0.0244	2.16	1.00	18.14	17.74	8.31	...	8.17	8.24	8.11	7.60	-1.54

Table C.2: **Our sample of SF low-mass galaxies in A1367**

# (1)	R.A. J2000 hh mm ss (2)	DEC J2000 dd mm ss (3)	z (4)	R/R_{200} (5)	$\Sigma_{4,5}$ (6)	g (7)	i (8)	$M_\star$ $M_\odot$ (9)	$M_{\rm HI}$ $M_\odot$ (10)	OH PMC09 (11)	OH PP04 (12)	OH P10 (13)	OH DORS (14)	NO PMC09 (15)
133	11 48 22.32	20 39 02.88	0.0265	1.41	0.88	17.84	17.20	8.79	...	8.43	8.43	8.12	8.29	-1.35
134	11 48 24.84	18 56 26.16	0.0214	1.49	1.03	17.76	17.01	8.81	...	8.28	8.30	...	...	-1.43
135	11 48 24.96	21 13 40.80	0.0248	1.92	1.50	17.88	17.45	8.61	...	8.36	8.42	8.10	7.92	-1.60
136	11 48 28.41	19 45 36.00	0.0187	1.09	0.76	17.80	17.36	8.25	8.97	8.36	8.36	...	...	-1.42
137	11 48 33.41	20 40 57.36	0.0235	1.47	0.83	17.66	17.09	8.50	...	8.35	8.40	8.13	7.65	-1.47
138	11 48 39.07	21 21 47.16	0.0265	2.09	1.50	17.16	16.91	8.76	...	8.35	8.36	8.32	8.15	-1.15
139	11 48 43.75	21 00 53.64	0.0259	1.78	1.25	16.27	15.43	9.69	...	8.66	8.74	8.56	8.58	-0.90
140	11 48 53.81	21 17 38.40	0.0244	2.06	1.63	16.14	15.45	9.46	...	8.71	8.72	8.51	8.49	-1.03
141	11 48 54.65	21 15 20.88	0.0256	2.02	1.72	18.04	17.51	8.58	...	8.45	8.41	8.27	7.68	-1.35
142	11 48 58.39	20 22 35.40	0.0226	1.36	0.67	17.35	16.60	9.06	...	8.63	8.63	...	...	-1.12
143	11 48 58.97	21 05 10.68	0.0280	1.88	1.50	17.95	17.68	8.33	...	8.12	8.23	8.08	...	-1.58
144	11 49 06.65	19 10 06.24	0.0209	1.48	0.90	16.39	15.80	9.05	...	8.54	8.56	...	...	-1.27
145	11 49 11.37	20 56 16.08	0.0237	1.79	1.24	17.38	16.50	9.23	...	8.64	8.72	8.55	8.52	-0.98
146	11 49 19.32	20 41 32.64	0.0234	1.64	0.92	17.66	16.78	9.08	...	8.61	8.67	8.50	8.34	-1.08
147	11 49 21.75	21 21 18.72	0.0224	2.19	1.51	17.00	16.15	9.27	...	8.62	8.73	...	...	-0.94
148	11 49 33.02	21 26 53.16	0.0280	2.30	1.43	16.97	16.33	9.21	...	8.65	8.69	8.54	8.63	-0.97
149	11 49 53.21	18 33 38.16	0.0194	2.09	0.44	17.22	16.35	8.55	...	8.44	8.44	...	...	-1.22
150	11 50 03.98	20 57 41.76	0.0277	1.99	1.72	18.16	17.41	8.85	...	8.57	8.50	8.43	8.38	-1.10
151	11 50 04.20	22 10 53.76	0.0254	3.09	1.08	17.98	17.25	8.83	...	8.58	8.58	...	...	-1.09
152	11 50 16.32	21 48 48.96	0.0264	2.76	1.64	16.97	16.22	9.31	...	8.60	8.63	8.49	8.43	-1.00
153	11 50 18.57	20 44 44.52	0.0224	1.89	1.05	18.03	17.45	8.48	...	8.39	8.40	...	...	-1.37
154	11 50 21.36	21 19 33.24	0.0226	2.33	1.76	16.40	15.73	9.21	...	8.54	8.50	...	...	-1.25
155	11 50 25.99	21 45 53.28	0.0256	2.74	1.55	18.02	16.74	9.54	...	8.73	8.77	8.54	8.58	-0.75
156	11 50 42.29	21 23 32.64	0.0276	2.45	1.43	17.87	17.20	8.92	...	8.44	8.45	8.35	8.40	-1.16
157	11 50 53.66	20 57 13.32	0.0265	2.15	1.66	17.86	17.41	8.55	...	8.36	8.37	8.13	8.13	-1.36
158	11 50 58.13	22 04 37.20	0.0249	3.11	1.81	17.56	16.89	8.98	...	8.51	8.51	8.37	8.34	-1.16
159	11 50 58.58	20 42 20.88	0.0204	2.02	1.28	17.97	17.34	8.49	...	8.27	8.29	...	...	-1.32
160	11 50 58.63	20 53 12.48	0.0269	2.13	1.80	17.85	16.96	9.15	...	8.50	8.50	8.33	8.35	-1.29
161	11 51 04.13	20 52 57.36	0.0248	2.15	1.78	18.07	17.55	8.52	...	8.23	8.25	8.18	7.78	-1.52
162	11 51 04.97	21 14 40.92	0.0270	2.41	1.71	17.86	17.45	8.56	...	8.21	8.25	8.19	7.57	-1.60
163	11 51 09.19	20 18 28.80	0.0204	1.88	1.17	18.13	17.45	8.48	...	8.49	8.44	...	...	-1.30
164	11 51 15.51	21 08 15.36	0.0236	2.36	1.86	17.71	17.08	8.68	...	8.38	8.39	...	...	-1.35
165	11 51 23.54	20 51 32.40	0.0229	2.20	1.57	17.52	17.04	8.75	...	8.37	8.40	...	...	-1.40

Table C.2: **Our sample of SF low-mass galaxies in A1367**

# (1)	R.A. J2000 hh mm ss (2)	DEC J2000 dd mm ss (3)	z (4)	R/R_{200} (5)	$\Sigma_{4,5}$ (6)	g (7)	i (8)	$M_\star$ $M_\odot$ (9)	$M_{\rm HI}$ $M_\odot$ (10)	OH PMC09 (11)	OH PP04 (12)	OH P10 (13)	OH DORS (14)	NO PMC09 (15)
166	11 51 26.85	18 57 54.72	0.0206	2.15	0.46	16.90	16.10	9.18	. . .	8.67	8.55	. . .	. . .	-1.18
167	11 51 27.48	21 18 16.20	0.0256	2.53	1.33	16.23	15.71	9.49	. . .	8.72	8.72	8.53	8.65	-0.53
168	11 51 28.95	18 34 54.84	0.0197	2.40	0.83	17.78	17.17	8.56	. . .	8.35	8.34	. . .	. . .	-1.48
169	11 51 42.22	20 39 40.32	0.0219	2.17	1.48	17.99	17.34	8.57	. . .	8.38	8.42	. . .	. . .	-1.48
170	11 51 49.51	21 09 14.76	0.0233	2.49	1.56	17.89	17.38	8.49	. . .	8.19	8.29	. . .	. . .	-1.72
171	11 51 52.46	18 32 47.04	0.0199	2.51	1.04	16.21	15.11	9.83	. . .	8.68	8.58	. . .	. . .	-1.07
172	11 51 55.66	19 38 45.24	0.0202	2.04	0.34	16.96	16.40	8.79	9.55	8.45	8.47	. . .	. . .	-1.38
173	11 51 57.29	20 47 53.52	0.0224	2.30	1.38	16.47	15.91	9.03	. . .	8.54	8.51	. . .	. . .	-1.15
174	11 51 58.56	22 03 30.24	0.0206	3.25	1.15	18.35	17.87	8.18	. . .	8.12	8.19	. . .	. . .	-1.40
175	11 52 00.82	17 44 56.76	0.0222	3.18	0.22	17.20	16.52	9.00	. . .	8.49	8.48	. . .	. . .	-1.44
176	11 52 26.76	18 21 02.16	0.0217	2.78	0.80	17.25	16.58	8.96	. . .	8.51	8.49	. . .	. . .	-1.27
177	11 52 32.95	22 18 34.56	0.0290	3.58	0.53	17.12	16.53	9.04	. . .	8.40	8.44	8.01	8.24	-1.34
178	11 52 52.73	17 36 04.32	0.0228	3.47	0.03	16.96	16.43	8.81	. . .	8.44	8.44	. . .	. . .	-1.38
179	11 52 56.88	20 26 34.80	0.0216	2.39	1.41	17.37	16.66	8.93	. . .	8.50	8.44	. . .	. . .	-1.38
180	11 53 10.83	20 26 33.36	0.0237	2.45	1.66	17.22	16.61	8.85	. . .	8.29	8.40	8.02	7.59	-1.49
181	11 53 15.99	20 37 52.68	0.0216	2.54	1.94	17.35	16.74	8.80	. . .	8.44	8.44	. . .	. . .	-1.26
182	11 53 18.34	20 06 26.64	0.0207	2.41	0.83	16.60	16.41	8.73	9.66	8.14	8.22	. . .	. . .	-1.58
183	11 53 23.64	17 22 24.60	0.0228	3.76	-0.21	16.96	16.04	9.35	. . .	8.65	8.62	. . .	. . .	-1.15
184	11 53 38.11	18 18 58.32	0.0203	3.06	0.54	16.75	16.25	8.57	. . .	8.29	8.37	. . .	. . .	-1.47
185	11 53 50.47	20 27 05.76	0.0230	2.63	1.46	17.51	16.92	8.56	. . .	8.43	8.39	8.32	8.06	-1.30
186	11 53 54.14	21 15 00.36	0.0230	3.01	0.90	16.36	15.61	9.40	. . .	8.55	8.55	8.47	8.39	-1.07
187	11 53 55.85	20 33 06.12	0.0232	2.68	1.66	16.27	15.66	9.21	. . .	8.47	8.44	8.35	8.08	-1.22
188	11 54 07.80	20 36 32.76	0.0236	2.75	1.39	17.24	16.76	8.65	. . .	8.46	8.40	8.33	7.82	-1.30
189	11 54 10.32	20 44 48.48	0.0214	2.82	1.46	16.35	15.71	9.12	. . .	8.50	8.50	. . .	. . .	-1.20
190	11 54 22.23	21 04 22.44	0.0237	3.02	0.98	18.29	17.64	8.57	. . .	8.36	8.38	8.18	8.24	-1.53
191	11 54 45.65	20 54 21.96	0.0228	3.03	0.97	18.06	17.16	8.92	. . .	8.56	8.57	8.47	8.41	-1.22

Note: The columns are the same as in Table C.1. In column 10 we quote the HI mass, as derived by Cortese et al. (2008b) HI data.

Table C.3: **Our sample of SF low-mass galaxies in A779**

#	R.A. J2000 hh mm ss	DEC J2000 dd mm ss	z	R/R_{200}	$\Sigma_{4,5}$ Mpc^{-2}	g mag	i mag	$M_\star$ $M_\odot$	OH PMC09	OH PP04	NO PMC09
(1)	(2)	(3)	(4)	(5)	(6)	(7)	(8)	(9)	(10)	(11)	(12)
01	09 16 08.40	34 14 45.24	0.0237	2.66	0.31	17.59	17.15	8.53	8.29	8.30	-1.43
02	09 16 15.55	34 43 20.64	0.0227	3.55	0.64	18.19	17.37	8.80	8.47	8.59	-1.39
03	09 17 31.13	33 28 31.79	0.0221	1.67	0.54	17.23	16.14	9.44	8.64	8.86	-0.71
04	09 17 40.56	33 00 52.56	0.0232	2.60	0.24	16.43	15.29	9.88	8.71	8.70	-0.79
05	09 18 03.22	34 45 38.88	0.0215	3.11	0.64	17.23	16.72	8.67	8.49	8.52	-1.35
06	09 18 10.99	33 39 55.45	0.0249	1.06	0.67	17.94	17.54	8.37	8.19	8.28	-1.62
07	09 18 22.80	32 56 04.92	0.0264	2.62	-0.50	17.95	17.20	8.89	8.25	8.43	-1.72
08	09 18 54.58	33 31 35.76	0.0190	0.92	-0.50	18.21	17.74	8.17	8.36	8.35	-1.32
09	09 19 13.06	33 18 56.16	0.0224	1.39	0.73	17.79	17.04	8.78	8.53	8.54	-1.35
10	09 19 31.13	33 38 52.08	0.0237	0.41	1.35	16.49	16.38	8.51	8.06	8.15	-1.49
11	09 19 31.27	33 26 03.84	0.0227	1.01	1.34	17.35	16.75	8.84	8.37	8.36	-1.24
12	09 19 45.41	33 23 57.12	0.0239	1.09	1.67	18.11	17.59	8.44	8.41	8.39	-1.41
13	09 19 49.11	33 31 59.52	0.0213	0.70	1.50	17.66	17.43	8.13	8.19	8.24	-1.46
14	09 19 53.85	33 42 01.07	0.0189	0.21	-0.50	18.00	17.66	8.19	8.27	8.29	-1.52
15	09 20 05.50	33 23 05.64	0.0248	1.15	0.65	17.11	16.30	9.24	8.60	8.65	-1.30
16	09 20 12.93	33 37 54.49	0.0221	0.47	1.56	17.20	16.42	9.08	8.63	8.72	-1.07
17	09 20 21.36	34 14 18.60	0.0246	1.42	0.31	16.85	16.35	8.89	8.33	8.35	-1.30
18	09 20 43.95	33 39 16.92	0.0236	0.64	1.23	18.12	17.32	8.69	8.51	8.48	-1.35
19	09 21 06.31	33 34 19.19	0.0265	0.97	0.17	17.00	15.91	9.72	8.67	8.75	-0.98
20	09 21 33.84	33 46 50.52	0.0237	1.06	1.43	17.24	16.46	9.14	8.56	8.52	-1.22
21	09 21 35.83	33 43 30.72	0.0242	1.09	1.18	17.48	16.83	8.87	8.53	8.50	-1.21
22	09 21 42.96	33 21 51.48	0.0235	1.66	1.18	17.52	16.73	8.99	8.54	8.54	-1.25
23	09 21 48.94	33 44 50.63	0.0229	1.21	1.28	17.15	16.75	8.55	8.40	8.33	-1.51
24	09 22 02.95	33 51 51.84	0.0241	1.38	1.36	16.50	15.73	9.39	8.65	8.69	-1.05
25	09 22 14.64	33 56 15.71	0.0201	1.55	0.11	15.99	15.31	9.34	8.55	8.58	-1.23
26	09 22 18.91	33 04 38.64	0.0253	2.55	0.17	17.65	17.23	8.58	8.34	8.32	-1.33
27	09 22 20.81	33 15 02.16	0.0212	2.18	0.83	17.69	17.05	8.63	8.40	8.41	-1.37
28	09 22 54.65	33 08 31.56	0.0217	2.65	0.86	17.12	16.44	8.95	8.37	8.40	-1.37
29	09 23 21.79	34 43 42.96	0.0275	3.54	-0.50	18.13	17.55	8.66	8.52	8.52	-1.24
30	09 23 39.96	33 58 51.95	0.0217	2.42	0.04	17.74	16.95	8.88	8.63	8.63	-1.06
31	09 23 40.73	32 53 00.60	0.0242	3.53	0.11	16.75	16.26	8.95	8.47	8.47	-1.36

Note: Column 1: order number for our sample of A779 SF galaxies; column 2: right ascension in hours, minutes, and seconds; column 3: declination, in degrees, arcminutes, and arcseconds; column 4: redshift as given in SDSS; column 5: R/R_{200} distance from the cluster center in R_{200} units; column 6: log $\Sigma_{4,5}$ the logarithm of the density to the average of the projected distances to the fourth and fifth nearest neighbors in Mpc^{-2}; column 7: observed g magnitude given in SDSS; column 8: observed i magnitude given in SDSS; column 9: log$M_\star$ log stellar mass given in SDSS; column 10: log+12(O/H) derived by PMC09 calibration of N2; column 11: log+12(O/H) derived by PP04 calibration; column 12 : log(N/O) derived by PMC09 calibration.

Table C.4: **Our sample of SF low-mass galaxies in A634**

# (1)	R.A. J2000 hh mm ss (2)	DEC J2000 dd mm ss (3)	z (4)	R/R_{200} (5)	$\Sigma_{4,5}$ Mpc^{-2} (6)	g mag (7)	i mag (8)	$M_\star$ $M_\odot$ (9)	OH PMC09 (10)	OH PP04 (11)	NO PMC09 (12)
01	08 10 42.67	57 13 42.96	0.0260	2.87	0.21	16.03	15.22	9.71	8.64	8.73	-1.00
02	08 12 16.58	57 58 31.08	0.0264	0.92	1.68	17.26	16.37	9.36	8.64	8.69	-1.01
03	08 12 26.93	57 50 09.24	0.0266	1.04	1.60	16.80	15.90	9.66	8.67	8.67	-0.78
04	08 12 37.75	58 11 27.96	0.0284	0.86	0.80	17.77	17.15	8.81	8.19	8.26	-1.70
05	08 13 17.21	58 21 41.40	0.0255	1.04	1.15	18.14	17.25	9.05	8.61	8.70	-0.89
06	08 13 32.54	58 08 10.68	0.0255	0.47	1.35	19.63	19.18	8.50	8.40	8.43	-1.42
07	08 13 39.91	58 13 30.37	0.0290	0.62	1.21	17.81	17.08	9.00	8.56	8.58	-1.32
08	08 13 48.98	57 09 03.25	0.0274	2.67	0.40	17.62	16.85	9.07	8.57	8.55	-1.30
09	08 14 09.94	57 24 43.20	0.0275	1.89	0.96	17.18	16.30	9.40	8.59	8.55	-1.27
10	08 14 33.46	58 08 53.17	0.0282	0.29	1.43	18.18	17.30	9.04	8.63	8.59	-1.14
11	08 14 35.83	58 21 57.96	0.0293	0.93	1.00	17.21	16.81	8.69	8.35	8.33	-1.37
12	08 15 05.09	58 21 25.57	0.0260	0.93	1.58	17.05	16.53	8.92	8.52	8.52	-1.29
13	08 15 23.42	58 23 39.85	0.0260	1.07	1.63	17.16	16.34	9.29	8.70	8.72	-0.94
14	08 15 28.15	57 39 03.60	0.0266	1.23	1.14	17.21	16.57	8.94	8.41	8.38	-1.47
15	08 15 32.90	57 40 05.88	0.0263	1.19	1.12	17.52	16.54	9.37	8.66	8.69	-0.99
16	08 15 42.22	57 20 42.72	0.0268	2.13	0.83	16.37	15.39	9.83	8.72	8.70	-0.76
17	08 15 42.43	58 10 45.12	0.0277	0.59	1.52	17.02	16.56	8.94	8.30	8.32	-1.42
18	08 16 04.27	58 04 15.60	0.0246	0.59	0.72	16.90	16.53	8.71	8.29	8.30	-1.36
19	08 16 17.16	58 49 04.08	0.0268	2.36	0.68	17.36	16.59	9.14	8.34	8.44	-1.64
20	08 16 32.45	57 33 27.00	0.0266	1.65	1.11	16.19	15.33	9.76	8.68	8.73	-0.81
21	08 16 34.06	57 59 39.84	0.0285	0.80	1.07	16.45	15.72	9.41	8.56	8.61	-1.01
22	08 16 34.85	57 03 03.60	0.0289	3.06	-0.10	17.54	16.91	8.93	8.47	8.50	-1.42
23	08 16 52.92	58 30 21.60	0.0258	1.62	1.18	18.10	17.22	9.25	8.56	8.65	-1.06
24	08 18 04.78	58 05 22.92	0.0263	1.38	0.91	17.72	16.90	9.15	8.42	8.37	-0.97
25	08 18 05.64	57 07 15.96	0.0286	3.09	0.03	17.40	16.20	9.77	8.69	8.77	-0.84
26	08 18 13.03	57 46 39.00	0.0272	1.65	0.65	16.75	16.16	9.14	8.45	8.43	-1.29

Note: he columns are the same as in Table C.3.

Bibliography

Abadi, M. G., Moore, B., & Bower, R. G. 1999, MNRAS, 308, 947 (Cited on pages 3 and 96.)

Abell, G. O., Corwin, Jr., H. G., & Olowin, R. P. 1989, ApJS, 70, 1 (Cited on pages 20, 22 and 103.)

Abramson, A., Kenney, J. D. P., Crowl, H. H., et al. 2011, AJ, 141, 164 (Cited on pages 4, 6, 133 and 154.)

Aguerri, J. A. L., Iglesias-Paramo, J., Vilchez, J. M., & Muñoz-Tuñón, C. 2004, AJ, 127, 1344 (Cited on page 171.)

Alloin, D., Collin-Souffrin, S., Joly, M., & Vigroux, L. 1979, A&A, 78, 200 (Cited on pages 114 and 119.)

Alonso-Herrero, A., García-Marín, M., Rodríguez Zaurín, J., et al. 2010, A&A, 522, 7 (Cited on page 59.)

Amorín, R. O., Pérez-Montero, E., & Vílchez, J. M. 2010, ApJ, 715, L128 (Cited on pages 84, 87, 147 and 150.)

Asari, N. V., Cid Fernandes, R., Stasińska, G., et al. 2007, MNRAS, 381, 263 (Cited on pages 48, 55 and 93.)

Asplund, M., Grevesse, N., Sauval, A. J., & Scott, P. 2009, ARA&A, 47, 481 (Cited on pages 54 and 93.)

Baldry, I. K., Glazebrook, K., Brinkmann, J., et al. 2004, ApJ, 600, 681 (Cited on page 137.)

Baldwin, J. A., Phillips, M. M., & Terlevich, R. 1981, PASP, 93, 5 (Cited on pages 54, 70, 104, 135 and 138.)

Balkowski, C., & Chemin, L. 2005, in The Magnetized Plasma in Galaxy Evolution, ed. K. T. Chyzy, K. Otmianowska-Mazur, M. Soida, & R.-J. Dettmar, 223–230 (Cited on pages 4 and 154.)

Balkowski, C., Vollmer, B., & Cayatte, V. 2001, Astrophysics and Space Science Supplement, 277, 393 (Cited on page 3.)

Balogh, M., Eke, V., Miller, C., et al. 2004, MNRAS, 348, 1355 (Cited on pages 8, 107 and 137.)

Balogh, M. L., Morris, S. L., Yee, H. K. C., Carlberg, R. G., & Ellingson, E. 1999, ApJ, 527, 54 (Cited on pages 8 and 151.)

Barmby, P., & Huchra, J. P. 1998, AJ, 115, 6 (Cited on pages 22, 99, 100, 101 and 104.)

Barnes, J. E., & Hernquist, L. 1996, ApJ, 471, 115 (Cited on page 8.)

Bekki, K. 2009, MNRAS, 399, 2221 (Cited on pages 7 and 170.)

Bekki, K., & Couch, W. J. 2003, ApJ, 596, L13 (Cited on page 6.)

Bekki, K., Owers, M. S., & Couch, W. J. 2010, ApJ, 718, L27 (Cited on page 100.)

Bekki, K., Tsujimoto, T., & Chiba, M. 2009, ApJ, 692, L24 (Cited on page 169.)

Bell, E. F., & de Jong, R. S. 2001, ApJ, 550, 212 (Cited on page 121.)

Bell, E. F., McIntosh, D. H., Katz, N., & Weinberg, M. D. 2003, ApJS, 149, 289 (Cited on page 79.)

Berg, D. A., Skillman, E. D., & Marble, A. R. 2011, ApJ, 738, 2 (Cited on pages 16 and 144.)

Bird, C. M., Davis, D. S., & Beers, T. C. 1995, AJ, 109, 920 (Cited on pages 26, 30, 37, 83, 100, 106 and 109.)

Blanton, M. R., Lupton, R. H., Schlegel, D. J., et al. 2005a, ApJ, 631, 208 (Cited on page 137.)

Blanton, M. R., & Roweis, S. 2007, AJ, 133, 734 (Cited on pages 79 and 105.)

Blanton, M. R., Dalcanton, J., Eisenstein, D., et al. 2001, AJ, 121, 2358 (Cited on page 135.)

Blanton, M. R., Schlegel, D. J., Strauss, M. A., et al. 2005b, AJ, 129, 2562 (Cited on page 137.)

Bolzonella, M., Kovač, K., Pozzetti, L., et al. 2010, A&A, 524, 76 (Cited on page 9.)

Boselli, A., & Gavazzi, G. 2006, PASP, 118, 517 (Cited on page 9.)

Bravo-Alfaro, H., Cayatte, V., van Gorkom, J. H., & Balkowski, C. 2000, AJ, 119, 580 (Cited on pages 4 and 154.)

—. 2001, A&A, 379, 347 (Cited on page 4.)

Bresolin, F. 2008, in The Metal-Rich Universe, ed. G. Israelian & G. Meynet, 155 (Cited on page 14.)

Bresolin, F., Gieren, W., Kudritzki, R., et al. 2009, ApJ, 700, 309 (Cited on pages 14, 73 and 113.)

Briel, U. G., Henry, J. P., & Boehringer, H. 1992, A&A, 259, L31 (Cited on page 21.)

Brinchmann, J., Charlot, S., White, S. D. M., et al. 2004, MNRAS, 351, 1151 (Cited on pages 100, 104, 138 and 150.)

Brooks, A. M., Governato, F., Booth, C. M., et al. 2007, ApJ, 655, L17 (Cited on page 16.)

Brüggen, M., & De Lucia, G. 2008, MNRAS, 383, 1336 (Cited on page 4.)

Bruzual, G., & Charlot, S. 2003, MNRAS, 344, 1000 (Cited on pages 54, 79 and 100.)

Burbidge, E. M., Burbidge, G. R., Fowler, W. A., & Hoyle, F. 1957, Reviews of Modern Physics, 29, 547 (Cited on page 1.)

Burns, J. O., Rhee, G., Owen, F. N., & Pinkney, J. 1994, ApJ, 423, 94 (Cited on page 30.)

Caldwell, N., & Rose, J. A. 1997, AJ, 113, 492 (Cited on page 7.)

Calura, F., Pipino, A., Chiappini, C., Matteucci, F., & Maiolino, R. 2009, A&A, 504, 373 (Cited on pages 16 and 168.)

Calzetti, D., Kinney, A. L., & Storchi-Bergmann, T. 1994, ApJ, 429, 582 (Cited on pages 59 and 123.)

Cardelli, J. A., Clayton, G. C., & Mathis, J. S. 1989, ApJ, 345, 245 (Cited on pages 114, 122, 123 and 138.)

Carlberg, R. G., Yee, H. K. C., & Ellingson, E. 1997, ApJ, 478, 462 (Cited on page 21.)

Carter, D., Mobasher, B., Bridges, T. J., et al. 2002, ApJ, 567, 772 (Cited on page 170.)

Cayatte, V., van Gorkom, J. H., Balkowski, C., & Kotanyi, C. 1990, AJ, 100, 604 (Cited on pages 4 and 154.)

Cedrés, B., Iglesias-Páramo, J., Vílchez, J. M., et al. 2009, AJ, 138, 873 (Cited on pages 19, 31, 32, 36, 39, 45, 46 and 154.)

Cen, R., & Ostriker, J. P. 1999, ApJ, 519, L109 (Cited on pages 2 and 4.)

Chabrier, G. 2003, PASP, 115, 763 (Cited on page 79.)

Chung, A., van Gorkom, J. H., Kenney, J. D. P., Crowl, H., & Vollmer, B. 2009, AJ, 138, 1741 (Cited on pages 4, 5 and 154.)

Cid Fernandes, R., González Delgado, R. M., Storchi-Bergmann, T., Martins, L. P., & Schmitt, H. 2005a, MNRAS, 356, 270 (Cited on page 54.)

Cid Fernandes, R., Gu, Q., Melnick, J., et al. 2004, MNRAS, 355, 273 (Cited on page 54.)

Cid Fernandes, R., Mateus, A., Sodré, L., Stasińska, G., & Gomes, J. M. 2005b, MNRAS, 358, 363 (Cited on page 54.)

Conselice, C. J. 2006, ApJ, 638, 686 (Cited on page 8.)

Contini, T., Treyer, M. A., Sullivan, M., & Ellis, R. S. 2002, MNRAS, 330, 75 (Cited on page 16.)

Cooper, M. C., Tremonti, C. A., Newman, J. A., & Zabludoff, A. I. 2008, MNRAS, 390, 245 (Cited on pages 16, 36, 83, 84, 99 and 153.)

Cortese, L., Gavazzi, G., & Boselli, A. 2008a, MNRAS, 390, 1282 (Cited on page 21.)

Cortese, L., Gavazzi, G., Boselli, A., et al. 2006, A&A, 453, 847 (Cited on pages 21 and 97.)

Cortese, L., Gavazzi, G., Boselli, A., Iglesias-Paramo, J., & Carrasco, L. 2004, A&A, 425, 429 (Cited on page 21.)

Cortese, L., Marcillac, D., Richard, J., et al. 2007, MNRAS, 376, 157 (Cited on page 6.)

Cortese, L., Minchin, R. F., Auld, R. R., et al. 2008b, MNRAS, 383, 1519 (Cited on pages 155 and 210.)

Cresci, G., Mannucci, F., Maiolino, R., et al. 2010, Nature, 467, 811 (Cited on page 150.)

Cresci, G., Mannucci, F., Sommariva, V., et al. 2012, MNRAS, 421, 262 (Cited on page 147.)

Dalcanton, J. J. 2007, ApJ, 658, 941 (Cited on pages 16 and 150.)

Davé, R., Finlator, K., & Oppenheimer, B. D. 2011, MNRAS, 416, 1354 (Cited on pages 16, 126, 144, 150, 168, 169 and 170.)

Davé, R., Finlator, K., Oppenheimer, B. D., et al. 2010, MNRAS, 404, 1355 (Cited on page 16.)

De Grandi, S., Ettori, S., Longhetti, M., & Molendi, S. 2004, A&A, 419, 7 (Cited on page 172.)

De Lucia, G., Kauffmann, G., & White, S. D. M. 2004, MNRAS, 349, 1101 (Cited on pages 16 and 168.)

de Rossi, M. E., Tissera, P. B., & Scannapieco, C. 2007, MNRAS, 374, 323 (Cited on page 168.)

Dekel, A., Birnboim, Y., Engel, G., et al. 2009, Nature, 457, 451 (Cited on page 150.)

Denicoló, G., Terlevich, R., & Terlevich, E. 2002, MNRAS, 330, 69 (Cited on page 14.)

Dickey, J. M. 1997, AJ, 113, 1939 (Cited on pages 26, 40, 41, 80, 82, 90, 91, 177, 178, 179 and 181.)

Dong, X., Wang, T., Yuan, W., et al. 2007, ApJ, 657, 700 (Cited on pages 41, 70 and 71.)

Donnelly, R. H., Markevitch, M., Forman, W., et al. 1998, ApJ, 500, 138 (Cited on page 21.)

Dors, O. L., Krabbe, A., Hägele, G. F., & Pérez-Montero, E. 2011, MNRAS, 415, 3616 (Cited on pages 73, 119, 120, 141, 142, 187 and 204.)

Dressler, A. 1980, ApJ, 236, 351 (Cited on pages 8, 95, 107, 108, 137 and 167.)

Drory, N., Bender, R., & Hopp, U. 2004, ApJ, 616, L103 (Cited on page 79.)

Duc, P., Braine, J., Lisenfeld, U., Brinks, E., & Boquien, M. 2007, A&A, 475, 187 (Cited on page 91.)

Duc, P., Cayatte, V., Balkowski, C., et al. 2001, A&A, 369, 763 (Cited on pages 36, 86, 88 and 133.)

Duc, P., Papaderos, P., Balkowski, C., et al. 1999, A&AS, 136, 539 (Cited on pages 86 and 88.)

Edmunds, M. G. 1990, MNRAS, 246, 678 (Cited on pages 86, 91, 130 and 155.)

Edmunds, M. G., & Pagel, B. E. J. 1984, MNRAS, 211, 507 (Cited on page 114.)

Ellison, S. L., Patton, D. R., Simard, L., & McConnachie, A. W. 2008, ApJ, 672, L107 (Cited on pages 16 and 147.)

Ellison, S. L., Simard, L., Cowan, N. B., et al. 2009, MNRAS, 396, 1257 (Cited on pages 36, 79, 83, 99, 153 and 154.)

Erb, D. K., Shapley, A. E., Pettini, M., et al. 2006, ApJ, 644, 813 (Cited on pages 15 and 151.)

Ferrini, F., Molla, M., Pardi, M. C., & Diaz, A. I. 1994, ApJ, 427, 745 (Cited on page 93.)

Finlator, K., & Davé, R. 2008, MNRAS, 385, 2181 (Cited on pages 16, 126, 144 and 168.)

Finn, R. A., Zaritsky, D., McCarthy, D. W., et al. 2005, ApJ, 630, 206 (Cited on pages 9, 21 and 167.)

Fukugita, M., Shimasaku, K., & Ichikawa, T. 1995, PASP, 107, 945 (Cited on pages 82 and 121.)

Fumagalli, M., Gavazzi, G., Scaramella, R., & Franzetti, P. 2011, A&A, 528, 46 (Cited on page 6.)

Gallazzi, A., Charlot, S., Brinchmann, J., White, S. D. M., & Tremonti, C. A. 2005, MNRAS, 362, 41 (Cited on pages 93 and 150.)

Garcia-Rissmann, A., Vega, L. R., Asari, N. V., et al. 2005, MNRAS, 359, 765 (Cited on page 54.)

Gavazzi, G., Boselli, A., Mayer, L., et al. 2001, ApJ, 563, L23 (Cited on pages 6, 8, 90, 133, 154, 157, 159 and 167.)

Gavazzi, G., Boselli, A., Pedotti, P., Gallazzi, A., & Carrasco, L. 2002, A&A, 396, 449 (Cited on pages 108 and 109.)

Gavazzi, G., Cortese, L., Boselli, A., et al. 2003, ApJ, 597, 210 (Cited on pages 6 and 21.)

Giovanelli, R., Haynes, M. P., & Chincarini, G. L. 1981, ApJ, 247, 383 (Cited on page 26.)

Giovanelli, R., Haynes, M. P., Kent, B. R., et al. 2005, AJ, 130, 2598 (Cited on page 155.)

González Delgado, R. M., Leitherer, C., & Heckman, T. M. 1999, ApJS, 125, 489 (Cited on page 54.)

Gunn, J. E., & Gott, J. R. 1972, ApJ, 176, 1 (Cited on page 3.)

Guseva, N. G., Izotov, Y. I., Papaderos, P., et al. 2001, A&A, 378, 756 (Cited on page 54.)

Hägele, G. F., Díaz, A. I., Terlevich, E., et al. 2008, MNRAS, 383, 209 (Cited on pages 12 and 59.)

Haines, C. P., Gargiulo, A., La Barbera, F., et al. 2007, MNRAS, 381, 7 (Cited on pages 9, 10, 106 and 167.)

Haines, C. P., La Barbera, F., Mercurio, A., Merluzzi, P., & Busarello, G. 2006, ApJ, 647, L21 (Cited on pages 10 and 167.)

Haynes, M. P., Giovanelli, R., Martin, A. M., et al. 2011, AJ, 142, 170 (Cited on pages 155 and 204.)

Henry, R. B. C., Balkowski, C., Cayatte, V., Edmunds, M. G., & Pagel, B. E. J. 1996, MNRAS, 283, 635 (Cited on page 36.)

Henry, R. B. C., Pagel, B. E. J., & Chincarini, G. L. 1994, MNRAS, 266, 421 (Cited on page 36.)

Henry, R. B. C., Pagel, B. E. J., Lasseter, D. F., & Chincarini, G. L. 1992, MNRAS, 258, 321 (Cited on page 36.)

Hernández-Fernández, J. D., Vílchez, J. M., & Iglesias-Páramo, J. 2012, ApJ, 751, 54 (Cited on page 3.)

Hopkins, A. M. 2004, ApJ, 615, 209 (Cited on page 1.)

Hopkins, A. M., & Beacom, J. F. 2006, ApJ, 651, 142 (Cited on page 3.)

Huang, Z., & Sarazin, C. L. 1996, ApJ, 461, 622 (Cited on pages 26, 31, 80, 90 and 178.)

Hudson, D. S., Mittal, R., Reiprich, T. H., et al. 2010, A&A, 513, A37 (Cited on pages 30 and 100.)

Hwang, H. S., Park, C., Elbaz, D., & Choi, Y.-Y. 2012, A&A, 538, A15 (Cited on page 106.)

Iglesias-Páramo, J., Boselli, A., Cortese, L., Vílchez, J. M., & Gavazzi, G. 2002, A&A, 384 (Cited on pages 19, 31, 33, 157, 159 and 160.)

Iglesias-Páramo, J., Boselli, A., Gavazzi, G., Cortese, L., & Vílchez, J. M. 2003a, A&A, 397, 421 (Cited on page 26.)

Iglesias-Páramo, J., van Driel, W., Duc, P., et al. 2003b, A&A, 406, 453 (Cited on pages 36, 37 and 78.)

Israel, F. P. 1997, A&A, 328, 471 (Cited on page 155.)

Jaffé, Y. L., Aragón-Salamanca, A., Kuntschner, H., et al. 2011, MNRAS, 417, 1996 (Cited on page 154.)

James, P. A., Shane, N. S., Beckman, J. E., et al. 2004, A&A, 414, 23 (Cited on page 32.)

Jansen, R. A., Fabricant, D., Franx, M., & Caldwell, N. 2000, ApJS, 126, 331 (Cited on page 80.)

Kapferer, W., Kronberger, T., Ferrari, C., Riser, T., & Schindler, S. 2008, MNRAS, 389, 1405 (Cited on page 157.)

Kapferer, W., Ferrari, C., Domainko, W., et al. 2006, A&A, 447, 827 (Cited on page 169.)

Kapferer, W., Kronberger, T., Breitschwerdt, D., et al. 2009, A&A, 504, 719 (Cited on pages 6, 163, 167 and 169.)

Kauffmann, G., Heckman, T. M., White, S. D. M., et al. 2003, MNRAS, 341, 33 (Cited on pages 70, 71, 79, 105, 125 and 138.)

Kenney, J. D. P., & Koopmann, R. A. 1999, AJ, 117, 181 (Cited on page 154.)

Kenney, J. D. P., van Gorkom, J. H., & Vollmer, B. 2004, AJ, 127, 3361 (Cited on pages 4 and 154.)

Kennicutt, R. C. 1998, ApJ, 498, 541 (Cited on pages 9, 80 and 159.)

Kennicutt, R. C., Bresolin, F., & Garnett, D. R. 2003, ApJ, 591, 801 (Cited on pages 14 and 113.)

Kennicutt, Jr., R. C. 1983, AJ, 88, 483 (Cited on page 8.)

Kennicutt, Jr., R. C., Lee, J. C., Funes, José G., S. J., Sakai, S., & Akiyama, S. 2008, ApJS, 178, 247 (Cited on page 31.)

Keres, D., Yun, M. S., & Young, J. S. 2003, ApJ, 582, 659 (Cited on page 155.)

Kewley, L. J., & Dopita, M. A. 2002, ApJS, 142, 35 (Cited on pages 14 and 72.)

Kewley, L. J., Dopita, M. A., Sutherland, R. S., Heisler, C. A., & Trevena, J. 2001, ApJ, 556, 121 (Cited on pages 70 and 71.)

Kewley, L. J., & Ellison, S. L. 2008, ApJ, 681, 1183 (Cited on pages 14 and 72.)

Kewley, L. J., Geller, M. J., & Barton, E. J. 2006, AJ, 131, 2004 (Cited on page 16.)

Kewley, L. J., Jansen, R. A., & Geller, M. J. 2005, PASP, 117, 227 (Cited on pages 113 and 134.)

Kobulnicky, H. A., Kennicutt, R. C., & Pizagno, J. L. 1999, ApJ, 514, 544 (Cited on pages 72 and 73.)

Kobulnicky, H. A., & Skillman, E. D. 1997, ApJ, 489, 636 (Cited on pages 113 and 134.)

Koopmann, R. A., Haynes, M. P., & Catinella, B. 2006, AJ, 131, 716 (Cited on page 154.)

Koopmann, R. A., & Kenney, J. D. P. 2004, ApJ, 613, 866 (Cited on pages 4, 5, 94 and 154.)

Köppen, J., & Hensler, G. 2005, A&A, 434, 531 (Cited on page 130.)

Köppen, J., Weidner, C., & Kroupa, P. 2007, MNRAS, 375, 673 (Cited on page 16.)

Kronberger, T., Kapferer, W., Ferrari, C., Unterguggenberger, S., & Schindler, S. 2008, A&A, 481, 337 (Cited on pages 6, 7, 90, 163 and 167.)

Lamareille, F., Mouhcine, M., Contini, T., Lewis, I., & Maddox, S. 2004, MNRAS, 350, 396 (Cited on pages 15 and 120.)

Lamareille, F., Brinchmann, J., Contini, T., et al. 2009, A&A, 495, 53 (Cited on page 15.)

Lara-López, M. A., Cepa, J., Bongiovanni, A., et al. 2010, A&A, 521, L53 (Cited on pages 86 and 147.)

Larson, R. B. 1974, MNRAS, 169, 229 (Cited on pages 16 and 168.)

Larson, R. B., Tinsley, B. M., & Caldwell, C. N. 1980, ApJ, 237, 692 (Cited on page 7.)

Leccardi, A., & Molendi, S. 2008, A&A, 487, 461 (Cited on page 172.)

Ledlow, M. J., Voges, W., Owen, F. N., & Burns, J. O. 2003, AJ, 126, 2740 (Cited on pages 21, 22, 102 and 103.)

Lee, H., McCall, M. L., & Richer, M. G. 2003, AJ, 125, 2975 (Cited on pages 36, 90, 91, 92 and 133.)

Lee, H., Skillman, E. D., Cannon, J. M., et al. 2006, ApJ, 647, 970 (Cited on pages 15, 17, 120, 121, 122, 125, 126, 127, 144 and 168.)

Leitherer, C., Schaerer, D., Goldader, J. D., et al. 1999, ApJS, 123, 3 (Cited on page 143.)

Lequeux, J., Peimbert, M., Rayo, J. F., Serrano, A., & Torres-Peimbert, S. 1979, A&A, 80, 155 (Cited on pages 15 and 120.)

Levy, L., Rose, J. A., van Gorkom, J. H., & Chaboyer, B. 2007, AJ, 133, 1104 (Cited on pages 4 and 167.)

Lewis, I., Balogh, M., De Propris, R., et al. 2002, MNRAS, 334, 673 (Cited on pages 107, 108 and 109.)

Li, C., & White, S. D. M. 2009, MNRAS, 398, 2177 (Cited on page 79.)

Lilly, S. J., Le Fevre, O., Hammer, F., & Crampton, D. 1996, ApJ, 460, L1 (Cited on page 1.)

López-Sánchez, A. R., & Esteban, C. 2010, A&A, 517, 85 (Cited on page 74.)

Lovisari, L., Schindler, S., & Kapferer, W. 2011, A&A, 528, 60 (Cited on page 172.)

Maccagni, D., Garilli, B., & Tarenghi, M. 1995, AJ, 109, 465 (Cited on pages 26 and 100.)

Madau, P., Ferguson, H. C., Dickinson, M. E., et al. 1996, MNRAS, 283, 1388 (Cited on page 1.)

Magrini, L., Vílchez, J. M., Mampaso, A., Corradi, R. L. M., & Leisy, P. 2007, A&A, 470, 865 (Cited on pages 14 and 113.)

Mahajan, S., Haines, C. P., & Raychaudhury, S. 2010, MNRAS, 404, 1745 (Cited on pages 10, 36, 100, 133, 134, 135, 138, 167 and 170.)

—. 2011, MNRAS, 412, 1098 (Cited on pages 97, 98, 133, 134, 135 and 167.)

Maiolino, R., Nagao, T., Grazian, A., et al. 2008, A&A, 488, 463 (Cited on pages 15 and 151.)

Mamon, G. 1996, in Third Paris Cosmology Colloquium, ed. H. J. de Vega & N. Sánchez, 95 (Cited on page 8.)

Mannucci, F., Cresci, G., Maiolino, R., Marconi, A., & Gnerucci, A. 2010, MNRAS, 408, 2115 (Cited on pages 16, 86, 124, 147 and 150.)

Mannucci, F., Cresci, G., Maiolino, R., et al. 2009, MNRAS, 398, 1915 (Cited on pages 15 and 151.)

Marconi, G., Matteucci, F., & Tosi, M. 1994, MNRAS, 270, 35 (Cited on page 168.)

Martín-Manjón, M. L., García-Vargas, M. L., Mollá, M., & Díaz, A. I. 2010, MNRAS, 403, 2012 (Cited on page 101.)

Martín-Manjón, M. L., Mollá, M., Díaz, A. I., & Terlevich, R. 2008, MNRAS, 385, 854 (Cited on page 101.)

Mateus, A., Sodré, L., Cid Fernandes, R., & Stasińska, G. 2007, MNRAS, 374, 1457 (Cited on page 83.)

Matteucci, F. 1994, A&A, 288, 57 (Cited on page 168.)

McCall, M. L., Rybski, P. M., & Shields, G. A. 1985, ApJS, 57, 1 (Cited on page 114.)

McGaugh, S. S. 1991, ApJ, 380, 140 (Cited on pages 14, 72 and 73.)

Merlin, E., & Chiosi, C. 2006, A&A, 457, 437 (Cited on page 9.)

Meynet, G., & Maeder, A. 2002, A&A, 390, 561 (Cited on pages 90 and 157.)

Michel-Dansac, L., Lambas, D. G., Alonso, M. S., & Tissera, P. 2008, MNRAS, 386, L82 (Cited on page 16.)

Mihos, J. C., Harding, P., Feldmeier, J., & Morrison, H. 2005, ApJ, 631, L41 (Cited on pages 8 and 9.)

Mihos, J. C., & Hernquist, L. 1996, ApJ, 464, 641 (Cited on page 8.)

Miller, J. S., & Mathews, W. G. 1972, ApJ, 172, 593 (Cited on pages 59 and 80.)

Moles, M., Bettoni, D., Fasano, G., et al. 2004, A&A, 418, 495 (Cited on pages 40 and 93.)

Mollá, M., García-Vargas, M. L., & Bressan, A. 2009, MNRAS, 398, 451 (Cited on page 163.)

Mollá, M., Vílchez, J. M., Gavilán, M., & Díaz, A. I. 2006, MNRAS, 372, 1069 (Cited on pages 13, 15 and 93.)

Monreal-Ibero, A., Vílchez, J. M., Walsh, J. R., & Muñoz-Tuñón, C. 2010, A&A, 517, 27 (Cited on pages 59 and 74.)

Moore, B., Lake, G., & Katz, N. 1998, ApJ, 495, 139 (Cited on page 8.)

Moore, B., Lake, G., Quinn, T., & Stadel, J. 1999, MNRAS, 304, 465 (Cited on page 8.)

Mori, M., & Burkert, A. 2000, ApJ, 538, 559 (Cited on page 3.)

Mouhcine, M., Baldry, I. K., & Bamford, S. P. 2007, MNRAS, 382, 801 (Cited on pages 36, 79, 83 and 153.)

Mouhcine, M., Kriwattanawong, W., & James, P. A. 2011, MNRAS, 412, 1295 (Cited on page 137.)

Moustakas, J., & Kennicutt, Jr., R. C. 2006, ApJ, 651, 155 (Cited on page 14.)

Neumann, D. M., Lumb, D. H., Pratt, G. W., & Briel, U. G. 2003, A&A, 400, 811 (Cited on page 21.)

Oppenheimer, B. D., Davé, R., Kereš, D., et al. 2010, MNRAS, 406, 2325 (Cited on pages 168 and 169.)

Osterbrock, D. E. 1989, Astrophysics of gaseous nebulae and active galactic nuclei (Cited on pages 114, 138 and 143.)

Owen, F. N., Keel, W. C., Wang, Q. D., Ledlow, M. J., & Morrison, G. E. 2006, AJ, 131, 1974 (Cited on page 6.)

Owers, M. S., Couch, W. J., Nulsen, P. E. J., & Randall, S. W. 2012, ApJ, 750, L23 (Cited on page 6.)

Pagel, B. E. J., Edmunds, M. G., Blackwell, D. E., Chun, M. S., & Smith, G. 1979, MNRAS, 189, 95 (Cited on pages 11, 114 and 138.)

Peimbert, A., & Peimbert, M. 2010, ApJ, 724, 791 (Cited on page 73.)

Penny, S. J., Conselice, C. J., de Rijcke, S., et al. 2011, MNRAS, 410, 1076 (Cited on page 151.)

Pérez-Montero, E., & Contini, T. 2009, MNRAS, 398, 949 (Cited on pages 13, 70, 72, 73, 78 and 130.)

Pérez-Montero, E., & Díaz, A. I. 2003, MNRAS, 346, 105 (Cited on page 114.)

Pérez-Montero, E., & Díaz, A. I. 2005, MNRAS, 361, 1063 (Cited on pages 13 and 14.)

Pérez-Montero, E., & Vílchez, J. M. 2009, MNRAS, 400, 1721 (Cited on page 114.)

Pettini, M., & Pagel, B. E. J. 2004, MNRAS, 348, L59 (Cited on pages 14, 72 and 119.)

Pilyugin, L. S., Grebel, E. K., & Mattsson, L. 2012, ArXiv e-prints (Cited on pages 116, 119, 120 and 187.)

Pilyugin, L. S., Mollá, M., Ferrini, F., & Vílchez, J. M. 2002, A&A, 383, 14 (Cited on pages 36, 86 and 88.)

Pilyugin, L. S., & Thuan, T. X. 2005, ApJ, 631, 231 (Cited on pages 13, 14 and 72.)

Pilyugin, L. S., Vílchez, J. M., & Contini, T. 2004, A&A, 425, 849 (Cited on page 113.)

Pilyugin, L. S., Vílchez, J. M., & Thuan, T. X. 2010, ApJ, 720, 1738 (Cited on pages 14, 72, 73 and 78.)

Poggianti, B. M., Bridges, T. J., Komiyama, Y., et al. 2004, ApJ, 601, 197 (Cited on pages 7 and 167.)

Poggianti, B. M., Smail, I., Dressler, A., et al. 1999, ApJ, 518, 576 (Cited on pages 8 and 167.)

Poggianti, B. M., von der Linden, A., De Lucia, G., et al. 2006, ApJ, 642, 188 (Cited on pages 105, 137 and 167.)

Poggianti, B. M., Desai, V., Finn, R., et al. 2008, ApJ, 684, 888 (Cited on page 9.)

Poggianti, B. M., Aragón-Salamanca, A., Zaritsky, D., et al. 2009a, ApJ, 693, 112 (Cited on pages 7 and 169.)

Poggianti, B. M., Fasano, G., Bettoni, D., et al. 2009b, ApJ, 697, L137 (Cited on page 169.)

Porter, S. C., Raychaudhury, S., Pimbblet, K. A., & Drinkwater, M. J. 2008, MNRAS, 388, 1152 (Cited on pages 100, 133, 167 and 170.)

Quilis, V., Moore, B., & Bower, R. 2000, Science, 288, 1617 (Cited on page 7.)

Radovich, M., Ciroi, S., Contini, M., et al. 2005, A&A, 431, 813 (Cited on pages 40, 70 and 93.)

Relaño, M., Monreal-Ibero, A., Vílchez, J. M., & Kennicutt, R. C. 2010, MNRAS, 402, 1635 (Cited on page 138.)

Reverte, D. 2008, PhD thesis, Univ. Granada (Cited on pages 9, 19, 32, 33, 34, 80, 108, 163, 164, 165 and 166.)

Reverte, D., Vílchez, J. M., Hernández-Fernández, J. D., & Iglesias-Páramo, J. 2007, AJ, 133, 705 (Cited on page 181.)

Rines, K., Geller, M. J., Kurtz, M. J., & Diaferio, A. 2005, AJ, 130, 1482 (Cited on pages 8, 9, 10, 106, 107, 137 and 154.)

Roediger, E., & Hensler, G. 2005, A&A, 433, 875 (Cited on page 4.)

Roettiger, K., Burns, J. O., & Loken, C. 1996, ApJ, 473, 651 (Cited on page 100.)

Rupke, D. S. N., Kewley, L. J., & Barnes, J. E. 2010, ApJ, 710, L156 (Cited on page 16.)

Salim, S., Rich, R. M., Charlot, S., et al. 2007, ApJS, 173, 267 (Cited on page 150.)

Sánchez-Janssen, R., Iglesias-Páramo, J., Muñoz-Tuñón, C., Aguerri, J. A. L., & Vílchez, J. M. 2005, A&A, 434, 521 (Cited on pages 26 and 100.)

Sanderson, A. J. R., Ponman, T. J., & O'Sullivan, E. 2006, MNRAS, 372, 1496 (Cited on page 100.)

Savaglio, S., Glazebrook, K., Le Borgne, D., et al. 2005, ApJ, 635, 260 (Cited on page 15.)

Schindler, S., & Diaferio, A. 2008, Space Sci. Rev., 134, 363 (Cited on pages 169 and 172.)

Schindler, S., Kapferer, W., Domainko, W., et al. 2005, A&A, 435, L25 (Cited on page 169.)

Searle, L. 1971, ApJ, 168, 327 (Cited on page 114.)

Shapley, A. E., Coil, A. L., Ma, C.-P., & Bundy, K. 2005, ApJ, 635, 1006 (Cited on page 15.)

Shields, G. A. 1974, ApJ, 193, 335 (Cited on page 114.)

Shields, G. A., Skillman, E. D., & Kennicutt, R. C. 1991, ApJ, 371, 82 (Cited on page 36.)

Shimasaku, K., Fukugita, M., Doi, M., et al. 2001, AJ, 122, 1238 (Cited on page 151.)

Skillman, E. D., Kennicutt, R. C., & Hodge, P. W. 1989, ApJ, 347, 875 (Cited on pages 15 and 120.)

Skillman, E. D., Kennicutt, R. C., Shields, G. A., & Zaritsky, D. 1996, ApJ, 462, 147 (Cited on pages 36, 86 and 94.)

Smith, R. J., Lucey, J. R., Hudson, M. J., et al. 2009, MNRAS, 392, 1265 (Cited on pages 36 and 170.)

Smith, R. J., Lucey, J. R., Price, J., Hudson, M. J., & Phillipps, S. 2012, MNRAS, 419, 3167 (Cited on pages 133, 134, 167 and 171.)

Smith, R. J., Lucey, J. R., Hammer, D., et al. 2010, MNRAS, 408, 1417 (Cited on pages 6, 154 and 167.)

Solanes, J. M., Manrique, A., García-Gómez, C., et al. 2001, ApJ, 548, 97 (Cited on page 154.)

Spitoni, E., Calura, F., Matteucci, F., & Recchi, S. 2010, A&A, 514, 73 (Cited on pages 16 and 168.)

Springel, V., White, S. D. M., Jenkins, A., et al. 2005, Nature, 435, 629 (Cited on pages 133 and 171.)

Storchi-Bergmann, T., Calzetti, D., & Kinney, A. L. 1994, ApJ, 429, 572 (Cited on page 13.)

Strateva, I., Ivezić, v., Knapp, G. R., et al. 2001, AJ, 122, 1861 (Cited on pages 137 and 151.)

Struck, C. 1999, Phys. Rep., 321, 1 (Cited on page 8.)

Sun, M., Donahue, M., Roediger, E., et al. 2010, ApJ, 708, 946 (Cited on page 6.)

Sun, M., Donahue, M., & Voit, G. M. 2007, ApJ, 671, 190 (Cited on pages 4, 6, 133, 154, 159 and 167.)

Sun, M., & Murray, S. S. 2002, ApJ, 576, 708 (Cited on page 21.)

Tacconi, L. J., Genzel, R., Neri, R., et al. 2010, Nature, 463, 781 (Cited on page 150.)

Tarenghi, M., Chincarini, G., Rood, H. J., & Thompson, L. A. 1980, ApJ, 235, 724 (Cited on pages 101 and 106.)

Tassis, K., Kravtsov, A. V., & Gnedin, N. Y. 2008, ApJ, 672, 888 (Cited on page 168.)

Tecce, T. E., Cora, S. A., & Tissera, P. B. 2011, MNRAS, 416, 3170 (Cited on page 169.)

Tecce, T. E., Cora, S. A., Tissera, P. B., Abadi, M. G., & Lagos, C. D. P. 2010, MNRAS, 408, 2008 (Cited on pages 4, 155 and 167.)

Terlevich, A. I., Caldwell, N., & Bower, R. G. 2001, MNRAS, 326, 1547 (Cited on page 137.)

Tissera, P. B., De Rossi, M. E., & Scannapieco, C. 2005, MNRAS, 364, L38 (Cited on page 168.)

Tolstoy, E., Hill, V., & Tosi, M. 2009, ARA&A, 47, 371 (Cited on page 168.)

Tonnesen, S., & Bryan, G. L. 2008, ApJ, 684, L9 (Cited on page 157.)

—. 2009, ApJ, 694, 789 (Cited on page 4.)

Tonnesen, S., Bryan, G. L., & van Gorkom, J. H. 2007, ApJ, 671, 1434 (Cited on pages 3 and 167.)

Toribio, M. C., Solanes, J. M., Giovanelli, R., Haynes, M. P., & Martin, A. M. 2011, ApJ, 732, 93 (Cited on page 157.)

Tremonti, C. A., Heckman, T. M., Kauffmann, G., et al. 2004, ApJ, 613, 898 (Cited on pages 14, 15, 72, 100, 104, 120, 126, 138 and 168.)

Treu, T., Ellis, R. S., Kneib, J., et al. 2003, ApJ, 591, 53 (Cited on pages 3, 8 and 167.)

Vaduvescu, O., Kehrig, C., Vilchez, J. M., & Unda-Sanzana, E. 2011, A&A, 533, 65 (Cited on page 134.)

Vaduvescu, O., McCall, M. L., & Richer, M. G. 2007, AJ, 134, 604 (Cited on pages 15, 36, 84, 86, 87, 88, 90, 92 and 133.)

van Zee, L., & Haynes, M. P. 2006, ApJ, 636, 214 (Cited on pages 90, 91, 113, 120, 121, 122, 125, 130, 134 and 157.)

van Zee, L., Skillman, E. D., & Haynes, M. P. 2006, ApJ, 637, 269 (Cited on pages 113, 120 and 134.)

Vila Costas, M. B., & Edmunds, M. G. 1993, MNRAS, 265, 199 (Cited on page 13.)

Vilchez, J. M. 1995, AJ, 110, 1090 (Cited on pages 36 and 133.)

Vilchez, J. M., & Esteban, C. 1996, MNRAS, 280, 720 (Cited on page 14.)

Vílchez, J. M., & Iglesias-Páramo, J. 2003, ApJS, 145, 225 (Cited on pages 36, 84 and 88.)

Vilchez, J. M., & Pagel, B. E. J. 1988, MNRAS, 231, 257 (Cited on page 114.)

Vílchez, J. M., Pagel, B. E. J., Diaz, A. I., Terlevich, E., & Edmunds, M. G. 1988, MNRAS, 235, 633 (Cited on pages 14 and 113.)

Vollmer, B., Balkowski, C., Cayatte, V., van Driel, W., & Huchtmeier, W. 2004, A&A, 419, 35 (Cited on pages 4 and 154.)

Vollmer, B., Cayatte, V., Balkowski, C., & Duschl, W. J. 2001, ApJ, 561, 708 (Cited on pages 3, 7 and 95.)

Vollmer, B., Cayatte, V., van Driel, W., et al. 2001, A&A, 369, 432 (Cited on pages 4 and 154.)

Vulcani, B., Poggianti, B. M., Fasano, G., et al. 2012, MNRAS, 420, 1481 (Cited on page 9.)

Weidner, C., & Kroupa, P. 2005, ApJ, 625, 754 (Cited on page 2.)

—. 2006, MNRAS, 365, 1333 (Cited on page 2.)

Werner, N., Durret, F., Ohashi, T., Schindler, S., & Wiersma, R. P. C. 2008, Space Sci. Rev., 134, 337 (Cited on page 171.)

Yagi, M., Yoshida, M., Komiyama, Y., et al. 2010, AJ, 140, 1814 (Cited on pages 6, 154, 159 and 167.)

Yasuda, N., Fukugita, M., Narayanan, V. K., et al. 2001, AJ, 122, 1104 (Cited on pages 79 and 85.)

Yoshida, M., Yagi, M., Komiyama, Y., et al. 2012, ApJ, 749, 43 (Cited on page 6.)

—. 2008, ApJ, 688, 918 (Cited on pages 6 and 167.)

Zabludoff, A. I., & Franx, M. 1993, AJ, 106, 1314 (Cited on page 100.)

Zahid, H. J., Bresolin, F., Kewley, L. J., Coil, A. L., & Davé, R. 2012, ApJ, 750, 120 (Cited on pages 15 and 16.)

Zahid, H. J., Kewley, L. J., & Bresolin, F. 2011, ApJ, 730, 137 (Cited on pages 15 and 79.)

Zaritsky, D., Kennicutt, R. C., & Huchra, J. P. 1994, ApJ, 420, 87 (Cited on pages 15 and 120.)

Zwicky, F., Sargent, W. L. W., & Kowal, C. 1969, PASP, 81, 224 (Cited on pages 91 and 179.)

List of Abbreviations

AGN	Active Galactic Nucleus
BCG	Brightest Cluster Galaxy
CAHA	Centro Astronómico Hispano Alemán
ICM	Intracluster Medium
INT	Isaac Newton Telescope
IMF	Initial Mass Function
ISM	Interstellar Medium
KS	Kolmogorov-Smirnov
LZR	Luminosity-Metallicity Relation
MZR	Mass-Metallicity Relation
NOT	Nordic Optical Telescope
ORM	Observatorio del Roque de los Muchachos
RPS	Ram-Pressure Stripping
SED	Spectral Energy Distribution
SDSS	Sloan Digital Sky Survey
S/N	Signal-to-Noise
SN	Supernovae
SF	Star-Forming
SFH	Star Formation History
SFR	Star Formation Rate
SSP	Single Stellar Population
TDC	Tidal Dwarf Candidate
WHT	William Herschel Telescope

Resources

I acknowledge financial support from the Spanish Ministerio de Ciencia e Innovación under grant FPU AP2006-04622 and from the Spanish PNAYA project ESTALLIDOS (AYA2010-21887-C04-01 and AYA2007-67965-C02).

The INT and WHT are operated on the island of La Palma by the Isaac Newton Group in the Spanish Observatorio del Roque de los Muchachos of the Instituto de Astrofísica de Canarias. I acknowledge CAT for the allocation of telescope time to this thesis and I thank the support astronomers of WHT (ING) for Service Time observations on June 26-27, 2009 and the directors of IAC and ING for the allocation of DDT on July 19, 2009.

This research has made use of the NASA/IPAC Extragalactic Database (NED), which is operated by the Jet Propulsion Laboratory, California Institute of Technology, under contract with the National Aeronautics and Space Administration.

IRAF is distributed by the National Optical Astronomical Observatory, which is operated by the Associated Universities for Research in Astronomy, Inc., under cooperative agreement with the National Science Foundation.

I have benefitted from Sloan Digital Sky Survey (SDSS) database. Funding for the SDSS, SDSS-II, and SDSS-III was provided by the Alfred P. Sloan Foundation, the Participating Institutions, the National Science Foundation, the U.S. Department of Energy, the National Aeronautics and Space Administration, the Japanese Monbukagakusho, the Max Planck Society, and the Higher Education Funding Council for England. The SDSS was managed by the Astrophysical Research Consortium for the Participating Institutions. The SDSS-III web site is http://www.sdss3.org/. SDSS-III is managed by the Astrophysical Research Consortium for the Participating Institutions of the SDSS-III Collaboration including the University of Arizona, the Brazilian Participation Group, Brookhaven National Laboratory, University of Cambridge, University of Florida, the French Participation Group, the German Participation Group, the Instituto de Astrofisica de Canarias, the Michigan State/Notre Dame/JINA Participation Group, Johns Hopkins University, Lawrence Berkeley National Laboratory, Max Planck Institute for Astrophysics, New Mexico State University, New York University, Ohio State University, Pennsylvania State University, University of Portsmouth, Princeton University, the Spanish Participation Group, University of Tokyo, University of Utah, Vanderbilt University, University of Virginia, University of Washington, and Yale University.

The ROSAT project is run by the German Aerospace Center (DLR) (former DARA), Bonn, by order of the Bundesministerium für Bildung, Wissenschaft, Forschung und Technologie (BMBF).